University of
Strathclyde
Science

Development of Novel Analytical Pipelines for the Evaluation of Ribonucleic Acid Therapeutics

A thesis presented for the degree of Doctor of Philosophy from the
Strathclyde Institute of Pharmacy and Biomedical Sciences.
Supervised by Prof Zahra Rattray and Prof Yvonne Perrie.

By

Callum G. Davidson

2026

Declaration of Authenticity

‘This thesis is the result of the author’s original research. It has been composed by the author and has not been previously submitted for examination which has led to the award of a degree.’

Copyright Statement

'The copyright of this thesis belongs to the author under the terms of the United Kingdom Copyright Acts as qualified by University of Strathclyde Regulation 3.50. Due acknowledgement must always be made of the use of any material contained in, or derived from, this thesis.’

Signed:

Date:

25/02/2026

Acknowledgements

When writing my thesis acknowledgements, I think about the village of people behind me, without whom this PhD and thesis would not have been possible. I am beyond rich in life because I have all of you continuously cheering me on and allowing me to flourish and achieve my goals.

Firstly, I want to thank my supervisor Prof Zahra Rattray for her continued support, enthusiasm and critical insights which have been invaluable in helping me grow personally and as an academic researcher. I am thankful for your mentorship and help in setting the foundations for my future endeavours. I am grateful to Prof Yvonne Perrie for her secondary supervision, collaboration and guidance throughout my studies. I am also thankful for the insights and feedback from Prof Nik Rattray throughout my PhD. I would also like to acknowledge and thank EPSRC for funding my PhD and travel bursary, which has allowed me to disseminate my research locally, nationally, and internationally, experiences which I am extremely grateful for.

A special thank you goes to Tan our MMS facility technician and FFF whisperer, for your continued help, patience and support. It’s been an absolute pleasure and delight working with you throughout my PhD. Deep gratitude goes to the wider Rattray Translational Pharmaceutical Lab for all their collaboration, support and fun over the years of my PhD. Thank you to the strath student Recruitment and International Office, from undergrad to PhD, I have loved being a student ambassador and being one of the many student faces of the university. It has been a pleasure working with you all. Also, a big shoutout to all the SIPBS Robertson Wing estates staff, your humour, authenticity and conversations have been great! Thank you to all my collaborators over my PhD studies, your input has been greatly appreciated and helped shape me into a better researcher.

To my Mum and Dad, Yvonne and Kevin, I wish I had the words to articulate the level of thanks I have for you both for being my biggest supporters throughout my studies and life. I am forever grateful for your continued unconditional love, support, encouragement and being the best parents I could have ever hoped for. Without you both, I certainly wouldn’t be the person I am today and that if I ‘*think Shamu and Believe’* I truly can do anything I put my mind to. This achievement is as much yours as it is mine.

A heartfelt thank you goes to my fiancé, Błażej, your calming nature and grounding presence has been a major source of comfort during my PhD. Thank you for always reminding me what’s important in life and for always being in my corner. You have an incredible way of making me smile and laugh without trying and I am beyond lucky to have you by my side.

Special thanks go to my sister and brother, Emma and Andrew. Your encouragement, hilarity and support mean the world to me, and I count myself incredibly lucky and fortunate to have you both in my life. I can’t forget to thank Lottie, our four-legged hairy wain, love you Lotts. To my grandparents, I thank you for your love and enthusiasm in listening to and asking about my activities during my PhD.

To my friends and divas who have been by my side throughout this, I thank you all deeply and because of you, I have been changed for good. Thank you for your endless support and memories over the years, and for the plenty more that are yet to come. To my straths finest, Erin, Dr Tricia, Dr Maria, Dr Zoe, Rana, and Lisa hen, thank you all for making my PhD journey so incredible. It truly wouldn’t have been the same without you, and I’ll remember it all too well!!

And finally, this thesis could not have been completed without entertainment of ‘The Eras Tour’ and ‘The Mayhem Ball’ provided by Dr Taylor Swift and Lady Gaga, respectively. The values you have taught through your music have been inspiring, and motivational which I will continue to hold dear in my future endeavours.

I dedicate my thesis in heartfelt, loving memory to my wonderful Auntie Jean. Whose courage, honesty, and compassion will forever be an inspiration.

Abstract

Nanomedicines represent an emerging therapeutic class, which supersede traditional small molecule drugs. As nanomedicines are inherently complex, analysis of their associated critical quality attributes (CQAs) is essential to ensure accurate and representative physicochemical characterisation for downstream translation. Of these nanomedicines, lipid nanoparticles (LNP) encapsulating nucleic acid therapeutics, specifically ribonucleic acid (RNA) therapeutics demonstrate unmatched applicability for inherited conditions, treatment resistant disease and rare illness. RNA therapeutics act on protein-mediated pathways by preventing, correcting, or modulating the production of specific proteins. Depending on the therapeutic design, they can elicit an immune response to drive antibody generation or regulate gene expression through targeted gene silencing or activation mechanisms.

Unencapsulated RNA-based therapeutics face several biological delivery barriers, which have driven the widespread adoption of LNP-based drug delivery systems, and contributing to the approval of several RNA-LNP nanomedicines. However, the incorporation of RNA cargo in LNP drug delivery systems, adds an additional layer of complexity to these formulations, increasing the need for robust analytical techniques for quantifying associated critical quality attributes within early discovery and development settings. Despite the rapid growth in RNA-LNP technologies and research, advances in analytical pipelines for these therapeutics have not kept pace, resulting in a significant knowledge gap and a lag in the development of complementary and orthogonal techniques required for the comprehensive characterisation of RNA-LNP associated CQAs. Conventional analytical methods currently relied upon within the field present resolution challenges, which under characterise, complex therapeutics, creating the need for novel pipelines to ensure enhanced and robust characterisation of candidate therapeutics to advance through early development trials.

Therefore, the central hypothesis underpinning this thesis is that current analytical methods used to characterise RNA and RNA-LNP formulations provide limited understanding of their physicochemical parameters that reflect the true physical state of these complex therapeutics. This limited analytical resolution in resolving the effects of formulation and process-related parameters, poses a barrier to the efficient clinical translation of novel and emerging RNA-LNP nanomedicines, in addition to pre-existing undesired immunogenicity, and lack of overall selective tissue targeting.

To investigate this hypothesis, RNA drug substance and model systems were investigated across the RNA to LNP translation process, using a suite of pipeline approaches with varying resolution and orthogonality. By examining RNA prior to and following incorporation into LNP

delivery systems, this work aims to improve mechanistic understanding of how formulation variables shape CQA outputs and, ultimately, therapeutic performance. **Chapter 1** defines current analytical techniques, their applications and limitations, whilst introducing state-of-the-art pipelines for RNA and RNA-LNP CQA quantification, addressing the need for higher-resolution analysis of candidate nanomedicines within early development settings to inform candidate selection.

Chapter 2 details the method development of hydrophilic interaction liquid chromatography (HILIC), hyphenated with online photodiode array (PDA) and mass spectrometry (MS)-based detectors. This study compared analytical resolution across different MS platform systems, comparing single quadrupole (SQ) with Orbitrap (orbi) for antisense oligonucleotide (ASO) detection and impurity quantification. Of the six oligonucleotides (ONs) tested, two ON impurity profiles matches between SQ/orbi evaluation, two ON impurity abundances were higher on the SQ than orbi and two ON impurity abundances were higher on orbi than SQ. Orthogonal techniques, including gel electrophoresis and ion-pairing reverse-phase liquid chromatography (IPRP-LC), were incorporated to support separation and quantification. Together, these results established an analytical framework capable of differentiating ASO drug-substance CQAs that are undetectable with conventional, lower-resolution methods.

Building on the ASO drug substance analytics, **chapter 3** applied a multi-platform pipeline to the analysis of ASO-LNP formulation, with varying lipid nitrogen headgroup to RNA phosphorous backbone group (N/P ratio), ionisable lipid composition (SM102, MC3), microfluidics flow rate ratio (FRR), and total flow rates (TFR). Using an orthogonal analytical pipeline incorporating frit-inlet asymmetric flow field flow fraction (FI-AF4) with online UV, multiangle- and dynamic- light scattering, the study revealed marked differences in particle size, size distribution and morphology-based across the ASO-LNP formulation panel, differences that could not be fully discerned by conventional low-resolution analytical techniques. Formulations parameters such as main ionisable lipid choice and microfluidic total flow rate were key formulation parameters impacting exploratory analytical ASO-LNP CQA outputs.

Findings from chapter 2 and 3 highlight CQA output changes using ASOs as a drug substance incorporated into an ASO-LNP drug product. **Chapter 4** investigated Poly(A) as a model mRNA cargo encapsulated widely during LNP formulation composition and process-related studies. Despite its widespread use, Poly(A) quality attributes remain uncharacterised across commercial vendors, Poly(A) samples from three vendors were evaluated for their Poly(A) chain length and molecular weight (MW) distributions as a function of vendor, whilst comparing their associated CQAs using enhanced orthogonal analytical techniques. Poly(A) vendor

CQAs and their downstream impact on LNP CQAs were evaluated to gain insights into Poly(A) CQA effects on LNP formulations. Poly(A) size and heterogeneity showed clear vendor-specific trends. However, when these Poly(A) samples were incorporated into LNP formulations under controlled microfluidics manufacturing conditions, vendor-specific differences did not translate into measurable changes in LNP CQAs. Correlative analyses provided deeper insights into relationships between RNA attributes and formulation outputs, demonstrating the value of enhanced analytics for model RNA systems, underpinning classical colloidal stability DLVO theory.

Early assessment of candidate nanomedicine formulations remains crucial for establishing changes in LNP CQAs during formulation and process development. In **chapter 5**, impact of formulation process parameters, short-term refrigerated stability and frozen storage stability on LNP CQAs were examined using a model DOTAP-Poly(A) LNP formulation. An AF4-MD pipeline provided high-resolution measurements of particle concentration, size, distribution, and shape. AF4 analysis of cationic LNPs proved challenging due to electrostatic interactions with the anionic separation membrane, leading to particle loss. Membrane preconditioning strategies were implemented to mitigate these interactions, enabling successful analysis across formulations with differing physicochemical attributes. These findings reinforce the need for robust high-resolution analytics during early formulation and stability assessment, which show that > 20% sucrose (w/v) is needed for enhanced cryoprotectant properties to prevent DOTAP-LNP aggregation from frozen storage to ambient temperature cycling.

The results presented in this chapter demonstrate that the incorporation of asymmetric-flow field-flow fractionation hyphenated to inline multidetector system (AF4-MD) enhanced RNA-LNP CQA analysis beyond lower resolution techniques. **Chapter 6** applied a computational approach to further advance insights into CQAs by applying AF4-based elution profiles towards a data-processing pipeline. These insights highlight size (2-6) and RNA load (2-7) subpopulations within a panel of RNA-LNP formulations using different constituent lipids and nucleic acid payloads. In-depth analysis of these results provided higher resolution insights into internal LNP nanoarchitecture, linking size, RNA loading and morphology with key sub-populations. Advanced data-processing also highlights corresponding weight fractions of RNA per formulation and associated numbers of RNA per LNP formulation to further link with size, size distribution and morphology parameters. This approach enhanced insights beyond the scope of the RiboGreen^{TM} encapsulation assay to determine nucleic acid loading numbers. The computational-based approach enhanced CQA insights beyond the resolution-power of AF4 separation and detection systems, by highlighting key-populations with varied RNA concentration levels, differing size, morphology and internal architectures.

Collectively, this thesis advances the application of field-flow fractionation–based analytics for RNA therapeutics, demonstrating resolution and insight that surpass existing pipelines widely used in the field. Comparative studies with mass spectrometry further highlight complementary strengths and define where each method offers the greatest analytical value. The analytical strategies developed throughout this thesis provide a foundation for improved characterisation of RNA and RNA-LNP systems, supporting more reliable development and translation of next-generation RNA therapeutics for improved patient outcomes.

List of Publications

- **Davidson C.G.**, Abdulrahman R, Punnabhum P, *et al.* The use of orthogonal analytical approaches to profile lipid nanoparticle physicochemical attributes.*, Nano Futures*., **2024**; 8(3):035001. (https://doi.org/10.1088/2399-1984/ad70e6)
- Forrester, J.; **Davidson, C.G.**; Blair, M., *et al.* Low-Cost Microfluidic Mixers: Are They up to the Task? *Pharmaceutics,* **2025**, 17, 566. (https://doi.org/10.3390/pharmaceutics17050566)
- Considine P., Punnabhum P., **Davidson CG**., et al, Insights into the aggregation properties of a novel therapeutic Immunoglobulin E., *mAbs,* **2025,** 17(1), 2512211. (https://doi.org/10.1080/19420862.2025.2512211)
- **Davidson C.G.**, Kapsali, E., Ioannou, S., *et al.* The Use of Enhanced Analytical Pipelines for the Characterisation of Poly(A) and Poly(A)-LNP Formulation Critical Quality Attributes, **2025,** 22 (12), 7383. (https://doi.org/10.1021/acs.molpharmaceut.5c00614)

List of Oral and Poster Presentations

Oral Presentations:

- *Next Generation Lipid Nanoparticle Therapeutic Stability Evaluation,* University of Strathclyde Doctoral Research Group, Summer DSMS 2023, **C. G. Davidson**, R. Abdulrahman, Y. Perrie, Z. Rattray.
- *Orthogonal Pipelines for Lipid Nanoparticle Evaluation*, Federation of Analytical Chemistry and Spectroscopy Societies SciX 2023, **C. G. Davidson**, R. Abdulrahman, P. Punnabhum, Y. Perrie, Z. Rattray.
- *High-Resolution Orthogonal Techniques for Separating and Detecting Impurities in Antisense Oligonucleotide Therapeutics,* Joint Pharmaceutical Analysis Group 2024, **C. G. Davidson**, P. Punnabhum, G. Farrell, Y. Perrie, Z. Rattray.
- *Evaluation of Purity Profiles in Next-Generation RNA Therapeutics,* University of Strathclyde Doctoral Research Group, Winter DSMS 2024, **C. G. Davidson**, P. Punnabhum, G. Farrell, Y. Perrie, Z. Rattray.
- *Orthogonal Analytical Insights into Nucleic Acid Therapeutics,* CPI MMIC Analytical Methods Forum 2025, **C. G. Davidson**, E. Kapsali, Y. Perrie, Z. Rattray. (invited talk)
- *Enhanced Analytical Insights into Ribonucleic Acid Therapeutics,* SIPS CBD Seminar Session 2026, **C. G. Davidson**, E. Kapsali, Y. Perrie, Z. Rattray. (invited talk)

Poster Presentations:

- *Go with The Flow – High Resolution Nanoparticle Metrology,* ETPN NanoMed Europe Conference 2023, **C. G. Davidson**, R. Abdulrahman, P. Punnabhum, Y. Perrie, Z. Rattray.
- *Higher or Lower? – The Resolution of Analytical Pipelines for the Evaluation of RNA-Lipid Nanoparticles*, Academy of Pharmaceutical Sciences PharmSci 2023, **C. G. Davidson**, R. Abdulrahman, M. Cairns, Y. Perrie, Z. Rattray.
- *Would You Like a Carrier With That? – High Resolution Analysis of RNA With and Without a Lipid Nanocarrier System,* International Symposium on Field- and Flow-based Separations 2024, **C. G. Davidson**, P. Punnabhum, Y. Perrie, Z. Rattray.
- *Lipid Nanoparticle Critical Quality Attribute Evaluation using Orthogonal Analytical Techniques,* Malvern Panalytical 3rd Pharma Conference 2024, **C. G. Davidson**, R. Abdulrahman, M. Cairns, Y. Perrie, Z. Rattray.
- *Orthogonal Analytical Insights from RNA Drug Substances to Lipid Nanoparticle Drug Products,* Academy of Pharmaceutical Sciences PharmSci 2025, **C. G. Davidson**, E. Kapsali, Y. Perrie, Z. Rattray.
- *Characterisation of Nucleic Acid Drug Substance to Drug Product Critical Quality Attributes,* Strathclyde Institute of Pharmacy and Biomedical Sciences PG Research Day 2025, **C. G. Davidson**, E. Kapsali, Y. Perrie, Z. Rattray.

List of Funding

- Bursary (£250) – Royal Society of Chemistry Glasgow and the West of Scotland Local Selection Committee, June 2024.
- Bursary (£500) – The Chromatographical Society Grass Roots 7, 'Introduction to oligonucleotide characterisation', June 2025.

List of Teaching Opportunities

- Supervision of three MSc Advanced Drug Delivery research projects.
    - 1x 2022-23, 2x 2023-24.
- Pure and Applied Chemistry laboratory demonstration.
    - 1st year undergraduate groups between 2022-2025.

Abbreviations

AF4	Asymmetric Flow Field-Flow Fractionation
AI	Artificial Intelligence
ALC	(4-hydroxybutyl)azanediyl]di(hexane-6,1-diyl) bis(2-hexyldecanoate)
aSEC	Analytical Size Exclusion Chromatography
AUC	Area Under the Curve
ASO	Antisense Oligonucleotide
BP	Base Pairs
BSA	Bovine Serum Albumin
C12	1,1′-[[2-[4-[2-[[2-[bis(2-hydroxydodecyl)amino]ethyl](2-hydroxydodecyl) amino]ethyl]-1-piperazinyl]ethyl]imino]bis-2-dodecanol
CGE	Capillary Gel Electrophoresis
CHOL	Cholesterol
CQA	Critical Quality Attribute
DLS	Dynamic Light Scattering
DMG-PEG2000	1,2-dimyristoyl-rac-glycero-3-methoxypolyethylene glycol-2000
DNA	Deoxyribonucleic Acid
DoE	Design of Experiments
DOTAP	1,2-dioleoyl-3-trimethylammonium-propane
dRI	Differential Refractive Index
DSPC	1,2-distearoyl-sn-glycero-3-phosphocholine
EAF4	Electrical Asymmetrical Flow Field-Flow Fractionation
EE	Encapsulation Efficiency
ELS	Electrophoretic Light Scattering
FDA	U.S. Food and Drug Administration
FFF	Field-Flow Fractionation
FI	Frit-Inlet
FI-AF4	Frit-Inlet Asymmetric Flow Field-Flow Fractionation
FLD	Fluorescence Detector
FLP	Full Length Product
FRR	Flow Rate Ratio
GFP	Green Fluorescent Protein
HILIC	Hydrophilic Interaction Liquid Chromatography
HMWS	High Molecular Weight Species
HPLC	High-Performance Liquid Chromatography

ICH	International Council for Harmonisation
IVT	*In-Vitro* Transcription
LC	Liquid Chromatography
LMWS	Low Molecular Weight Species
LNA	Locked Nucleic Acid
LNP	Lipid Nanoparticle
MALS	Multi-Angle Light Scattering
MB	Mass Balance
MC3	((6Z,9Z,28Z,31Z)-Heptatriaconta-6,9,28,31-tetraen-19-yl-4-(dimethylamino)butanoate)
MD	Multi-Detector
mRNA	Messenger Ribonucleic Acid
MS	Mass Spectrometer
MW	Molecular Weight
MWCO	Molecular Weight Cut-Off
N/P Ratio	Nitrogen-to-Phosphorus Ratio
NP	Nanoparticle
nRMSE	Normalised Root Mean Square Error
NTA	Nanoparticle Tracking Analysis
Orbi	Orbitrap Mass Spectrometer
PBS	Phosphate Buffered Saline
PDA	Photodiode Array
PDI	Polydispersity Index
PEG	Polyethylene Glycol
Poly(A)	Polyadenylic Acid
QC	Quality Control
R_G	Radius of Gyration
R_H	Hydrodynamic Radius
RISC	RNA-Induced Silencing Complex
RNA	Ribonucleic Acid
RNA-LNP	RNA–Lipid Nanoparticle
RMS	Root Mean Square
RMSE	Root Mean Square Error
RSV	Respiratory Syncytial Virus
SAXS	Small-Angle X-Ray Scattering
SEC	Size Exclusion Chromatography
SF	Shape Factor

SHM	Staggered Herringbone Micromixer
SM102	heptadecan-9-yl-8-[2-hydroxyethyl-(6-oxo-6-undecoxyhexyl)amino] octanoate
S/N	Signal-to-Noise Ratio
TE	Tris-EDTA Buffer
TFR	Total Flow Rate
TTR	Transthyretin
UHPLC	Ultra-High Performance Liquid Chromatography
UV	Ultraviolet

Contents

List of Figures

List of Supplementary Figures

List of Tables

List of Supplementary Tables

List of Equations

Chapter 1

1. Introduction

1.1. Current Therapeutic Landscape

Why take medicine? To prevent or reduce the prevalence of disease, injury or pain, to improve health and overall quality of life. Through combinatorial interactions between medicine-drug target, a response is delivered and mode of action produced for effective management. Traditional medicines consist of synthetic small molecules (e.g. paracetamol, ibuprofen), which require a receptor mediated target to exert their therapeutic effect. Of the total human proteome, only 4-11 % has been targeted by approved drugs, leaving untapped potential and a need for new therapeutic modalities (1,2). Conventional medicines are widely used across therapeutic domains to improve patient prognosis. Traditional small molecule drugs are constrained by their pharmacokinetic and pharmacodynamic properties, requiring the design of effective dosing strategies to ensure optimal therapeutic efficacy and minimal off-target adverse events (3).

Therapeutic limitations traditionally associated with -small molecule drugs can be overcome by formulating medicines at the nanoscale (1–100 nm). Nanomedicine has emerged from advances in nanomaterials, biomedical engineering, and pharmaceutical sciences. Nanoscale materials possess unique size-, shape-, composition-, and surface dependent- properties that enhance the pharmacological and biological performance of therapeutic agents, thereby increasing the likelihood of successful clinical translation (4).

Nanomedicine is defined by the European Medicines Agency (EMA) in 2010 as;

> *"The application of nanotechnology in view of making medical diagnosis or treating or preventing diseases. It exploits the improved and often physical, chemical and biological properties of materials at the nanometre scale"* (5).

A recent review of the nanomedicine market landscape detailed that there are approximately 100 clinically-approved nanomedicines, with a further 563 candidates undergoing various phases of clinical trial evaluation (6–8). These nanomedicine compositions can be broadly classified as organic based nanoparticles (NPs), inorganic based nanoparticles, and biological delivery systems. **Table 1.1** denotes the classes of delivery platforms and exemplar associated systems (9,10).

***Table 1.1** - Current marketed nanomedicine compositions according to constituent materials, *used for intracellular delivery (7,11).*

Nanomedicine Drug Delivery Platforms		
Organic	**Inorganic**	**Biological**
Liposomes(12)*	Polymeric NPs(13)*	Viral Vectors(14)*
Lipid NPs(15)*	Metallic NPs(16)	Cell-derived vehicles(17)*
Emulsions(18)	Nanocrystals(19)	Molecular Conjugates(20)

Lipid based nanomedicines have become a dominant platform in therapeutic nanomedicine development. Shan *et al.* reported that approximately 30% of nanomedicine candidates under clinical investigation were lipid-based (6,7), highlighting the growing popularity and clinical success of lipid-based nanomedicines. Among these, liposomes represent the most clinically-established modality, with the regulatory approval of Doxil® in 1995 catalysing liposome use in small molecule formulated systems (21).

In recent years, interest has increasingly focused on lipid-based nanoparticles (LNPs), particularly following the landmark approval of Onpattro® in 2018. Onpattro® is the first LNP-enabled therapeutic to reach the clinic and consists of a lipid formulated small interfering RNA (siRNA) designed for gene silencing (22,23). Its approval catalysed a wave of LNP-based RNA medicines, most notably the Pfizer/BioNTech and Moderna COVID19 vaccines authorised in 2021, and more recently, Moderna's mRESVIA® vaccine for respiratory illness (23–25). These developments have firmly established LNPs as a clinically validated platform for the delivery of nucleic acid therapeutics.

1.2. Ribonucleic Acid Drugs

Overcoming the limitations inherent in traditional small molecule therapeutics, that require interaction with extracellular or plasma membrane receptors to initiate a biological response (26), nucleic acid drugs have emerged as a promising alternative capable of targeting a broader spectrum of diseases mechanisms in areas of unmet clinical need (27,28). Instead, RNA molecules act through direct hybridisation or interaction with complementary nucleic acid sequences in the cell cytoplasm, where they modulate gene expression through mechanisms such as mRNA degradation, translational inhibition, or protein expression (antigen, antibody, signalling protein, enzyme, gene editor). This receptor-independent mechanism of action enables highly specific and programmable regulation of intracellular pathways, thereby broadening the scope of diseases that can be targeted using RNA therapeutics.

Over the past decade, the use of synthetic RNA molecules in cellular function has garnered significant research interest. This surge is driven by advancements in molecular biology research, discovery of the RNA interface, and detailed insights into disease pathways, all of which have led to the development of advanced therapeutics. The first RNA-based drug, Fomivirsen® was approved in 1998 (29), since which the RNA central dogma has been exploited as targets for various coding and non-coding RNA therapeutics (30,31).

1.2.1. Classes of RNA Drugs

The main classes of clinically approved RNA therapies can be categorised as antisense oligonucleotides (ASOs), short interfering double-stranded RNA (siRNA) and messenger RNA (mRNA). ASO/siRNA are typically 10-30 nucleotides long, whereas mRNAs are ~1,000 nucleotides in length, depending on the biological target. siRNAs are composed of a sense RNA strand paired with a complementary antisense strand that guides sequence-specific gene silencing. mRNA therapeutics are commonly associated with enabling protein expression for immune system activation, whereas ASOs and siRNAs are linked to mRNA degradation or for altering protein expression linked to genetic diseases.

1.2.1.1. RNA Drug Mechanisms of Action

With differing applications of RNA drugs, their mechanism of action remains a critical evaluator to ensure therapeutic bioavailability. **Figure 1.1** highlights mechanistic overview of approved RNA therapeutic classes, siRNA and mRNA.

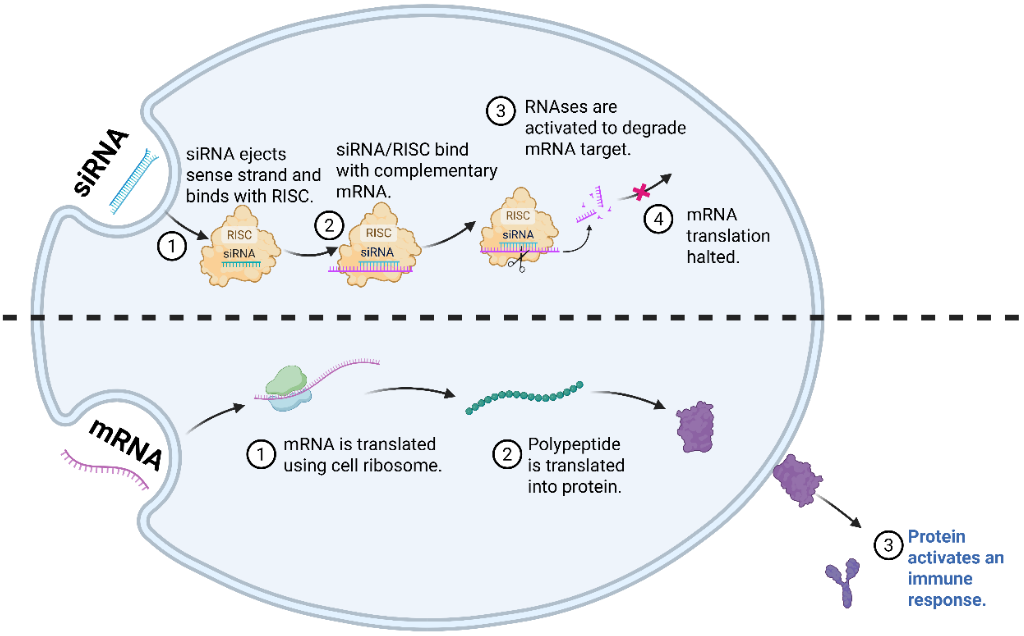

Figure 1.1 - Approved nucleic acid drugs and associated mechanisms of action on reaching the cellular cytoplasm. Made with BioRender®..

On reaching the target cellular domain, the nucleic acid enters the cell *via* endocytic uptake following surface electrostatic interactions or association with cell-specific receptors. Once internalised and following endosomal escape, RNA therapeutic mechanisms of action vary. The sense strand of siRNA is ejected and a single antisense strand binds with cellular RNA-Induced silencing complex (RISC). Subsequently, the RISC/siRNA binds with the complementary mRNA target sequence. On complexation, RNAses degrade the mRNA target, thus halting further cellular translational processes (**Figure 1.1**). siRNAs can be used to silence genes involved in disease progression, or to correct hereditary conditions (32,33). Alternatively, delivered mRNA molecules are translated using ribosome cellular machinery into a polypeptide molecule. The polypeptide intermediate is further translated into resultant protein which mRNA drug encodes for. The produced protein can be utilised to exhibit an immune response and enable an activation of immune system to produce antibodies against the encoded protein, preventing disease onset or rapid decline (34,35).

1.2.2. Challenges in RNA Drug Development

The goal of RNA delivery is to improve patient outcomes in inherited conditions, genetic or treatment resistant diseases, by directly correcting underlying aberrant genetic or molecular disease pathways. For RNA-based drugs to exert their intended therapeutic effects, they must successfully overcome a series of chemical, biological, and physiological barriers. These challenges span molecular stability, intracellular trafficking, immune recognition, and biodistribution, all of which must be addressed to enable effective bench-to-bedside clinical translation.

RNA degradation *in vivo* is primarily driven by RNA nucleases (RNAses), which poses a major biological barrier to the efficient distribution of RNA therapeutics to target cells/tissues or organs. Owing to RNAs being large, strongly anionic, and hydrophilic under physiological conditions (36). RNA molecules readily attract and bind cationic species, forming adducts or analogues that further influence their stability and biodistribution. Their anionic charge at physiologic pH also prevents passive diffusion across the plasma membrane, increasing their exposure to nucleases, which accelerates their degradation (37). Therefore, current approved ASO/siRNA-based therapeutics are predominantly administered *via* ocular or spinal cord localised delivery, or are targeted for hepatic drug delivery (30,38,39), whereas mRNA vaccines are administered intramuscularly and use passive uptake linked with their stealth design for hepatic uptake. To overcome the substantial challenges associated with delivery of intact RNA to intracellular sites of action, various delivery strategies have been developed that are discussed in **section 1.2.3**.

Formulation-related barriers that RNA-based drugs face, include a consideration of their physical stability within the formulation and environmental factors, which can impact shelf-life (40). While RNA drugs are generally stable when formulated in a compatible storage buffer, the choice of buffer system and formulation additives must also be considered to enhance both stability and delivery performance, while maintaining therapeutic efficacy.

1.2.3. Delivery of RNA-based Therapies

Platforms used for RNA delivery typically include one of three strategies: the use of chemical modifications, direct bioconjugation to a targeting ligand, or encapsulation within a nanocarrier to protect the RNA from degradation and promote efficient intracellular delivery.

1.2.3.1. Chemical Modification

Singular nucleotide monomers can be chemically modified through a variety of substitutions and alterations to enhance target specificity, sensitivity, affinity, and overall therapeutic stability. Chemical modifications are implemented during the synthesis of RNA drugs.

The synthetic approach used to manufacture RNA-based drugs is largely dictated by the size and structural complexity of the target molecule. Small RNAs, typically ranging in 10-30 nucleotides (-mers) are commonly synthesised through solid-phase synthesis, using a cyclical catalytic process in which monomers are sequentially added to a solid support until the target sequence is synthesised (41,42). In contrast, larger RNAs (e.g. >100-mer) are synthesised by enzymatic routes, often using *in-vitro* transcription (IVT) templates derived from *E.coli* to produce mRNAs (43,44).

Irrespective of the synthetic route employed, RNA drugs must undergo post manufacture processing and purification prior to clinical use. A major challenge associated with each process is the presence of process-related impurities, which are difficult to separate, isolate and remove from target molecular sequence due to high similarity of molecular weights. These hard to separate impurities are mainly composed of $n+1$, $n-1$ impurities, where n is the target chain length of the desired RNA drug (45,46). Therefore, synthetic RNA drugs must be profiled for their impurities prior to their incorporation into formulations. Since chemical modifications are included within nucleic acid drug synthesis, the main modifications of a singular monomer include phosphate backbone modification, 2'-ribose sugar substitutions and ribose conformational changes (39,47–49).

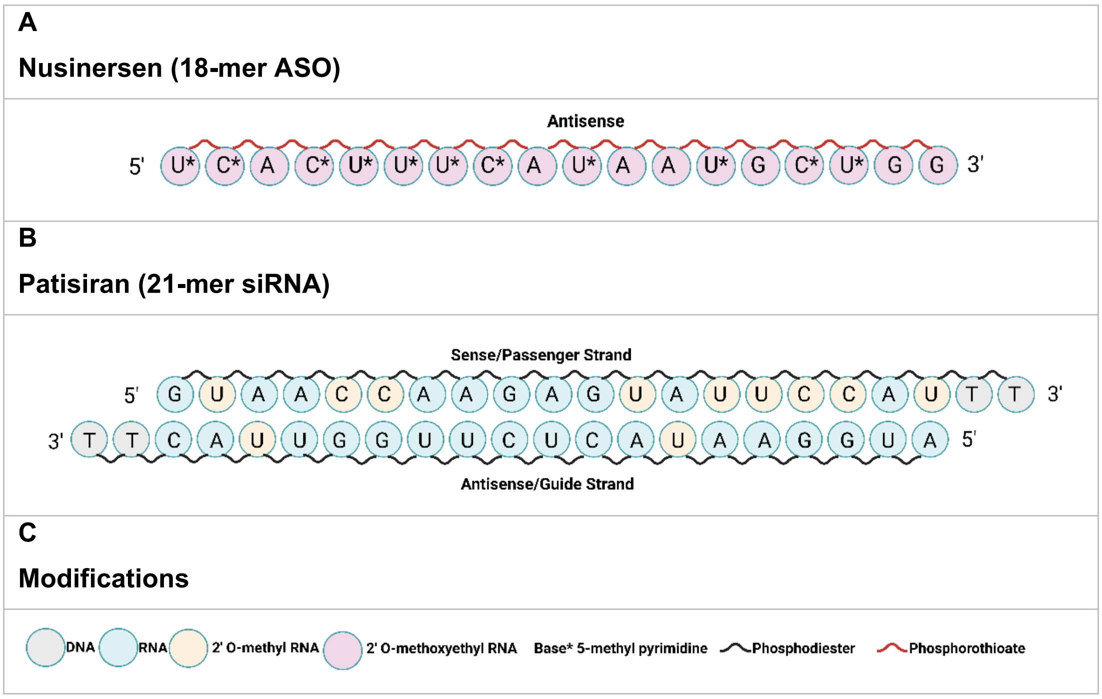

Figure 1.2 *- Clinically approved RNA therapeutic chemical modifications, showing A) Nusinersen ASO, B) Patisiran ASO and C) associated chemical modifications. Adapted from (35 using BioRender®).*

The primary objective of oligonucleotide chemical modification is to improve RNA stability *in-vivo*, ensuring that the molecule remains intact long enough to reach its intended target and exert its therapeutic effect. These modifications aim to prevent premature degradation, enhance target affinity, and minimise off-target interactions. As illustrated in **Figure 1.2** several key chemical alterations are commonly employed (**Table 1.2**).

Table 1.2 – Chemical Modification differences versus unmodified and standard nucleobases. Created in ChemDraw.

Modification	Unmodified	Modified
Backbone	PO 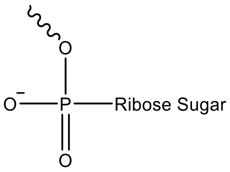	PS 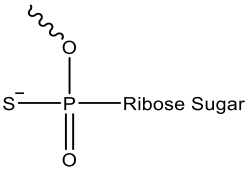
Ribose Sugar	2' OH 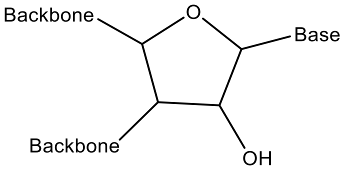	2' OMe 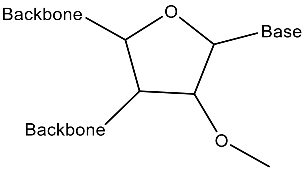
Ribose Sugar	2'-OH 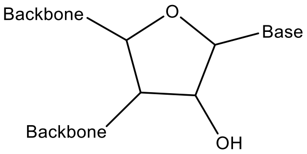	2' MOE 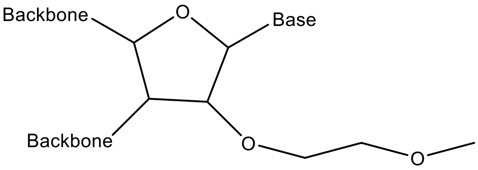
Nucleobase Methylation	5' unmodified cytidine 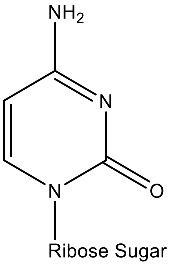	5' methylcytidine 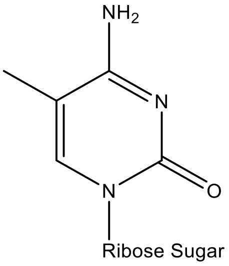

Ribose sugar modifications, such as the substitution of the native 2′-hydroxyl group in RNA with 2′-O-methyl or 2′-O-methoxyethyl groups, improve hybridization affinity while removing the reactive hydroxyl group and replacing it with a less electronegative substituent. Additionally, 5-methylation of pyrimidine bases, specifically cytosine and uridine, introduces hydrophobic patches that strengthen base stacking interactions and enhance RNA resistance to hydrolytic deamination, which converts cytosine to uracil. This modification has been utilized in clinically approved antisense oligonucleotides such as Mipomersen and Inotersen.

Finally, the phosphorothioate (PS) modification involves replacing a non-bridging oxygen in the phosphodiester backbone with sulfur. This substitution significantly increases resistance to nuclease-mediated degradation, thereby extending therapeutic half-life in biologically complex environments. However, PS linkages also introduce chiral centres at the phosphorus atom, conferring additional stereochemical complexity to the backbone.

1.2.3.2. Bioconjugation Delivery Strategies

Bioconjugation strategies prioritise the delivery of nucleic acid therapeutics to enhance targeting to the desired site of action. Bioconjugates are primarily attached to RNA drug cargo through covalent modification, allowing for stable carrier-drug payload attachment. Bioconjugates include lipids (50), peptides (51,52), antibodies (53–55), aptamers, polymers (56) and small molecules (38,57).

These conjugates have three distinct components*:(i)* the carrier, *(ii)* a linker connecting the carrier to payload, and the *(iii)* RNA drug. Each bioconjugate component must be considered during the conjugate design stage to reduce overall synthesis complexity, improve conjugate chemical and biological stability, and increase bioavailability. Interest has grown within the nucleic acid conjugate field in the conjugation of ASOs to triantennary *N*-acetylgalactosamine (GalNAC) for liver-receptor recognition and uptake (58,59). Lipidated peptide drugs have also been shown to enhance cellular uptake thus improving their pharmacokinetic properties (60,61). These enhancement principles could be transferable to oligonucleotides to improve nucleic acid drug bioavailability. (62) as well as an increased oligonucleotide bioavailability through antibody conjugation (53,54). Translating existing knowledge from small molecule and lipid/antibody conjugates towards larger, hydrophilic nucleic acid drug molecules can be applied to enhancing RNA-based drug bioavailability and stability.

1.2.3.3. Nanoparticle-Based Delivery Systems

Various nanoparticle platforms ranging from organic, inorganic and biological based systems can be used for the delivery of bioactive drug cargo (63–69) (**Table 1.1**). Viral vectors have been considered for their use in RNA delivery, however due to immunogenicity, RNA cargo loading limitations and scalability, they remain within design and conceptual studies. Polymeric nanoparticles have been considered for RNA delivery due to their favourable manufacturability and inherent monodispersity. However, they suffer from low biocompatibility due to charge dense polymer usage and limited RNA encapsulation efficiency (70). Metallic NPs (gold, silver, iron oxide, zinc) are predominantly used as theranostics that consist of multilayered nanoparticles, requiring complex synthesis pipelines limiting their use. Key factors affecting RNA delivery include poor drug loading (<50 %) on the nanoparticle surface through electrostatic passive adsorption, limited particle surface area, (71) and the known toxicity profiles associated with metal-based NPs (72).

1.3. Lipid-based Nanocarriers

Lipid-based nanocarriers have emerged as promising RNA delivery systems, with their bioinspired design, efficient RNA encapsulation (>95%) during manufacture and fusogenic properties allowing drug cargo release. A study by Egli *et al.*(73), highlighted that RNAs required less chemical modification with the use of a lipid nanocarrier than RNA delivery alone. RNA-LNPs are used to overcome formulation and biological translational barriers in recent years, proving a popular and successful choice over metallic or polymeric nanoparticles.

A phospholipid bilayer is one of the oldest biological systems known in evolutionary biology, and in 1965, the first lipid bilayer particle was discovered by Bangham *et al.* (74) when examining suspensions of phospholipids in water. The lamellar structured self-assembled particles were coined as banghasosomes, which were renamed liposomes in 1968 by Sussa *et al.* (75). The study of cell bilayers has underpinned the discovery of liposomes and LNPs. Liposomes have been used to deliver small molecule drugs, whereas LNPs are predominantly used to deliver anionic RNA drugs. Although there are many inherent similarities between liposomes and LNPs, they differ notably in their structural and physicochemical features (**Table 1.3**).

***Table 1.3** – Differences in the structural and drug delivery properties of liposome and LNPs as nanocarriers. Figure adapted from (76). Created in BioRender®.*

Liposome	**Lipid Nanoparticle**
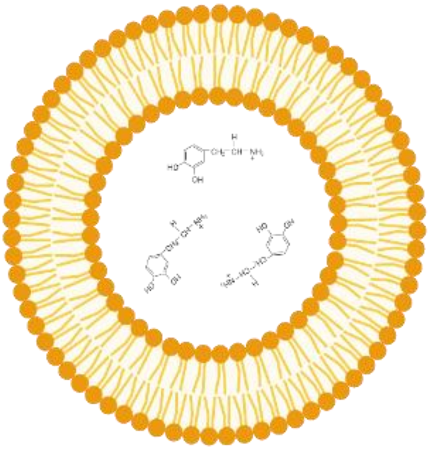	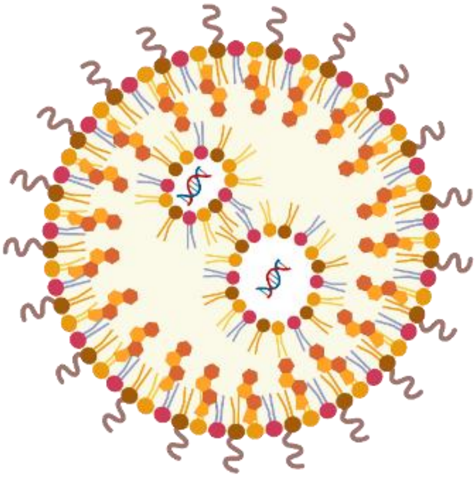
Single, or multiple bilayers of lipids around the core.	Single, outer layer of lipids.
Contains an aqueous core where drugs can be actively loaded after manufacture from pH gradient across the lamellar bilayer at temperatures below the lipid transition point.	Lipid nanoparticles contain an RNA drug encapsulated lipid core, surrounded by a secondary layer of lipids, the drug cargo is encapsulated during the manufacture process at ambient temperature.
Both systems can be manufactured using thin film hydration, solvent injection, and microfluidics **(section1.3.2).**	
Liposomes are made of 3-4 components, i) phospholipid, ii) sterol, iii) Pegylated lipid and iv) small molecule drug.	LNPs are made of 5 main components, i) main ionisable lipid, ii) sterol, iii) helper phospholipid, iv) pegylated lipid and v) nucleic acid payload.
CQAs: • **Size =** 60-100 nm • **PDI =** < 0.2 • **ZP** -30 mV to near neutral. • **% EE =** > 80%	CQAs: • Size = 60-120 nm • PDI = < 0.2 • ZP = -10 mV - +10 mV • % EE = > 90%

Of the 90 commercially available nanomedicines (11), the main approved lipid based nanocarriers are liposomal as the technology has been researched significantly longer than LNPs (77,78). **Table 1.4** details the list of FDA-approved marketed lipid nanocarrier drug formulations.

Table 1.4 *- Approved Marketed Lipid Nanocarrier Formulated Drugs by the FDA (15) for medicinal use only, not including other formulation types, vitamins or cosmetics. Drug loaded, lipid carrier therapeutic application and approval year are tabulated from 1995-2021.*

Drug Loaded	***Lipid Carrier***	***Drug Type***	***Clinical Indication***	***Approval Year***
Doxorubicin	Liposome	Small Molecule	Karposi sarcoma, ovarian cancer, multiple myeloma	1995
Amphotericin B lipid complex	Liposome	Small Molecule	Fungal infection	1995
Daunorubicin	Liposome	Small Molecule	Karposi sarcoma	1996
Amphotericin B	Liposome	Small Molecule	Fungal Injection	1997
Cytarabine	Liposome	Small Molecule	Lymphoma	1999
Poractant Alfa	Liposome	Small Molecule	Lung activator for stress disorder	1999
Verteporfin	Liposome	Small Molecule	Decreased vision, ophthalmic hiscomaplastia	2000
Perflutren	Liposome	Small Molecule	Ultrasound contrast agent	2001
Octocog alfa	Liposome	Small Molecule	Haemophilia A	2004
Mifamurtide	Liposome	Small Molecule	Myosarcoma	2009
Vincristine	Liposome	Small Molecule	Acute lymphocytic blood clot	2012
Irinotecan	Liposome	Small Molecule	Pancreatic cancer	2015
Cytarabine: daunorubicin	Liposome	Small Molecule	Acute myeloid leukaemia	2017
Patisiran siRNA (Onpattro®)	Lipid Nanoparticle	RNA	Transthyretin (TTR)-mediated amyloidosis	2018
Pfizer/BioNTech mRNA (Comirnaty®)	Lipid Nanoparticle	RNA	COVID-19	2021
Moderna mRNA (Spikevax®)	Lipid Nanoparticle	RNA	COVID-19	2021
Moderna mRNA (mRESVIA®)	Lipid Nanoparticle	RNA	Respiratory Disease	2024

1.3.1. Components of Lipid Nanoparticles

LNPs are complex systems and are composed of four constituent molecular groups which are: **i)** a main ionisable/cationic lipid, a **ii)** sterol, a **iii)** helper phospholipid, and a **iv)** PEGylated lipid. These molecular groups used in LNP formulations can be categorised based on structural composition (**Table 1.5**).

Table 1.5 *- Lipid Compositions of Approved RNA-LNP therapeutics. LNP components of each formulated therapeutic are denoted for Onpattro®, Comirnaty®, Spikevax® and mRESVIA® (23,25).*

LNP Component	***Onpattro®***	***Comirnaty®***	***Spikevax®***	***mRESVIA®***
Ionisable Lipid	MC3	ALC-0315	SM102	SM102
Sterol	CHOL	CHOL	CHOL	CHOL
Helper Lipid	DSPC	DSPC	DSPC	DSPC
PEGylated Lipid	DMG-C-PEG$_{2000}$	ALC-0159	DMG-PEG$_{2000}$	DMG-PEG$_{2000}$
Lipid Mol. %	50:38.5:10:1.5	46.3:42.7:9.4:1.6	50:38.5:10:1.5	50:38.5:10:1.5

All approved RNA-LNPs follow a trend of the ionisable lipid occurring at the highest percentage by composition, followed by the sterol group, the helper lipid, and the PEGylated lipid occurring at the smallest molar percentage composition of a RNA-LNP. Each therapeutic also follows a standardised 50:38.5:10:1.5 mol% of ionisable lipid: sterol: helper lipid: PEGylated lipid. Each lipid component used within RNA-LNP formulation can be categorized into separate molecular classes.

Ionisable/Cationic Lipids

This class of lipid comprises the main component of the LNP (~50%) and dictates the overall surface charge of the LNP dependent upon the dispersity and location of the ionisable/cationic lipid within the LNP. **Table 1.6** lists commonly used ionisable/cationic lipids in LNP formulation.

Table 1.6 *- Ionisable Lipid Class, their corresponding Chemical Structure, and physicochemical properties.*

Lipid Class	Lipid Name	Physicochemical Properties
Cationic	1,2-dioleoyl-3-trimethylammonium-propane **(DOTAP)** 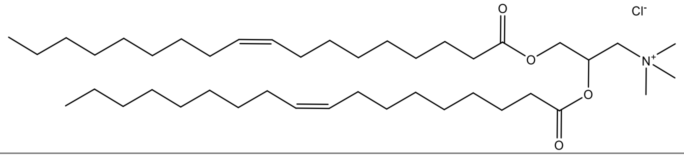	-Permanent cationic quaternary amine group -Ester linkers, unsaturated tails
Ionisable	(6Z,9Z,28Z,31Z)-heptatriaconta6,9,28,31-tetraen-19-yl-4-(dimethylamino)-butanoate **(MC3)** 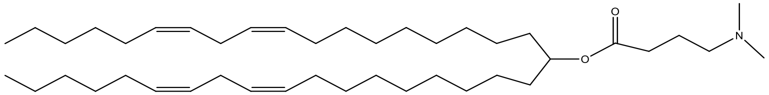	-Cationic charge under acidic conditions (pH 5-6) -Tertiary amine headgroups, ester linkers, unsaturated tails, pKa = 6.44
Ionisable Branched	8-[(2-hydroxyethyl)[6-oxo-6-(undecyloxy)hexyl]amino]-octanoic acid, 1-octylnonyl ester **(SM102)** 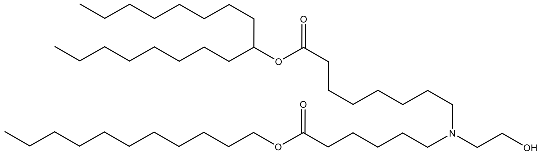	-Cationic under acidic pH conditions (pH 5-6) -Tertiary amine headgroups, ester linkers, saturated linear and branched tails, pKa = 6.75
Ionisable Branched	**ALC-0315** 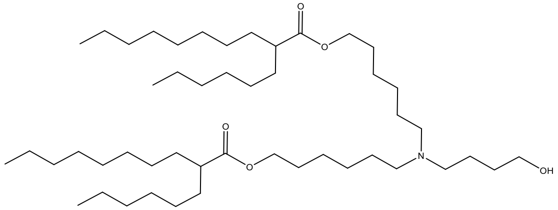	-Cationic charged in acid conditions (pH 5-6) -Tertiary amine headgroup, ester linkers, saturated branched tails, pKa = 6.09

The design of the main ionisable lipid is important as the headgroup, linker and lipid tails have significant impact on the lipid physicochemical properties and resultant RNA-LNP formulations. Changing the ionisable lipid headgroup alters its polarity and affects how it electrostatically interacts with the negatively charged RNA during formulation. Typically, these headgroups range from primary to quaternary amines, with tertiary amines being the most common in clinically approved lipid formulations. All linkers used are biodegradable esters, which are rapidly cleared *in vivo* (79). Lipid tails impact overall lipid physicochemical properties and subsequent LNP formulation attributes through their branching, further enhancing their packing potential and overall three-dimensional geometry. The tail structure and design of the lipid impact lipid pK_a, lipophilicity, fluidity, and fusogenicity. The physical geometry of main ionisable/cationic lipid (cylindrical *versus* cone) is another key component within lipid design/selection process as the main lipid will pack and release encapsulated drug cargo differently. From **Table 1.6**, lipid chain lengths vary around 18-22 molecules, with varying degree in branching, contributing to their packing shape and associated packing value (**Table 1.7**).

The Lipid Critical Packing Parameter is a key quality parameter in lipid design when considering the main ionisable lipid of choice for LNP formulation. This parameter defines the geometry of ionisable lipid self-assembly within endogenous anionic endosomal lipids, to release RNA drug cargo into cell cytoplasm. The critical packing parameter *(P_C)* can be predicted through **Equation 1.1**.

$$P_C = \frac{V}{A\, l_C}$$

Equation 1.1 *– Lipid Critical Packing Parameter on the prediction of lipid geometry where V = the volume of alkyl chains, A = area of the lipid headgroup and l_C = length of the alkyl chains.*

Lipid structures presented in **Table 1.6** have a predicted $P_C \geq 1$ to ensure that RNA cargo is released successfully. Denoted in **Table 1.7** is the predicted packing parameter values, packing shape and structures formed on interaction with anionic endogenous lipids to release RNA encapsulated cargo.

***Table 1.7** – Lipid Critical Parameters and corresponding predicted packing geometries and supramolecular structures formed.*

Packing Value	***Packing Shape***	***Structure Formed***
$P_C < \frac{1}{3}$	Cone 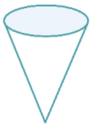	Spherical Micelles 
$\frac{1}{3} < P_C < \frac{1}{2}$	Truncated Cone 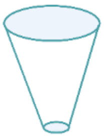	Cylindrical Micelles 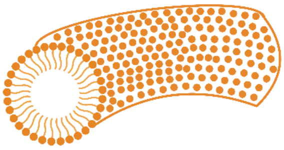
$\frac{1}{3} < P_C < \frac{1}{2}$	Truncated Cone 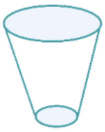	Flexible Bilayer 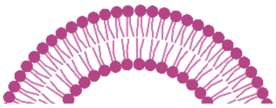
$P_C \approx 1$	Cylinder 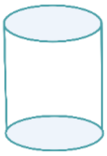	Planar Bilayer 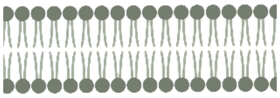
$P_C > 1$	Inverted Truncated Cone 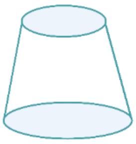	Inverted Micelles 

As pH changes with manufacture and endosomal maturation, conformations of lipids/RNA will change. During manufacture acidic pH dominated causing tight packing geometries between lipid protonated headgroup and RNA anionic backbone. On neutralisation, headgroups are deprotonated and lipid/RNA structures become more ordered. Consequently, on endosomal uptake and maturation to acidic pH, ionisable headgroups are protonated producing similar structures to intial manufacture, The structures of DOTAP and MC3 will adopt a planar bilayer conformation, whereas SM102 and ALC-0315 will adopt an inverted micelle conformation on complexation with endogenous negatively charged lipids, both conformations facilitate the release of RNA into targeted cells.

Unlike the approved formulations in **Table 1.5**, DOTAP has not been used as a cationic/ionisable lipid component in approved RNA-LNP formulations. DOTAP-LNPs have a lower circulation time and are cleared more rapidly from systemic circulation compared to MC3-LNPs, confirming that DOTAP LNPs are more prone to clearance *via* the reticuloendothelial system than MC3 (80). This association along with known cytotoxicity, confirmed that the permanent cationic charge of DOTAP is incompatible with biological systems, when compared with MC3 lipids, which is neutral, more biocompatible and is used in clinical formulations. The second highest composition molecular group used within RNA-LNP formulations is the sterol group.

Sterols

The key sterol used within approved commercial LNPs to-date is Cholesterol (23), denoted below **Figure 1.3**.

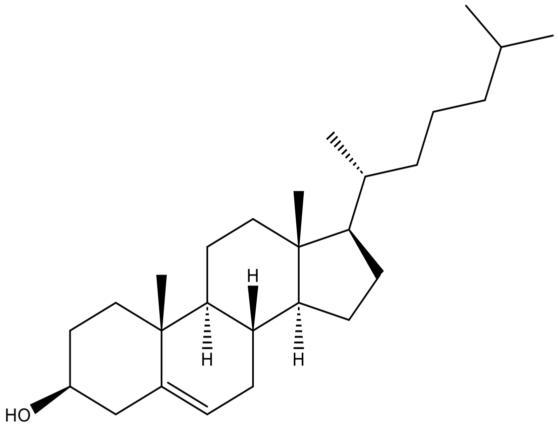

Figure 1.3 *- The chemical structure of cholesterol used within Onpattro®, Comirnaty®, and Spikevax® (81). Made with ChemDraw.*

Cholesterol is used to stabilise (82–84) the phospholipid layer and provides rigidity to prevent LNP fragmentation under stress, and reduce drug cargo leakage from LNPs. Cholesterol has been demonstrated to increase the circulation half-life of liposomes by reducing protein corona formation. Sterols also aid LNP cellular uptake by adsorbing native Apolipoprotein E (ApoE), which mediates endocytic internalisation of LNPs (85).

Cholesterol has a single polar hydroxyl (OH) group, which gives it weak hydrophilicity. This causes the sterol to orient itself at the interface of lipophilic tail and hydrophilic head of the other lipids in the LNP. Cholesterol does not remain in its soluble form throughout the LNP as the molar ratio is in excess, demonstrating that cholesterol crystallises in the inner LNP core with the ionisable lipids and drug cargo (86,87).

Beyond cholesterol use in three authorised RNA-LNP formulations, additional sterol derivatives have been explored to further optimise LNP formulation. *β*-sitosterol produces a larger sized RNA-LNP, similar RNA loading and a significantly higher transfection capability than cholesterol in LNP formulations (88).

Helper Phospholipids

Similar to sterols, the helper phospholipid used in Onpattro® and COVID-19 vaccinations is 1,2-distearoyl-sn-glycero-3-phosphocholine (DSPC) (8,22,83), the chemical structure of which is denoted as follows:

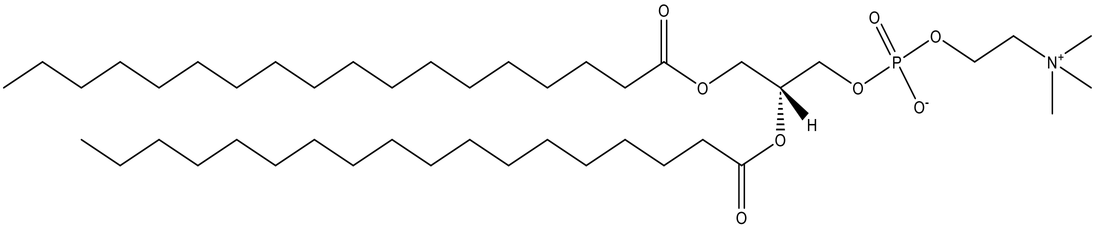

Figure 1.4 *– Structure of Helper Phospholipid, 1,2-distearoyl-sn-glycero-3-phosphocholine (DSPC) (81), made with ChemDraw.*

DSPC functions as a helper lipid that enhances LNP rigidity (82) and typically represents approximately 10% of the overall lipid molar ratio within the LNP formulation. Zhang *et al.* (89) further demonstrated that the helper lipid composition directly affects LNP biodistribution. Their findings revealed that LNP formulations formulated with 1,2-dioleoyl-sn-glycero-3-phosphoethanolamine (DOPE) predominantly accumulated in the liver, while those containing DSPC showed preferential accumulation in the spleen. The molecular structure of DOPE is illustrated below.

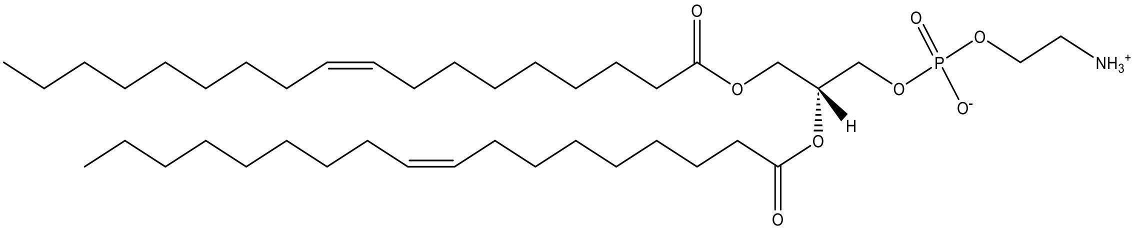

Figure 1.5 *- Structure of Helper Lipid, 1,2-dioleoyl-sn-glycero-3-phosphoethanolamine (DOPE) (83). Made with ChemDraw.*

Structurally, DSPC carries a zwitterionic phosphocholine head group containing a trimethylammonium moiety, while DOPE contains a smaller phosphorthanolamine head group. The smaller head group in DOPE promotes tighter packing and increased membrane fusion, whereas the DSPC bulkier head group stabilizes the bilayer structure. Furthermore, DSPC contains saturated alkyl chains, while DOPE incorporates two monounsaturated tails. These structural distinctions markedly influence the biodistribution and accumulation behaviour of RNA-LNPs. It has been hypothesised that DSPC forms an ordered arrangement on the outer surface of the LNP, suggesting that its head group plays a critical role in mediating cellular uptake following the dissociation of the PEG moiety from its lipid anchor (89).

PEGylated Lipid

The PEGylated lipid plays a vital role in the stability, biocompatibility and targeting of LNPs *in vivo*, prolonging circulation time and reducing clearance. Although PEGylated lipids only comprise 1-2% of the overall molar ratio of lipids in RNA-LNP formulation, the PEGylated lipid plays an equally important role as other lipid components in LNP formulations. Since the PEG group is covalently attached to an anchored lipid (90), the PEGylated lipid orients itself within the outer lipid layer of the LNP, with the PEG_{2000} moiety protruding from the surface of the particle into suspension. The PEG lipid is used for passive targeting *via* the enhanced permeability and retention effect.

All current approved LNP formulations (23) **Table 1.5** employ different structured PEG lipid analogues. Spikevax® uses DMG-PEG_{2000}, whereas Onpattro® uses DMG-C-PEG_{2000} and Comirnaty® uses the ALC-0159 based lipid. The structures of DMG-$PEG_{2000,}$ DMG-C-PEG_{2000} and ALC-0159 are shown as follows:

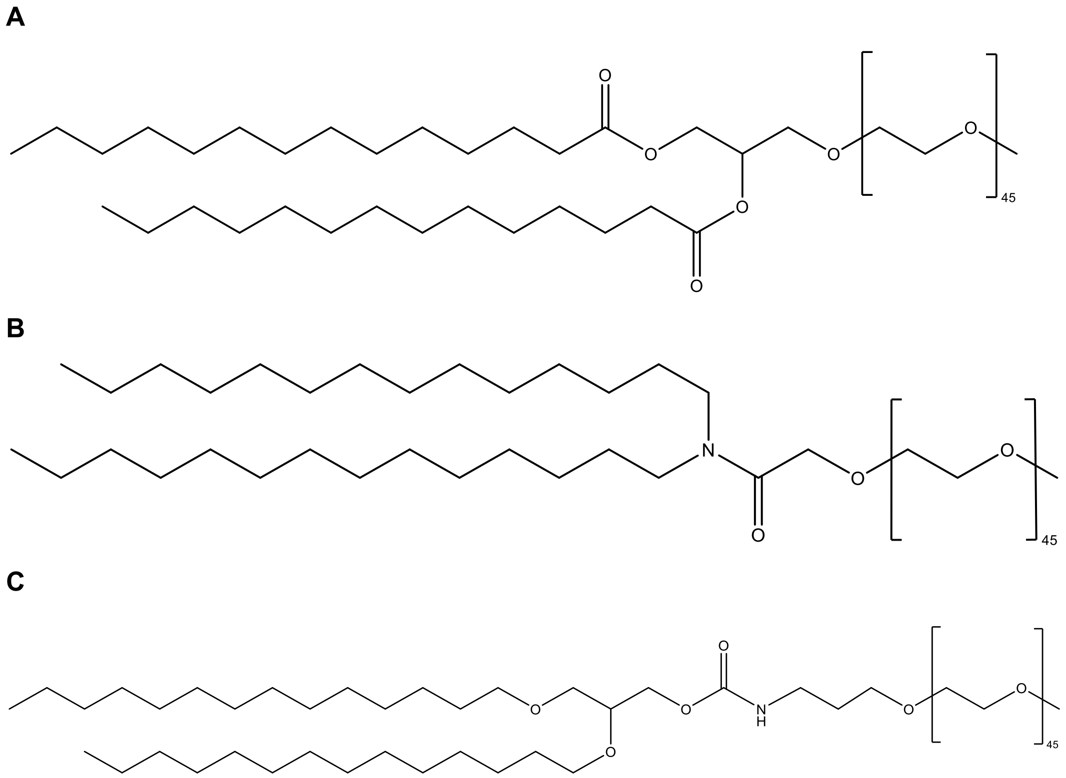

***Figure 1.6** – The chemical structure of A) DMG-PEG2000 lipid used in the Spikevax® formulation, B) ALC-0159 PEG lipid analogue used in the Comirnaty® COVID-19 vaccine and C) DMG-C-PEG2000 PEG lipid analogue used in Onpattro® . Made with ChemDraw.*

Structurally, the primary differences between the three PEGylated lipids arise from the composition of their linker moieties. The three lipids share a common architecture, with all hydrophobic tails consisting of a 14-carbon alkyl chain and each possessing identical repeating polyethylene glycol units as their hydrophilic domain.

The size of the PEG moiety in PEGylated lipids is a critical parameter, as its molecular weight will significantly impact PEG shedding from the surface of the RNA-LNP *in vivo*. PEG groups are conjugated to their associated lipid anchors *via* a biodegradable linker group. For example, DMG-PEG$_{2000}$ is linked through two ester groups, and ALC-0159 and DMG-C-PEG$_{2000}$ are connected by more stable amide bonds. Similar to the biodegradable linkers found in ionisable lipid structures, linkers in the PEG groups are susceptible to hydrolysis and shed from the surface.

The low molecular weight of the PEG moiety plays a dual role in modulating this shedding process. PEG chains with lower molecular weights tend to remain associated with the LNP surface and elicit the production of neutralising anti-PEG antibodies, potentially compromising therapeutic efficacy. On the contrary, PEG groups with a large molecular weight dissociate too rapidly from the LNP surface and are cleared to the liver (91,92). Therefore, optimising PEG molecular weight and linker chemistry is important for balancing immune evasion with therapeutic efficacy and circulation time.

1.3.2. Manufacturing Approaches for RNA-Lipid Nanoparticle Formulations

The formulation strategy and type of lipid nanocarrier utilised will depend on multiple interrelated variables, including the physicochemical properties of the payload drug (hydrophilicity or lipophilicity), the intended region of the LNP in which the drug is contained, and the inherent stability of the payload. These factors play a pivotal role in determining the most appropriate formulation conditions.

Additionally, LNP formulation design must align with pre-specified structural and functional attributes of the LNP. Critical quality attributes (CQAs) such as particle size, shape, zeta potential, polydispersity index (PDI), drug loading, and overall formulation stability are essential parameters that guide LNP formulation design.

There are various methods for manufacturing lipid nanocarriers with advancements in formulation technologies. **Table 1.8** summarises the more well-known and used, lipid nanocarrier manufacturing methods.

__Table 1.8__ - Lipid nanocarrier formulation methods used to encapsulate anionic drug cargo, each method is briefly described with associated benefits and limitations of use.

Methods	Benefits	Limitations
Thin Film Hydration (93–95)	Simple produced, compatible with all organic solvents	Use of toxic organic solvents, small-scale production
Solvent Injection (96–98)	Simple process, quick and reproducible	Organic solvent removal difficult, sterilisation required
Top-Down Extrusion (99–101)	Controls liposome size after methods like thin film hydration	Shear and stress may impact loaded drug cargo
Microfluidics (102–104)	Reproducible, scalable, ease of use	Complete organic solvent removal difficult

Microfluidics-based methods of lipid nanocarrier manufacture are most reported in the literature due to the versatility in controlling particle key quality attributes, scalability and opportunity for continuous manufacturing. Although organic solvent removal is difficult, downstream purification processes such as tangential flow filtration, dialysis, or spin column centrifugation can be used to remove residual organic solvent. Within the context of this thesis, RNA-LNPs were formulated using microfluidic mixing and were purified using dialysis/spin column centrifugation.

1.3.2.1 Microfluidics

Microfluidics is a modern technique based on solvent injection and nanoprecipitation, which rapidly mixes miscible aqueous and organic phases using laminar flow to produce LNPs, which encapsulate a target RNA drug during formulation (105). This RNA-LNP production method is the popular choice of considered techniques in **Table 1.8** as RNA-LNP size, shape, polydispersity (PDI), surface charge, encapsulation efficiency (%EE), and mass balance (%MB) critical quality attributes can be optimised through the variation of microfluidic process parameters. These parameters include microfluidic chip design, total flow rate (TFR) and flow rate ratio (FFR), lipid molar ratio, nitrogen to phosphorous (N/P) ratio, organic phase selection, aqueous phase ionic strength and aqueous phase pH. Impact of these process parameters on resultant LNP CQAs are detailed below.

Table 1.9 - LNP formulations process parameter impact on resultant CQAs.

Parameter	CQA			
	Size	**Size Distribution**	**Surface Charge**	**RNA Loading %**
Chip Design	No significant impact on overall LNP CQAs.			
Mixing Total Flow Rate ↑	Decrease.	Decrease.	No reported.	No reported.
Mixing Flow Rate Ratio ↑	Decrease.	Decrease.	No reported.	No reported.
Ionisable Lipid Molar Ratio	Impact on case-by-case basis.			
N/P Ratio	Dependant on RNA drug cargo used			
Organic Phase	No observed impact on overall LNP CQAs.			
Aqueous Phase Ionic Strength ↑	Increase.	Increase.	Anionic to Cationic.	No impact.
Aqueous Phase pH ↓	Decrease.	No reported.	No reported.	No reported.

The formulation of LNPs relies on the self-assembly of lipids in an organised structure under rapid mixing. The self-assembly process is based on lipid/cargo intermolecular interactions. As the drug-aqueous phase is in excess, the reaction will increase in polarity from the non-polar lipid-organic phase through to the final polar formulated drug-loaded LNPs (106). Electrostatic interactions are initially exploited between the anionic group of the drug cargo and the cationic quaternary amine group of the cationic lipid, which form inverted micelles (79,107). The collision of these early stage and precursor LNPs are the widely-accepted mechanism for cargo distribution within the centre of the LNP based on computational modelling (86,108). Subsequently, lipophilic interactions and Van der Waals (VDW) intermolecular forces between alkyl tails of the phospholipids/non-polar regions of cholesterol dominate, and enlarge LNP size as polarity of the miscible phases increase and produce the outer layer of the particle seen in **Table 1.3** (86). Self-assembly is based on weak intermolecular electrostatic and dipole interactions; therefore, drug loaded LNPs are inherently soft nanoparticles which are readily deconstructed.

Most common buffers used for each phase are alcohols for the organic phase, and a pH modified salt/buffer agent solution for the aqueous phase (82,103,109,110). Although ethanol is mainly used for the organic phase and challenging to remove, salt buffer selection and pH adjustment are optimised for each specific encapsulation.

Microfluidic Chip Design

Reported chip geometries used in microfluidics manufacturing, include the use of Y-shaped staggered herringbone (SHM), toroidal, T-junction and baffle-shaped micromixer designs. The most popular and studied chip design is a Y-shaped staggered herringbone micromixer, designed to shorten mixing time and enhance control within the mixing process (111).

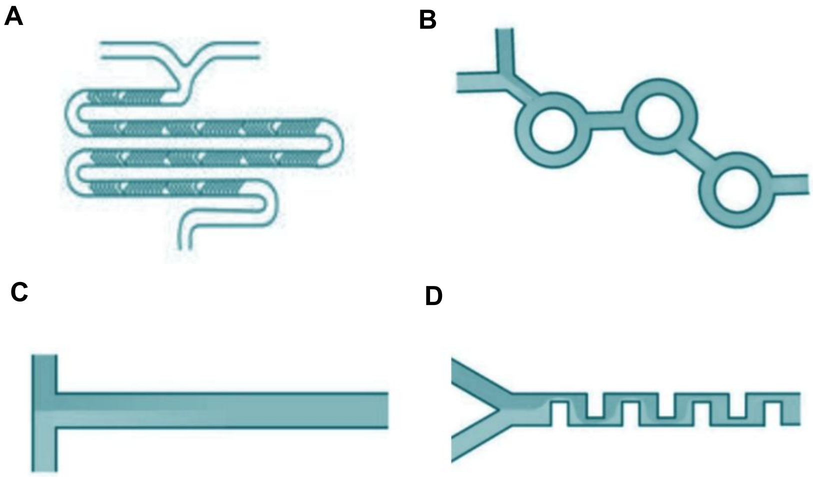

Figure 1.7 *– Different microfluidic chip architectures. A) staggered herringbone micromixer (SHM), B) toroidal mixer, C) T-junction mixer and D) baffle mixer. Adapted from (112,113), created in BioRender®.*

The design of the microfluidic micromixer chip design has a relatively low impact on particle characteristics, when compared to the influence of mixing and formulation parameters. Webb *et al.* demonstrated minor changes in particle size and PDI when comparing small scale-based SHM with high-throughput, large scale toroidal chip geometry (112). Although a variety of chip architectures are on the market, few experimental studies have directly compared physicochemical properties of resultant LNP formulations across multiple micromixer geometries. As microfluidics technology continues to evolve, chip geometries continue to perform comparatively and produce equivalent batches of RNA loaded LNPs, irrespective of the chip design employed.

Total Flow Rate (TFR) and Flow Rate Ratio (FRR)

Many studies have sought to streamline LNP formulation parameters and identify critical process parameters that impact LNP CQAs. Among these, TFR and FRR have been consistently identified as critical process parameters (81,114,115). Jaradat *et al.* demonstrated the impacts of both TFR and FRR on LNP size (116), showing that when liposomes where prepared with a change in TFR from 1 mL/min to 3 mL/min (at a constant FRR), the resulting particles doubled in size. When a constant TFR was applied and a higher aqueous to organic ratio (4:1) used, a 20% reduction in liposome size was observed compared to lower aqueous: organic ratios (2:1).

An increase in the aqueous phase proportion of the FRR during microfluidic mixing generally produced smaller liposomes compared with both 2:1 and 3:1 FRRs. This may be attributed to the presence of excess cargo drug, which can promote the tighter packing of the liposome bilayer around their drug cargo, thereby decreasing the particle diameter and overall average batch particle size. Terada *et al.* also evaluated the impact of TFR and FRR on the physicochemical properties of siRNA encapsulated LNPs using a design of experiments (DoE) approach (117). FRR had a more pronounced effect on particle size and PDI compared with TFR. However, TFR changed particle size, but the observable difference was not equivalent to changes observed by FRR alterations. Roces *et al* reported that both FRR and TFR impacted particle physical characteristics, and their results correlated with Terada *et al.* where FRR was found to be more impactful on LNP properties than TFR (81,117).

Other parameters such as lipid molar ratios, nitrogen head group of main ionisable lipid to RNA molecule phosphate group backbone (N/P ratio), buffer phases and the type of drug being encapsulated, also impact particle attributes but not as significantly as TFR and FRR (71,72).

Lipid Molar Ratio

Various lipid molar ratios have been extensively studied to optimise LNP formulations for nucleic acid delivery (24,81,83,114). Despite the diversity of the lipid molar ratios and compositions, a commonly adopted “standard” ratio has emerged from the clinically-approved formulations of Onpattro® and Spikevax®, which utilise a lipid ratio of 50:38.5:10:1.5 for ionisable lipid, cholesterol, helper lipid and PEGylated lipid, respectively (118–120).

The nitrogen/phosphorous (N/P) Ratio

The N/P ratio defines the molar ratio between ionisable/cationic nitrogen groups present in the lipid headgroups and anionic phosphate groups of the RNA sugar backbone. This parameter plays a crucial role in determining the physicochemical properties and biological performance of LNPs, dictated by RNA loading. A wide range of N/P ratios from 0.5:1 to 15:1 has been reported in the literature (81,121–123). Within the context of RNA therapeutics, a variety of payloads can be encapsulated into LNP delivery systems.

Table 1.10 - Nitrogen/phosphorus ratio and associated RNA type with approximate molecular weights

RNA Type	Approx. Chain Length	Typical N/P Ratio
siRNA/ASO	15-30 bp	4:1 (124) 3:1 (125) 4-6:1 (126) 5:1 (127)
mRNA	> 1000 bp	6:1 (84,110,128–130) 4.5:1 (131) 1-12:1 (132) 0.65:1 (133) 3-6:1 (134)
Large RNA	> 3000 bp	15:1 (135) 8:1 (109,136–139) 12:1 (121)

Generally, smaller nucleic acid payloads require lower overall nitrogen-to-payload ratios for effective encapsulation, with progressively higher ratios observed as payload size increases. As payload size grows, the emergence of secondary, tertiary, and quaternary RNA structures can further influence encapsulation efficiency during LNP formulation. However, a standardised platform approach has yet to be established, meaning formulation screening remains largely case-specific during early-stage development.

Organic/Aqueous Phases

Both organic and aqueous phases play crucial roles within the microfluidic mixing of RNA and lipidic phases during RNA-LNP formulation. Organic solvent selection is a key factor in ensuring lipid solubility, prior to microfluidic mixing, whilst remaining compatible with mixing cartridge material during formulation. Organic solvent choice must be assessed when purifying formulations to ensure biocompatibility to ensure that International Council for Harmonisation (ICH) guidelines are met with residual solvent limit < 5000 ppm (140).

The ionic strength and pH of the aqueous phase buffer are critical formulation parameters, as both influence LNP size, encapsulation efficiency, and polydispersity index (PDI). The primary function of the aqueous buffer is to support the electrostatic and hydrophobic interactions between the ionisable lipid and the nucleic acid payload during nanoparticle formation. A range of buffer systems, including citrate, acetate, and HEPES, have been evaluated at acidic pH values (typically pH 3–6). Since pH governs the protonation state of ionisable lipid headgroups, lower pH conditions are generally employed to ensure sufficient protonation to facilitate RNA encapsulation.

Investigations into ionic strength have indicated minimal impact on critical quality attributes (CQAs) at moderate salt concentrations; however, levels exceeding approximately 300 mM have been associated with particle deformation and blebbing (141). Overall, buffer pH and ionic strength appear to exert greater influence on LNP physicochemical properties than the specific buffer salt employed (142–147). Nakamura *et al.* further highlighted the importance of optimising aqueous phase parameters by systematically evaluating the effects of pH and ionic strength variation on LNP particle size distribution (148), with high ionic strength buffers and higher pH (less acidic) buffers producing larger sized LNP formulations,

1.3.3. RNA-LNP Biological Fate

Administration route of RNA-LNP therapeutics represents an additional layer of complexity within LNP design, whereby therapeutics are injected intravenously, intramuscularly, inhaled or delivered locally (149–151). Upon administration, the LNP protects encapsulated RNA cargo from various external degradation and serves to deliver to target areas. The journey typically begins with RNA-LNP introduction at the injection site with the spontaneous interaction with endogenous serum proteins leading to the formation of a biomolecular corona (152–154).

The corona is composed of a two-layer system, the first layer is the hard corona which forms at the LNP-corona interface where proteins and material are held tight to the LNP surface. The second layer is the soft corona which is composed of further biomaterial, however it is a loose formed structure which can absorb and desorb molecules (155,156). Biomolecular corona formation and composition is influenced by RNA-LNP formulation surface characteristics, and which components orient at the external surface of the particle. The corona will also reflect the route of administration due to bioavailability of endogenous material within the injection site area (157).

Once in circulatory pathways *in vivo*, RNA-LNPs must avoid immune response activation and enzymatic degradation. The biomolecular corona complexed system further modulates biodistribution, cellular interactions and clearance pathways. Due to particle enhanced permeation and retention effect (EPR), particles remain within circulatory system until cellular receptor interaction and internalisation through endocytosis pathways (158).

Following particle internalisation, a major bottleneck is endosomal escape, which is a critical step in cytosolic RNA release. Endosomal escape occurs in three main stages: (i) endosome formation, where internalised pH remains ~ 6.2, followed by (ii) endosome maturation, denoted by a decrease in pH to ~pH 4, since ionisable lipids have been designed with endosomal escape in mind (pKa ~6), and fusogencitiy physical structure. In stage iii, main ionisable lipid (50% molar lipid ratio) protonation is activated, facilitating interaction with the anionic endosomal lipids to release internal RNA drug cargo into the cytoplasm (159).

Once released, a therapeutic effect is exerted, ranging from RNA translation, gene silencing, splicing or RNA transcription blocking. With only 1-2% of RNA being released into the cytoplasm (160–163), more studies are required to track enhanced LNP endosomal uptake, endosomal escape and increase drug percentage release rates. These enhancements would decrease overall dosage requirements and lower toxicity risks and adverse reactions.

1.4. Analytical Pipelines for Evaluating RNA LNP Formulation Critical Quality Attributes

Comprehensive CQA analysis of RNA drug substance is routinely performed during API manufacturing; however, these analytical insights are often generated in isolation and rarely interface with formulation development until late-stage regulatory submissions. These separated approaches limit early understanding of how RNA integrity and purity influence LNP formulation performance, or conversely, how formulation and manufacturing processes impact RNA structural integrity (164,165). Strengthening the integration between RNA drug substance analytics and formulation science could provide a more predictive understanding of LNP quality attributes, thereby enhancing clinical translation and commercial robustness. By using high-resolution orthogonal analytical approaches, enhanced insights into CQAs can be achieved through hyphenation to multiple inline detectors for quantifying various associated parameters within a single sample analysis (size, size distribution, surface charge, morphology, drug localisation). Whereas a single analytical method quantifies less CQAs (size, size distribution).

1.4.1. RNA Drug Substance CQAs

Ensuring the quality and consistency of RNA drug substances is paramount. To guarantee their safety and efficacy, RNA drug substances must undergo comprehensive analytical evaluation. This involves assessing key attributes such as purity, identity, and potency using advanced techniques. Among the most employed methods are electrical separation techniques, such as capillary gel electrophoresis, and chromatographic approaches like liquid chromatography, both of which provide high-resolution insights into RNA integrity and performance (166).

1.4.1.1. RNA Integrity

The application of an electric field to RNA-based drugs enables the estimation of chain length and molecular weight determination. As RNA molecules are separated based on their size and charge, thus being a key factor in evaluation RNA purity and chain lengths distributions within given RNA drug substance samples prior to formulation use.

Table 1.11 *- Comparison of electrical-based system for RNA purity evaluation.*

RNA Type	Slab Gel Electrophoresis	Capillary GE
siRNA/ASO (167,168)	Main use with polyacrylamide for separation.	Higher resolution use with fluorescent detection and quantification for duplex/single strands.
mRNA (45,169,170)	Agarose % altered to reflect mRNA size along with mRNA denaturation. Quick visual check of mRNA drug. Lacks resolution for enhanced insights.	Routine analysers used for size distributions profiles for quantitative integrity analysis. Lacks resolution for sequence identity.

Due to their inherent anionic properties arising from the phosphate backbone, RNA molecules migrate through an electrical field, with smaller fragments migrating further than larger molecules. Electrophoretic techniques routinely perform a comparison between unknown RNA sample against known RNA molecular weight/base pair ladder for the identification of estimated chain length distributions. Slab GE methods provide a quick screening method to run RNA samples prior to further investigation by high resolution analytical techniques like CGE. However, CGE cannot confirm RNA identity unless coupled to downstream mass spectrometry for fragmentation, detection and further deconvolution for chain length mapping.

1.4.1.2. Chromatographic-based approaches

Liquid chromatography (LC) is a powerful separation technique that exploits the physicochemical properties of analytes to achieve separation based on their competing interactions with the mobile (eluent) and stationary phases. LC systems typically comprise a pump, operating under either isocratic or gradient conditions, mixing valves, and an inline column packed with a stationary phase. Separation occurs as analytes differentially partition between the two phases, driven by their unique chemical characteristics. Chromatographic reosltuion is defined as a measure of the degree of separation between two adjacent sample component peaks (171,172).

Most LC-based separations employ a mixed organic–aqueous mobile phase system, although steric and size-based interactions can also be utilised. Since RNA is inherently hydrophilic, it preferentially partitions into the aqueous phase. This behaviour can be exploited for both RNA separation and purification. Given the chemical complexity of RNA molecules, a range of chromatographic modes have been developed and applied for their characterisation and identity confirmation.

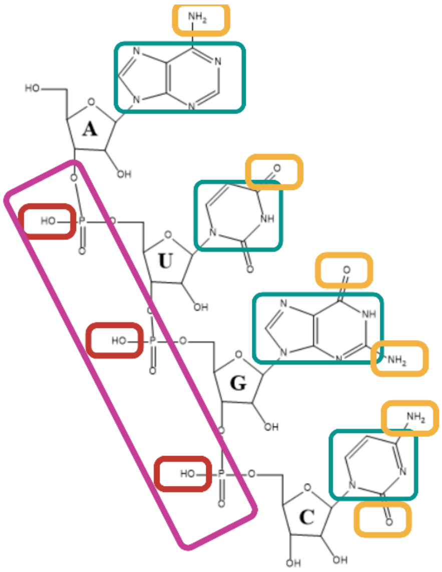

Figure 1.8 *- RNA separation modes using liquid chromatography techniques using an exemplar 4-mer PO unmodified sequence. Each colour highlights a different functional group for LC exploitation. Red for -OH deprotonation for anion exchange (AEX), pink for reverse phase (RP) backbone hydrophobicity, teal for pi-pi electron stacking and yellow for hydrogen bonding using hydrophilic interaction (HILIC). Remade from (173)*

Among these, three principal types of LC are commonly used for RNA analysis: reverse-phase (RP), hydrophilic interaction (HILIC), and anion-exchange (AEX) chromatography. Each method targets different molecular properties and functional groups on the RNA to achieve effective separation.

In reverse-phase LC (RP-LC), ion-pairing reagents are introduced to neutralise the negatively charged phosphate backbone of RNA and minimise interactions with residual silanol groups on the hydrophobic stationary phase. This process increases the overall hydrophobicity of the RNA, promoting retention on the column (174–176). Separation is then achieved by gradually increasing the organic content of the mobile phase; RNA molecules elute once the solvent strength reaches a critical level that favours their transition back into the mobile phase for detection.

Conversely, hydrophilic interaction liquid chromatography (HILIC) operates on the opposite principle (177–179). Here, the stationary phase is hydrophilic, and the mobile phase gradient starts with a high organic content, often ~ 90%. Under these conditions, RNA interacts strongly with the hydrophilic stationary phase. With increasing introduction of the aqueous proportion of the mobile phase, the solvation of RNA increases, weakening these interactions. When the aqueous concentration reaches a critical threshold, the RNA elutes from the column and proceeds to the online detector.

In anion-exchange chromatography (AEX), separation is based on electrostatic interactions (44,180,181). The stationary phase carries a positive charge, allowing it to bind the negatively charged RNA. Elution is achieved by gradually increasing the salt concentration in the mobile phase. As ionic strength rises, salt ions compete with RNA for binding sites on the stationary phase, disrupting these electrostatic interactions and causing the RNA to elute.

Various detection systems can be coupled to flow-based separation systems (e.g. CE and LC), from photodiode array (PDA) absorbance for concentration evaluation to mass spectrometers (MS) for mass: charge ratio (m/z) identity analysis. **Figure 1.9** depicts a simplified schematic of an LC-PDA-MS system.

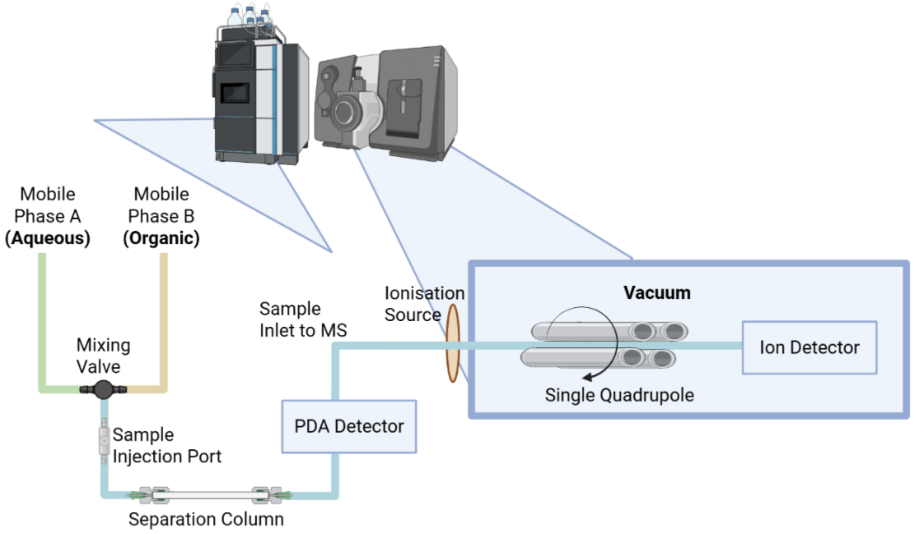

***Figure 1.9** – A simplified overview of LC-PDA-MS separation and hyphenated detection system pipeline.*

The PDA detector directs multiple wavelengths of light through the sample as it passes the flow cell, measuring absorbance at each wavelength. RNA, containing aromatic nucleotide bases, exhibits a characteristic absorbance around 260 nm. This enables real-time monitoring of RNA elution from the column and quantification of concentration *via* the Beer–Lambert Law.

As components elute according to concentration, the absorbance at 260 nm increases proportionally with the number of unconjugated aromatic residues. PDA detection is non-destructive and can be used independently or coupled with downstream mass spectrometry-based analysis.

Following LC-based separation, mass spectrometry (MS) provides molecular identification and quantification. The eluted sample is first vapourised and ionised within the MS source under high voltage, generating charged species that are introduced into a high-vacuum system. These ions are separated based on their mass-to-charge (m/z) ratios using a quadrupole or series of quadrupoles in tandem (triple quadrupole) configuration. The resulting ion signals are detected and converted into spectra, allowing determination of RNA identity, purity, and potency.

Currently, ion-pair reverse phase LC-MS is the gold standard with enhanced sensitivity and separation of small RNAs, with mRNA requiring digestion to allowed for successful ionisation.

1.4.2. Measurement of RNA-LNP Formulation CQAs

1.4.2.1. Size and Size Distribution

Dynamic light scattering (DLS) is a commonly used particle sizing technique due to minimal sample preparation, ease of use, and rapid readout (182). DLS is a batch-mode technique, which utilises particle light scattering intensity fluctuations caused by particle Brownian motion from which a correlation curve is derived to analyse time-dependant fluctuations in the intensity of scattered light (183,184). The diffusion coefficient of particles undergoing Brownian motion are calculated, from which the particle size can be derived using the Stokes-Einstein Equation (**Equation 1.2**).

$$d(H) = \frac{k\,T}{3\,\pi\,\eta\,D}$$

***Equation 1.2** – Stokes-Einstein Equation, relating particle size to diffusion rates. Where, d(H) = hydrodynamic diameter (nm), k = Boltzmann's constant(J/K), T = absolute temperature (K), and η = viscosity(pa/s).*

Another routinely used technique, which benefits from higher resolution in nanoparticle size sub-population detection is Nanoparticle Tracking Analysis (NTA). Resoltuion within particle detection is defined as technique sensitivty in analysis particle parameters from bulk ensemble to particle-by-particle level. NTA is considered a high-resolution particle sizing technique as it measures sample particle size on a particle-by-particle basis (185). A syringe driver flows particles through a defined flow path at a constant flow rate. The particles are illuminated with a laser, and flow rate time-based light scattering data is collected. Similar to DLS, particle size measurements by NTA are derived from measured particle diffusion using the Stokes-Einstein Equation. NTA measures size distribution through calculation of distribution-based size data, and since particles are detected as a number-based method, an estimated concentration of particles per mL of sample can be determined (186,187).

1.4.2.2. Zeta Potential

Zeta potential measurements define the overall surface charge of the RNA-LNP. LNP surface charge ranges from anionic to near neutral and cationic charges dictated by LNP formulation composition. Zeta potential is a key measured CQA as it not only defines surface charge under specific buffer pH conditions but also provides further insights into how the formulation will interact with endogenous biomacromolecules and cells upon *in vivo* administration.

Electrophoretic light scattering measured the fluctuations in scattered light relative to the particle velocity moving to opposing charged capillary. This velocity is calculated to electrophoretic mobility using Henry equation and zeta potential can be calculated by applying the Smoluchowski approximation.

$$U_E = \frac{2\,\varepsilon\,\zeta\,f(ka)}{3\,\eta}$$

***Equation 1.3** - Calculation of electrophoretic mobility using Henrys Law.*

Where U_E defines electrophoretic mobility, ε represents the dielectric constant, ζ is the zeta potential f(ka) is Henry's function, where the Smoluchowski approximation is applied (1.5) for aqueous based colloidal dispersions containing moderate electrolyte concentrations, and η is colloidal viscosity. Formulation stability is also conferred through zeta potential measurements as DLVO theory (188) states that colloidal system interactions are a balance of attractive Van Der Waals and repulsive electrostatic interparticle forces.

1.4.2.3. Quantification of RNA Encapsulation

A widely adopted assay for quantifying RNA encapsulation efficiency in LNPs formulations is the RiboGreen™ assay. This fluorescence-based assay enables the differentiation between encapsulated and unencapsulated RNA by measuring total RNA content following LNP lysis, and comparing it to the amount of free RNA present in intact LNP suspensions. The encapsulation efficiency is typically calculated using a mass balance approach, where the measured RNA concentration is compared against a standard calibration curve generated from known RNA concentrations to determine the percentage of RNA recovery. The assay relies on the RiboGreen dye, which selectively hybridises to the RNA, and emits a fluorescence signal proportional to the exact concentration of RNA. Although the precise mechanism of interaction between the RiboGreen™ dye and RNA remains proprietary, the assay is considered a gold standard in the field due to its high sensitivity, specificity, and reproducibility. Additionally, it is compatible with high-throughput workflows, making it particularly valuable for screening and optimizing LNP formulations.

1.4.3. Novel and Emerging Analytical Pipelines for RNA-LNP Formulation Evaluation

The rapid advancement of RNA LNP formulation strategies has been key for driving the success of approved RNA-LNP formulations. However, the development of analytical techniques has not progressed at a comparable rate, resulting in a technological gap that limits comprehensive understanding of formulation CQAs to further increase LNP clinical translation (189).

Advanced analytical methodologies have the potential to provide deeper insights during early-stage discovery and development (190), particularly in evaluating therapeutic candidates and refining formulation strategies (191). Despite their potential, these enhanced analytical pipelines often require specialist training and advanced method development, which can hinder their routine adoption. Nevertheless, they offer significant advantages over conventional techniques, particularly in terms of sensitivity, resolution, and the ability to inform early LNP formulation development efforts. State-of-the-art separation and detection technologies are increasingly being integrated into analytical workflows, offering more robust and detailed assessments of LNP properties, including particle heterogeneity, encapsulation efficiency, and stability.

1.4.3.1. High Resolution Mass Spectrometry

In the evolution of mass spectrometry, Orbitrap mass spectrometry represents a significant advancement from earlier discussed quadrupole technologies (192). While traditional quadrupole systems single (Q1) or triple (Q1, Q2, Q3) rely on oscillating electric fields for mass filtering in a linear configuration for targeted quantification. Triple quadrupole systems employ tandem mass filter with precursor selection in Q1, collision-induced fragmentation in Q2 and product ion quantification in Q3. In contrast, the Orbitrap introduces a fundamentally different detection principle using electrostatic ion trapping.

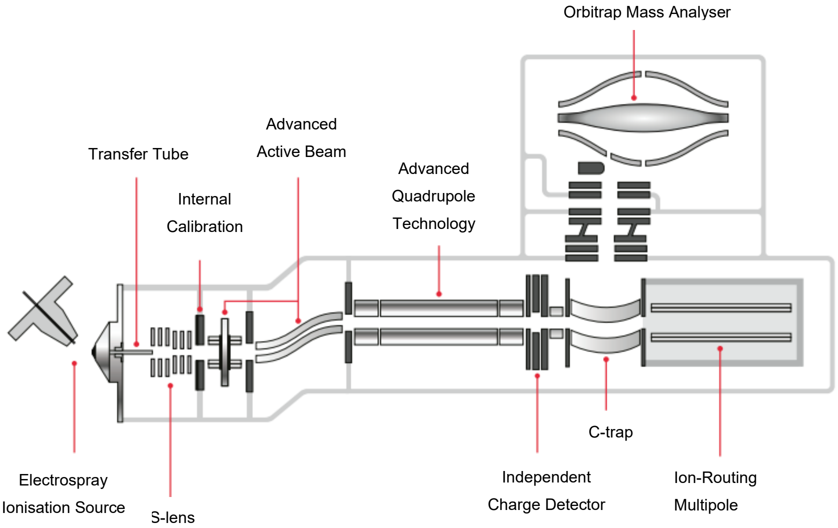

***Figure 1.10** - Thermo Orbitrap® Exploris 240 MS detection system for enhanced analytical m/z characterisation.*

Ions are initially guided through beam optics and quadrupole filters into the c-trap, which accumulates and focuses sample ions before injection into the Orbitrap analyser. Unlike magnetic or radiofrequency-driven quadrupoles, the Orbitrap relies on a purely electrostatic field, where ions oscillate around a central spindle-shaped electrode. This motion is directly related to ion mass-to-charge ratio, with frequency inversely proportional to the square root of m/z (193). The result is high-resolution, accurate mass detection of sample ions at sub parts per million mass accuracy, which enables differentiation of various molecular weight species with ultra-high precision.

1.4.3.2. Field-Flow Fractionation

Field-flow fractionation (FFF) is a relatively modern separation analytical technique, pioneered in the 1960s by Calvin Giddings (194). The technique uses a diffusion-based approach to separate colloidal dispersions-based size within a porous membrane covered channel.

$$t_R = \frac{\pi \eta d_H w^2}{2kT}\frac{V_c}{V}$$

***Equation 1.4** - Giddings equation for FFF based size separation. Where t_R is retention time, η is viscosity, d_H is particle hydrodynamic diameter, w is channel thickness, k is Boltzmann constant, T is temperature and V_c is volumetric channel flow and V is volumetric channel outlet flow.*

Asymmetric-flow FFF (AF4), builds upon these principles by using a parabolic flow profile in tandem with a perpendicular cross-flow force field, which are applied to the separation channel. As the cross-flow decays, particles are separated based on their diffusivity heights within the channel. The parabolic flow profile flows the particles towards the channel outlet hyphenated online detectors in series. In AF4, separation is split into three steps, A) injection, B) focus and C) elution, highlighted in **Figure 1.11**.

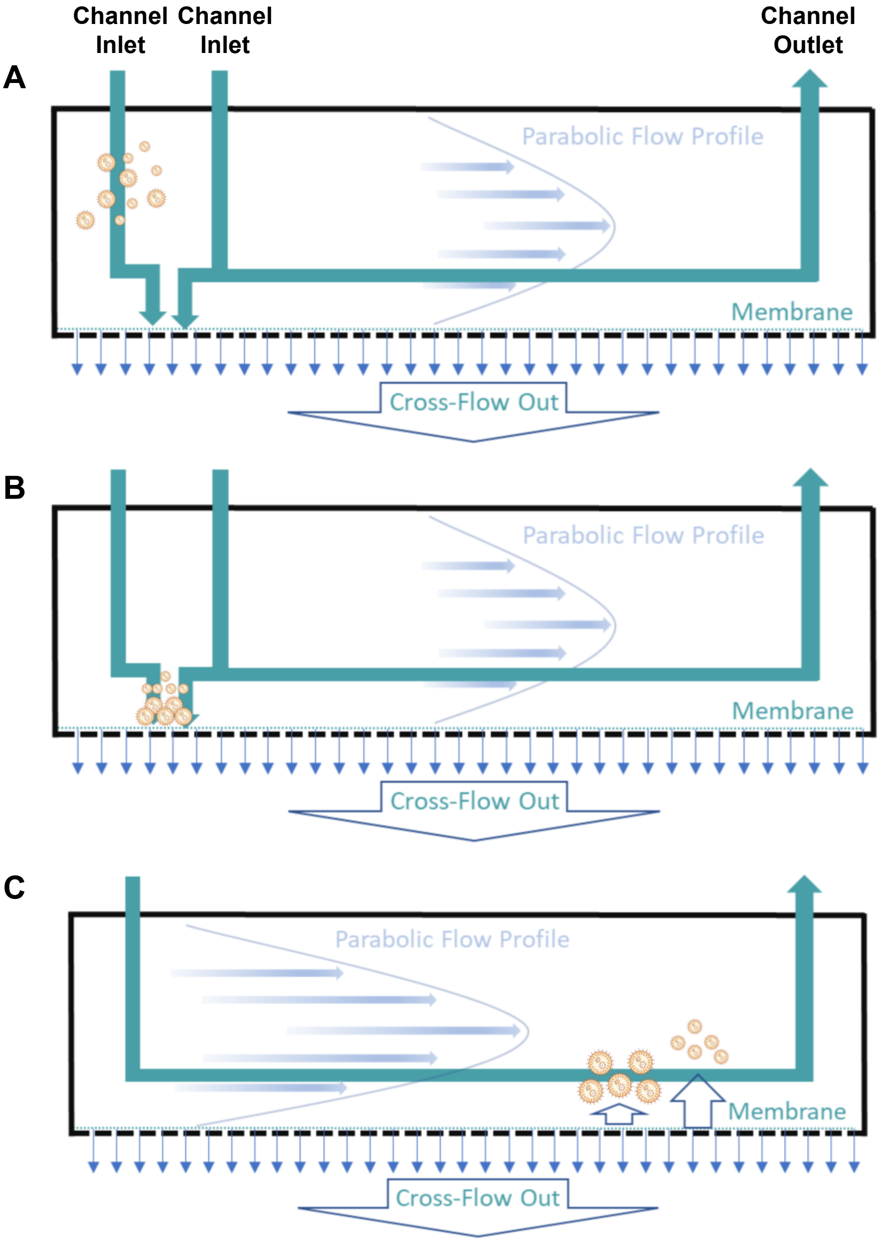

Figure 1.11 *- AF4 separation process steps, A) sample injection, B) sample focussing, and C) sample elution.*

The sample is first injected into the channel. With the cross-flow applied, the sample is driven downward toward the channel membrane. Simultaneously, a focus flow is introduced, concentrating the sample into a narrow band within the channel. Once the focusing step is complete, the focus flow is stopped, allowing parabolic and cross-flow to dominate. A programmed cross-flow decay is then applied, enabling size-based separation through diffusion, with detection occurring at the channel outlet.

Compared to conventional size exclusion chromatography, AF4 offers a gentler separation technique, making it well-suited for soft nanomaterials and RNA-LNP formulations by eliminating column-induced shear stress. However, AF4 is not entirely stress free; significant sample-membrane interactions can occur during the focusing step. To mitigate this, tailored membrane chemistries (PES, modified regenerated cellulose) can be employed to reduce non-specific binding and sample adsorption. Alternatively, implementing a frit-inlet (FI) channel configuration, alongside careful membrane chemistry selection can eliminate the need for the focusing step.

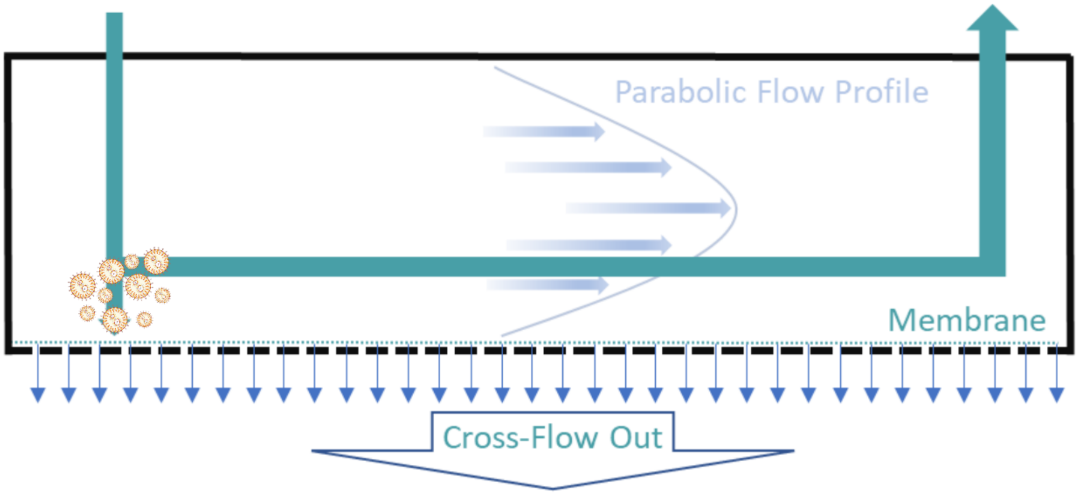

***Figure 1.12** — Frit-inlet AF4 (FI-AF4) system injection, and elution step.*

FI-AF4, uses focus flow as part of the channel inlet flow for the sample to accumulate on the membrane, allowing the sample to disperse over a larger area rather than a smaller, defined space through focussing. Samples elute based on diffusion-based size separation and flow *via* channel outlets to online detectors. FI-AF4 has been the preferred separation method for soft materials over conventional AF4 due to a reduction in forced membrane interactions. However, shear stress on soft materials is not completely negated as the analyte is still required to accumulate on the membrane prior to crossflow decay diffusion separation in channel outlet detection.

Another subgroup of AF4 uses an electrical force field channel application to separate components based on their electrical properties as well as size for enhanced diffusion and separation. Electrical asymmetric-flow field-flow fractionation (EAF4) is a new subgroup, which was introduced in 2015.

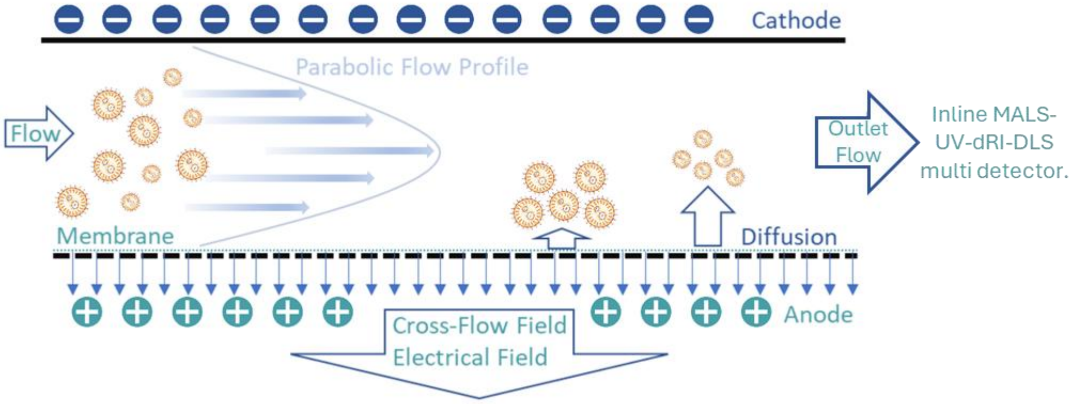

Figure 1.13 *- EAF4 channel schematic, highlighting flow and electrical based separation through dual force field usage with cationic LNPs as an exemplar sample.*

The integration of flow-based and electrical-based force fields enables enhanced separation performance compared to AF4 alone (195). Upon sample injection and focusing onto the accumulation wall, an oppositely charged top plate introduces an electrostatic force that promotes diffusion upwards through attraction, while the applied cross-flow simultaneously drives the sample downward toward the membrane. A dynamic balance is established between electrostatic attraction to the top plate and perpendicular cross-flow pressure. When combined with a programmed cross-flow decay, particles are permitted to diffuse further into the channel, with movement facilitated by electrostatic attraction from the top plate and repulsion from the membrane. The application of an electric field also allows for real-time measurement of electrophoretic mobility and zeta potential of separated sub-populations, offering greater resolution of surface charge properties compared to conventional batch-mode zeta analysis.

While these advanced AF4 systems offer novel separation capabilities, their utility is limited without integrated online detection.

Inline Hyphenated Detectors

FFF systems offer enhanced separation of otherwise batch mode focussed soft material analytics, various detectors can be hyphenated online, with soft material focus, light scattering and absorbance remain key for material quality analysis and quantification.

Light Scattering

Multi-angle light scattering (MALS) can be used to confer radius of gyration and molar distribution information on RNA/RNA-LNP samples. The system uses similar principles to DLS, with the enhancement of multiple scattering angle detectors can produce further insights than large-sized bias within DLS analysis. Since small particles scatter light in all direction, MALS can detect and analyse light scattering based on the angle of detection (7-156 ° over 21 angles), at small or large angles. The use of MALS can define the radius of gyration, which is calculated from the root mean square of the centre of mass of the particle. MALS data are then fitted to various processing models, which assume correctional morphology assumptions. These models include Zimm, random coil and sphere, based on sample morphology assumptions and best light scattering angle data fit, each model is chosen dependant on material being analysed. DLS can also be used online, superseding batch-mode conventional DLS measurements with population distribution characterisation. Like batch-mode DLS measurements, online DLS uses the same principle, calculating hydrodynamic size based on 173° particle non-invasive back scattering angle. Combining MALS and DLS size data can be used to estimate particle morphology by calculating associated shape factor (196), with the use of radius of gyration, R_G, from MALS detector divided by hydrodynamic radius, R_H, from DLS, further enhancing insights into morphology-based particle population distribution.

UV Absorbance

Similar to conventional UV detectors (260 nm) used in chromatography, AF4-based systems use UV absorbance to track active RNA drug distribution profile and for the calculation of separation recovery through sample cross-flow and direct channel injection to evaluate AF4 method quality (197). Specific UV wavelengths can be utilised at various sensitivities to ensure appropriate signal detection without saturating the UV detector. As both PDA and UV detectors are used to track RNA across chromatographic and AF4 techniques respectively, PDA can monitor the entire UV/Vis spectrum (190-800 nm), whereas UV detector can only monitor 1-4 selective wavelengths.

FFF-based separation and online detection systems represent a class of non-invasive techniques, which maintain the structural integrity of the RNA-LNP sample, while delivering maximum CQA outputs and enhanced analytical insights in population-based distributions.
Growing interest in RNA-based drugs as nanomedicines has highlighted both their immense potential and the significant translational barriers they face. Although RNA drugs offer unique advantages including programmability, potent biological activity, and broad therapeutic applications, their clinical translation is limited by inherent molecular instability, susceptibility to nuclease degradation, immunogenicity and poor cellular uptake. These limitations necessitate the use of chemical modifications and advanced drug delivery platforms to ensure stability, targeted delivery, and therapeutic efficacy. LNPs have emerged as one of the most promising delivery technologies for RNA therapeutics. Their ability to enhance bioavailability, improve biocompatibility, and enable efficient drug encapsulation capabilities has positioned them at the forefront of RNA drug development.

1.5. Thesis Overview, Aims and Objectives

1.5.1. Thesis Overview

Wider literature has demonstrated the importance of screening individual lipids within RNA-LNP formulations even at low molar ratios. On the combination of the four molecular groups with anionic RNA cargo, successful LNP formulation manufacture can be achieved through a variety of methods at different scales. With the rapidly evolving landscape of new lipid chemistries and advancements in microfluidics formulation parameter optimisation, a new generation of modern lipids is emerging (24,79,198,199), which interact differently with drug cargo by virtue of their chemical characteristics. The wider literature has investigated lipid packing distributions, densities, and geometries to bridge the theoretical knowledge gap of lipid nanocarrier encapsulation using varying *in silico* approaches (atomistic, molecular dynamic, coarse-grained simulations) over the last decade (200–206). There remains a gap within current literature on detailed RNA-LNP physicochemical analysis and subsequent impact of RNA drug substance purity on overall LNP formulation critical quality attributes.

1.5.2. Thesis Aims and Objectives

The overall aim of this thesis is the development of novel analytical pipelines for the evaluation of RNA-based therapeutics, with a focus on how the implementation of high-resolution orthogonal analytics can provide deeper insights into conventional drug substance and drug product critical quality attribute evaluation within early discovery and pre-clinical development phases.

Chapter 1 details a broad introduction to nanomedicines, the need for advanced therapeutics, the use of ribonucleic acid drugs, utilisation of LNP-based drug delivery systems, their manufacture and analytical pipelines.

Chapter 2 explores analytical method development for the ASO therapeutic modality for gene silencing. This chapter outlines the chromatographical development of analytical methodology required to analysed synthesis-associated impurities within ASO manufacture. By cross-comparing different orthogonal techniques, chromatographic approaches, and the use of single and quadrupole mass spectrometry detection systems, results demonstrated that less-complex detection systems were viable and fit-for purpose to use within early drug substance testing across low resource settings.

Chapter 3, encapsulates ASOs into a LNP drug delivery system for enhanced CQA characterisation, focussing on the transition from drug substance to drug product. This chapter also investigated the incorporation of an ASO payload into LNP formulation drug delivery platform use to enhance early discovery studies to facilitate development and improve clinical translation.

Chapter 4 builds on the early characterisation reported in Chapters 2 and 3 by analysing drug substances using state-of-the-art pipelines for deeper analytical insights into drug substance CQAs. This chapter further assesses the translational impact of drug substance CQAs on LNP formulation CQAs. Building on the methodology used in chapter 3, an additional electrical force-force was utilised in tandem with a crossflow decay force-field to improve charge variant and size-based resolution in the assessment of three vendor specific Poly(A) drug substances. The use of the EAF4 multidetector system allows for population zeta potential calculation, molecular weight and molar mass distribution evaluations. To evaluate LNP formulation CQAs, pipelines developed in chapter 3 were used using clinically relevant ionisable LNP formulation compositions.

Chapter 5 highlights the evaluation of a model cationic RNA-LNP drug delivery system within early development using a suite of high-resolution analytical pipelines. Various stages within early development were considered and analysed including, process parameters, short term stability and frozen storage impact on formulation critical quality attributes. This work highlights pipeline LNP candidate formulation and the need for enhanced analytical techniques for early LNP candidate screening and selection ensuring maximum insights into CQA analysis to further develop next generation LNP candidates.

Chapter 6 utilises enhanced data analytical pipeline to elucidate high resolution AF4 sub-populations to further enhance simulation quality and link sub-population biophysical parameters with RNA loading across separated populations. Theoretically calculated sub-populations are then linked back to experimental data, which is correlated through differing formulation parameters e.g., ionisable lipid, RNA drug, N/P ratio, formulation buffer to start to model RNA-LNP formulation outcomes, for future predictive modelling.

Chapter 7 summarises the thesis with overall discussion of outcomes and positions the findings from this thesis in the broader context of the literature highlighting future work, and key conclusions.

Chapter 2

2. Antisense Oligonucleotide Analytics: Advancing the Understanding of Drug Substance Critical Quality Attributes

Single Quadrupole MS ASO quantification was deconvoluted by Shimadzu MSO collaborators Emily Armitage and Alan Barnes. Ion-pair reversed-phase chromatography and gel electrophoresis runs were conducted by Pascale Rae. All other experimental work was carried out by the author of this thesis.

Graphical Abstract

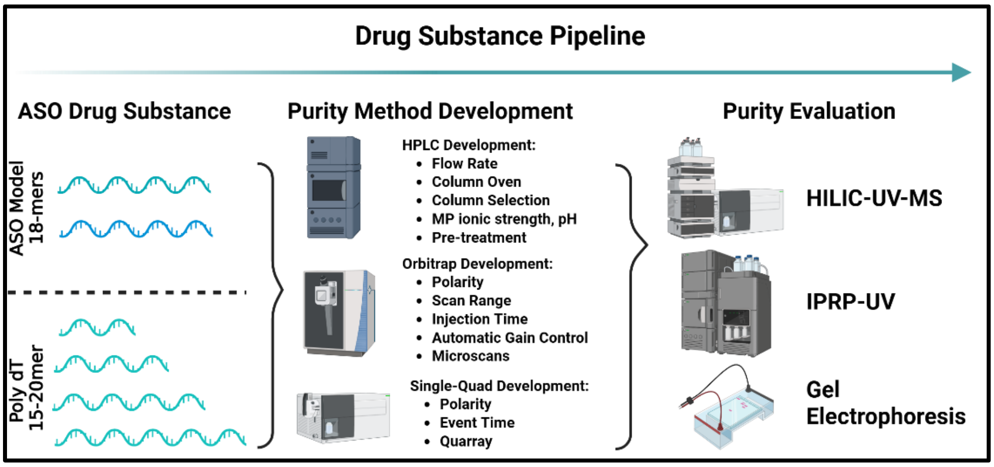

2.1. Introduction

Oligonucleotide (ON) therapeutics, typically 10-30 nucleotides in length, have demonstrated unprecedented therapeutic potential within pharmaceutical research. Their platform synthesis approach (42,207,208), variety of extensive chemical modifications (48,65,73) and broad-spectrum applicability have led to a new class of precision, genetic medicine. Among these, antisense oligonucleotides (ASOs) have shown success with the approval of 11 ASO therapeutics accounting for >50 % of all approved oligonucleotide therapeutic classes (209). These therapeutics have applications in HIV/AIDS treatment, cancer therapy and muscular dystrophy, showcasing their ability to target disease pathways, previously inaccessible to traditional small molecule drugs (73).

The solid-phase synthesis of ASOs involves stepwise catalytic addition of nucleotides under anhydrous conditions (41,42,208,210). However, this method is susceptible to introducing a range of impurities such as truncated sequences or deletion products that are chemically similar to the desired target full length product (FLP) and are difficult to resolve and quantify . These impurities pose analytical challenges due to their close molecular weights and physicochemical properties (36,46). While advances in analytical technologies have improved impurity profiling, quantification remains a key challenge during therapeutic development.

Liquid chromatography (LC) hyphenated mass spectrometry (MS) remains the gold standard for ON analysis, particularly when using ion-pair (IP) reversed-phase (RP) separation methods (211,212). Due to the anionic and hydrophilic nature of ASOs, IP reagents are required to passivate these attributes for successful reverse-phase compatibility. Common reagents include trialkylammonium salts and hexafluoroisopropanol to facilitate compatibility and separation (176,213,214). Numerous studies have extensively characterised ion-pairing (176,215), column selectivity (176,213,216), hyphenation with mass spectrometry-based systems (217,218) and types of ON under analysis (175,219,220). Despite IP-RP-LC separation effectiveness, IP reagents possess known toxicity profiles, with many laboratories requiring a dedicated system for single ASO quantification usage. Alternatively, hydrophilic interaction liquid chromatography (HILIC) has emerged in recent years as a non-toxic substitute for ASO separation and quantification (221). HILIC utilises inherent ASO hydrophilic properties by exploiting polar stationary phase interactions, combined with non-polar mobile phase gradient to enhance ASO retention and separation (177,179,222–224).

Advances in MS sensitivity have progressively lowered the limits of detection and quantification achievable in the analysis of ASOs. Despite these improvements, the increasing cost and the requirement for specialist technical expertise present significant barriers to their broader adoption across the sector. As a result, limited comparability exists between complex, high-resolution analytical platforms and more simplified detection techniques, which may hinder broader adoption in low-resource laboratory settings.

ASOs present significant analytical challenges in identification and purity analysis due to their structural complexity, sequence-defined nature, and the multi-step catalytically driven solid phase synthetic approach used in their manufacture. Process-related impurities commonly arise from incomplete coupling reactions, leading to deletion *(n-1)* or truncated sequences, as well as addition *(n+1)* products generated during inefficient capping or unintended side reactions (225,226).

To provide orthogonal confirmation of mass spectrometry-based identity and purity findings, gel electrophoresis is routinely implemented as a complementary technique. Gel electrophoresis exploits the anionic phosphodiester or phosphorothioate backbone of ASOs, enabling size-based separation according to molecular mass and migration behaviour under an applied electric current. Within the context of this chapter, the focus was on improving the detection of n–1 impurities, requiring a resolution sufficient to discriminate a mass difference of ~ 0.3 kDa, corresponding to the loss of a single nucleotide, an analytical challenge that simplified electrophoretic techniques are, under optimised conditions, capable of resolving.

Here, *n* denotes the number of nucleotides in the intended FLP sequence. Additional impurities may arise from aberrant capping, oxidation and incomplete deprotection steps, each of which generates species that are chemically and structurally similar to the target FLP. These similarities give rise to increased complexity of ASO separation and confound accurate purity determination.

Beyond process-related impurities, ASOs are also susceptible to various chemical, biological and environmental degradants, further contributing to their overall impurity profiles. Stability-related impurities include products of oxidation, hydrolytic cleavage, backbone phosphorothioate (PS) to phosphodiester (PO) conversion, nucleobase loss and base deamination (174). These impurities may arise during storage, handling or intensified under stressed conditions (elevated temperatures, light exposure, extreme pH). The formation of these degradation-based impurities can adversely impact ASO pharmacological activity, safety and translation (227,228).

Given these considerations, the aim of this study was to investigate the use of analytical methods routinely available in formulation laboratories, particularly those that lack high-resolution. Accordingly, this chapter focuses on assessing simplified, cost-effective, and environmentally sustainable analytical approaches that could facilitate broader adoption of ASO impurity profiling across diverse laboratory settings.

IP-RP chromatography remains the benchmark analytical technique for probing RNA-based drug purity; therefore, IP-RP-UV analysis was utilised in this work to classify low- and high-molecular-weight species in relation to the ASO FLP. This chapter explores the applicability of multimodal analytical approaches, incorporating nominal and accurate mass spectrometry methodologies, for determining ASO mass and confirming sequence identity. Nominal mass MS defines molecular mass using the most abundant isotope, averaged to the nearest integer value, whereas accurate mass MS relies on exact isotopic masses of specific elemental isotopes, providing decimal level precision in mass assignment (229).

Nusinersen was selected as the primary model sequence within this work (178) to test and validate the analytical pipeline developed. Nusinersen is an 18-mer phosphorothioate antisense oligonucleotide containing a variety of chemical modifications shown in **Figure 1.2.** The sequence structure has no reported secondary structures unlike typical mRNA long chain sequences, however algorithms like RNA-Fold can predict the propensity to form secondary structures. The predominant impurities associated with nusinersen include *n±1* species, which remain challenging to resolve using chromatography due to their minimal mass differences and structural similarity. A modified nusinersen sequence was also assessed, in which methylated bases were removed and sugar modifications were reduced from methoxyethyl to oxymethyl. To further benchmark MS pipelines and chromatographic performance across chemistries, Poly(dT) oligonucleotides of 15, 16, 18 and 20-mers in length with no backbone, sugar or nucleobase modifications were also analysed.

Results obtained from LC-MS analysis were cross-compared with standard IP-RP-UV and gel electrophoresis. Given the established use of IP-RP chromatography as a benchmark method, IP-RP-UV was utilised to assign low- and high-molecular-weight species in relation to the full-length product. It was hypothesised that through targeted optimisation, lower-complexity analytical platforms can attain a level of resolution in terms of chromatographic (separation) and mass spectral (detection) that are comparable to advanced MS-based approaches for ASO therapeutics for identity and purity analysis, although primary differences will be in sensitivity and limit of detection across the modes of measurement.

The primary objective of this work was therefore to evaluate and compare the resolving power, sensitivity and operational feasibility of IP-RP-UV, LC-MS and classical gel electrophoresis for ASO impurity profiling. By addressing the existing resolution and cost disparity between advanced and simplified analytical platforms, this research seeks to facilitate broader uptake and enhance the translational potential of oligonucleotide-based therapeutics.

2.2. Materials

Acetonitrile (LC-MS Grade), water (LC-MS Grade), formic acid and ammonium hydroxide were sourced from Fisher Scientific (Leicestershire, UK). Ammonium formate, ammonium acetate, HFIP and N,N-diisopropylethylamine were sourced from Merck (Gillingham, UK). Thermo Accucore HILIC column (100 x 2.1 mm, 2.6 µm, 80 Å, part #17526-102130), a Waters BEH HILIC column (100 x 2.1 mm, 1.7 µm, 130 Å, part #186003461) and a Waters BEH Amide column (150 x 2.1 mm, 1.7 µm, 130 Å, part #186004802) were used for analyte HILIC-based separation. Waters Oligonucleotide C18 column (100 x 2.1 mm, 1.7 µm, 130 Å, part #186009485) was utilised for ion-pairing experiments.

ON1 (Nusinersen) was sourced from MedChem Express (Wembley, UK), ON2-6 were manufactured by Integrated DNA Technologies as per **Table 2.1** .

***Table 2.1** – Model ON sequences, associated chemical modifications and molecular weights.*

ON	Sequence	Molecular Weight (Da)
ON1 – 18-mer	5'-UCACUUUCAUAAUGCUGG-3' 2'-MOE, PS, UC 5'-methyl	7127.2
ON2 – 18-mer	5'-UCACUUUCAUAAUGCUGG-3' 2'-OMe, PS	6179.9
ON3 – 15-mer	5'-TTTTTTTTTTTTTTT-3'	4501.0
ON4 – 16-mer	5'-TTTTTTTTTTTTTTTT-3'	4805.2
ON5 – 18-mer	5'-TTTTTTTTTTTTTTTTTT-3'	5413.6
ON6 – 20-mer	5'-TTTTTTTTTTTTTTTTTTTT-3'	6022.0

2.3. Methods

2.3.1. Urea Denaturing Gel Electrophoresis

Oligonucleotide samples and a 10/60 DNA ladder (Integrated DNA Technologies) were mixed with 2× RNA loading dye (Thermo Scientific) at a 1:1 (v/v) ratio. Samples were denatured at 90 °C for 2 min, briefly centrifuged to collect condensation, and loaded onto the gel. A total volume of 10 µL of each sample was loaded into each well of 15% Mini-PROTEAN® TBE-Urea precast gel (Bio-Rad). Gels were run in 1 x TBE running buffer (Bio-Rad) at a constant voltage of 200 V for 45–75 min in a Mini-PROTEAN Tetra Cell (Bio-Rad).

Following electrophoresis, gels were removed from the cassettes and stained with SYBR Green II (Thermo Scientific) diluted 1:10,000 in 1 x TBE buffer. Staining was performed with gentle agitation for 20 minutes at ambient temperature in the dark. Gels were imaged immediately after staining using a UV transilluminator (Syngene).

2.3.2. Ion-Pair Reversed-Phase (IP-RP) LC-UV

Sample analysis was conducted using a Waters ACQUITY Premier ultra-high-performance liquid chromatography (UHPLC) system (Milford, USA) equipped with a solvent manager, sample manager and PDA detector.

Table 2.2 – IP-RPLC-UV separation and detection parameters or ON1 and ON2 sequences.

Parameter	Value	
Column	Waters Premier Oligonucleotide BEH C18 (100 x 2.1 mm, 1.7 µm, part #186009485)	
UV Detector	260 nm	
Autosampler Temperature	4 °C	
Mobile Phase A	50 mM HFIP, 5 mM N,N-diisopropylethylamine in water	
Mobile Phase B	50 mM HFIP, 5 mM N,N-diisopropylethylamine in (50/50, v/v) Water/Acetonitrile	
Flow Rate	0.35 mL/min	
Injection Volume	2 µL	
Column Temperature	40 °C	
Gradient	Time (min)	% B
	0	10
	10	40
	10.1	10
	11.0	100
	11.1	10

2.3.3. HILIC-based Chromatographic Separation

Sample analysis was conducted using a Shimadzu Nexera ultra-high-performance liquid chromatography (UHPLC) system (Osaka, Japan) equipped with a flow controller (SCL-40), solvent delivery module (LC-40B-X3), auto-sampler (SIL-40C X3), column oven (CTO-40C). and photodiode array (PDA, SPD-M40).

***Table 2.3** – HILIC UHPLC Settings. *Final parameter value selected after method development. ON1/ON2 were utilised for column optimisation. ON1 was utilised for the optimisation of mobile phase ionic strength, pH, column temperature, flow rate and pre-treatment optimisations.*

Parameter	**Value**	
Column*	Waters Premier BEH Amide (150 x 2.1 mm, 1.7 µm, part #186004802)	
PDA	260 nm	
Autosampler Temperature	4 °C	
Mobile Phase A*	20 mM Ammonium Acetate	
Mobile Phase B	Acetonitrile	
Flow Rate*	0.3 mL/min	
Injection Volume	5 µL	
Column Temperature*	40 °C	
Needle/Seal Wash	Acetonitrile/Water, (50/50 v/v)	
Gradient	Time (min)	% B
	0	90
	45	50
	60	50
	60.1	90

2.3.4. High-resolution, Accurate Mass Determination by Orbitrap LC-MS

Sample analysis was conducted using a Thermo Vanquish ultra-high-performance liquid chromatography (UHPLC) system equipped with a binary pump, split sampler, column oven and inline Orbitrap Exploris 240 mass spectrometer (ThermoFisher Scientific).

The comparison between Orbitrap and single quadrupole mass spectrometry platforms remains important as orbitrap is considered the current gold standard considering ON identification, sequencing and impurity profiling. However, orbitrap analysers pose a barrier requiring excessive cost and specialist training for use, data analysis and interpretation, whereas single quadrupole systems are more cost effective and easier for general usage. These factors can enhance uptake and accessibility in low-resource settings.

***Table 2.4** - Orbitrap settings. *Final parameter value selected after method development. ON1/ON2 sequences were used for polarity and scan range optimisation. ON2 was used for AGC microscan and injection time optimisation.*

Parameter	**Value**
Ion Source	Heated Electrospray
Polarity*	Negative
Pressure Mode	Low Pressure
Negative Ion Voltage	2500 V
Sheath Gas	40
Sweep Gas	1
Auxiliary Gas	10
ITT Temperature	320 °C
Vaporiser Temperature	300 °C
MS^1 Resolution	120 k
MS^1 Miscroscans*	5
MS^1 AGC Target*	300
MS^1 Scan Range*	600-3000 m/z
MS^1 RF Lens	75 %
MS^1 Injection Time*	1000 ms

ON deconvolution was performed on Thermo BioPharma Finder 5.3 using the Intact Protein Deconvolution feature using XTRACT sliding window deconvolution with the following parameters: relative intensity threshold 1%, target average spectrum width = 0.2 min, number of detected intervals = 3, merge tolerance 30 ppm, maximum RT gap = 1 min, S/N threshold = 3, charge range 2-9, minimum number of charges detected = 3, relative abundance threshold = 0. Mass output ranges varied by roughly ± 1000 Da per ON FLP MW in **Table 2.1.** in negative ionisation mode.

2.3.5. Single Quadrupole (SQ) LC-MS

Sample analysis by single quadrupole LC-MS was conducted using a Shimadzu Nexera ultra-high-performance liquid chromatography (UHPLC) system (Osaka,Japan) equipped with a flow controller (SCL-40), solvent delivery module (LC-40B-X3), auto-sampler (SIL-40C X3), and column oven (CTO-40C). Inline detectors include photodiode array (PDA, SPD-M40) and single quadrupole mass spectrometer (LCMS-2050) equipped with electrospray ionisation source.

*Table 2.5 - SQ 2050 settings. *Final parameter value selected after method development. ON2 sequence was used for polarity, event time and qarray voltage optimisation.*

Parameter	Value
Ion Source	Electrospray
Polarity*	Negative
Nebulising Gas Flow	2 L/min
Drying Gas Flow	5 L/min
Heating Gas Flow	7 L/min
Desolvation Temperature	400 °C
Desolvation Line Temperature	250 °C
Mass Range	650-2000 m/z (ON1-2), 450-2000 m/z (ON3-6)
Event time* (Scan Speed)	1.0 s (1364 μ/s)
Qarray*	-25 V
Interface Voltage	-2 kV

ON deconvolution was carried out using Insight Biologics v 4.42.6.0, using MS deconvolution spectrum error margin 150 ppm, charge state of 2-9 with, MS spectrum settings of 150 ppm error margin, minimum error margin 500 mDa and a minimum reporting score of 0.1. Deconvolution output profiles were shown in the *n-1* mass range.

2.3.6. ON Linearity, Limit of Detection and Limit of Quantification

A series of six calibration curves (ON1/ON2) were prepared ranging from 0-1 mg/mL with 5 μL of each injected in duplicate from low to high concentrations. PDA, SQ and Orbi FLP peak areas were integrated manually using associated system software and associated peak areas were processed using linear regression to evaluate linearity, LOD and LOQs for ON1 and ON2, respectively, aligning with ICH Q2(R2) guidelines (171).

2.3.7. Statistical Analysis

Exploratory method development data are represented as a single technical replicate. Optimised ASO characterisation was averaged by defined duplicate or triplicate technical replicates. Orbitrap optimised method interpolations were done within Jupyter Notebooks (v2025.9.1) using python scripts (numpy, pandas, kernel 3.13.5) . Figures were graphed using OriginPro v 9.9.0.220.

2.4. Results

2.4.1. Gel Electrophoresis Separation

Denaturing urea gel electrophoresis was used to verify ON1 and ON2 molecular weight and assess their purity.

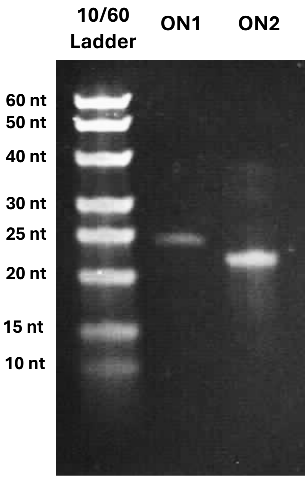

***Figure 2.1** –Denaturing Urea Gel Electrophoresis separation of a 10-60 nt RNA ladder and ON1 and ON2 sequences (10 µL @ 40 µg/mL ON loaded).*

Electrophoretic separation revealed distinct differences between both ON samples loaded at equivalent concentrations (10 µL, 40 µg/mL). ON1 migrated closer to the 25 nt ladder band, whereas ON2 migrated closer to 20 nt band (**Figure 2.1**). Although both sequences were 18 nts in length, neither were resolved below the 20 nts marker, resulting in an apparent overestimation of their size. This discrepancy is likely attributable to the extensive chemical modifications of these sequences, which can impact overall molecular electrophoretic mobility by increasing molecular mass and modifying their respective charge densities. Purity analysis (260/280) demonstrated sequence-based differences with a measured ON1 purity of 1.6, and ON2 purity of 2.1. ON1 displayed reduced fluorescence compared to ON2, which may reflect the impact of sequence modifications on SYBR dye binding, and ON purity. These modifications add additional weight onto the ON sequences, in comparison to unmodified comparators. Overall, while denaturing gel electrophoresis successfully confirmed the presence of intact oligonucleotides, its resolution was insufficient to discriminate closely related impurities, such as the *n-1* sequence resolution, highlighting a key limitation of this technique for ASO impurity analysis.

2.4.2. Ion-Pair Reversed Phase LC-UV

IPRP-UV separation was investigated to further investigate findings from gel electrophoretic analyses, whereby, ONs are separated based on hydrophobicity in reverse-phase chromatography, however with the addition of ion-pair additives to enhance the overall molecular hydrophobicity to enable RP compatibility and separation.

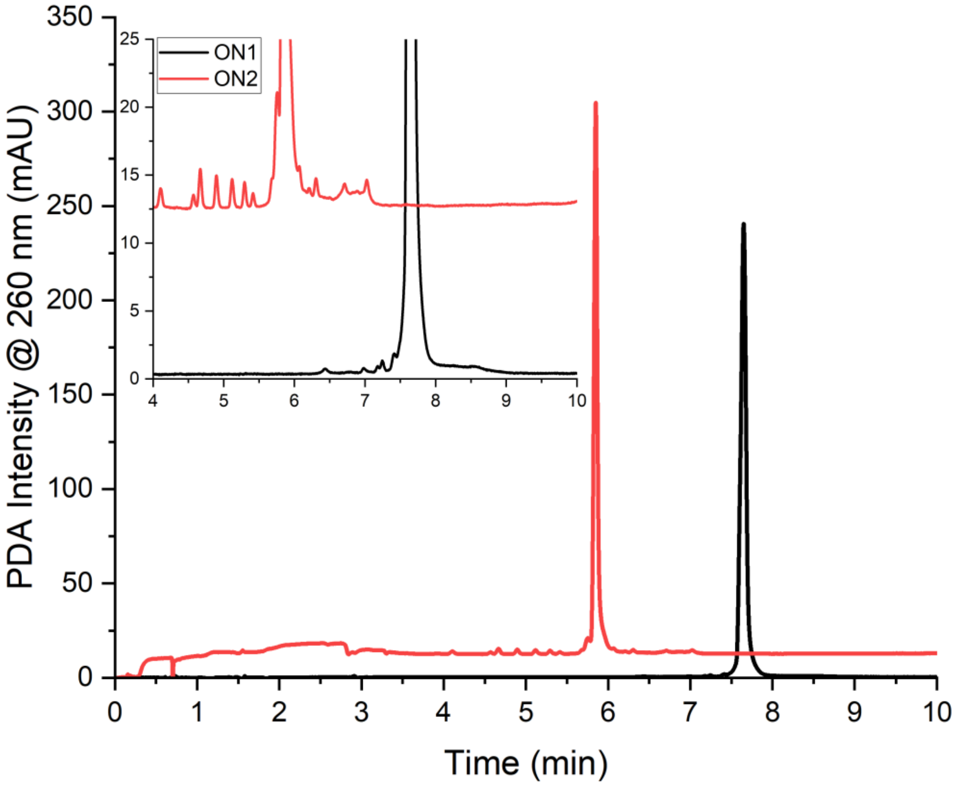

Figure 2.2 - IPRP-UV evaluation of ON1 and ON2 using blank subtracted UV separation profiles 2 µL of 0.1 mg/mL, (n=1).

Separation across IPRP proved successful, with ON1 and ON2 retaining and elution from a reverse-phase C18 column (**Figure 2.2**). ON1 showed enhanced retention (7.65 min), compared to earlier retention of ON2 (5.85 min), indicative of ON molecular level modifications producing overall macromolecular characteristics, enabling superior hydrophobic ON1 retention. ON2 produced a higher detector intensity (303 mAU), compared to ON1 (238 mAU) (**Figure 2.2**), these differences could be attributed to ON interaction with ion-pair reagents, with increased compatibility with ON2 over ON1. These intensity values align with purity (260/280) and electrophoresis results, with ON2 producing enhanced fluorescence compared to ON1 which producer less intense banding (**Figure 2.1**).

2.4.3. Method Development

2.4.3.1. *Optimisation of HILIC-based Separation*

Various LC parameters were optimised using online photodiode array (PDA) detection prior to hyphenation with SQ or orbitrap MS detection. Optimised parameters included column oven temperature **(Figure S 8.1),** column selection **(Figure S 8.2),** mobile phase ionic strength **(Figure S 8.3**), mobile phase pH **(Figure 2.3)**, flow rate **(Figure 2.4)** and sample pre-treatment conditions **(Figure 2.5)**.

Column oven temperature produced comparable elution profiles and signal intensities (150 mAu) at each temperature condition tested. However, an oven temperature of 40 °C resulted in the highest absorbance (160 mAu). Retention times and narrow peak shapes remained consistent across the temperature range, indicating the absence of temperature-induced sample aggregation.

Column selection was further evaluated to improve the separation performance for ON1 (**Figure S 8.2**), with enhanced retention observed using the Waters HILIC column over the Thermo Accucore HILIC, evidenced by a retention time shift of 6 seconds, and a 43% increase in PDA signal intensity. Although both columns use HILIC stationary phases and possess identical column volume (100 mm length, 2.1 mm internal diameter), they differ in their stationary phase particle size (2.6 µm (Thermo) versus 1.7 µm (Waters)), and pore size. The Thermo Accucore column uses 2.6 µm core–shell particles with an 80 Å pore size and non-end-capped silica, which exposes residual silanol groups capable of hydrogen bonding and ion-exchange interactions with ON1. In contrast, the Waters column uses 1.7 µm fully porous bridged-ethylene hybrid (BEH) silica particles with a larger 130 Å pore size, reducing unwanted secondary interactions and promoting more consistent HILIC partitioning. The smaller particle size associated with the Waters HILIC column increases the number of theoretical plates, and the fully porous particles offer larger internal surface area for enhanced analyte retention, with a larger pore size more suited to larger analyte molecules.

Mobile phase ionic strength was evaluated by comparing 10 and 20 mM ammonium acetate salt content (**Figure S 8.3**). The PDA signal increased by 40% upon doubling the mobile phase ammonium acetate content (10 mM: 235 mAU; 20 mM: 330 mAU), demonstrating a clear dependence on ionic strength. Higher salt content also enhanced stationary phase interactions, as evidenced by an 18-second increase in retention time, and a narrower full width at half-maximum (FWHM, 3 seconds), indicating improved chromatographic efficiency.

Next, the influence of mobile phase pH on ON1 separation **(Figure 2.3)** was investigated since it plays a crucial role in governing analyte-stationary phase interactions. Mobile phase pH also directly drives ON ionisation state and impacts intermolecular bonds and ON conformation, which can overall impact separation and detection.

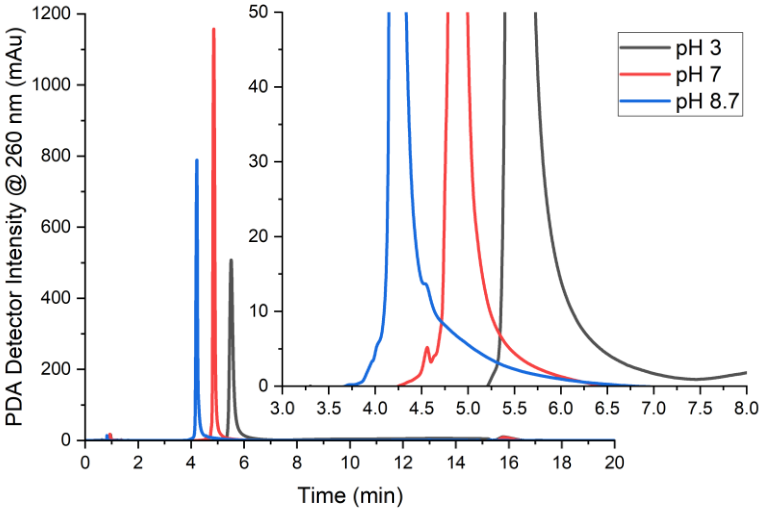

Figure 2.3 *– Exploratory mobile phase pH optimisation using ON1. LC separation profile uses Waters BEH HILIC column at 20 mM ammonium formate pH 3, 20 mM ammonium acetate pH 7, pH 8.7, 40 °C column oven, at 0.4 mL/min, 1 µg injection concentration, n=1.*

Neutral pH conditions (pH 7.0) produced the highest PDA signal intensity, followed by basic and then acidic pH conditions. Examination of ON1 retention behaviour also highlights that decreasing the mobile phase pH from basic to acidic, led to increased stationary phase retention. Peak width decreased progressively as pH increased, pH 3.0 (0.130 min), pH 7.0 (0.107 min) and pH 8.7 (0.106 min), aligning with peak FWHM decreases per pH value, pH 3.0 (0.130 min), pH 7.0 (0.062 min), and pH 8.7 (0.061 min).

Peak symmetry also varied with pH, with values of 1.865, 1.436, and 1.465 observed with increasing mobile phase pH, respectively. Considering that pH 7.0 produced the highest PDA intensity and the most symmetric FLP peak, this condition was selected for subsequent analyses. However, the diol-based HILIC stationary phase lacked sufficient selectivity to resolve ON-associated impurities. Therefore, a Waters BEH Amide column was explored for all subsequent HILIC studies (**Figure 2.4)**.

To accommodate a longer column (150 mm) and ensure sufficient column equilibration, the gradient was extended to improve separation and PDA detection. The performance of the amide column flow rate (0.2-0.4 mL/min) was subsequently evaluated to determine the separation efficiency of ON1 and associated impurities. Each separation was performed using an extended gradient with various separation profile times for each flow rate with relative column re-equilibration steps prior to subsequent sample injections.

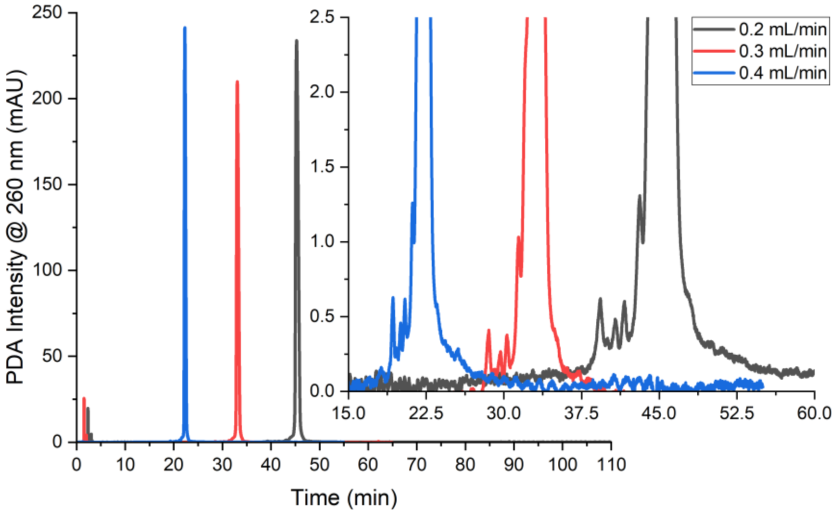

Figure 2.4 *- Flow rate optimisation using ON1 sample. LC separation profile uses Waters BEH Amide column at 20 mM ammonium acetate pH 7, 40 °C column oven, 1 µg injection concentration, n=1.*

Each flow rate resulted in similar purity profiles (number of detected peaks) with multiple pre-shouldering peaks, followed by the main ON FLP with all flow rates producing ON1 absorption values ~ 220 mAu. To maintain lower system pressure and a balance in overall separation time, a flow rate of 0.3 mL/min was selected as the optimum flow rate.

Next, sample pretreatment was investigated using a stacked co-injection of 9 µL ACN, 2 µL ON1, and 9 µL ACN to mimic starting gradient conditions containing 90% organic mobile phase.

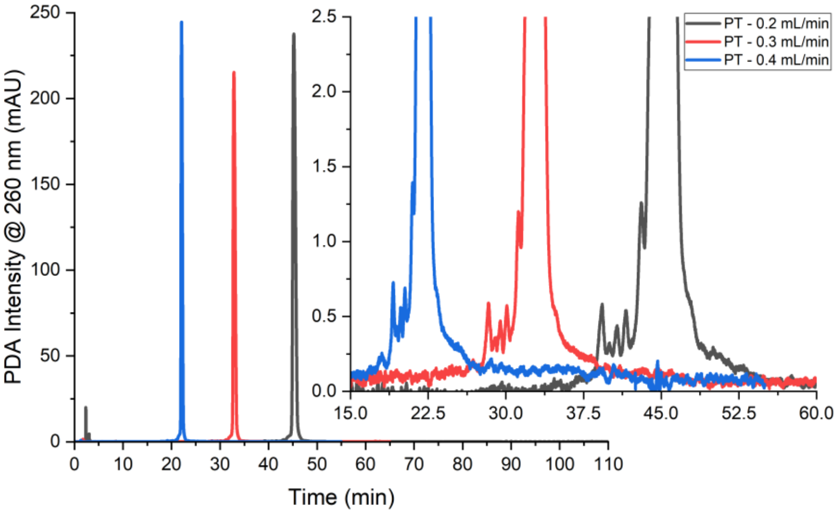

Figure 2.5 *– Sample pre-treatment exploratory optimisation using ON1 sample. LC separation profile uses Waters BEH Amide column at 20 mM ammonium acetate pH 7, 40 °C column oven, 1 µg injection concentration. Pre-treatment included stacking co-injection of MPA/B to equal gradient starting condition (9µL ACN-2uL ON1-9µL ACN), n=1.*

Comparison of sample pre-treatment conditions **(Figure 2.5)** and flow rates **(Figure 2.4)** demonstrates that pre-treatment had negligible impact on the chromatogram profiles of ON1. Variations in the organic phase composition and low injection volumes did not significantly alter the separation gradient, with negligible differences observed in retention behaviour or peak characteristics. A limitation of the pre-treatment optimisation experiments was that only ON1 FLP was tested in isolation without equivalent concentration spiking of *n±1* impurities.

The final HILIC parameters selected for coupling with online mass spectrometry analysis are summarised in below. These parameters were used for orbitrap and SQ transfer.

***Table 2.6** – Summarised HILIC optimisation parameters prior to mass spectrometry hyphenation. *Further optimised to Waters Amide column denoted in flow rate 0.3 mL/min optimised parameters. **extended gradient used to satisfy longer column volume.*

Parameter	**Optimised**	**PDA (260 nm) Peak**				
		Et (min)	Width (min)	Intensity (mAU)	Symmetry	Number
Column Oven	40 °C	5.41	0.144	160.7	2.453	1
Column*	Waters HILIC*	4.97	0.148	330.0	1.921	1
MP A, salt conc	20 mM	4.97	0.148	330.0	1.921	1
MP A pH	pH 7	4.86	0.107	1157.8	1.436	2
Flow Rate**	0.3 mL/min**	33.1	0.407	209.4	1.402	7
Pre-treatment	None	Not applicable.				

Since HILIC LC-PDA was successfully optimised, comparison between HILIC-PDA and IPRP-UV were demonstrated to evaluate comparability between both separation types. Peaks were separated into low molecular weight species (LMWS), full length product (FLP) and high molecular weight species (HMWS). FLP peak area was integrated and expressed as percentages values with pre-FLP peaks constituting LMWS and post-FLP peaks being HMWS.

***Table 2.7** - IPRP-UV and HILIC-PDA percentage purity ratios of LMWS, FLP and HMWS of ON1* and ON2‡. (*n=3, ‡n=2 ± STD, $^{\#}$n=1).*

Sample	**HILIC-PDA (%)**			**IP-RP-UV (%)**		
	LMWS	**FLP**	**HMWS**	**LMWS$^{\#}$**	**FLP$^{\#}$**	**HMWS$^{\#}$**
ON1	0.27 ± 0.15*	99.70 ± 0.15*	0.03 ± 0.01*	2.29	94.79	1.99
ON2	3.66 ± 0.08‡	95.34 ± 0.33‡	1.01 ± 0.25‡	8.05	83.76	7.68

Contrastingly to purity and electrophoresis results, ON1 produced overall higher purity, with a higher percentage of FLP under both HILIC (> 99%) and IPRP (> 94%) separation methods compared to ON2 (**Table 2.2**). Between HILIC and IPRP separation modes ON2 produced the greatest difference of FLP (11.58%) than ON1 (4.91 %). Enhanced LMWS, and HMWS were observed for both ON1 and ON2 when separated with IPRP compared to HILIC (**Table 2.2**).

2.4.4. High-resolution, Accurate Mass Determination by HILIC Orbitrap LC-MS

Following the successful optimisation of HILIC-based LC separation for ONs, mass spectrometry parameters were next optimised to ensure adequate system sensitivity and reliable detection of associated impurities. In this work, MS^1 optimisation was prioritised to enable a direct comparison between optimised methodology readouts and readout from SQ instrumentation. Although MS^1 analysis is sufficient for assessing mass accuracy, identity confirmation and impurity detection at the intact mass level, further optimisation of MS^2 parameters would be required to enable robust ON fragmentation and quantitative analysis of degradation on *n±1* species.

Parameter optimisation included ionisation polarity, scan range, automatic gain control (AGC), injection time (IT) and microscan number (US). Collectively, these settings determine ion transmission efficiency, spectral quality, and overall sensitivity of the orbitrap acquisition and detection. Polarity selection defines ionisation mode of ON, and scan range mass-to-charge (m/z) window over which ions are detected, with narrower ranges improving sensitivity for targeted species and wider ranges enabling untargeted detection. AGC regulates the number of ions accumulated in the C-trap prior to injection into the Orbitrap, balancing signal intensity against space-charge effects that can reduce mass accuracy and resolution. IT specifies the maximum duration allowed for ion accumulation; with longer IT enhancing sensitivity for low-abundance ions. US optimisation adjusts the number of individual ion injection-and-detection cycles (transients) that are summed together to produce a single final mass spectrum, higher microscans are better for improving low-abundance ions.

Initially mass spectrometry polarity in positive and negative ionisation modes and used dual switching modes were analysed to assess ON1 and ON2 profiles.

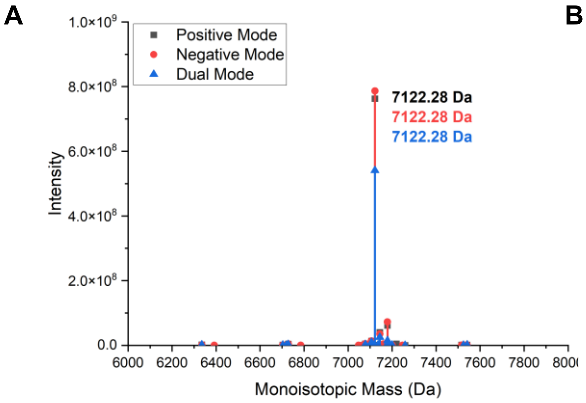

Figure 2.6 *- Deconvoluted Ionisation polarities evaluating A) ON1 and B) ON2 samples using positive, negative and dual switching modes.*

Across all separation profiles (**Figure S 8.4**), ON1 consistently produced higher ion counts than ON2 in each polarity mode tested. This outcome was expected given that ON1 represents a fully assembled 18-mer, whereas ON2 exhibited profiles consistent with lower molecular weight species. Deconvoluted spectra further supported these results with ON1 yielding higher monoisotopic mass intensity over ON2, and exhibiting a reduced number of lower molecular weight impurity peaks compared with ON2 **(Figure 2.6**). These results highlight that both ON1 and ON2 FLPs produced comparable signal intensities in positive and negative ionisation modes, whereas dual switching increased noise and led to higher background signals **(Figure S 8.4).**

To further enhance the sensitivity of impurity detection and overall purity profiling, multiple scan ranges settings were subsequently tested. Scan ranges tested in positive and negative ionisation mode included 450-2000 m/z, 800-4000 m/z, and 1000-8000 m/z. **Figure S 8.5** highlights separation profiles for ON1 and ON2 evaluations.

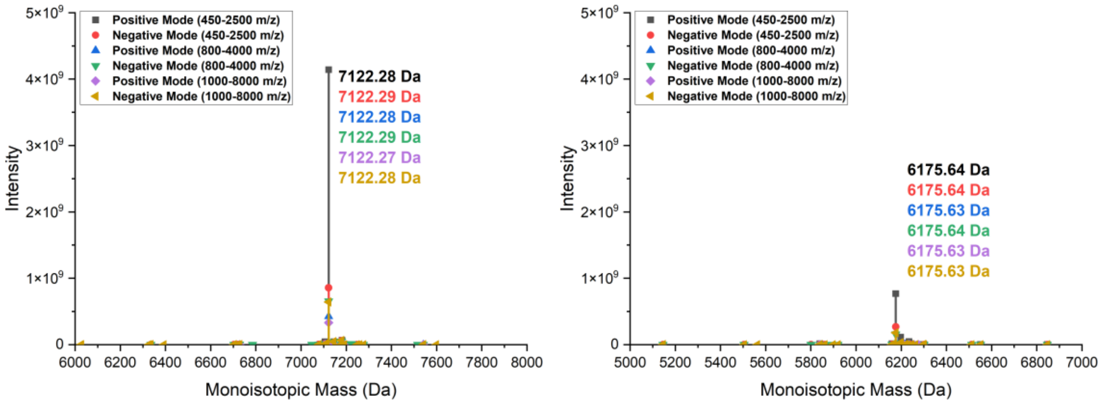

Figure 2.7 *– Orbitrap scan range optimisation in positive and negative ionisation modes across scan ranges 450-2500, 800-4000 and 1000-8000 m/z for A) ON1 and b) ON2,. Positive mode ON1/ON2 deconvolution parameters are displayed in **Table S 8.1** .*

Separation profiles in **Figure S 8.5** demonstrated that at the 450-2500 m/z scan range, the positive ionisation mode was sufficiently sensitive to detect ON associated impurities. However, ON FLP detection in negative mode exhibited superior sensitivity, denoted through higher ion counts and deconvoluted mass intensities for both ON1 and ON2. In the scan range 800-4000 m/z, similar trends were observed with negative mode superseding positive mode FLP detection sensitivity. Higher signal-to-noise (S/N) measurements were produced on increasing scan range m/z values filtering smaller values from detection, reducing background noise signals and increasing peak separation from background noise. Within the 800-4000 m/z TIC, the positive ionisation mode resulted in higher background signal compared with negative mode. Whereas, in negative mode, higher ion counts were noted for associated impurities across ON1 and ON2. Moving to higher scan range 1000-8000 m/z ON2, FLP TIC decreased compared to lower scan ranges, however ON2 associated impurities ion counts increased. Equivalent trends in FLP and impurity ion counts were also noted in ON1 profiles and exemplified through deconvoluted masses above (**Figure 2.7)**.

Consistent with polarity data, ON2 produced yielded lower intensity deconvoluted masses across all scan ranges examined when compared with ON1, and negative mode proved superior with ON detection sensitivity. To balance sensitivity, a scan range of 600-3000 m/z was chosen.

Further optimisation was carried out on the orbitrap mass spectrometer to evaluate AGC, IT, and US. A series of ramped injections were utilised by testing AGC 100, 300, 500, 1000 %, IT 10, 100, 1000 and US of 1, 5 and 10, totalling 36 injections using ON2 to optimise settings with a higher level of associated impurities.

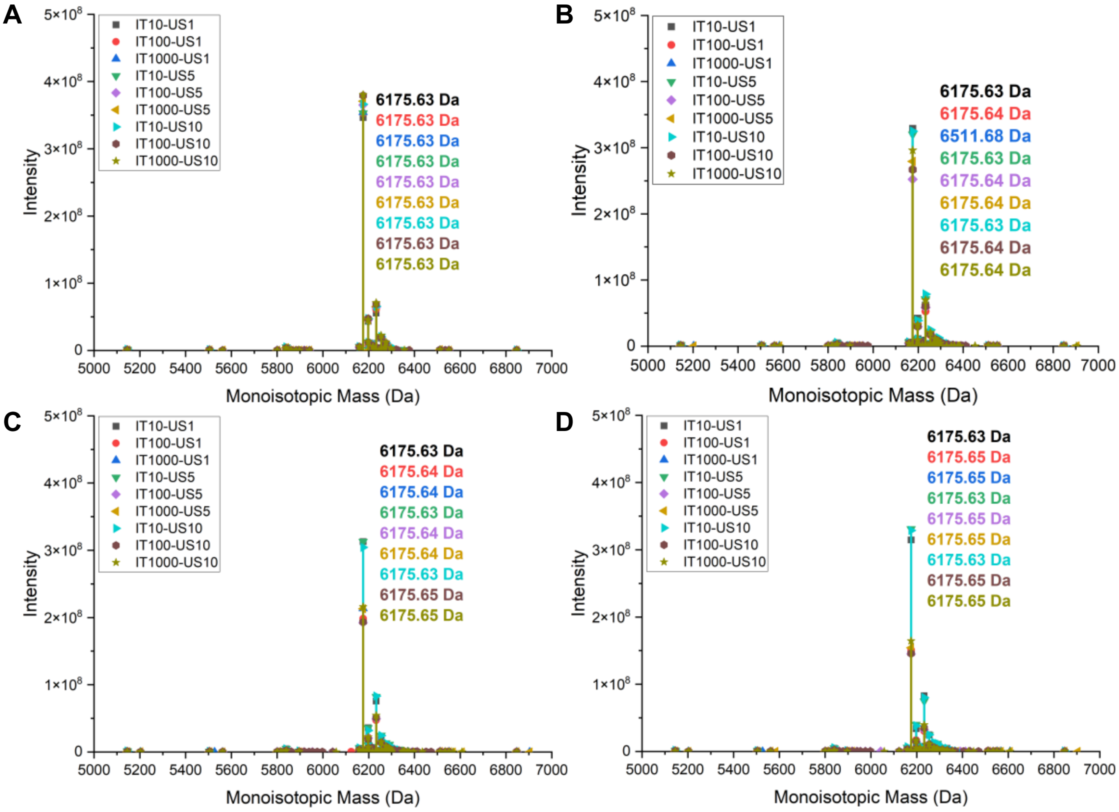

***Figure 2.8** – Deconvoluted AGC grouped ON2 evaluations with ramped IT and US experiments. A) AGC 100%, B) AGC 300%, C) AGC 500% and D) AGC 1000%, (n=1).*

Across all deconvoluted mass spectra **(Figure 2.8)**, the highest intensities were consistently observed at the lowest US (1), irrespective of injection time. This trend was evident across all AGC settings (100-500 %), except for the AGC 1000% setting. As AGC values increased, both intact mass intensities and TIC responses decreased from 100-1000 %. Notably, the AGC 100% produced the noisiest FLP peaks, and associated impurity ion counts followed an equivalent trend with a reduction in ion counts. Low microscan times also suffered from variable background signals, contributing to noisy profiles and skewed results **(Figure 2.8, Figure S 8.6)**. Variable baselines were noted across injection time settings, longer injection times lowered baseline signals across all AGC parameters tested. With these optimisation parameters being considered, experiments were narrowed to three optimisation parameters. AGC 300-1000 with longer injection times of 1000, and intermediate microscans of 5 to balance ion count sensitivity with background noise levels.

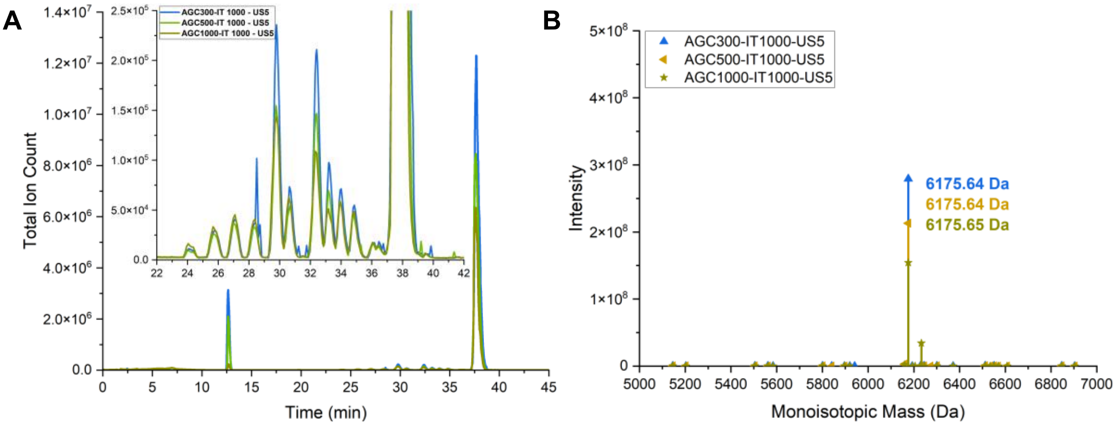

Figure 2.9 – TIC and deconvoluted masses of AGC 300, 500, 1000 % using Injection times of 1000 and 5 microscans, (n=1).

Each injection selected **(Figure 2.9),** highlights optimal separation and detection profiles for ON2 and associated manufacture impurities. By comparison, AGC 300% produced the highest TICs and mass intensities, compared to other two selected profiles. Therefore, this method was selected to support data-driven decision-making by enabling comparison of separation profile equivalence. A Python-based interpolation script was used to calculate the root mean squared error (RMSE), normalised RMSE, and R^2 values to validate the comparisons. The resulting data served as the input for assessing comparability between profiles.

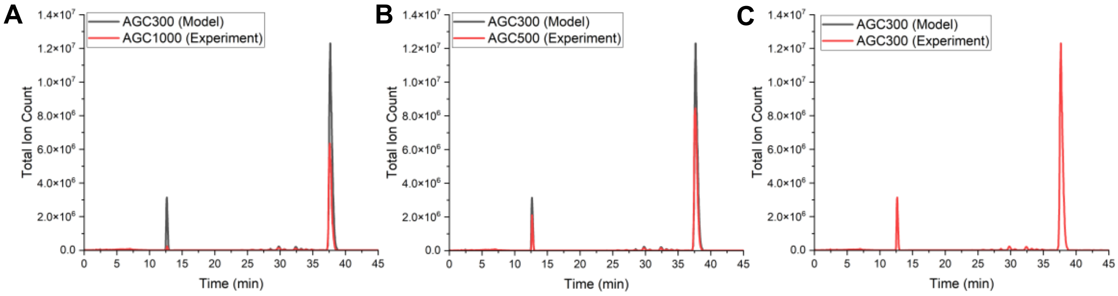

Figure 2.10 – interpolation of selected parameters for data-based comparison from AGC 300%. Comparisons include A) AGC 300 and 1000, B) AGC 300 and 500, and C) AGC 300 against itself.

Table 2.8 - Interpolation results of optimised method comparisons including RMSE, nRMSE and R^2, (n=1).

Method Comparison	RMSE	nRMSE	R^2
300-1000	894669	2.32	0.699
300-500	527319	1.86	0.815
300-300	1.068×10^{-10}	0.00	1.000

The data presented in **Figure 2.10** and **Table 2.8** further demonstrate that lower AGC settings yield greater similarity in detection performance, characterised by a higher rate of ion detection than higher AGC values (1000%). These comparisons are valid, as the positive control, method 300 assessed against itself, produced the expected outcomes of low RMSE and nRMSE values, and an R^2 of 1. By applying the optimised parameters established on the Orbitrap platform, additional performance improvements were performed on the 2050 SQ MS system.

2.4.4.1. SQ MS

In line with the Orbitrap method development workflow, SQ polarity, qarray source voltage, and associated event time were optimised, whilst maintaining LC-PDA conditions. A scan range of 650-2000 m/z range was selected to align with the reduced detection window of the SQ system (50-2000 m/z).

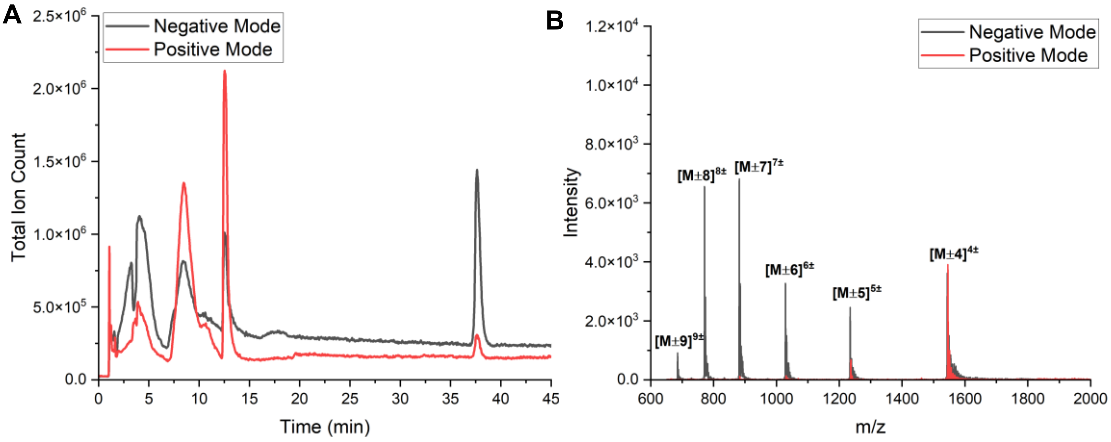

Figure 2.11 *- Single quadrupole polarity comparison of ON2 A) total ion count and B) associated peak mass charge ratio distributions, (n=1), 2.5 µg injection concentration.*

Consistent with the Orbitrap data, ionisation and detection of ON2 were successful in both positive and negative polarity modes using SQ MS (**Figure 2.11)**. As expected, the negative mode produced higher intensity TIC for the eluted ON (1.5×10^6) ions, compared with the positive mode, which produced 5.0×10^5 ions. However, positive ionisation mode produced a lower background intensity around 1.6×10^5, corresponding to a S/N of 3.63, whereas negative mode produced a background intensity of 2.6×10^6, giving a much higher S/N of 47.25 (scan range 650-2000 m/z) (**Figure 2.11)**. Aligned with TIC values, the m/z charge state envelope exhibited higher intensities along with a broader charge state distribution in negative mode (4-9 charges), relative to positive mode (4-7 charges). The lower m/z signal intensities observed in positive mode also make subsequent spectral deconvolution more challenging. Therefore, consistent with the Orbitrap findings, negative ion mode was selected for continued optimisation of in-source qarray voltages.

Quadrupole array voltages can be utilised to tune in-source fragmentation and suppression of adduct formation prior to quadrupole entry and m/z detection. Here, a range of negative voltages from 0 through to – 100 V were explored to evaluate in-source fragmentation and adduct generation.

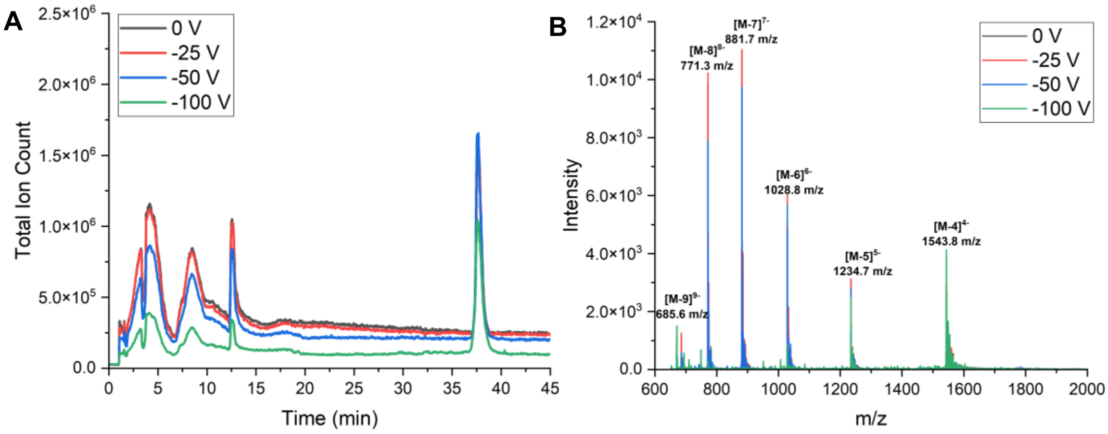

Figure 2.12 *- SQ qarray optimisation using ON2 A) total ion count and B) mass/charge ratio distribution across negative mode voltages (0-100) V, 2.5 µg injection concentration (n=1).*

Both TIC and m/z spectrums produced varying results as qArray voltages were increased **(Figure 2.12).** As qArray voltage is increased, background ions are decreased within the system, however a loss of smaller charge states were noted 8-6 **(Figure 2.12)**. Balancing background signals, TIC and m/z intensities, - 25V was selected as optimal as it produced comparable background signals, high TIC and highest intensity and most abundant m/z intensities across tested parameters. Subsequently, SQ event time was optimised further to enhance FLP detection and associated impurities.

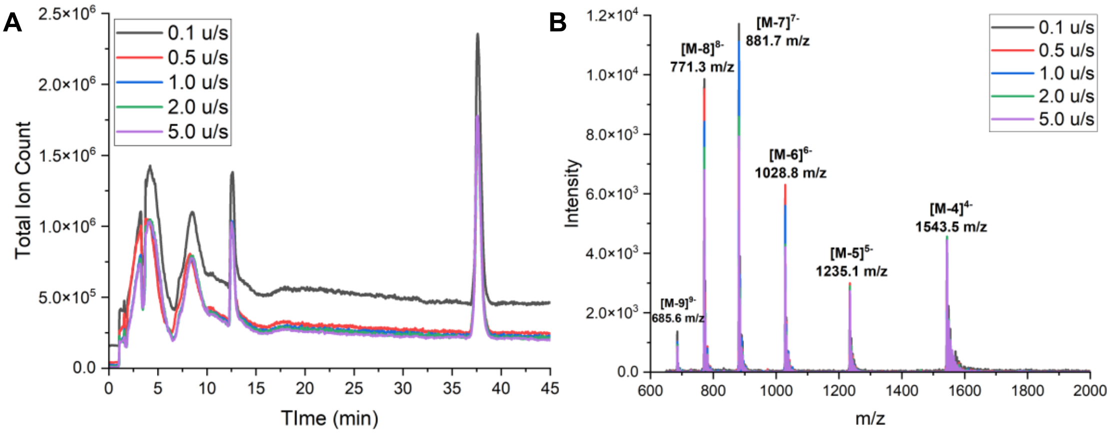

Figure 2.13 *- SQ event time from 0.1-5.0 s, for ON2, reflecting A) total ion count and b) m/z ratio intensity distributions, n=1, injection concentration 2.5 µg.*

Event time highlights the time utilised for scan range quantification, with high times producing considerably lower background from data, however, less data points are collected over the chromatographic peak, producing lower quality integrated data **(Figure 2.13).** To balance this, a moderate event time was selected to ensure sufficient time for scan speed across m/z quantifiable range, lower background signals and intense m/z peaks. Therefore, a 1.0 s event time was chosen as optimal for ON detection and quantification balancing low background, high TIC and m/z charge state intensities.

2.4.5. ASO LC-MS Characterisation

ON1-6 ASOs were quantified below using above developed MS methodologies, to assess the impact of overall purity on quantification linearity and evaluate limits of detection and quantification across LC-PDA-MS and LC-Orbitrap low- and high-resolution mass spectrometry setups. Resolution factor for developed methods were unable to be quantified due to co-elution of FLP and n-1 peaks typically (> 1.5). Deconvolution algorithms were required to analyse n-1 impurities co-eluting with FLP ON peak due to high chemical similarity and need for further baseline separation.

***Table 2.9** – LC-MS impurity determination using SQ and Orbitrap mass spectrometers, data corresponds to FLP elution peak deconvolution using associated platform algorithms (*n=3, **n=2).*

Sample	**LC-MS Impurity (Abundance %)**	
	SQ	**Orbitrap**
ON1*	*n-1* 0.43	*n-1* 0.03
ON2*	*n-1* 1.08	*n-1* 0.04
ON3**	*n-1* 1.21	*n-1* 1.24
ON4**	*n-1* 0.02	*n-1* 0.52
ON5**	*n-1* 0.03	*n-1* 0.28
ON6**	*n-1* 0.08	*n-1* 0.09

Comparing SQ and Orbitrap *n-1* impurity abundance highlights differences in impurity detection between ON1-5 (**Table 2.9).** Comparisons were most noticeable for ON3 with a difference of 0.03 % in *n-1* impurity detection, where larger differences were noted in ON2 at 1% impurity. The relationship between *n-1* impurities highlights detector sensitivity and potential false positive results, with unknown additions and potential *n-1* adduct masses being included with overall impurity abundances. However, because the instruments use different detection systems and proprietary deconvolution algorithms, smaller differences would be expected between the predicted and observed results than those denoted in **Table 2.9.**

2.4.6. HILIC-PDA-SQ

Next, detection system linearity and limits of detection and quantification of FLP peaks for ON 1 and ON2 samples were compared using a calibration curve of increasing concentrations.

***Table 2.10** – LC-PDA-MS ON1 and ON2 linearity, limit of detection, and limit of quantification, (n=2).*

Sample	**PDA**				**SQ MS**			
	R^2	LOD (µg)	LOQ (µg)	S/N	R^2	LOD (µg)	LOQ (µg)	S/N
ON1	1.000	0.043	0.130	13.0	0.999	0.134	0.406	40.6
ON2	0.998	0.082	0.247	24.7	0.999	0.131	0.396	39.6

Overall, PDA detection produced lower LOD and LOQ values across both ON1 and ON2 samples **(Table 2.10)**, signifying enhanced detection sensitivity compared to MS results. Baseline values were lowered in PDA as only one wavelength (260 nm) was analysed in comparison to a scan range of 650-2000 m/z; thus, MS instrumentation contains higher background noise levels. ON1 exhibited an ~ 50 % reduction in detectable values for PDA analysis and 30 % lower in SQ MS detector **(Table 2.10)**. These LOD and LOQ results contradict expected values with MS being more sensitive than PDA. SQ MS LOD and LOQ results could become lower if a narrower scan range was used and tailored to specific ON m/z charge state distributions or if a single, most abundant charge state was selected and monitored.

A key limitation of UV/PDA detection is that, while it can indicate the presence of low-, full-length, and high-molecular-weight species (LMWS, FLP, and HMWS), it cannot identify or quantitatively resolve co-eluting components. In particular, *n ± 1* truncation products may co-elute with the full-length product and be indistinguishable by UV, resulting only in an apparent or arbitrary purity value. In contrast, MS-based ionisation and quantification, especially when hyphenated with UV and overlaying chromatographic traces, enables more informative assessment based on both absorbance and mass. Definitive identification by UV alone could be achieved by calibration curve comparison using separate curves of ON FLP, and ON *n±1* impurities to improve impurity identification and quantification.

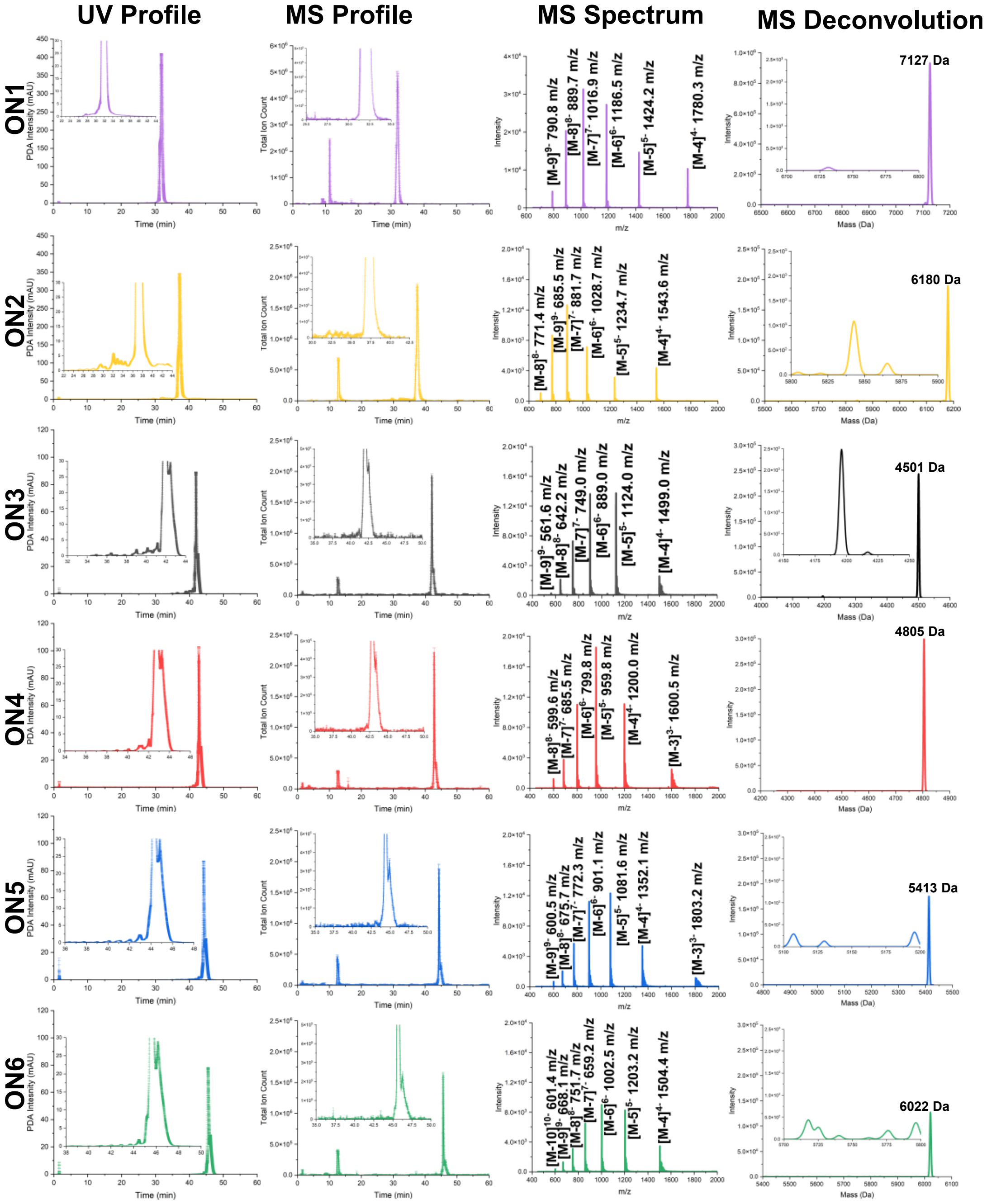

***Figure 2.14** - ON1-6 quantification, highlighting associated impurity analysis across HILIC LC-PDA-SQ. using PDA, MS TIC, MS m/z, and MS deconvolution with Shimadzu Biologics software. ON1-2 used 2.5 ug injection concentration, ON3-6 used a 0.5 µg injection concentration, (n=2 ± STD). UV/MS profiles were subtracted from a blank injection. MS deconvolution used non-blank-subtracted data files.*

Across each of the separated and detected ON samples **(Figure 2.14),** ON1 eluted first, meaning that the chemical modifications (base methylation, 2'MOE sugar) applied to the ON (**Table 2.1**) reduced its overall hydrophilicity as a lower percentage of mobile phase B was needed to elute it from the column. ON2 and then ON3-6 eluted towards the end of the separation gradient, inferring strong partitioning within the aqueous layer on the column. ON1, ON5, and ON6 produced the largest distribution of charge states with 7 being detected within the 650-2000 m/z range, whereas ON2-4 produced six charge states. Subsequent deconvolution profiles highlight impurity and adducted impurities along with FLPs **(Figure 2.14).**

2.4.7. HILIC-Orbitrap

Separation linearity, limit of detection, and limit of quantification were obtained for both ON1 and ON2 in **Table 2.11.**

***Table 2.11** – LC-PDA-MS ON1 and ON2 linearity, limit of detection, and limit of quantification, (n=2).*

Sample	**Orbitrap MS**			
	R^2	LOD (µg)	LOQ (µg)	S/N
ON1	0.999	0.051	0.155	15.5
ON2	0.999	0.147	0.446	44.6

Similar to **Table 2.10,** ON1 produced lower LOD and LOQ values compared to ON2, which could additionally count for modifications to the oligo itself. Orbitrap MS instrumentation produced lower overall LOD values, and similar LOQ values to the SQ system, highlighting comparability between the two detection systems.

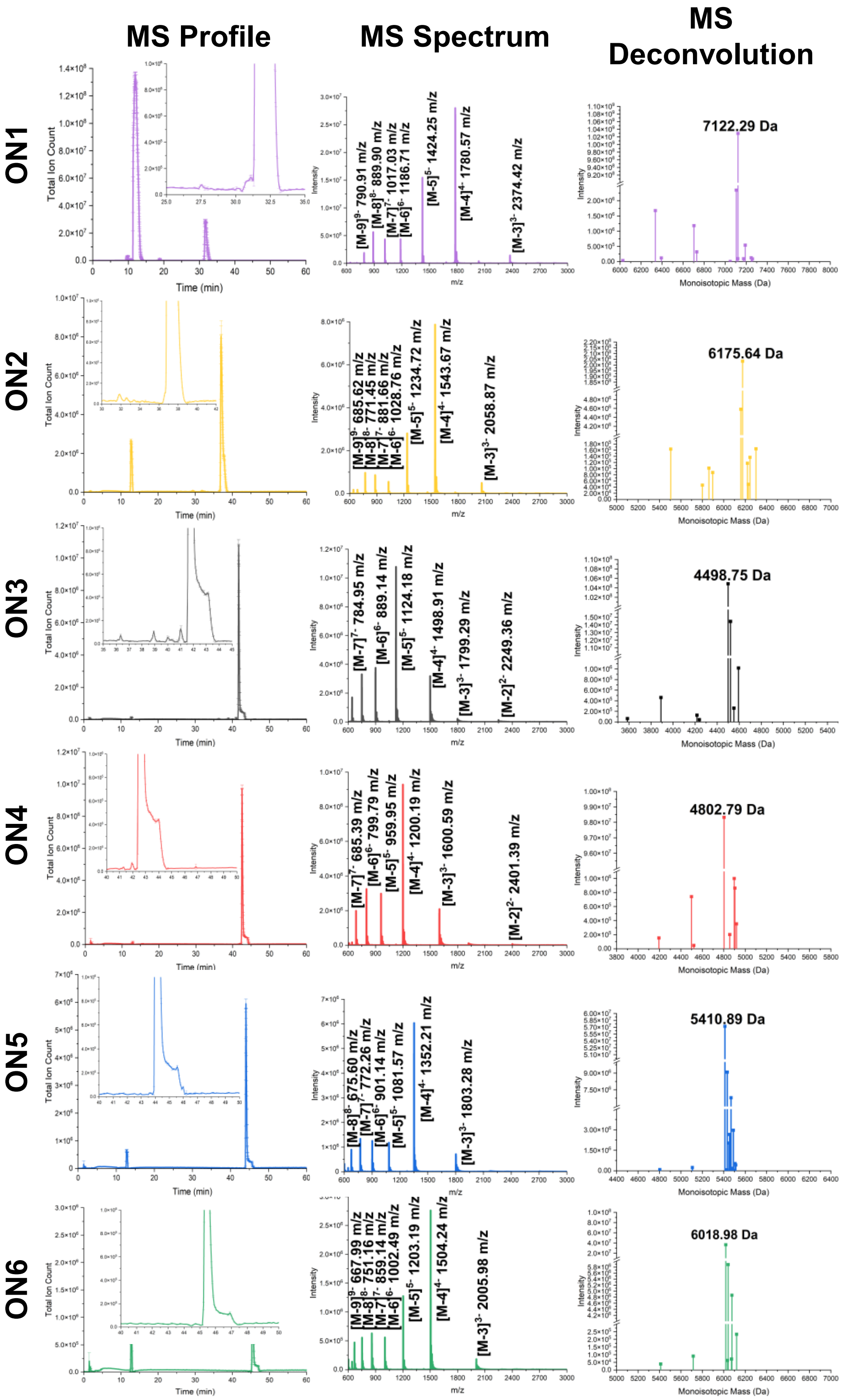

***Figure 2.15** – ON1-6 quantification, highlighting associated impurity analysis with the using HILIC LC Orbitrap MS. Using MS TIC, MS m/z, and deconvoluted spectra. ON1-2 used a 2.5 µg injection concentration, ON3-6 used a 0.5 µg injection concentration, (n=2 ± STD). MS profile data and deconvolution used non-blank-subtracted data files.*

Orbitrap data showed similar TIC and m/z profiles **(Figure 2.15)** for ONs comparable to SQ separation (**Figure 2.14)**. An equivalent number of charge states per ON was observed; however, fewer low charge states (low m/z) were detectable, alongside the appearance of an additional high charge state above m/z 2000 **(Figure 2.15)**. The extra charge state was detected due to the extended m/z range of the orbitrap compared to the SQ MS system **(Figure 2.15).**

2.5. Discussion

Therapeutic complexity of RNA-based therapies continues to increase as the field evolves towards addressing previously untreatable diseases and inherited conditions. Oligonucleotides therapeutics, particularly ASOs and mRNA provide a route to modulate or correct disease pathways at the transcript level, shifting interventions from symptomatic management to mechanism-directed prevention or correction. However, solid-phase synthetic routes for ASOs inevitably yield closely related impurities such as nucleobase deletion and truncated products since complete control over synthesis is not guaranteed. Because these impurities are of high similarity to the desired full-length product (FLP), there are challenges in their separation, identification, and quantification.

While recent advances in high-resolution instrumentation have improved the quantification of FLPs and associated impurities, their cost and accessibility impede widespread adoption. Therefore, this chapter focused on the development and comparison of high- and low-resolution mass spectrometry workflows, integrated with orthogonal chromatographic separation techniques (HILIC and IP-RP), and slab gel electrophoresis technique to establish pragmatic pipelines for impurity analysis in limited resource settings and using more environmentally sustainable solvents.

Initial gel electrophoresis results showed that inherent chemical modifications of ON1/ON2 impacted overall detected ON molecular weight, thus deviating from expected chain length distributions, with apparent mwt chain lengths that deviated from the known 18-mer chain lengths. Moreover, modification differences (5' UC methylation, 2' MOE) may account for dye binding differences producing an overall reduced ON1 interaction and so overall lower fluorescence compared to ON2 when loaded at equivalent concentrations.

IP-RP-UV was initially used as a benchmark chromatography method for ON purity assessment against HILIC-based chromatography to quantify the abundance of low- and high- molecular weight species relative to the FLP. Although not exhaustive for isobaric/isomeric species, this approach provided a robust orthogonal reference to support subsequent mass spectrometry-based identity and impurity confirmation. Previous studies have evaluated Nusinersen (ON1) and 18-mer ASOs using LC-MS for bioanalysis within different biomatrices (178,230,231), fluorescent particle/probe detection (232), and circular dichroism and nuclear magnetic resonance (233). IPRP comparative pipeline, highlighted sequence-dependant differences with analysing ON1 and ON2 (**Figure 2.2**), with ON2 containing lower FLP content (**Table 2.2**).

HILIC-PDA separation optimisation showed strong dependence on mobile phase salt content, pH and column stationary phase. Increasing the ammonium acetate salt content from 10 to 20 mM in tandem with diol-phase chemistry (**Figure S 8.3**), delayed elution and increased PDA signal, consistent with silanol suppression on the column that improves ON recovery and overall detection signal from the PDA detector. An increase in salt content can also passivate ON phosphate group charges using salt counter ions, enhancing analyte-stationary phase interactions and thus retention times.

Mobile phase pH remains a crucial factor and a molecular driver of ON group ionisation with respect to component group pKa activity (234,235). Within the mobile phase pH conditions tested **(Figure 2.3)**, the largest PDA detector signal was generated for pH 7 (neutral) conditions containing 20 mM ammonium acetate. This is consistent with pH-dependent ionisation of ON functional groups; conditions that minimise undesired electrostatic interactions (e.g., ON–ON or ON–surface) improved chromatographic efficiency and detection.

Since ONs are large hydrophilic molecules, a generic diol-stationary-phased was not able to provide enough molecular interactions between ON and column to separate inherent impurities aligning with previous literature (222,236). Therefore, an amide-based stationary phase column was used for subsequent separations **(Figure S 8.1, Figure 2.4)**. This amide stationary phase enhanced the resolution of separation, which successfully separated, previously non-separated components from ON FLP elution profile through enhanced hydrogen bonding between -NH and =O groups.

Next, hyphenation and optimisation of the Orbitrap MS and SQ MS were investigated. Initial Orbitrap polarity measurements accounted for ON specific ionisation differences with ON1 producing higher monoisotopic mass intensities than ON2 (**Figure 2.6**), reflecting ON1 increased hydrophobic chemical modifications, where sugar and base modifications are more readily at droplet surface, creating more ionised molecules and higher overall deconvoluted masses (237,238). Comparatively, ON2 molecules are more hydrophilic, remaining within the centre of droplet, thus less ionisation, resulting in a higher number of neutral molecules which are filtered out, reducing overall ion counts. Since dual ionisation mode produced enhance background noise, positive and negative single polarity modes were the focus of method development within further scan range optimisation (**Figure S 8.4**).

Orbitrap scan range produced decreased mass intensities when increasing scan ranges, filtering low mass ionised groups (**Figure 2.7**), corresponding with trending decreased total ion counts (**Figure S 8.5**). Balancing overall detectability, total ion count and m/z range limits, 600-3000 m/z within negative mode was chosen to continue orbitrap MS optimisation. Negative mode can exploit the overall PS backbone anionic nature to facilitate ionisation and enhance low abundant level detection.

Tuning AGC target, IT and US showed that higher AGC targets reduced deconvoluted mass intensity for ON2 (**Figure 2.8**, **Figure S 8.6**), consistent with space-charge related ion losses or over-filling prior to analysis. Increasing IT and transient duration reduced MS noise, and improved overall detection of low abundant species within the Orbitrap. Increasing US transients also produced the same trend of enhancing low abundant ion species detection (**Figure 2.8**, **Figure S 8.6**). Comparing overall selected parameters, allowed for a detailed view of FLP masses and associated adducts (**Figure 2.9**) with the use of computational pipeline for quantitative comparison of TIC separation profiles to information method development (**Figure 2.10**). The selected Orbitrap conditions (negative mode, 600-3000 m/z, AGC 300, IT 1000, US 5) provided the best compromise between sensitivity, resolution, and scan speed, enabling detailed FLP and adduct visualisation and supporting computational TIC profile comparison to guide method selection.

Given hardware differences in SQ MS mass filtering (quadrupole *vs* Orbitrap), SQ optimisation focused on polarity, in-source qarray voltage, and event time using a 600-2000 m/z scan range. Polarity differences in SQ MS highlight lower background noise within the positive polarity mode. However, the negative polarity mode produced an overall higher total ion count for ON2 and enhanced intensities across eight charge states (**Figure 2.11**), showing enhanced detection in negative polarity mode, in agreement with the Orbitrap MS findings.

Source qarray was then optimised to evaluate in-source fragmentation and adduct formation reduction. Increased ion m/z intensities were noted for lower charge states at -25V, signifying increased ion transmission into the quadrupole and signal intensity detected (**Figure 2.12**). Event time was then optimised to enhance detection sensitivity within the SQ MS setup. A range of times were evaluated (0.1-5 μ/s), ultimately, a qarray balance sufficient points across elution peak with sensitivity and spectral quality, hence 1.0 μ/s was selected for subsequent analyses (**Figure 2.13**).

By combining HILIC-PDA and optimised Orbitrap MS and SQ MS parameters, ON1-6 were quantified using developed methodology for evaluating and identifying associated impurities.

Comparing orbitrap and SQ MS quantification highlighted key differences in associated *n-1* impurities abundance (**Table 2.9**, **Figure 2.14**, **Figure 2.15**). While some variation was anticipated due to the use of different proprietary deconvolution algorithms, the magnitude and direction of the differences observed were unexpected. Contradictory abundance trends were evident for ON1, ON2, ON4, and ON5 between both MS platforms, whereas ON3 and ON6 showed closer agreement (**Table 2.9**, **Figure 2.14**, **Figure 2.15**). This suggests that the observed discrepancies are ON-dependent rather than systematic across all ONs tested across both MS platforms.

To further investigate whether differences in analytical sensitivity contributed to these inconsistencies, limits of detection (LOD) and quantification (LOQ) were determined for both SQ and Orbitrap MS methodologies (**Table 2.10**, **Table 2.11**). As expected, LOQ and LOD results showed a positive correlation with higher LODs resulting in higher LOQs. Comparing LOQ values across both orbitrap and SQ MS platforms revealed further ON-dependant sensitivity differences, for orbitrap MS, ON1 quantification was three times lower than ON2, whereas SQ MS produced more equivalent values (**Table 2.10**, **Table 2.11**) for both ON sequences. These differences could be due to ionisation efficiencies, and MS platform background noise. Despite these differences, SQ ON1/2 LOQs remained less than the LOQ for ON2 when using orbitrap MS.

Unusually, UV PDA detector LOD/LOQ values for ON1, ON2 produced lowest overall values compared to both MS platforms which remains unexpected as MS is widely regarded as achieving greater sensitivity than spectroscopic-based methodology (**Table 2.10**). In contrast, UV, PDA detection contributes lower background noise, enabling enhanced sensitivity, compared to background generated and adducted ions within MS platform detection.

2.6. Conclusions

Overall, this chapter demonstrates that ON analytical performance is strongly influenced by chemical modification, chromatographic conditions, and MS platform characteristics. The orthogonal optimised workflow provides a robust foundation for impurity profiling but also highlights the complexity of ON ionisation and the need for sequence-specific method refinement. Future work incorporating spiked impurity standards, non-linear gradient strategies, and targeted MS acquisition (e.g., single ion-monitoring) will further enhance quantification and support the development of more sustainable, cost-effective analytical methodologies for therapeutic oligonucleotides.

Chapter 3

3. Probing Antisense Oligonucleotide Lipid Nanoparticle Drug Product Critical Quality Attributes

All experimental work was performed by the author of this thesis.

Graphical Abstract

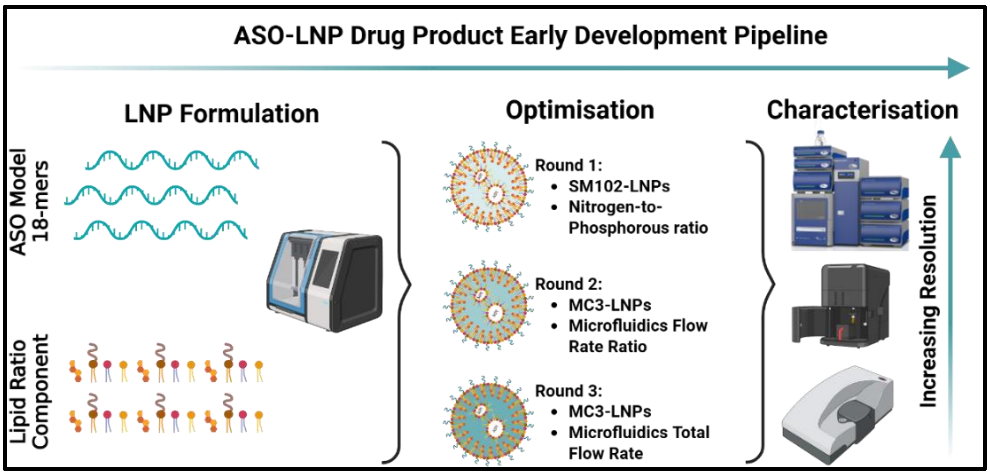

3.1. Introduction

Oligonucleotide (ON) therapeutics, typically 10–30 nucleotides in length, have emerged as a novel drug modality with unprecedented potential in pharmaceutical research. Their ability to modulate gene expression with high specificity stems from the discovery of RNA interference (RNAi), a mechanism whereby small RNA molecules regulate protein synthesis through RNA-mediated pathways (239). This process involves sequence-specific targeting of messenger RNA (mRNA), resulting in mRNA degradation and reduction in sequential transcription product, or inhibition of translation pathway. The discovery of RNAi unlocked a wide range of previously inaccessible disease targets to small molecules drugs, paving the way for innovative therapeutic strategies (73,240,241).

Of the platforms extensively under investigation in pharmaceutical industry portfolio pipelines, antisense oligonucleotides (ASOs) face significant clinical translation barriers and are faced with low success rates. ASOs are single chain, small RNA sequences, typically 10-30 nucleotides in length, which are primarily utilised within genetic engineering to inhibit protein product or correct protein production. Their mechanism of action occurs through binding to complementary mRNA sequences, enabling RNAse actively or skipping mRNA regions within amino acid and protein translation. ASOs face a series of degradation as biological barriers to their therapeutic efficacy. These biological obstacles include enzymatic degradation, renal clearance and extensive blood-serum protein binding, which can direct off-target toxicity. With ASOs being inherently polyanionic and hydrophilic in nature, their passage across hydrophobic cell membranes is limited, resulting in poor cellular uptake. Therefore, targeted delivery of ASOs is needed utilising alternative cellular uptake pathways whilst maintaining enhanced stability. Despite advancements in ASO chemical modification to improve stability, enhance target affinity and reduce enzymatic degradation, clinical translation of this therapeutic modality remains limited (48,242,243). Moving from ASO drug substance to ASO drug product analytics allows for the direct understanding of translatable critical quality attributes, ensuring overall insights between both stages of therapeutic formulation and development are comprehended, which can further enhance downstream candidate selection.

Circumventing these biological obstacles, lipid nanoparticle (LNP) encapsulation represents a choice to aid with delivery and cellular uptake challenges, while protecting ASOs from degradation in the bloodstream. Historically, LNP encapsulation of RNA drugs has focused on siRNA and mRNA encapsulation, being validated with the approval of Onapttro®, the first LNP delivery system to use small interfering RNA (siRNA) double stranded cargo (23,122,127). Other approved N-acetylgalactosamine (GalNAc)-ASO conjugates (58,244–246) utilise hepatic-receptor mediated targeting whilst LNPs offer a more versatile platform for the delivery of ASOs. Recent studies have investigated various molecular bioconjugates (antibody, peptide, lipid) for ASO delivery, however research within oligo conjugates remains within inception (54,247,248).

Whilst LNPs have been extensively studied for the delivery of siRNA and mRNA payloads (125,126,249), the encapsulation of single-stranded ASOs within LNPs remain under characterised (250–252). Therefore, in this chapter, addressed this gap by investigating ASO-LNP critical quality attributes (CQAs). This study seeks to address this knowledge gap by applying a pipeline of orthogonal analytical techniques to characterise ASO-loaded LNP formulations and define their CQAs. Key physicochemical parameters such as particle size, polydispersity, surface charge and encapsulation efficiency were evaluated using complementary and orthogonal techniques including dynamic light scattering (DLS), nanoparticle tracking analysis (NTA), asymmetric-flow field-flow fractionation (AF4), zeta potential (ZP) measurements and fluorescence-based assays (253,254). These methods provide a robust and multidimensional understanding of LNP formulation behaviour.

In addition, the impact of critical formulation parameters, including variations in the nitrogen-to-phosphate (N/P) ratio, ionisable lipid composition, microfluidics flow rate ratio (FRR) and total flow rate (TFR) on LNP formulation CQAs were investigated. The N/P ratio influences electrostatic interactions between the lipid components and ASO, affecting complexation efficiency and nanoparticle formulation stability. Ionisable lipid selection governs endosomal escape efficiency (160,161) and biocompatibility, while microfluidic mixing conditions directly impact nanoparticle size distribution and polydispersity (81,110,142). Understanding how these parameters influence ASO-LNP performance is essential for the rational design of effective delivery systems.

By optimising and characterising these formulation variables, this research aims to establish a reproducible framework for the development of ASO-LNP systems. Ultimately, improving the delivery efficiency of ASOs through LNP technology may unlock the full therapeutic potential of this drug class, expand the range of treatable diseases and facilitate the translation of next-generation nucleic acid medicines into clinical practice.

3.2. Materials

ON1 was manufactured by Integrated DNA Technologies (**Table 3.1**). DNA/RNA free water, 10× phosphate-buffered saline (PBS) pH 7.4, sodium citrate dihydrate and Quanit-IT RiboGreen^{TM} RNA Quantification Assay were acquired from ThermoFisher (Fisher Scientific, Leicestershire, UK) and 1N hydrochloric acid was sourced from Alfa Aesar. 8-[(2-hydroxyethyl)[6-oxo-6- 83 (undecyloxy)hexyl]amino]-octanoic acid, 1-octylnonyl ester (SM102), (6Z,9Z,28Z,31Z)-Heptatriaconta-6,9,28,31-tetraen-19-yl 4-(dimethylamino)butanoate (MC3) were purchased from BroadPharm (San Diego, CA, USA). 1,2-distearoyl-sn-glycero-3-phosphocholine (DSPC), 1,2-dimyristoyl-rac-glycero-3-methoxypolyethylene glycol-2000 (DMG-PEG 2000) were purchased from Avanti Polar Lipids 81 (Alabaster, AL, USA). Cholesterol (CHOL) and Amicon®-15 100 kDa MWCO regenerated cellulose spin columns were sourced from Sigma Aldrich (Merck, Gillingham, UK).

***Table 3.1** – Model ON sequences and associated molecular weight.*

ON	Sequence	Molecular Weight (Da)
ON – 18-mer	5’-UCACUUUCAUAAUGCUGG-3’ Modifications: 2’-OMe, PS	6179.9

3.3. Methods

3.3.1. Preparation of ASO-LNP Formulations by Microfluidics

LNP formulations were composed of SM102/MC3: CHOL: DSPC:DMG-PEG2000. All initial lipid stock solutions were prepared in ethanol at 5 mg/mL and combined at a 50:38.5:10:1.5 molar ratio for ionisable lipid: cholesterol:helper:PEG-lipid. ASOs were prepared in DNAse/RNAse free water at 2 mg/mL and diluted in 50 mM citrate buffer (pH 4), which was used as the aqueous phase. Lipid organic phase and ASO aqueous phases were injected simultaneously into the micromixer using parameters in **Table 3.2**. LNP formulations were purified using spin column centrifugation (100 kDa MWCO). Briefly LNPs were diluted (1:40) in PBS (pH 7.4) and centrifuged at 2,000 x g at 4 °C to remove residual ethanol.

Table 3.2 *- ASO-LNP Formulation Optimisation exploratory design. Formulation variations are highlighted in bold.*

LNP #	**Formulation Optimisation Parameter**			
	Ionisable Lipid	**N/P Ratio**	**Flow Rate Ratio**	**Total Flow Rate**
1	SM102	6	3	15
2	SM102	**12**	3	15
3	**MC3**	6	3	15
4	MC3	6	**6**	15
5	MC3	6	3	**5**

3.3.2. Characterisation of ASO-LNP Formulation CQAs

ASO-LNPs were characterised using a Zetasizer, RiboGreen™ assay, Nanoparticle tracking analysis (NTA), frit-inlet asymmetric-flow field-flow fractionation hyphenated with multiple inline detectors (FI-AF4-MD), and imaged by negative stain transmission electron microscopy using a previously reported method (254).

Dynamic light scattering particle size (Z-average) and polydispersity index (PDI) were determined using a Zetasizer Nano ZS system (Malvern Panalytical, Worcestershire, UK) equipped with a 633 nm Helium-Neon laser and a detection angle of 173° (non-invasive back scattering). Material parameters were set to 1.45 refractive index and 0.001 absorption. Unless otherwise stated, all measurements were performed at 25 °C and at a 1:10 dilution in PBS (pH 7.4) for all LNP samples. All measurements were performed in three independent replicate measurements consisting of at least two technical replicates.

***Electrophoretic light scattering* (ELS)** zeta potential surface charge was measured using ELS post manufacture/process test. Unless otherwise stated, all measurements were performed at 25 °C and at a 1:10 dilution in DNA/RNAse free water for all LNP samples. All ζ-potential measurements were performed using three biological replicate measurements consisting of at least two technical replicates.

RiboGreen^{TM} assay evaluated the encapsulation efficiency (EE) and drug recovery mass balance (MB) of the ASO cargo during LNP formulation. Both EE and MB were measured using the Quant-iT™ RiboGreen™ RNA Quantitation assay Kit (Thermo Fisher #4110) as per manufacturer instructions. The kit quantifies the total RNA and unentrapped RNA on the LNP surface to calculate the efficiency of drug encapsulation during formulation. The assay also determines recovery by comparing the total formulation RNA content to a theoretical RNA concentration. Corresponding fluorescence intensity of the RiboGreen™ signal was measured on the GloMax® Explorer GM3500 microplate reader (Promega, UK) at an excitation wavelength of 475 nm, with the emitted fluorescence measured at 500-550 nm. All fluorescence data were captured at ambient temperature (25 °C) using a GloMax® firmware version 4.29.0 and processed using GloMax® Fluorescence software version 3.1.0.

Nanoparticle tracking analysis *(NTA)* was used to measure particle size, distribution, and estimated particle concentration was conducted using a NanoSight NS300 system (Malvern Panalytical, UK), equipped with a 488 nm laser, low-volume flow cell, sCMOS camera, and automated syringe driver. Samples were diluted 1:10,000 in PBS (pH 7.4) and measured at 25 °C, with the infusion rate set at 50. Data acquisition involved the capture of five 60-second videos per sample at a camera level of 15. Analyses were performed using raw data algorithm and NTA software (version 3.4.003) with a detection threshold of five. Three independent measurements each with five technical replicates were performed for each sample.

***FI-AF4-MD* analysis** was performed using a flow field-flow fractionation system (Postnova Analytics, Germany) coupled with online multi-angle light scattering (MALS, PN3621), UV detection (260 nm, PN3242), and dynamic light scattering (Zetasizer Nano ZS, Malvern Panalytical). Separation was carried out using a frit-inlet (FI) channel with a 350 µm spacer and 10 kDa MWCO regenerated cellulose membranes. LNP samples (20 µL injection volume, 0.5 mg/mL) were injected using a 100 µL loop in triplicate. Elution was performed in PBS (pH 7.4) with an injection flow rate of 0.2 mL/min, a crossflow rate of 0.75 mL/min (exponential decay 0.2), and a detector flow rate of 0.3 mL/min. Data were processed using Nova FFF software (v2.2.0.1) applying the spherical MALS model (28–148°) for LNPs. Each LNP formulation was named according to the parameters in **Table 3.2**.

3.3.3. Statistical Analysis

Tukey's one way ANOVA tests were utilised to determine statistically significant differences between different ASO-LNP formulation critical quality attributes, where *p<0.05, **p<0.005, ***p<0.0005. Comparative and correlative statistical analyses were carried out to correlate ASO-LNP formulation critical quality attributes. Statistical and correlative analyses were conducted using MiniTab v 20.4and data were graphed using OriginPro version 9.9.0.220.

3.4. Results

The translation of RNA therapies into drug delivery platform has proven successful with the utility of LNPs as a popular choice for mRNA therapeutics. Therefore, the feasibility of LNP formulations for ASOs was explored using ON1 encapsulation (**Table 3.1**) in a panel of model ionisable LNP formulations (**Table 3.2**).

3.4.1. DLS, ELS, RiboGreen^{TM}, and NTA Evaluation of ASO-LNP Formulations

In the first instance, multi-resolution pipelines were utilised to initially quantify ASO-LNP CQAs through evaluating size, size distribution, surface charge, ASO encapsulation and ASO recovery. From these initial CQA investigation, preliminary insights can be obtained to provide deeper detail on manufacture-impact on ASO-LNP candidate exploration and further inform downstream evaluations.

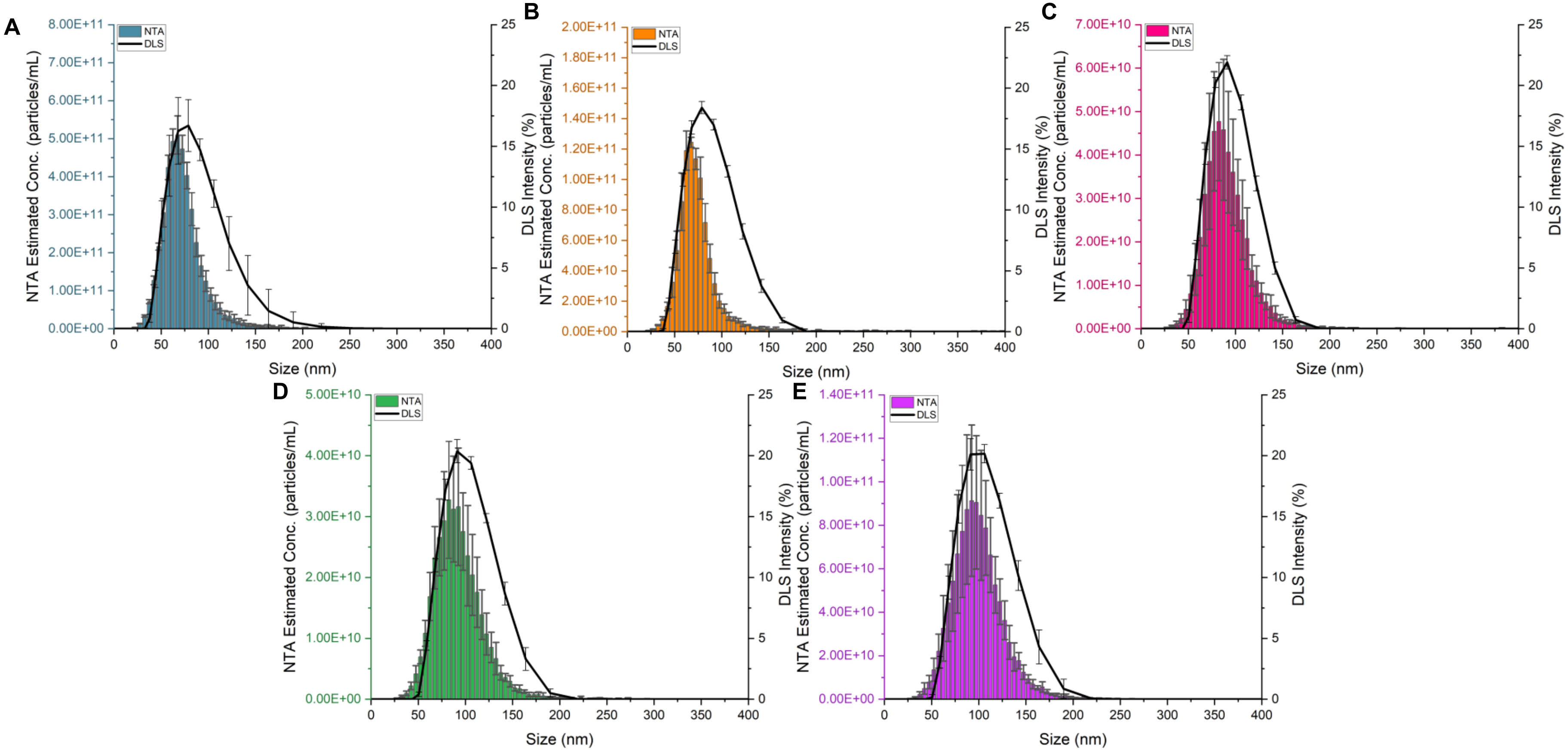

Figure 3.1 – ASO-LNP size-based distributions using NTA and DLS. A) LNP-1, B) LNP-2, C) LNP-3, D) LNP-4, and E) LNP-5. (data represents n=3, ± standard deviation).

LNP size distributions highlight differences between samples as a function of different formulation and process-related parameters. Comparing LNP formulation size distributions, **Figure 3.1,** shows that LNP-1 produced the lowest overall sizes, however the broadest size distributions (0.14 DLS PDI/ 0.72 NTA span). Other LNP formulations (2-5) do not follow equivalent size/size distribution trends, as formulation size increases, size distributions decrease (**Figure 3.1, Table 3.3, Table 3.4)**. Main ionisable lipid choice LNP-1 (SM102) and LNP-3 (MC3) produced the largest particle size difference under equivalent manufacture conditions (11 nm). Changing main ionisable lipid selection also reduced particle size distributions (PDI/span) (**Figure 3.1, Table 3.3, Table 3.4).**

To further quantify LNP size and size distribution CQAs, NTA was utilised to track formulations particle-by-particle, offering a higher resolution insight to classical batch mode DLS. Differences in LNP formulations were further highlighted through the differing measured particle concentrations for each LNP prototype **(Figure 3.2).** LNP-1 yielded formulations with 5×10^{11} particles/mL, followed by LNP-2 at 1.2×10^{11}, LNP-5 at 9×10^{10}, and LNP-3 and -4 formulations at ~ 5×10^{10}, respectively. These differences in estimated particle concentration by PTA showcase differences in post-spin column purification, with the LNP-1 formulation producing a 10-fold higher concentration than LNP-3/4 **(Figure 3.2)**. Notable differences in particle diameter were also observed between formulations, correlating with DLS intensity-based size measurement data (**Figure 3.1, Table 3.3)**. Corresponding NTA size distribution values are shown in **Table 3.4.**

.

Table 3.3 *- DLS, ELS and RiboGreen Assay output CQAs per each ASO-LNP sample. PDI: polydispersity index; ZP: zeta potential; EE: encapsulation efficiency; MB: mass balance; FRR: flow rate ratio; TFR: total flow rate. n=3 (mean ± standard deviation). Tukey Tests compared LNP1-2(*), LNP1-3(‡) and LNP3-4/5(#) where* $*p < 0.05$, $**p < 0.005$ *and* $***p < 0.0005$.

Sample	**Z-avgerage (d.nm)**	**Distribution Size (nm)**	**PDI**	**ZP (mV)**	**EE %**	**MB %**
SM102 LNP-1 (N/P: 6, FRR 3, TFR 15)	76.7 ± 6.7	82.4 ± 7.0	0.14 ± 0.07	-1.2 ± 0.3	98.0 ± 0.4	54.4 ± 10.6
SM102 LNP-2 (**N/P: 12**, FRR 3, TFR 15)	77.4 ± 1.1	84.1 ± 1.2	0.08 ± 0.01	-1.3 ± 0.3	$97.2 \pm 0.3^{*}$	50.3 ± 3.7
MC3 LNP-3 (N/P: 6, FRR 3, TFR 15)	87.5 ± 1.2	92.4 ± 1.2	0.04 ± 0.00	$-3.2 \pm 0.4^{\ddagger\ddagger}$	98.2 ± 0.2	39.8 ± 3.9
MC3 LNP-4 (N/P: 6, **FRR 6**, TFR 15)	$93.3 \pm 1.1^{\#}$	$99.7 \pm 1.8^{\#}$	0.06 ± 0.01	-2.9 ± 0.2	97.4 ± 0.6	35.2 ± 9.8
MC3 LNP-5 (N/P: 6, FRR 3, **TFR 5**)	$96.9 \pm 1.9^{\#\#\#}$	$103.3 \pm 2.8^{\#\#}$	0.05 ± 0.01	-3.3 ± 0.4	$97.0 \pm 0.4^{\#}$	43.8 ± 2.9

The results shown in **Table 3.3** demonstrate that optimising formulation conditions altered LNP CQAs. Z-average and cumulative distribution particle sizes increased progressively with sample number and associated formulation parameters. Increasing the N/P ratio (LNP-1 versus LNP-2) improved overall size distribution monodispersity, while increasing the lipid content had negligible effects on particle size, zeta potential and encapsulation efficiency, although a 5% reduction in mass balance was observed by Ribo Green **(Table 3.3).**

Switching the ionisable lipid from SM102 to MC3 (LNP-1 versus LNP-3) resulted in a larger particle size, reduced size distribution uniformity, a more negative zeta potential and a reduction in mass balance observed for LNP-3 **(Table 3.3).** Increasing the flow rate ratio from 3 to 6, (LNP-3 versus LNP-4) produced slightly larger particles, potentially highlighting increased RNA loading, or a more dilute lipid phase that favours the formation of larger LNPs. All remaining CQAs remained comparable **(Table 3.3)**. Reducing the total microfluidic flow rate from 15 to 5 mL/min (LNP-3 versus LNP-5), increased particle size by ~ 10 nm, while PDI remained low, with zeta potential and % EE remaining comparable. Notably, the % MB improved by ~4% **(Table 3.3).**

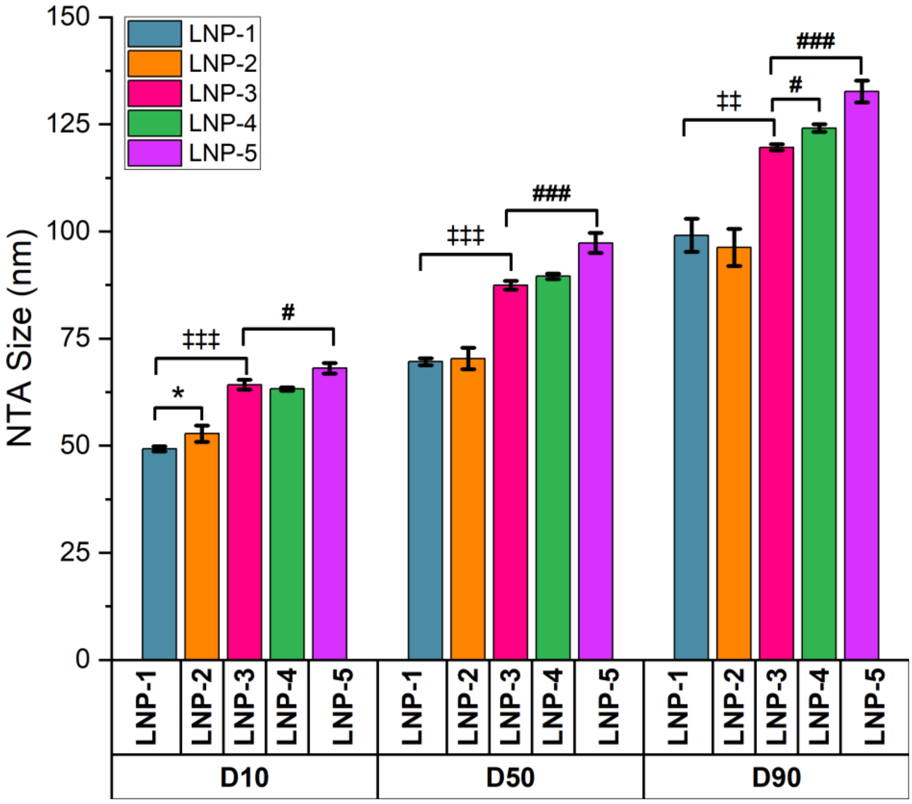

***Figure 3.2** - Nanoparticle tracking analysis distributional value percentiles (10, 50, 90) of ASO-LNP formulations 1-5, (n=3 ± STD). Tukey Tests compared LNP1-2(*), LNP1-3(‡) and LNP3-4/5(#) where *p < 0.05, **p < 0.005 and ***p < 0.0005.*

Table 3.4 *- NTA mean, mode, 10th, 50th, and 90th centile diameters, and corresponding span values for ASO-LNP formulations, (n=3, mean ± standard deviation). FRR: Flow Rate Ratio; TFR: Total Flow Rate. Tukey Tests compared LNP1-2(*), LNP1-3(‡) and LNP3-4/5(#) where *$p < 0.05$, **$p < 0.005$ and ***$p < 0.0005$.*

Sample	**Mean (nm)**	**Mode (nm)**	**D10 (nm)**	**D50 (nm)**	**D90 (nm)**	**Span**
SM102 LNP-1 **(N/P: 6**, FRR 3, TFR 15**)**	72.9 ± 1.6	66.3 ± 0.5	49.3 ± 0.6	69.6 ± 0.8	99.1 ± 3.9	0.72 ± 0.04
SM102 LNP-2 **(N/P: 12**, FRR 3, TFR 15**)**	74.4 ± 3.1	68.1 ± 3.9	52.8 ± 1.9*	70.3 ± 2.5	96.3 ± 4.3	0.62 ± 0.02*
MC3 LNP-3 (N/P: 6, FRR 3, TFR 15)	90.6 ± 1.1‡‡‡	83.5 ± 1.6‡‡‡	64.2 ± 1.1‡‡‡	87.4 ± 1.0‡‡‡	119.6 ± 0.7‡‡	0.63 ± 0.01‡
MC3 LNP-4 (N/P: 6, **FRR 6**, TFR 15)	92.5 ± 0.6	86.7 ± 1.9	63.2 ± 0.4	89.5 ± 0.6	124.1 ± 0.9$^{\#}$	0.68 ± 0.01$^{\#}$
MC3 LNP 5 (N/P: 6, FRR 3, **TFR 5**)	99.6 ± 2.2$^{\#\#}$	95.7 ± 5.5$^{\#}$	68.1 ± 1.2$^{\#}$	97.3 ± 2.3$^{\#\#\#}$	132.7 ± 2.5$^{\#\#\#}$	0.66 ± 0.01

NTA measurements showed similarities between mean and mode particle diameters for all LNP formulations, indicating minimal contributions from larger particles within each population, with an average mean/mode size of ~ 80 nm (**Table 3.4)**. The small differences between mean and mode measured particle diameters suggest that spin-column purification may have removed a proportion of smaller-sized particles, increasing overall size uniformity within each sample. These observations were further supported by the span values (**Table 3.4),** which followed the same trends as the PDI data. LNP-1 exhibited the broadest size distribution (0.72), whereas the remaining LNP formulations displayed narrower spans (0.62-0.68). Mode particle diameters increased progressively across samples by up to 30 nm, with LNP-5 formulations containing the largest particles (**Table 3.4).** Distributional values **(Figure 3.2, Table 3.4)** demonstrate, formulation and manufacture process impacts on LNP sub-population generation, with overall D10, D50 and D90 increased sizes with further investigating parameters.

3.4.2. FI-AF4-UV-MALS-DLS Evaluation of ASO-LNP Formulations

To perform further in-depth analysis of the ASO LNP formulations, AF4 was used to provide size-based separation of LNP particles based on their hydrodynamic diameters, which are governed by their diffusion in the channel flow. The use of AF4 techniques supersedes NTA by physically separating formulations according to their size prior to detection, thereby reducing the influence of coincident scattering events on measured particles size and improving resolution across polydisperse samples. For the purposes of this study, frit inlet AF4 was multiplexed with a UV detector for RNA quantification, MALS for measuring the particle radius of gyration and molar mass approximation, and online DLS, for the measurement of hydrodynamic radius. Combining readout from the online MALS and DLS detectors, the shape factor was approximated, providing insights into LNP formulation morphology (R_G/R_H) and inherent structural differences between the LNP formulation.

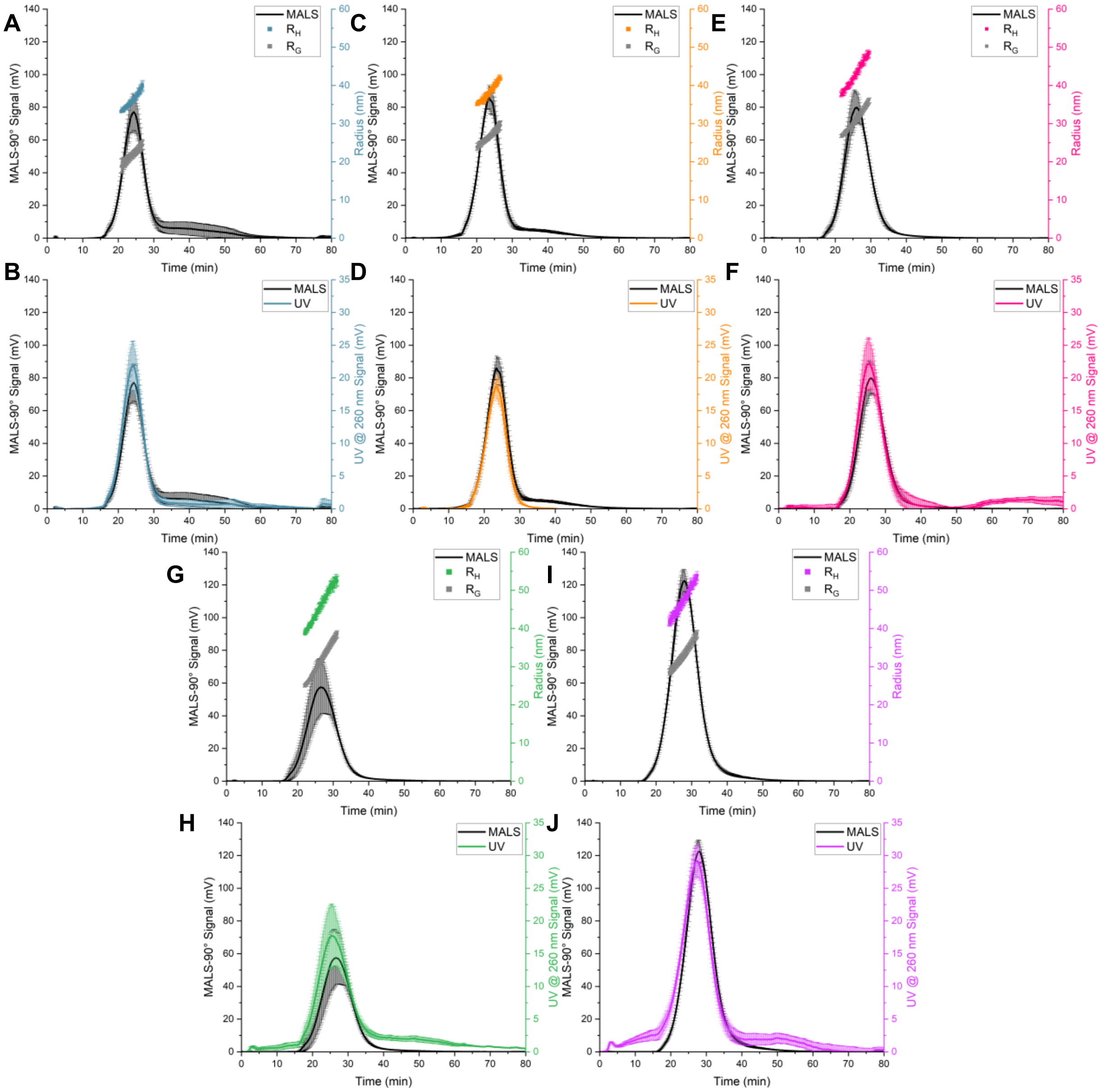

***Figure 3.3** - FI-AF4-MALS fractograms of ASO-LNP formulations. MALS-90° detector signal with FWHM integrated R_G, R_H values and MALS-90°/UV (260 nm) elution profiles traces, respectively for LNP-1 A(A&B), LNP-2(C&D), LNP-3(E&F), LNP-4(G&H) and LNP5(I&J), (n=3). Error bars represent mean ± standard deviation.*

LNP1-5 formulations exhibited high percent LNP recovery (>84%) after separation and detection **(Table S 9.1)**, along with successful AF4-based separation and sufficient UV/MALS/DLS detector signals **(Figure 3.3).** Each fractogram highlights a monomodal peak, characteristic of a monodisperse LNP formulation, although LNP-1 and LNP-2 formulations had a low abundance secondary peak (~20% area under curve) eluting after 30 minutes (**Figure 3.3). ** The lack of ASO leakage demonstrates ASO-LNP stability for LNP1-5 formulations (**Figure 3.3**)**.** Enhanced distributional values for each R_G, R_H **(Figure 3.4).**

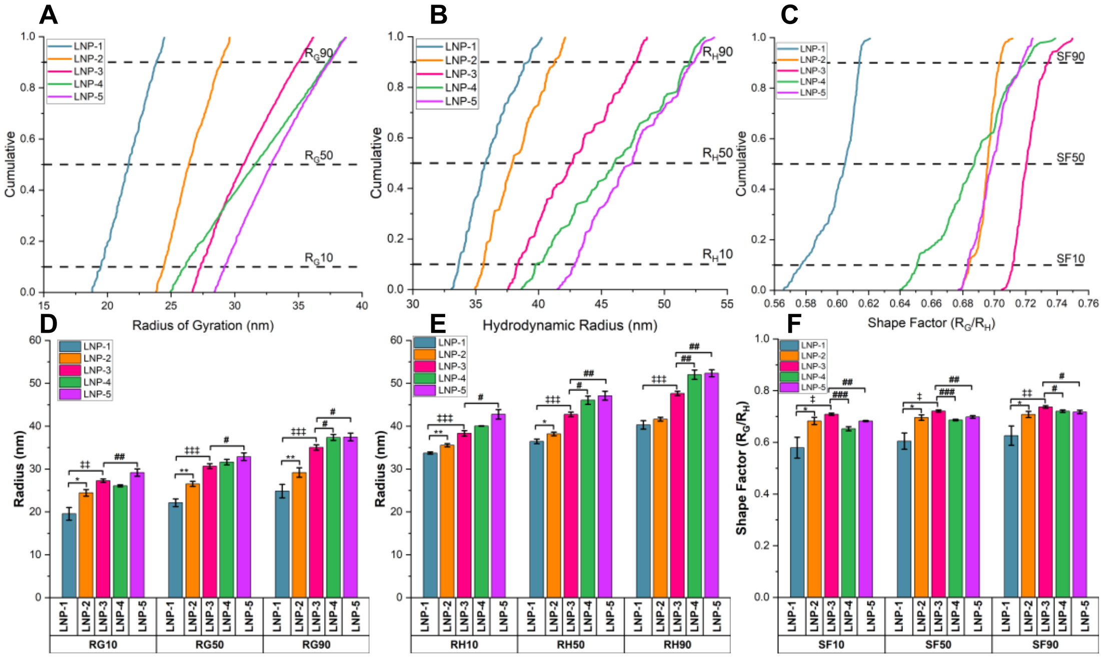

*__Figure 3.4__ - FI-AF4-UV-MALS-DLS distribution values for FWHM integrated elution profiles for ASO-LNP formulations. A) R_G distribution B) R_H distribution, C) shape factor distribution. D) R_G distribution values, factor E) R_H distribution values and F) shape factor distribution values. Tukey Tests compared LNP1-2(*), LNP1-3(‡) and LNP3-4/5(#) where *$p < 0.05$, **$p < 0.005$ and ***$p < 0.0005$, (n=3), error bars represent mean ± standard deviation.*

The LNP-1 formulation was found to consistently produce the smallest LNP size values and shape factor ratio (~0.6). This morphology displayed a departure from spherical '0.775' shape factor, indicating a dense core/shell geometry (**Figure 3.4)** (255)**.** Other LNP formulations exhibited larger R_G, R_H, and shape factor values, with the shape factor values trending towards a more spherical geometry. Further in-depth analysis of the LNP formulation distribution indicates a higher measured particle size within LNP 2-5 formulations across 10, 50 and 90 values, this increasing size trend does not align with shape factor values, as differing shape factor values were produced across LNPs samples (**Figure 3.4, Table S 9.1).**

3.4.3. ASO-LNP CQA Output Correlative Evaluations

By combining analytical technique CQA outputs, correlative impact between measured physicochemical attributes can be obtained, and LNP groupings can be visualised to show relationships between LNPs and CQAs.

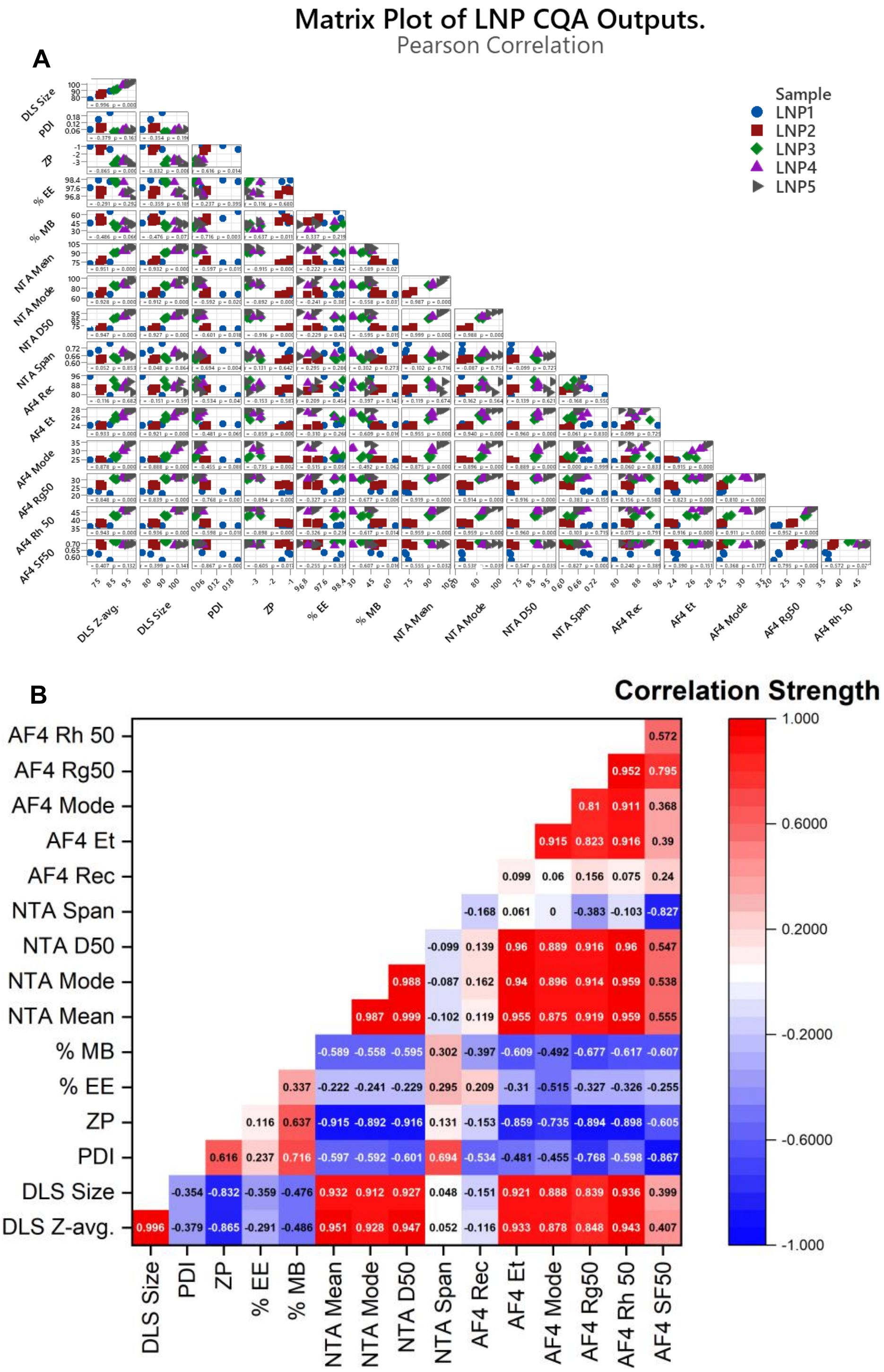

	DLS Size	PDI	ZP	% EE	% MB	NTA Mean	NTA Mode	NTA D50	NTA Span	AF4 Rec	AF4 Et	AF4 Mode	AF4 Rg50	AF4 Rh 50	AF4 SF50
AF4 Rh 50															0.572
AF4 Rg50														0.952	0.795
AF4 Mode													0.81	0.911	0.368
AF4 Et												0.915	0.823	0.916	0.39
AF4 Rec											0.099	0.06	0.156	0.075	0.24
NTA Span										-0.168	0.061	0	-0.383	-0.103	-0.827
NTA D50									-0.099	0.139	0.96	0.889	0.916	0.96	0.547
NTA Mode								0.988	-0.087	0.162	0.94	0.896	0.914	0.959	0.538
NTA Mean							0.987	0.999	-0.102	0.119	0.955	0.875	0.919	0.959	0.555
% MB						-0.589	-0.558	-0.595	0.302	-0.397	-0.609	-0.492	-0.677	-0.617	-0.607
% EE					0.337	-0.222	-0.241	-0.229	0.295	0.209	-0.31	-0.515	-0.327	-0.326	-0.255
ZP				0.116	0.637	-0.915	-0.892	-0.916	0.131	-0.153	-0.859	-0.735	-0.894	-0.898	-0.605
PDI			0.616	0.237	0.716	-0.597	-0.592	-0.601	0.694	-0.534	-0.481	-0.455	-0.768	-0.598	-0.867
DLS Size		-0.354	-0.832	-0.359	-0.476	0.932	0.912	0.927	0.048	-0.151	0.921	0.888	0.839	0.936	0.399
DLS Z-avg.	0.996	-0.379	-0.865	-0.291	-0.486	0.951	0.928	0.947	0.052	-0.116	0.933	0.878	0.848	0.943	0.407

***Figure 3.5** – Analytical technique CQA outputs A) sample grouping distribution and B) heatmap of Pearson correlations between CQAs for ASO-LNPs.*

Correlative heatmaps provide further insights into CQA connections across tested formulations **(Figure 3.5).** Mapping of LNP samples indicate groupings of samples within comparative CQA output values. Grouping distributions vary from CQAs comparisons, however it can be noted that LNP-1 is the most separated sample in terms of dissimilar CQA values **(Figure 3.5).** Heatmap values display correlative strength between samples were CQAs have a positive (> 0.6), negative (<-0.6) or contain no relationship (0.0). Across analysed CQA outputs, as ZP increased toward 0 mV, PDI increased, RNA mass balance also increased as ZP increased. Size-based CQAs also produced strong positive correlations with sizes increases seen across all formulations across increasing resolution-based techniques **(Figure 3.5).** Strong negative CQA correlations were noted across size-based CQAs compared against ZP values, were as ZP decreased in charge, particle size increased **(Figure 3.5).** CQAs without a relationship showed (0.0 ± 0.3) were mainly produced when comparing EE values with DLS, ELS and NTA outputs **(Figure 3.5).** LNP-1-2, 3-5 showed tighter groupings, which suggest that changes in N/P ratio, TFR and FRR produced a more incremental impact within CQA correlations, compared to lipid choice/identity. Enhancing LNPs design through formulation optimisation will continue to advance as deeper insights into CQA analyses become possible.

3.5. Discussion

ASO-based drugs have garnered increased research interest due to their modular platform manufacture approaches and broad applicability of novel disease and genetic condition targets. Currently, ASOs are typically administered in their unconjugated pristine form, or are conjugated to GalNAc, a triglyceride moiety used for hepatic targeting. Although LNPs have emerged as a popular choice of delivery system for mRNA vaccines and siRNA payloads, their application in ASO payload encapsulation remains under reported in the literature. In this study, an orthogonal pipeline approach was used to characterise ASO-LNP critical quality attributes using a variety of formulation conditions in **Table 3.2.**

Initial DLS-based results revealed monomodal LNP particle size distributions (**Figure 3.1),** with SM102-LNPs producing smaller hydrodynamic diameters than MC3-LNPs. Low PDI values (**Table 3.3)** across samples indicated uniform particle populations and demonstrated that robust manufacture and purification processes by microfluidic formulation and spin column centrifugation purification. High reproducibility was denoted through small standard deviations across size and PDI values (**Table 3.3).** All LNP formulations had negative zeta potential values, indicating colloidal stability defined by DLVO theory (188). Encapsulation efficiencies exceeded 97% for all formulations, indicating effective incorporation and retention of ASOs during formulation (**Table 3.3**). However, ASO mass balance recovery remained low averaging

~ 52% (LNP-1/2) and ~ 40% (LNP-3/4/5), indicating high losses of ASOs across formulation and purification (**Table 3.3).** These loses could be attributed to smaller LNPs being filtered during purification, the size of ASOs (18-mer) payloads having no recorded secondary interactions to further enhance singular RNA interaction with ionisable lipids during formulation, which would impact encapsulation and further recovery.

Enhancing CQA resolution beyond DLS, NTA was employed to analyse LNP populations on a particle-by-particle basis, with particles size derived from diffusion coefficient using the Stokes-Einstein equation. These enhanced NTA insights showcase similar trends noted with DLS with increasing particle sizes across tested LNP formulations (**Figure 3.2, Table 3.4).** Initial particle concentration differences between formulations highlights post-spin column concentration differences with LNP-1 producing the highest concentration compared to a 10-fold decrease compared to LNP-4 (**Figure 3.2**). Comparing both formulations show that changing ionisable lipid composition and microfluidic FRR contributed to increased particle dilution and particle detection (**Figure 3.2**). FRR impact aligns with LNPs using different sized RNA cargo (81).Further comparing formulations, span values remain low, highlight formulation monodispersity (**Table 3.4)** without secondary aggregate peaks noted ~ 5000 nm within DLS z-average profiles (**Figure 3.1**).

To probe ASO-LNP structure and composition in greater depth, AF4 was applied to physically separate nanoparticles based on their diffusion-governed hydrodynamic diameters **(Figure 3.3, Figure 3.4)**. AF4 addressed the limitations of NTA by eliminating coincident detection artefacts and enabling fraction-specific characterisation. AF4 method performance highlighted high sample recovery (>85 %), supporting reliable downstream analysis with online detectors. MALS-90° traces were integrated at FWHM where R_G and R_H values could be obtained and utilised to infer particle shape factor morphology **(Figure 3.3, Table S 9.1)**. Overlaid UV/MALS profiles highlighted thar ASOs co-eluted with LNPs indicating successful ASO loading and structural stability of the formulations during separation. Larger-size particle sizes eluted at later timepoints, however evaluating LNP1/2 shows a decrease of 0.5-minute elution time but a larger size of 2 nm (**Table S 9.1).** This disparity could be due to the lower RNA concentrations in LNP-2 using a higher N/P ratio producing overall larger particles, which are less dense than LNP-1 with differing morphologies, in alignment with shape factor values (**Figure 3.4, Table S 9.1)**. Distributional values offered deeper insights into CQA evaluation over R_G and R_H and shape factor profiles (**Figure 3.4, Table S 9.1)**, with similar morphologies produced between D50-90 for all formulations apart from LNP-1. Integrating CQA outputs across orthogonal analytical techniques further strengthens our understanding of how these attributes interrelate and can be leveraged to guide rational ASO-LNP design. This study demonstrates that the choice of ionisable lipid significantly effects CQA clustering, as reflected in zeta potential and size-related outputs (**Figure 3.5**), highlighting further emphasis on surface charge as an indicator of colloidal stability within ASO-LNPs through DLVO theory (188), and subsequent impact of overall main ionisable lipid selection within early ASO-LNP candidate screening. Early ASO-LNP candidates should continue to be evaluated across independent, orthogonal analytical pipelines to ensure high-quality data that informs downstream decision-making and the candidate selection process.

3.6. Conclusions

Understanding ASO-LNP formulation conditions can further enhance the use of LNP delivery systems as a platform approach, departing from hepatic targeting whilst also reducing ASO chemical modification, enhancing more sustainable ASO manufacture. Exploratory results demonstrated that formulation optimisation produced comparable results in terms of associated CQA outputs, with larger differences noted through ASO mass balance. Future work includes spin column centrifugation with lower MWCO and alternative purification techniques to increase ASO mass balance and recovery of the formulations. Future work could also include conjugating targeting moieties to external LNP surface for targeted delivery to ensure precise and specific ASO delivery and enhancing endosomal release through incorporating cell penetrating and endosomal escape peptides. The use of enhanced analytical orthogonal pipeline demonstrated deeper insights in into output CQAs can inform design of further ASO-LNP candidate therapeutics.

Chapter 4

Received: 29 April 2025 / Revised: 13 October 2025 / Accepted: 20 October 2025 / Published: 29 October 2025, *ACS Molecular Pharmaceutics*, **22 (12), 7383-7399**
https://doi.org/10.1021/acs.molpharmaceut.5c00614

4. The Use of Enhanced Analytical Pipelines for the Characterisation of Poly(A) and Poly(A)-LNP Formulation Critical Quality Attributes

Callum G. Davidson[1], Eleni Kapsali[1], Savvas Ioannou[2], Bojan Kopilovic[3], Muattaz Hussain[1], Yvonne Perrie[1], Zahra Rattray[1]*
[1]Strathclyde Institute of Pharmacy and Biomedical Sciences, University of Strathclyde, Glasgow, G4 0RE.
[2]School of Molecular Biosciences, University of Glasgow, Glasgow, G11 6EW
[3]School of Chemical, Materials and Biological Engineering, University of Sheffield, Sheffield, S1 3JD.
*Corresponding author: Zahra Rattray (zahra.rattray@strath.ac.uk)

This chapter includes the full text of the published article in ACS Molecular Pharmaceutics including the introduction, methods, results and conclusions. For this work, I primarily designed and carried out all experiments, except CGE and TEM experiments. Analyses, data visualisation and manuscript drafting was performed by the author of this thesis.

Graphical Abstract

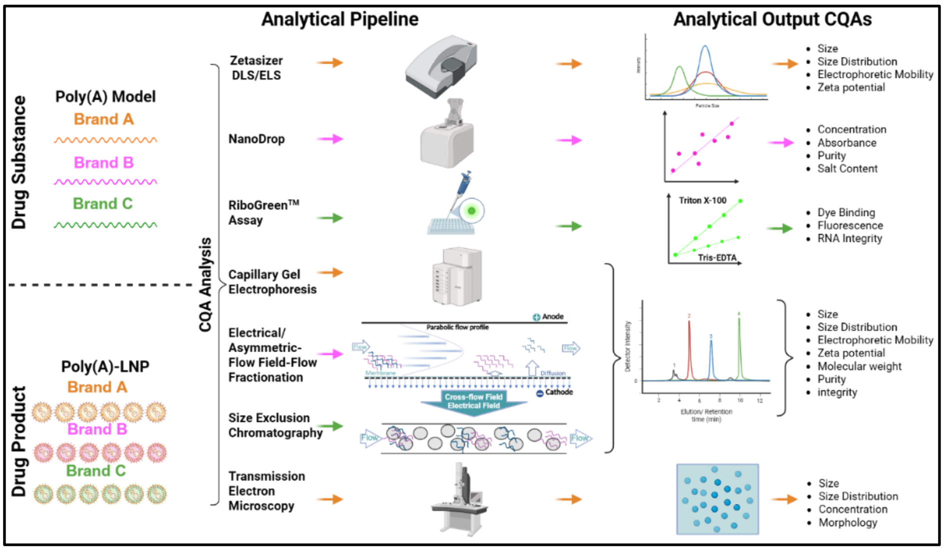

4.1. Introduction

Nucleic acid therapeutics have gained significant attention in the pharmaceutical and drug delivery fields (27) owing to the global implementation of COVID-19 mRNA mass vaccination programs. The successful clinical translation of ribonucleic acid-encapsulated lipid nanoparticle (RNA-LNP) drug delivery systems has played a pivotal role in this surge, with the market expected to grow to $48 billion by 2036.(256) This momentum is further driven by the U.S. Food and Drug Administration (FDA) approval of RNA-LNP-based therapies/vaccines, including Onpattro®, Comirnaty®, Spikevax®,(23,78,120) and most recently, the Moderna respiratory syncytial virus vaccine *mRESVIA®* in 2024.(25)

Drug delivery systems are engineered to protect encapsulated RNA cargo against degradation, ensuring safe and effective delivery to target intracellular domains. Unlike conventional drugs, RNA drug substances bypass the need for an active protein-mediated therapeutic site by binding to endogenous cellular RNAs, halting and/or regulating disease pathways. This paradigm shift has led to the discovery of candidate RNA drug substances against a broad spectrum of novel therapeutic targets.(242,257–261) However, due to their inherent large and hydrophilic nature, RNA therapeutics face unique translational challenges, requiring enhanced chemical modifications or advanced delivery systems. Chemical modifications to RNA-based drug substances can be introduced at the phosphate backbone, ribose sugar, or nucleobase.(48,73,258) These modified RNAs can be encapsulated in a variety of delivery systems including antibodies, lipids, polymers and nanoparticles ,(259–261) with lipid nanoparticles (LNPs) being prominent due to their formulation simplicity. RNA-LNPs are typically produced by microfluidic mixing an organic lipid phase with an aqueous RNA phase, followed by purification into a neutral buffer prior to analysis of physicochemical critical quality attributes.

Polyadenylic acid (Poly(A)) has emerged as a popular choice for use as a model RNA drug substance for LNP formulation prototyping, ranging from LNPs manufactured with cationic-LNPs(112,254) to ionisable-LNPs(109,262,263) and different structured ionisable-LNPs.(81,128,264) In the absence of existing RNA and LNP drug substance/drug product reference materials, Poly(A)-LNPs are widely used as a control formulation to assess the impact of manufacturing process parameters on formulation critical quality attributes (CQAs). Since the stability of RNA drug substance cargo is a major determinant of drug product performance, both pre-formulation and post-formulation attributes of the RNA must be assessed. In particular, the source of the RNA, i.e., the RNA manufacturer, may influence these attributes, highlighting the need for systematic comparison of drug substance quality and its effect on drug product formulation.

A range of analytical techniques are used to quantify RNA drug substance attributes, ranging from chromatographic to light scattering, electrophoretic and mass spectrometry-based methods. Chromatographic approaches remain the gold-standard, with advancements in separation modalities expanding the separation toolbox to include a larger repertoire of column stationary phases, including hydrophilic interaction liquid chromatography,(179,180,265) ion-exchange (212,266), and hydrophobic ion-pair chromatography (175,176,267), aqueous based separation techniques such as size exclusion chromatography.(268–270). More recently, flow field-flow fractionation (FFF) (271–273) coupled with light scattering-based detectors enabling high-resolution interrogation of nucleic acid and LNP size distribution profiles based on analyte molecular diffusion for size-based detection. Electrophoresis is another routine technique for electrical based-separation (274,275) and detection of multiple molecular weight RNA species with agarose gel systems and specialist capillary electrophoretic instruments being adopted as analytical methods (276,277). Beyond advancements in separation technologies, detection methods multiplexed to separation-based approaches have seen routine adoption of triple quadrupole mass spectrometry, and ion-mobility mass spectrometry for high resolution detection of purity and conformational analysis, respectively.(278–281)

Despite the widespread use of Poly(A) in LNP formulation studies, critical quality attributes of Poly(A) remain under-characterized. With previous studies focussing Poly(A) in the context of therapeutic mRNA tails (> 100 bases), (267,282,283) and further impact on mRNA translation (284–286). Therefore, comprehensive comparative analyses of drug substance sequences from different manufacturers are currently lacking, highlighting the need for deeper investigation of these sequences as model nucleic acid drugs. As Poly(A) has been under characterised, it was not treated as a generic material as Poly(A) sequence length versus function remains unknown for singular Poly(A) use. In this study, three, commercially available Poly(A) drug substances from three anonymised manufacturers, (Brand A, Brand B, and Brand C) were assessed and evaluated the impact of their encapsulation in a model LNP formulation as three formulations referred to as A-LNP, B-LNP and C-LNP.

This study aims to enhance knowledge of model Poly(A) critical quality attribute impact on LNP formulation attributes, ultimately seeking to produce better standardised controls for LNP bench to bedside translation. Results demonstrated that the chain length distribution associated with different Poly(A) brands vary, using a variety of pre-formulation and post-formulation buffers. Findings demonstrated that despite observable Poly(A) molecular weight differences, SM102-LNPs exhibited no significant differences in variation of their associated drug product CQAs. However, further work is needed to evaluate the impact of Poly(A) drug substance CQA variability in LNP drug products manufactured with differing lipid compositions and ratios.

4.2. Materials

Poly(A) was purchased from three manufacturers (Merck, Roche, and Cytiva). DNA/RNA free water, 10X phosphate-buffered saline (PBS) pH 7.4, sodium citrate dihydrate and Quanit-IT RiboGreen^{TM} RNA Quantification Assay were acquired from ThermoFisher (Fisher Scientific, Leicestershire, UK) and 1N hydrochloric acid was sourced from Alfa Aesar.

8-[(2-hydroxyethyl)[6-oxo-6- 83 (undecyloxy)hexyl]amino]-octanoic acid, 1-octylnonyl ester (SM102) were purchased from BroadPharm (San Diego, CA, USA). 1,2-distearoyl-sn-glycero-3-phosphocholine (DSPC), 1,2-dimyristoyl-rac-glycero-3- methoxypolyethylene glycol-2000 (DMG-PEG 2000) were purchased from Avanti Polar Lipids 81 (Alabaster, AL, USA). Cholesterol (CHOL) and Amicon®-15 100 kDa MWCO regenerated cellulose spin columns were sourced from Sigma Aldrich (Merck, Gillingham, UK).

4.3. Methods

Methods include the analysis of Poly(A) within several buffer types, citrate pH 6 (50 mM), citrate pH 4 (50 mM) representing pre-formulation LNP buffers and 1 × PBS pH 7.4 representing a neutral and biocompatible buffer for Poly(A) drug substance use, and also reflect Poly(A) buffer combination post-LNP formulation purification.

4.3.1. NanoDrop Assay

A NanoDrop was used to verify Poly(A) sample concentration, accounting for lyophilised salt content within gravimetrically weight samples. Analyte concentration was calculated using the Beer-Lambert Law.

$$A = \varepsilon * c * l$$

Equation 4.1 *- Beer-Lambert Law.*

Where A is the absorbance, ε the molar absorptivity constant, c the concentration and l the path length, with an absorbance value equal to 1 representing 40 µg of single stranded RNA. Calibration curves (0.5-2.0 mg/mL) Poly(A) were prepared from a 10 mg/mL stock (DNA/RNA water) and diluted in either PBS, 50 mM citrate buffer (pH 4 and pH 6) to perform concentration calibrations. 2 µL of each theoretical concentration level was measured at 260 nm using NanoDrop, to evaluate RNA dilution linearity and NanoDrop limit of detection and limit of quantification.

4.3.2. RiboGreen Assay™

Integrity of branded Poly(A) was measured using the Quant-iT™ RiboGreen™ RNA Quantitation assay Kit (Thermo Fisher #4110) and using 0-1000 ng/mL calibration curves investigating the impact of triton X-100 on Poly(A) and fluorescent dye binding using TE buffer. As Triton X-100 is used to lyse Poly(A)-LNPs and facilitate the release of encapsulated Poly(A), its potential impact on RNA sample integrity was carefully assessed. In addition, assay linearity, limit of detection (LOD), and limit of quantification (LOQ) were evaluated for each Poly(A) drug substance to ensure assay robustness and reliability across all samples.

The fluorescence intensity signal of RiboGreen™ was measured on a GloMax® Explorer GM3500 microplate reader (Promega, UK) at an excitation wavelength of 475 nm, with the emitted fluorescence measured 500-550 nm. All fluorescence data were captured at ambient temperature (25 °C) using GloMax® firmware version 4.29.0 and processed using GloMax® Fluorescence software version 3.1.0.

4.3.3. Dynamic Light Scattering (DLS)

Particle size (Z-average) and polydispersity index (PDI) were measured by dynamic light scattering (DLS) using a Zetasizer Nano ZS system (Malvern Panalytical, Worcestershire, UK) equipped with a 633 nm Helium-Neon laser and a detection angle of 173° (non-invasive back scattering). Unless otherwise stated, all measurements were performed at 25 °C and at a 1:100 dilution from stock 10 mg/mL in DNA/RNA free water to 0.1 mg/mL in corresponding buffer. All measurements were performed in three independent replicate measurements consisting of at least two technical replicates.

The diffusion coefficient at different concentrations (0.5 – 6.25 mg/ml) was measured for branded Poly(A) samples in PBS and 50 mM citrate buffer (pH 6 and pH 4) and to subsequently calculate the diffusion self-interaction parameter (K_D), a measure of self-association (287).

$$D = D_0\,(1 + K_D c + \cdots)$$

***Equation 4.2** – Self-interaction parameter (K_D) measured by dynamic light scattering.*

Where D is the diffusion coefficient, D_0 the maximum diffusion coefficient at infinite solute dilution and c the concentration of solute in solution.

4.3.4. Electrical Asymmetrical-Flow Field Flow Fractionation (EAF4)

An AF2000 Asymmetric-Flow Field-flow fractionation (AF4) module (Postnova Analytics, Germany) hyphenated with multiple inline detectors including a multiangle light scattering (MALS- PN3621, Postnova Analytics), a UV detector (PN3242, 260 nm- Postnova Analytics) and a DLS Zetasizer Nano ZS system (Malvern Panalytical, Worcestershire, UK) was used to perform separation and inline analysis of Poly(A). An electrical AF4 separation channel, with a channel spacer thickness of 500 µm, and a 10 kDa molecular weight cut-off (MWCO) amphiphilic regenerated cellulose membrane was used for Poly(A) separation, with a 100 µL sample injection loop, and an injection volume of 20 µL. Phosphate buffer (1.25 mM, pH 7.4) was used as the carrier liquid, and an injection flow rate of 0.2 mL/min, cross-flow rate of 1.5 mL/min (linear power decay), and a detector flow rate of 0.5 mL/min were used as elution conditions. Neutral (0.0 mA) and positive (+1.0 mA) currents were applied to the EAF4 channel. Each Poly(A) sample was injected in three technical replicates (0.25 mg/mL). Poly(A) recovery (% Rec) was calculated as per established protocol.(254) Optimised method quality was verified against International Organisation for Standardisation publication ISO/TS/21362:2021.(288)

Molecular weight and molar mass distributions of Branded Poly(A)s were determined using direct injection parameters (neutral current, 0.5 mL/min tip flow, 0.0 mL/min cross-flow for 25 minutes, 12.5 µg sample) into hyphenated detector series. Direct injection traces were processed at full-width half-maximum (FWHM) MALS-90 ° detector signal using 52-124 ° detector angles and random coil data fitting.

4.3.5. Electrophoretic Light Scattering (ELS)

ζ-potential surface charge was measured using ELS. Unless otherwise stated, all measurements were performed at 25 °C and at an equivalent dilution factor to EAF4 channel in phosphate buffer (1.25 mM, pH 7.4). All ζ-potential measurements were performed using two independent replicates consisting of at least two technical measurements.

4.3.6. Size Exclusion Chromatography (SEC)

Analytical SEC (aSEC) was performed on the AF2000 Asymmetric-Flow Field-flow fractionation (AF4) module (Postnova Analytics, Germany) hyphenated with multiple inline detectors (as per **section 4.3.4**), using a TOSOH TSKgel UP-SW2000 column (300 x 4.6 mm, 2 µm) and 1 × PBS pH 7.4 isocratic mobile phase with a corresponding flow rate of 0.2 mL/min and equivalent injection concentration to **section 4.3.4**. The UV detector sensitivity was reduced to +1.0 output.

4.3.7. Capillary Gel Electrophoresis (CGE)

Poly(A) integrity CQA was assessed by capillary gel electrophoresis (CGE) using a 5200 Fragment Analyzer System (Agilent United States).(289) Fragment separation and detection were performed with the DNF-471 RNA Kit (15 nt) (Agilent), which contains an RNA separation gel, dsDNA inlet buffer, TE rinse buffer, intercalating dye, RNA diluent marker (15 nt), an RNA ladder ranging from 200-6,000 nt, and a capillary conditioning solution. A FA 12-Capillary Array Short, 33 cm (Agilent) was employed for the analysis.

Poly(A) samples were initially diluted to ~100 ng/µL, followed by a 1:12 dilution in RNA diluent marker to achieve a target final concentration of ~ 4 ng/µL. Prior to each run, a pre-run voltage of 8 kV for 30 seconds was applied. Capillaries were conditioned with the provided conditioning solution and rinsed twice with TE buffer. Capillaries were filled with separation gel under pressure, and samples were introduced by voltage injection (5 kV for 4 seconds). Electrophoretic separation was carried out at 8 kV for 45 minutes. Detection was achieved *via* laser-induced fluorescence, facilitated by the intercalating dye present in the separation gel. The resulting electropherograms were used to evaluate Poly(A) integrity based on fragment size distribution and fluorescence intensity.

4.3.8. Poly(A)-Lipid Nanoparticle Formulations

To further evaluate the impact of Poly(A) brand on LNP critical quality attributes, ionisable lipid formulations of SM102-LNPs were composed of SM102:CHOL:DSPC:DMG-PEG2000. All initial lipid stock solutions were prepared in ethanol at 5 mg/mL and combined at a 50:38.5:10:1.5 molar ratio for ionisable lipid:cholesterol:helper:PEG-lipid. Branded Poly(A) was prepared in DNAse/RNAse free water at 1.5 mg/mL, verified by Nanodrop, and diluted in 50 mM citrate buffer (pH 6), which was used as the aqueous phase. Lipid organic phase and Poly(A) aqueous phases were injected simultaneously into the micromixer at a 3:1 aqueous:organic flow rate ratio (FRR), and a 15 mL/min total flow rate (TFR) with an NP ratio of 6:1. The final lipid theoretical concentration after microfluidic preparation was 1.25 mg/mL, with a corresponding theoretical Poly(A) concentration of 0.055 mg/mL. LNP formulations were purified using spin column centrifugation (100 kDa MWCO). Briefly LNPs were diluted (1:40) in 1 × PBS pH 7.4 and centrifuged at 2,000 xg at 4 °C. Branded LNPs were further characterised using Zetasizer, RiboGreen^{TM}, Nanoparticle tracking analysis (NTA) and frit-inlet asymmetric-flow field-flow fractionation hyphenated with multiple inline detectors (FI-AF4-MD) as previously reported.(254)

Nanoparticle tracking analysis (NTA) of particle size, distribution, and estimated particle concentration was conducted using a NanoSight NS300 system (Malvern Panalytical, UK), equipped with a 488 nm laser, low-volume flow cell, sCMOS camera, and automated syringe driver. Samples were diluted 1:10,000 in PBS (pH 7.4) and measured at 25 °C, with the infusion rate set at 50. Data acquisition involved five 60-second videos per sample at a camera level of 15. Analyses were performed using NTA software (version 3.4.003) with a detection threshold of five. Two independent biological replicates, each with five technical replicates, were analysed per sample.

FI-AF4-MD analysis was performed using a field-flow fractionation system (Postnova Analytics, Germany) coupled with multi-angle light scattering (MALS, PN3621), UV detection (260 nm, PN3242), and dynamic light scattering (Zetasizer Nano ZS, Malvern Panalytical). Separation was carried out using a frit-inlet (FI) channel with a 350 µm spacer and 10 kDa MWCO regenerated cellulose membrane. LNP samples (20 µL injection volume, 0.5 mg/mL) were injected using a 100 µL loop in triplicate. Elution was performed in PBS (pH 7.4) with an injection flow rate of 0.2 mL/min, a crossflow rate of 0.75 mL/min (exponential decay 0.2), and a detector flow rate of 0.3 mL/min. Data were processed using Nova FFF software (v2.2.0.1) applying the spherical MALS model (32–136°) for drug product LNPs.

Transmission Electron Microscopy with negative staining was used to image LNP formulations for their morphology, in tandem with AF4 shape factor ratio. Copper grids with carbon film 400 were used (Agar Scientific, AGS160-4) and glow-discharged prior to sample application. A volume of 10 µL of LNP suspension was applied to the grid and incubated for 15 minutes. Excess sample was removed by filter paper adsorption, and the grid was rinsed once with dH2O, followed by a 5-minute fixation with 2% Glutaraldehyde. Samples were then washed three times with dH2O (30 seconds per wash) and 2% Uranyl Acetate applied for 5 minutes. Excess dye was removed by blotting using filter paper and the grids left to dry at ambient temperature for 15 minutes. Samples were imaged using a JEM transmission electron microscope operated at 120 kV, at 30,000, 80,000, and 150,000× magnifications. LNP circularity was quantified from images acquired at the 30,000× magnification in ImageJ® software (v.1.8.0).

Each formulation was named A-LNPs, B-LNPs and C-LNPs as per Poly(A) branded manufacturer. Comparative statistical analyses were carried out to correlate Poly(A) drug substance with LNP drug product critical quality attributes.

4.3.9. Statistical Analysis

The corresponding mean ± standard deviation (SD) was calculated for all experiments with a minimum of two independent and two technical replicates, unless otherwise stated. A one-way Analysis of Variance (ANOVA) was performed to highlight statistical significance of comparative analytical data using Dunnett and Tukey tests. Statistical analyses were performed using Minitab® version 20.4 software. Data were graphed using Origin Pro version 9.9.0.220.

4.4. Results

4.4.1. Electrical Asymmetrical-Flow Field Flow Fractionation (EAF4)

To our knowledge, for the first time, an EAF4 method to evaluate Poly(A) critical quality attributes multiplexed with inline detectors has been developed. The benefit of using EAF4, is the ability to simultaneously profile molecular size and charge properties. Samples formulated in citrate pH 4 buffer were not analysed due to prior observations of irreversible gelation, which could block FFF membranes. An electrical modality in tandem with a flow-based external field was used to separate Poly(A) fractions according to their surface charge and diffusion-based size parameters. Since RNAs are inherently anionic, separations were performed under neutral and a positive current (reverse polarity) to examine separation enhancement using inline hyphenated UV detector at 260 nm. Electrophoretic mobility and resultant zeta-potential of separated fractions were calculated from electrical and flow-based separation fields.

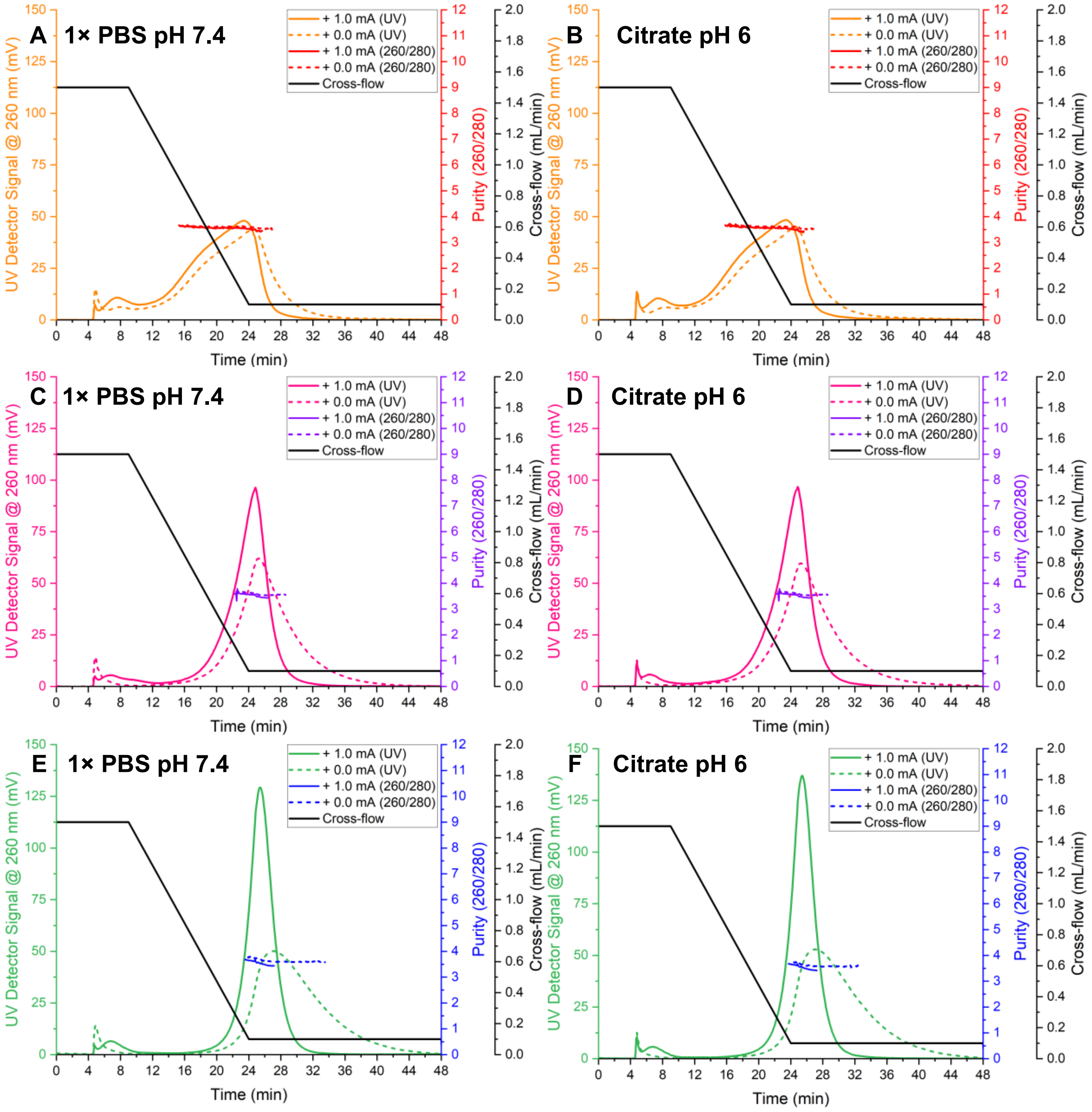

__Figure 4.1__ - EAF4-UV fractogram traces using 0.0 mA and +1.0 mA currents to separate Brand A Poly(A) in A) PBS, B) Citrate pH 6. Brand B C) PBS, and D) Citrate pH 6. Brand C in E) PBS, F) Citrate pH 6. Poly(A) injected at 5 µg. UV elution profiles n=3, purity ratio (260/280) n=2.

Table 4.1 *- EAF4-MD Poly(A) Elution Parameters (n=3) ns = no significant difference between buffer elution times under *neutral and ‡positive conditions using Tukey Test.*

Brand	Buffer	Current (mA)	Elution Time (min)	Peak Width (min)	Recovery (%)
Brand A	1 × PBS pH 7.4	Neutral (0.0)	24.5 ± 0.2*	9.8	93.6 ± 0.2
		Positive (+1.0)	23.2 ± 0.8‡	9.3	94.5 ± 1.9
	Citrate pH 6	Neutral (0.0)	24.4 ± 0.3*	9.9	95.6 ± 2.9
		Positive (+1.0)	23.3 ± 0.5‡	9.3	95.3 ± 4.2
Brand B	1 × PBS pH 7.4	Neutral (0.0)	25.3 ± 0.2*	6.6	92.3 ± 2.2
		Positive (+1.0)	24.8 ± 0.1‡	4.1	95.8 ± 2.2
	Citrate pH 6	Neutral (0.0)	25.3 ± 0.2*	6.2	93.9 ± 1.2
		Positive (+1.0)	24.9 ± 0.1‡	4.1	95.2 ± 1.3
Brand C	1 × PBS pH 7.4	Neutral (0.0)	27.1 ± 0.2*	8.5	95.0 ± 1.6
		Positive (+1.0)	25.4 ± 0.1‡	3.2	98.4 ± 0.8
	Citrate pH 6	Neutral (0.0)	27.1 ± 0.3*	8.4	94.8 ± 2.2
		Positive (+1.0)	25.5 ± 0.1‡	3.2	98.6 ± 1.8

EAF4-based separation of Poly(A) drug substances achieved a >92 % recovery **(Table 4.1)** from the developed method under neutral and positive current separation conditions, in line with current flow field-flow fractionation ISO standards.(288) Across all buffer combinations and branded manufacturers of Poly(A) examined, the application of a positive electrical current in the EAF4 channel enhanced the separation of Poly(A) relative to neutral current (0 mA) conditions. This demonstrates enhanced size and surface charged-based separation pipeline through the elution time shift of ~1.2 min for Brand A, ~0.5 min for Brand B and, ~1.7 min for Brand C **(Table 4.1)**. UV peak FWHM decreased with the application of the positive current, further signifying enhanced separation with a reduction in peak width of ~0.6 min for Brand A, ~2.2 min for Brand B, and ~5.2 min for Brand C **(Figure 4.1, Table 4.1)**. With enhanced separation, the UV_{260} signal increased across all brands with Brand C producing the highest increase at 159.0%, Brand B producing 55.6% and Brand A producing 8.7%. The purity ratio was calculated as a ratio of the UV peak FWHMs at 260 and 280 nm **(Figure 4.1)**.

Under neutral separation conditions, no significant differences were observed between PBS and citrate pH 6 buffer elution times, highlighting increased channel eluent buffer dilution factor. The Poly(A) brands eluted by ascending order of elution time was A<B<C, indicating Brand A Poly(A) is primarily composed of lower molecular weight species and chain lengths in comparison to Brand B and Brand C. Throughout analysis, purity values remained constant

with the application of a positive change channel, indicating that Poly(A) samples from branded manufacturers were of similar purity (> 3, **Figure 4.1**).

MALS and DLS signals associated with EAF4 samples were low in signal strength; therefore, Poly(A) enhanced direct injection were utilised, negating a separation field resulting from higher channel dilution under EAD4-based separation conditions. Poly(A) samples were increased to 12.5 µg from EAF4 separated 5 µg injection concentration. Since no significant difference between elution times of Poly(A) buffer type under neutral conditions, 1 × PBS pH 7.4 buffer was used for Poly(A) dilution prior to direct injection at the higher concentration.

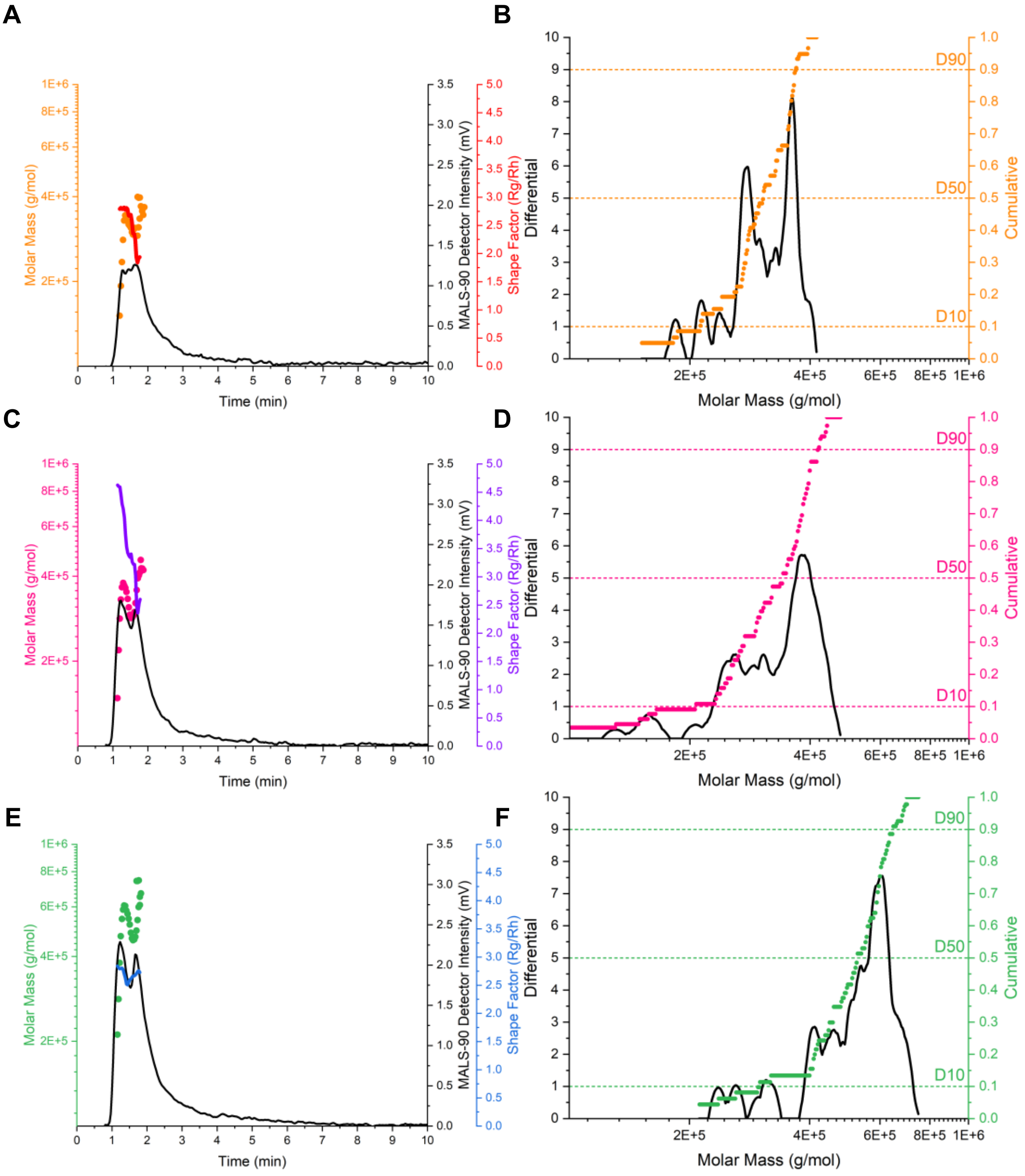

***Figure 4.2** - Direct Injection (12.5 µg) Poly(A) evaluation using Brand A Poly(A) A) MALS, B) molar mass distribution, Brand B Poly(A) C) MALS, D) molar mass distribution, Brand C Poly(A) E) MALS and F) molar mass distribution for 1 × PBS pH 7.4. Molar mass distributions integrated at FWHM MALS-90° detector signal. n=3*

Table 4.2 *- EAF4 enhanced Direct Injection Molecular Weight and Molar Mass distribution of Poly(A) brands diluted in 1 × PBS pH 7.4, n=3.*

Brand	Extinct. Coeff. (mL/g*cm)	Molecular Weight (Da)	Molar Mass D10 (g/mol)	Molar Mass D50 (g/mol)	Molar Mass D90 (g/mol)	Span $(\frac{D90-D10}{D50})$	EAF4 PDI
Brand A	43.6	297467	212558	304914	367905	0.51	1.06
Brand B	40.8	315867	207512	342946	418276	0.61	1.12
Brand C	40.5	508200	298918	528388	648662	0.66	1.10

Table 4.3 *- EAF4 enhanced Direct Injection estimated chain lengths of Poly(A) brands diluted in 1 × PBS pH 7.4, n=3.*

Brand	Est. Chain Length (MW/343)	Est. Chain Length D10 (D10/343)	Est. Chain Length D50 (D50/343)	Est. Chain Length D90 (D90/343)
Brand A	867	620	889	1073
Brand B	921	605	1000	1219
Brand C	1482	871	1540	1891

Poly(A) elution times remained consistent across samples due to channel direct injection in the absence of external cross-flow and applied electrical fields **(Figure 4.2A, C, E)**. However, the MALS-90° elution profiles **(Figure 4.2A, C, E)** revealed clear differences in detector intensities across equivalent injected concentrations of branded Poly(A) drug substance. Brand A produced the lowest detector signal, followed by Brand B and, with Brand C exhibiting the highest intensity. These elution profiles indicate underlying chain length size and size distribution differences within each Poly(A) branded manufacturer, with lower size and higher size distributions producing lower intensity, broader elution profiles (Brand A), contrasted with, higher size and lower size distributions producing higher intensity and narrower elution profiles (Brands B and C).

Poly(A) size and size distribution trends were further reflected in molar mass distribution profiles **(Figure 4.2B, D, F)**, which highlighted branded manufacturer molar mass size increased from Brand A through Brand B, and Brand C. However, molar mass distributional span and EAF4 PDI **(Table 4.2)**, showed contrasting nuanced trends, with span values increasing from Brand A to Brand B and then Brand C. with, EAF4 PDI values noting increasing polydispersity from Brand A to Brand C, followed by Brand B. These contrasting differences in chain length and size dispersity could be due to direction injection mode with the inherent the lack of separation in resolving key chain length and size sub-populations.

Overall, FFF direct injection data aligns with EAF4-UV findings, emphasising manufacturer-specific differences in Poly(A) CQAs. Molecular weight and molar mass distributions (D10, D50, D90) confirm Brand A produced consistent lower molecular weight species, followed by Brand B which produced intermediate sizes and Brand C producing the highest size and lowest polydisperse sample of the three analysed brands. Estimated Poly(A) chain lengths were calculated from molecular weight data and molar mass distribution profiles using the expected molecular weight of a single adenylic acid monomer (343 Da) **(Table 4.3).** Brand A Poly(A) produced nucleotide (nt) chain lengths of 620-1073 nts, with Brand B producing nucleotide chain lengths of 605-1219 nts, and Brand C exhibiting nucleotide chain lengths of 871-1891 nts.

Further analysis of Poly(A) morphology was obtained with decreased channel dilution factors due to direct injection mode, inline DLS R_H values were obtained and shape factor (R_G/R_H) determined. Shape factor data were averaged over direction injection peak FWHM to produce averages of 2.5 (Brand A), 3.5 (Brand B) and 2.7 (Brand C) **(Figure 4.2)**. Signifying random coil (>1.2) shape factor morphologies for Brands A, B and C, linking chain lengths with extended spatial structural conformations, typically associated with polymers. Morphological ratios can provide deeper insights into structural conformations and manufacturer impact with different molecular weight chain lengths.

Lastly, using the EAF4 pipeline in positive and neutral separation conditions the charge distribution profile of Poly(A) was determined. Where Poly(A) electrophoretic mobility and zeta potential parameters can be derived to probe the relationship between Poly(A) structures across manufacture source.

4.4.1.1. Offline ELS determination of Electrophoretic Mobility and Zeta Potential

Further insights into Poly(A) zeta potential distribution were determined using conventional offline electrophoretic light scattering and derived orthogonally from high resolution EAF4-based separation hyphenated with UV.

Table 4.4 – Electrophoretic mobility and zeta potential of Poly(A) determined using ELS (n=2, ± STD) and EAF4-UV, (n=3, ± STD).

		ELS		EAF4-UV		
Brand	**Buffer**	Electrophoretic Mobility (μmcm/Vs)	Zeta Potential (mV)	Electrophoretic Mobility (μmcm/Vs)	Electrophoretic Mobility R^2	Zeta Potential (mV)
Brand A	**1 × PBS pH 7.4**	-0.3 ± 0.2	-3.5 ± 2.4	-0.2 ± 0.1	0.9720	-2.4 ± 1.0
	Citrate pH 6	-0.4 ± 0.4	-5.5 ± 5.2	-0.2 ± 0.1	0.9853	-2.8 ± 1.0
Brand B	**1 × PBS pH 7.4**	-0.2 ± 0.2	-2.5 ± 2.6	-0.1 ± 0.0	0.9965	-1.1 ± 0.5
	Citrate pH 6	-0.7 ± 0.4	-9.4 ± 5.6	-0.1 ± 0.0	0.9876	-1.1 ± 0.5
Brand C	**1 × PBS pH 7.4**	-1.1 ± 0.4	-14.1 ± 5.3	-0.3 ± 0.0	0.9975	-3.7 ± 0.4
	Citrate pH 6	-1.0 ± 0.4	-12.2 ± 5.0	-0.3 ± 0.0	0.9992	-3.3 ± 0.3

All charge-related parameter data obtained from ELS and EAF4 consistently produced negative electrophoretic mobility and zeta potential values due to the inherent anionic profile of RNA.

Zetasizer ELS measurements highlight with increasing brand chain length, buffer-averaged electrophoretic mobility decreased to more negative values Brand A (-0.35 μmcm/Vs), Brand B (-0.45 μmcm/Vs) and Brand C (-1.05 μmcm/Vs) **(Table 4.4)**. calculated zeta potential also followed equivalent, buffer-averaged results with increased chain length Poly(A) producing more negative surface charges. Variation between individual buffers could reflect counterion diffusion and partial neutralisation of anionic phosphate backbone charges and differences in final solution ion concentrations from water dilution, with PBS samples producing approximately 10 mM sodium chloride concentration recommended for zeta potential analysis.(290,291) EAF4 analysis showed increased consistency between measured electrophoretic mobilities between buffers, showing high channel dilution and diluting out the impact of storage/manufacture buffer on measured measurements. The consistency is further reflected in zeta potential measurements which were derived from electrophoretic mobility calculations.

Our results in **Table 4.4** demonstrate that switching the buffer from PBS to citrate results in variations in the calculated zeta potentials vary in value. This trend is observed with brands A and B, whereas Brand C deviates by exhibiting a decrease in calculated zeta potential from PBS to citrate buffer. These changes could be due to Poly(A) conformational differences within citrate buffer with Brand C having the highest molecular weight species and estimated chain lengths of three tested Poly(A) vendors. Statistical analysis using a Tukey post-hoc test revealed no significant differences in calculated zeta potentials between PBS and citrate buffers for ELS and EAF4 systems apart, except for Brand B under ELS conditions, which showed a statistically significant change. Differences between manufacturer brands were less clear using EAF4 as Brands A and C produced similar electrophoretic mobility and zeta potential values, whereas brand B produced the lowest electrophoretic mobility and zeta potential values. EAF4-MD electrophoretic mobility data showed significant, linear correlation between 0.0 mA neutral, and +1.0 mA applied currents showcased by $R^2 > 0.97$ across all electrically separate Poly(A)s **(Table 4.4)**, highlighting a high data quality of fit, producing reliable electrophoretic mobility and zeta potential measurements for associated electrically separated Poly(A) samples. EAF4 data provided deeper insight into charge-based distribution profiles of branded samples, highlighting further manufacturer-based impact on Poly(A) CQAs.

4.4.2. Analytical Size Exclusion Chromatography (aSEC)

Analytical size exclusion chromatography (aSEC) was used as an orthogonal separation technique to further quantify branded manufacturer brand impact on Poly(A) critical quality attributes.

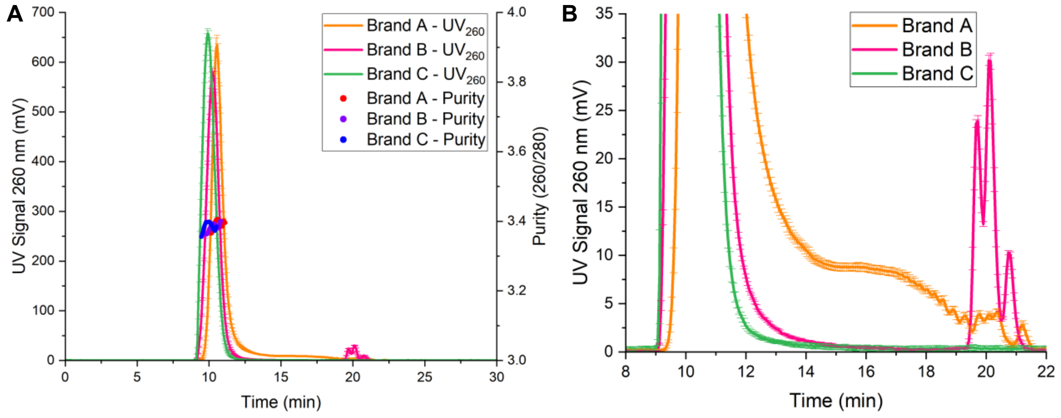

***Figure 4.3** – SEC-UV analysis of Branded Poly(A) drug substances A) 260 nm absorbance and purity (260/280 FWHM), B) focussed UV detector separation profiles, n=2 ± STD).*

Chromatogram profiles for aSEC-UV data highlight singular monomodal peaks across all Poly(A) brands analysed with Brand C producing the earlier retention time (9.9 min) followed by Brand B (10.3 min) and Brand A (10.6 min) **(Figure 4.3A)**. Smaller particle sizes and

Poly(A) molecular weights were observed with multimodal peaks for Brands A eluting between 14-22 min, and Brand B eluting between 19-22 min **(Figure 4.3B)**. UV traces signified that Brand A contains a larger MW and chain length distribution, followed by Brand B and Brand C characterised by monodispersed MW and chain lengths. aSEC-UV data further verifying EAF4-UV elution profiles. A key limitation of aSEC was reduced sample interaction with the stationary phase and AF2000 system pressure limit (15 bar), indicated by early elution within the first column volume (~25 minutes). Despite this, measurable size-based separation was still achieved. aSEC-MALS successfully detected Poly(A) samples at lower concentration than EAF4 direct injection, producing retention time trends consistent with UV profiles, confirming effective, albeit limited, separation

To further confirm EAF4 and aSEC results, capillary gel electrophoresis coupled with fluorescence was utilised to separate and quantify Poly(A) vendor specific chain length distributions and Poly(A) integrity. Associated results highlight RNA ladder distribution, Poly(A) branded samples and positive control eGFP mRNA separation (**Figure S 10.4**). CGE findings, additionally confirm overall high-level Poly(A) chain length and molecular weight polydispersity within each branded vendor. CGE results also demonstrate a low signal intensity for the Poly(A) in comparison to GFP positive control mRNA (**Figure S 10.4**). These findings are in agreement with A<B<C in terms of chain length and molecular weight distributions.

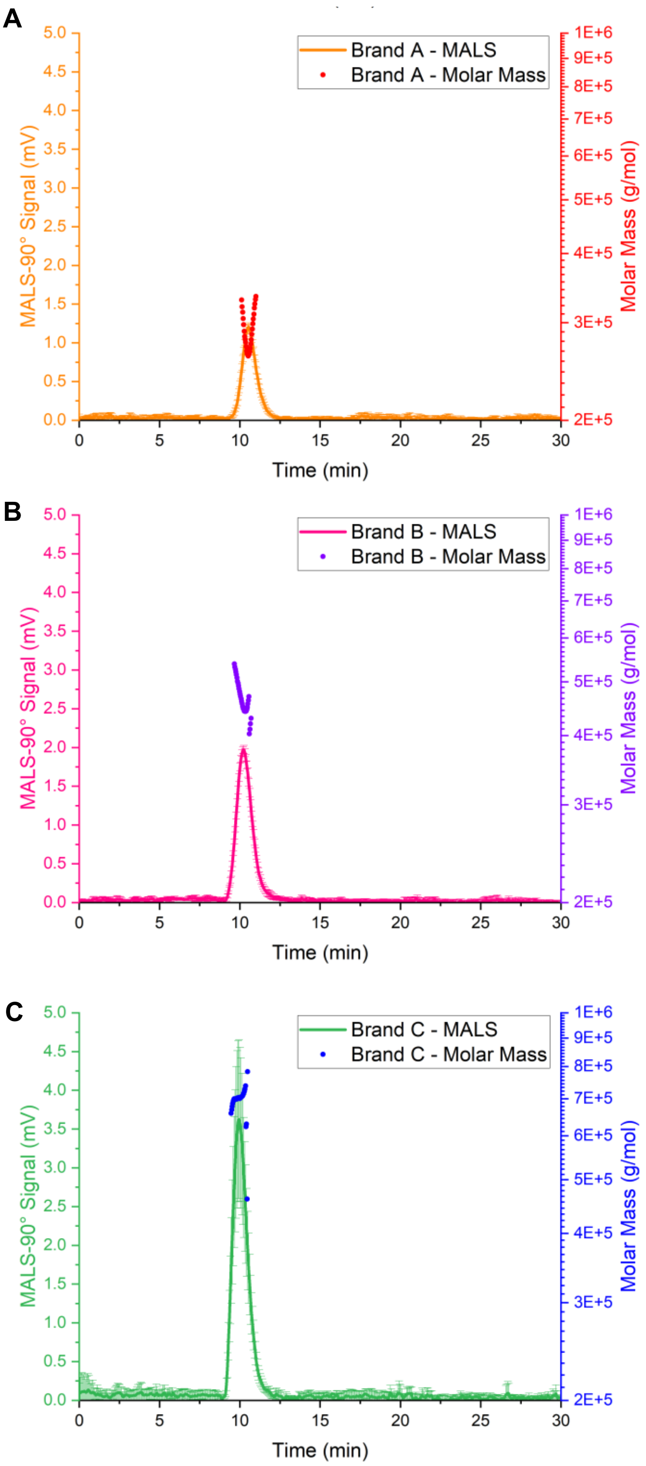

***Figure 4.4** - Corresponding aSEC-MALS traces of A) Brand A, B) Brand B, and C) Brand C Poly(A) (5 µg injection conc). (n=2 ± STD).*

Analysis of Poly(A) MW trends by aSEC-MALS confirmed findings from EAF4-MALS direct injection data, that Brand C produced the highest MALS-90° signal and estimated molar mass distribution species across the MALS-90° FWHM profile. An equivalent trend was observed with Brand B and Brand A, in descending order of MALS signal and molar mass distribution **(Figure 4.4)**. As aSEC-UV confirms high to low size-based separation, while unexpected fluctuations were noticed in the molar mass distributions of MALS-90° FWHM profiles are likely due to poor half-maximum peak signal intensity (< 1.25 mV), in tandem with lower flow rates, lower injection concentrations, and lower stationary phase interaction, than EAF4 separation and direct injection modes. Purity estimations (260/260) were 3-4, highlighting a similar high-quality Poly(A) sample, irrespective of the Poly(A) brand **(Figure 4.3A)**, confirming EAF4 values.

4.4.3. Impact of Poly(A) on Lipid Nanoparticle Critical Quality Attributes

To further quantify the impact of Poly(A) molecular weight species and polydispersity on LNP CQAs, each Poly(A) brand was encapsulated in an ionisable SM102 lipid nanoparticle (LNP) formulation.

Table 4.5 *– Branded Poly(A)-LNP drug product size attributes, measured by dynamic light scattering (DLS), electrophoretic light scattering (ELS), and RiboGreen^{TM} Assay for Poly(A) encapsulation efficiency (%EE) and mass balance recovery (% MB), (n=3 ± STD).*

	Zetasizer (DLS/ELS)				**RiboGreen^{TM} Assay**	
LNP	**Z-average (d.nm)**	**Distribution Size (nm)**	**PDI**	**Z-potential (mV)**	**% EE**	**% MB**
Brand A	65.7 ± 7.1	71.6 ± 7.5	0.12 ± 0.05	-3.1 ± 1.9	99.4 ± 0.8	82.3 ± 6.8
Brand B	65.9 ± 6.9	71.1 ± 7.5	0.12 ± 0.05	-3.8 ± 2.9	99.1 ± 1.0	97.7 ± 12.0
Brand C	68.5 ± 6.6	73.1 ± 7.2	0.13 ± 0.07	-3.4 ± 2.3	98.9 ± 1.3	97.0 ± 8.3

Initial CQA analyses highlighted similar z-average and size distributions between branded Poly(A) manufactured LNPs, with A-LNPs and B-LNPs producing the smallest z-average) and distribution-based sizes, whilst C-LNPs produced the largest z-average (68.5 nm) and distribution-based sizes (73.1 nm) **(Table 4.5)**. No significant differences were noted between LNP drug product DLS measured z-average and distributional sizes when comparing manufacturer branded Poly(A) drug substance despite distinct differences in Poly(A) manufacturer molecular weights. PDI, zeta potential and Poly(A) encapsulation efficiency data produced equivalent results, highlighting the consistency of using standardised formulation and purification processes **(Table 4.5)**. Poly(A) mass balance recovery results differed by 18 % across the formulations, with A-LNPs producing the lowest recovery at 82.3 % and B-LNP with 97.7 %.

To further explore the observed differences in Poly(A) LNP mass balance across brands, the RiboGreen™ assay was employed using calibration curves generated with each Poly(A) sample in assay buffer, alongside an rRNA standard, to assess both concentration accuracy and RNA integrity within the assay. All Poly(A) samples showed strong linear responses **(Figure S 10.5)** with high correlation coefficients ($R^2 > 0.98$) across both Triton X-100 and TE buffer conditions **(Table S 10.3)**, confirming assay compatibility. No significant differences in calibration linearity were observed between the Poly(A) drug substances within each buffer group, apart from the rRNA standard. While all Poly(A) brands produced consistent fluorescence profiles, differences in relative fluorescence intensities across equivalent concentration levels were identified **(Table S 10.4, Table S 10.5)**, with up to a 66% difference between Brands A and C, 33% between Brands B and C, and no significant difference between Brands A and B. These results confirm that Poly(A) is fully compatible with the RiboGreen™ assay for total and unencapsulated RNA quantification and suggest that observed mass balance discrepancies across LNP formulations likely stem from formulation-specific or structural factors, rather than incompatibility with the assay.

After investigating mass balance differences, Nanoparticle Tracking Analysis (NTA) was used to deepen our understanding of the size distribution profile of branded Poly(A) LNPs in higher resolution than DLS.

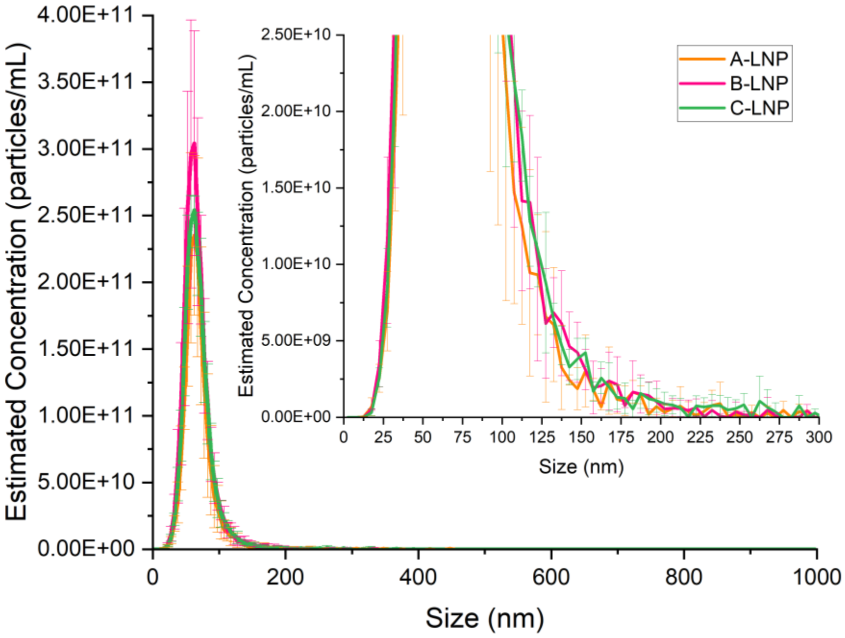

***Figure 4.5** - Nanoparticle Tracking Analysis particle size distribution profiles of Branded Poly(A)-LNP s using raw data exports, (n=3, ± STD).*

NTA demonstrated particle-by-particle tracking, highlighting key similarities between formulations alike DLS z-average and PDI values. Poly(A)-LNP formulations produced highly monodispersed particle size distribution profiles, characterised by a monomodal peak **(Figure**

4.5). Mean LNP sizes were highly similar at ~ 67 nm across all formulations, with corresponding mode sizes ~ 61 nm **(Table S 10.6)**. Formulation monodispersity was also confirmed through distributional span data, with each formulation producing similar values of 0.68 (A-LNP), 0.71 (B-LNP) and, 0.73 (C-LNP) **(Table S 10.6)**. With using spin column purification, equivalent estimated particle concentrations were achieved across all three LNP formulations (~2.6x10^{11} particles/mL) **(Table S 10.6)**.

Zetasizer and NTA data showed highly similar CQAs across the Poly(A) A-LNP, B-LNP and C-LNP formulations. Frit inlet asymmetric-flow field-flow fractionation was used to profile formulation characteristics, enabling size- and morphological evaluation.

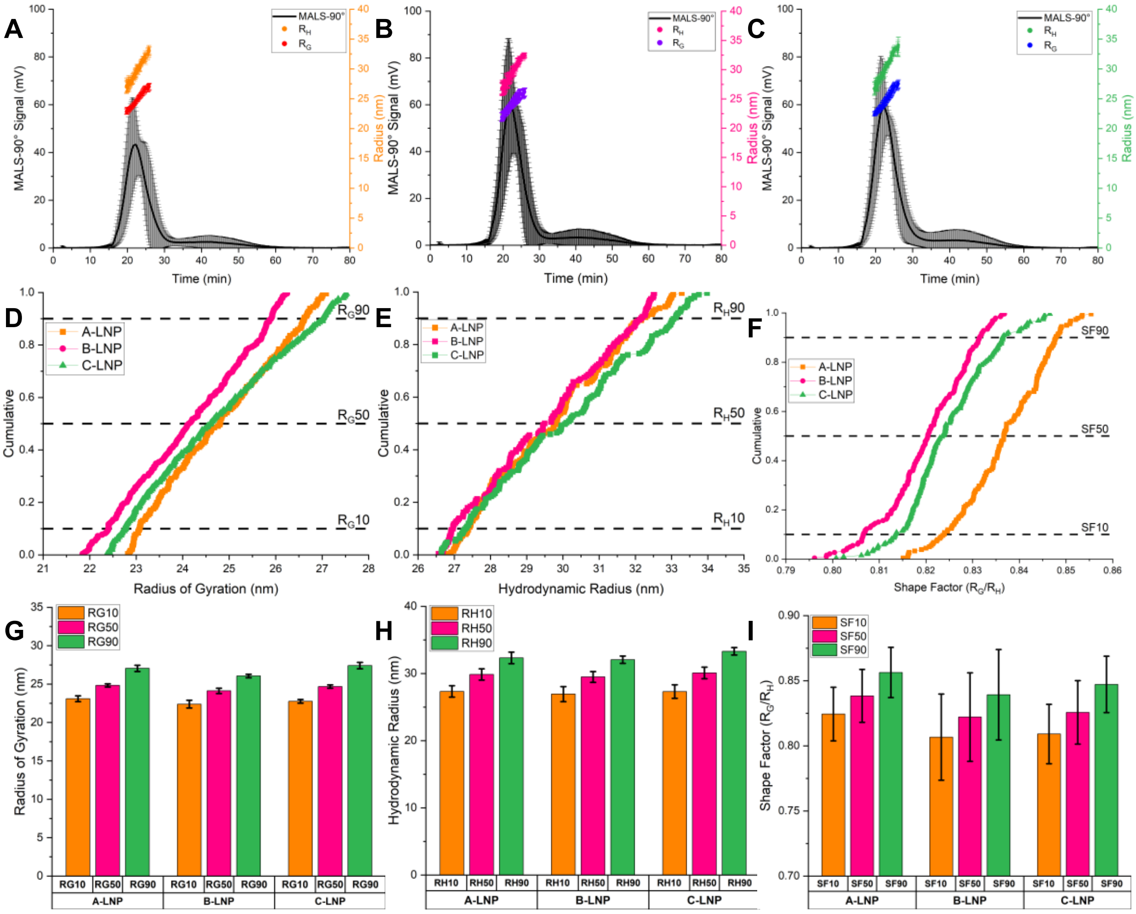

Figure 4.6 *- FI-AF4-MD of Poly(A) LNP formulations. MALS-90° elution profiles with FWHM integrated radius of gyration and hydrodynamic radii for A) A-LNPs, B) B-LNPs, and C) C-LNPs. (n=3 ± STD). Cumulative distributions for D) radius of gyration, E) hydrodynamic radius, and F) shape factor (n=3), with respective 10, 50 and 90 distributional values for G) radius of gyration, H) hydrodynamic radius, and I) shape factor for A-LNPs, B-LNPs and C-LNPs, (n=3 ± STD).*

Our previous developed LNP-based AF4 separation method(254) was used for LNP formulations, resulting in high percentage recoveries (>88 %) and high MALS 90° detector signals (> 40 mV**) (Figure 4.6, Table S 10.7)**. A and C-LNPs produced channel elution times 22.3 min, corresponding to a mode radius of gyration (R_G) sizes of 24.7 nm and 24.6 nm, respectively. B-LNPs eluted earlier at 21.9 min and produced mode R_G sizes of 24.2 nm (**Table S 10.7**). A-LNPs produced a MALS 90° signal of 43.3 mV, B-LNPs 60.0 mV and C-LNPs a signal intensity of 59.2 mV **(Figure 4.6)**. Separated LNPs **(Figure S 10.6)** have shown to contain Poly(A) drug through overlapping UV (260 nm) trace quantifying drug absorbance and MALS-90° trace analysing LNP scattering, highlighting drug loading. Cumulative distributional data (**Figure 4.6D-F**) highlights further formulation monodispersity through narrow ranges of radius of gyration (6 nm), hydrodynamic radius (7 nm) and shape factor (0.06). B-LNPs produced the smallest radius of gyration distributions, denoted by a left shift to a smaller size range **(Figure 4.6D)**, whereas A-LNP and C-LNP produced similar R_G size distribution, indicated by overlapping profiles **(Figure 4.6D)**. Hydrodynamic radii distribution **(Figure 4.6E)** showed similar sizes from R_H10-50 distributional values across three branded Poly(A) formulation types, from R_H50-90 R_H10-50 , brand C-LNPs produced larger sizes of LNPs, with a right shift towards a larger size range. Brand B and C-LNPs produced similar trending shape factor values across the FWHM distribution, whereas A-LNPs produced larger shape factor values across the 0.1-0.9 distribution **(Figure 4.6E)**. Nuanced differences between branded Poly(A)-LNP formulations cumulative distributional R_G, R_H and shape factor data were compared **(Figure 4.6F-I,Table S 10.7)** to evaluate distributional values between formulations. To further confirm AF4 shape factor morphologies, electron microscopy was used to image A, B and C-LNPs for further insights and comparisons.

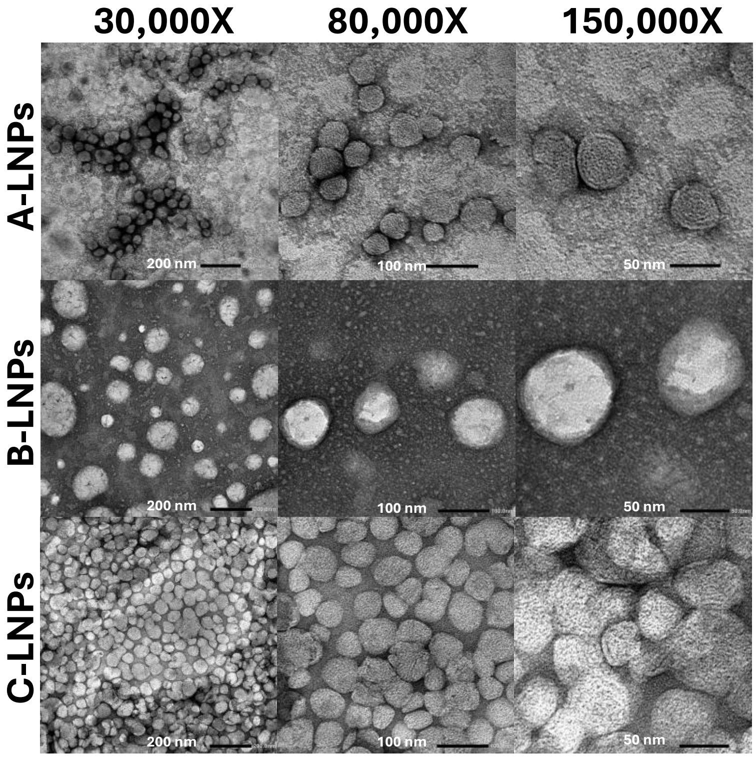

***Figure 4.7** – Negative stain transmission electron microscopy of Poly(A)-LNP batches with increasing magnification.10 µL of 1.25 mg/mL (formulation concentration) LNPs were imaged, A minimum of 30 particles were analysed to obtain circularity data. (n=1).*

Negative stain-TEM proved successful for imaging Poly(A)-LNPs, where each formulation highlighted deviation from spherical morphology. Circularity measurements for associated LNP formulations were 0.785 (A-LNPs), 0.785 (B-LNPs) and 0.779 (C-LNPs), respectively. With 1.0 equating spherical morphology, a 22% decrease was determined, departing from a complete spherical assumption. The shape factor derived from each LNP formulation directly aligns with the shape factor data determined for AF4, where 0.775 assumes a perfect sphere with average SF90 (**Table S 10.7)** of 0.847, producing an 9.3 % increase in shape factor from spherical towards elongated morphologies.

Collectively across LNP analytical pipelines, no significant differences in CQAs between A-C LNP formulations were found, highlighting that differences in branded Poly(A) chain length were not sufficiently large to produce significant differences in LNP CQAs. Correlation Between Poly(A) Drug Substance and Poly(A)-LNP CQAs Collective CQA outputs from branded Poly(A) drug substance and Poly(A)-LNP drug products were correlated to link drug substance with drug product, to further deepen our understanding of pharmaceutical development.

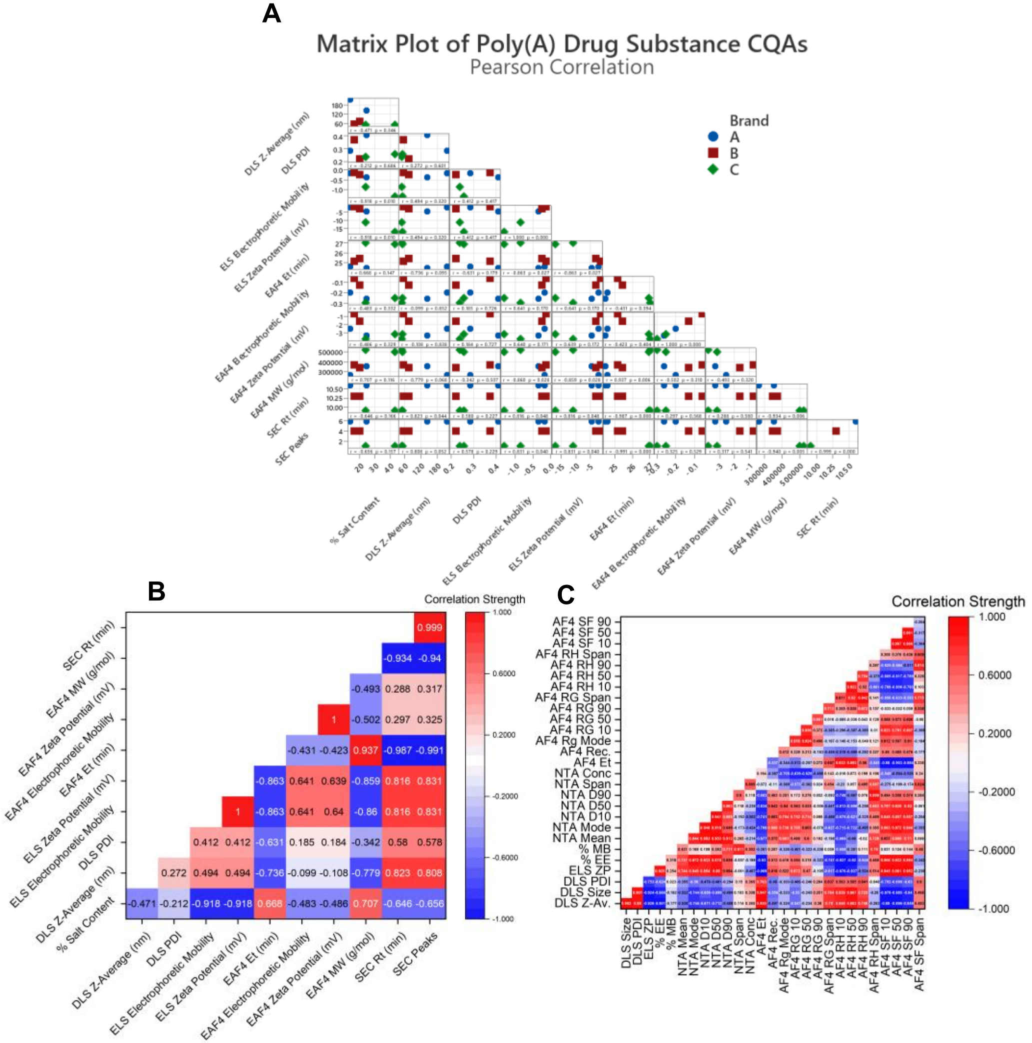

Figure 4.8 *- Correlation of Poly(A) CQAs from Drug Substance, and Drug Product. A) Matrix plot of drug substance CQAs with associated B) correlation strength heatmap, and C) LNP drug product correlation strength heatmap.*

On comparison of drug substance versus drug product matrices and correlation plots **(Figure 4.8),** the drug substance matrix shows tight groupings of branded Poly(A) CQAs, further highlighting differences in drug substances according to Poly(A) brand **(Figure 4.8A)**. Correlation strength drug substance plot further exemplified the relationship between analysed CQAs. Strong positive correlations (>0.6) include salt content and EAF4 elution time, SEC retention time, SEC peak number with ELS electrophoretic mobility and ELS zeta potential, EAF4 elution time and Poly(A) molecular weight **(Figure 4.8B)**. Strong negative correlations (>-0.6) include salt content and ELS electrophoretic mobility and ELS zeta potential, EAF4 elution time with DLS z-average, DLS PDI, and ELS electrophoretic mobility and ELS zeta potential, and DLS z-average and EAF4 molecular weight **(Figure 4.8B)**.

With no significant differences between LNP formulations determined, all LNP technique CQA outputs were combined in a correlation matrix to evaluate relationships between CQAs outputs and their strength **(Figure 4.8C).** CQA outputs were split into two plots with zetasizer, RiboGreen^{TM} and NTA CQA outputs in one plot with all FI-AF4-MD outputs in another plot. Trending tight grouping of drug substance did not translate to LNPs across all brands when analysing matrix plot due to high similarities between the branded Poly(A)-LNP formulations **(Figure S 10.7A)**.

No formulations produced high batch-to-batch consistency, indicative of tight grouping/clustering of replicates when comparing analytical CQA outputs from DLS, ELS, NTA and RiboGreen^{TM} assay **(Figure S 10.7A**). As a result, an increase in strong positive and strong negative correlations was seen between DLS, ELS, RiboGreen^{TM} and NTA CQAs. Strong positive correlations (> 0.6) were noted between DLS CQAs (z-average, size and PDI), NTA CQAs (Mean, Mode, D10, D50, D90), mass balance and NTA D90 and NTA span measurements **(Figure S 10.7B)**. Strong negative correlations (>-0.6) were observed between ELS Zeta potential and DLS CQAs (Z-average, size and PDI), Poly(A) % EE and DLS CQAs (Z-average, size and PDI **(Figure S 10.7B)**. Neither strong positive or negative correlations were noted between Poly(A) % MB and DLS, ELS, % EE, NTA CQAs (mean, mode, D10, D50, D90, conc).

Depper insights into size and morphology distributions were highlighted through matrix plot of AF4 CQAs **(Figure S 10.7C)**. Interestingly, even with no statistically significant differences between formulations, CQAs derived from AF4 measurements highlighted differences in correlation strengths between measured distributional outputs **(Figure S 10.7D)**. Strong positive correlations (> 0.6) were noted between 24.8 % of CQA outputs **(Figure S 10.7D)**. Strong negative correlations (>-0.6) were observed between 12.4 % of CQAs, including, AF4 elution time and shape factor distributions (SF10, SF50, SF90). 62.8 % of AF4 CQA outputs produced neither strong positive nor strong negative correlative relationships.

4.5. Discussion

Within the therapeutic nanomedicine landscape, interests in LNP-based delivery systems are only increasing, whilst the critical impact of active drug substance remain under-evaluated causing a gap in drug substance to drug product evaluative impact. In this study, three commercially available Poly(A)s were compared using combinatorial analytical pipelines and evaluated their impact within an LNP-based drug product system using established analytical pipelines, to bridge the gap and translate differences in nucleic acid drug substance attributes to LNP drug product.

Different biophysical techniques were used to characterise and evaluate potential differences between branded Poly(A) drug substances to assess their intrinsic critical quality attributes from associated salt content, quantification assay suitability, aggregation probability, size and size distribution through standardised techniques, novel surface charge separation and orthogonal chromatographic methodologies, to enable a larger overview of branded drug substances as a collective. Despite clear physicochemical differences between branded Poly(A) drug substances, LNP formulation mitigates these variabilities, producing consistent and comparable LNPs.

Previous studies(292–295) have shown that RNAs can form secondary and tertiary higher-order structures using complementary base-pair interactions. However, as Poly(A) exists as single-stranded RNA, other intermolecular forces, aside from classic base pairing interactions, play a crucial role in driving Poly(A) potential conformational and physiochemical changes under pre-formulation conditions relevant to drug delivery systems. Poly(A) structural conformation has previously been studied in-depth using various biophysical analytical techniques, using short chain Poly(A),(296,297) self-association,(298) and helical conformations,(299) with complementary Polyuridylic acid (Poly(U))(300) under various pH, temperature and ionic strength conditions.

The combinatorial approach in our study highlighted salt content, and concentration differences **(Figure S 10.1,Table S 10.1)**. DLS data highlighted poor scattering of Poly(A)s through high standard deviations between replicate samples across brands and manufacture buffers, indicating that DLS cannot be adopted as an analytical technique for drug substance analysis **(Figure S 10.2,Table S 10.2)**. Gelation noticed during DLS analysis was not highlighted through differences in diffusion coefficient with dilution in different buffers used during the manufacture of LNPs **(Figure S 10.3)**.

To our knowledge, this is the first report of applying EAF4 to the analysis of nucleic acid-based drug substance. Optimisation of the EAF4 separation resulted in recoveries in excess of 92%, highlighting excellent separation and detection ability using neutral and positive currents in addition to crossflow external separation force fields **(Table 4.1)**. Poly(A) samples exhibited enhanced separation with the application of a positive current within the EAF4 channel, highlighted through a shift in retention times, with smaller Poly(A) chain lengths eluting earlier, followed by larger chain lengths **(Figure 4.1)**. EAF4 data highlight that Brand A Poly(A) drug substance contained a higher dispersity of chain lengths in comparison to the monodispersed, intense, narrow peaks observed with Brand B and Brand C Poly(A)s **(Figure 4.1)**. Comparing Poly(A) samples diluted in citrate pH 6 and PBS, showed no significant differences in elution profiles **(Table 4.1)**. All Poly(A) brands tested produced high purity ratios comparing 260/280, with all brands producing values ~3.5 over an integrated FWHM elution peak, irrespective of the current applied within the channel **(Figure 4.1)**. Since EAF4 sample injection into the channel produced high dilution, MALS signals were not recovered from separated Poly(A) samples, however enhanced Poly(A) concentration (12.5 µg) direction injections were used to obtain MALS data per each branded manufacturer **(Figure 4.2, Table 4.2)** to evaluate and estimate molecular weight and sample molar mass distributions.

Aligning with separation data, direct injection data show that Poly(A) molecular weight increased between different Poly(A) brands, with Brand A having lower molecular weight and chain length Poly(A)s than Brand B and Brand C **(Table 4.3)**. Brand A produced the smallest MALS signal and thus produced a lower overall span/PDI values, whereas Brand B and Brand C Poly(A) produced higher MALS signals and trending with higher span/PDI values **(Table 4.2)**, following a converse trend from monodispersed EAF4 separation data. Shape factor (R_G/R_H) data was obtained, producing differing estimated morphologies for each brand with expected random coil (~1.5), differences could be caused by low inline DLS signals (< 50 kcps) **(Figure 4.2)**, so further investigation would be required for morphological differences between branded Poly(A)s as a drug substance.

With the novel use of EAF4, Poly(A) electrophoretic mobility and zeta potential can be calculated from the use of neutral and positive currents applied to the separation channel and compared to conventional batch-mode offline ELS zetasizer electrophoretic mobility and zeta potential evaluations (**Table 4.4**). Our results reaffirm successful separation with calculated inherent anionic zeta potential of the Poly(A) branded samples, from superior quality electrophoretic mobility results ($R^2 > 0.97$). Differences between zetasizer ELS electrophoretic mobility and zeta potential **(Table 4.4)** could be due to dilution factors within the channel and contribution of Poly(A) sample buffer to zetasizer ELS measurements from potential higher concentration samples.

To further confirm EAF4 data , aSEC-UV-MALS was used as an orthogonal separation technique to evaluate Poly(A) molecular weight species and estimated chain length distributions **(Figure 4.3, Figure 4.4)**. Chromatogram traces from aSEC-UV produced high purity ratios, aligning with EAF4-UV fractogram traces, confirming EAF4-UV molecular weight and chain length differences between the different Poly(A) drug substance brands, with Brand C eluting earlier, followed by Brand B and then Brand A, highlighting the expected opposing order from EAF4-UV results **(Figure 4.3).** With aSEC-UV data producing enhanced detector signals, differences in size distributions were noted with Brand A containing higher levels of smaller molecular weight species, followed by Brand B and Brand C containing a single peak distribution **(Figure 4.3).** Additionally, CGE was utilised to further verify the use of AF4 as a novel analytical methodology for profiling molecular weight distribution. Our CGE results are in agreement with previous EAF4 and aSEC results, with high polydispersity observed across all vendors, with increasing chain lengths (A<B<C), (**Figure S 10.4**). These results demonstrate vendor specific Poly(A) distributions across each tested brand.

With differences noted in branded Poly(A) drug substance molecular weights and associated chain length distributions, fundamental impact within a lipid nanoparticle delivery system as a collective drug product was evaluated. Standardised ionisable formulations of SM102: CHOL: DSPC: DMG-PEG2K were used to encapsulate branded Poly(A)s during microfluidic formulation, and downstream purification and buffer exchange was achieved using centrifugal spin columns and 1 × PBS pH 7.4 buffer. Established LNP analytical pipelines were utilised for evaluation of A-LNP, B-LNP and C-LNP formulations, including zetasizer DLS/ELS, RiboGreen^{TM}, NTA and FI-AF4-MD techniques.

Initial DLS size and PDI results indicate highly monodisperse LNP formulations (PDI < 0.2) of similar z-average and size distributions (60-70 nm). Further drug product similarities were noted with zeta potential (-3.5 mV), % EE (> 98%) and % MB (>80%) with no statistically significant differences between A-LNPs, B-LNPs and C-LNPs **(Table 4.5)**. Using 100 kDa MWCO spin columns during formulation could selectively remove smaller LNP populations, resulting in comparable size distributions across drug products. This impact would be most evident in A-LNPs, formulated with Brand A Poly(A), which exhibited a smaller chain length, but broader molecular weight range. The presence of smaller LNPs formed from lower molecular weight species would be filtered out during centrifugation, resulting in a higher z-average, reduced PDI, and lower overall Poly(A) recovery in mass balance calculations compared to the more monodisperse B-LNPs and C-LNPs derived from Brands B and C. Further RiboGreen^{TM} assay analysis highlighted despite branded manufacturer, all Poly(A)s behaved similarly within the assay, proving compatibility and retained integrity **(Figure S 10.5, Table S 10.3)**.Concentration levels within assay calibration curves showed significant differences between brands however, independent replicates produced small standard deviation between measurements, highlighting narrow data range and cause for significant differences.

NTA as a single particle tracking approach was used to profile the impact of Poly(A) input materials on LNP formulations, relating particle Brownian motion to size using the Stokes-Einstein equation. NTA size distribution profiles exhibited no statistically significant differences between branded Poly(A) drug product LNP formulations **(Figure 4.5, Table S 10.6)** further emphasising the enhanced reproducibility of formulation and purification processes within the model LNP formulation utilised. Although NTA remains a high-resolution technique compared to conventional DLS as an ensemble method, NTA does not incorporate separation of samples, which was addressed in this study by using FI-AF4 methodology coupled with inline UV-MALS-DLS.

Outputs from AF4, including R_G, R_H and shape factor morphology data were used to further profile A-LNP, B-LNP and C-LNP formulations **(Figure 4.6, Table S 10.7, Figure S 10.6).** Previous similarity trends between formulations were also realised using AF4 separation and detection methodology, with no statistically significant difference between branded Poly(A) formulations. Although no statistically significant differences were noted, nuanced differences were determined when comparing formulation cumulative distribution R_G, R_H and shape factor values **(Figure 4.6,Table S 10.7)**. Where lower MALS distributional and R_G span values were evaluated being B-LNPs, with higher R_G90 sizes producer by C-LNPs with an accompanying higher R_G span **(Table S 10.7)**. DLS R_H sizes produced an equivalent trend aligning with MALS data that B-LNPs produced lower R_H **(Table S 10.7)**Shape factor distributions also followed similar trends with lowest values produced by B-LNPs. However increased shape factor distribution values were produced from A-LNPs, while shape factor span was highest for C-LNPs **(Table S 10.7).** AF4 shape factor morphology was confirmed by analysis of LNP negative stain-TEM micrographs, where circularity was analysed to cross-compare orthogonal techniques (**Figure 4.7**). AF4 highlighted at 9.3 % deviation and TEM demonstrated at 21.7 % deviation from spherical towards elongated LNP morphologies showing spherical to oval particle shapes.

Critical quality attributes remain key descriptors of biophysical characteristics of advanced therapeutics and novel nanomedicine quality. CQAs can be further utilised within matrix grouping and correlation analysis to further enhance our knowledge of analytics. This enables a pivot towards deep analytical networking and application of artificial intelligence and machine learning algorithms to process these correlative outcomes and provide improved therapeutics to boost therapeutic translatability. Here, drug substance CQA outputs **(Figure 4.8A-B)** and drug product CQAs outputs **(Figure 4.8C, Figure S 10.7A-D**) were correlated, to gain deeper insight into how manufacturer-specific attributes influence both Poly(A) input material and resultant LNP formulations. Poly(A) drug substance matrix showed tight groupings due to differences in molecular weight and chain length distributions, when encapsulated into a LNP drug product. These differences were reduced, and drug product formulations produced no significance differences between LNP formulations, highlighting robust formulation, and purification methods. While Pearson's correlations were used to assess relationships between CQA outputs, the number of experimental replicates requires interpretations to be made with caution. These correlations offer preliminary insights and further confirmation of relationships would require additional experimental replicate testing to enhance the statistical power and robustness. When analysing LNP drug product correlation plot **(Figure S 10.7)**, zeta potential plays a key role in colloidal stability through the DLVO theory.(292–294) Using the correlation plot, LNP zeta potential displayed strong negative correlations with DLS z-average, distribution size, PDI, AF4 elution time and R_G span. Highlighting that as these CQAs increase in value, zeta potential decreases **(Figure S 10.7)**, which overall emphasises the fundamental impact of zeta potential on overall formulation CQAs and technique analytical outputs. Other fundamental relationships can be viewed with size and size distributions of drug products comparing DLS z-average, DLS size, DLS PDI, NTA Mean, NTA mode, NTA distributions (10, 50, 90, span), AF4 R_G mean and $R_{G,}$ R_H, and shape factor distributions (10, 50, 90, span). These results and correlations should be interpreted within the context of the specific Poly(A) brands and SM102 LNP formulation conditions used in this study, with further work being a requirement to test lipid:RNA ratios, main ionisable lipid changes, lipid molar ratio changes, storage buffer changes, drug substance sourcing and sequence specificity.

4.6. Conclusion

Using a combinatorial analytical pipeline, clear differences in different Poly(A) brands were demonstrated. Brand A exhibited lower molecular weights with broader molar mass distributions, while Brand B showed intermediate properties, and Brand C presented the highest molecular weights with a narrower, monodisperse distribution. Despite these distinctions at the drug substance level, no statistically significant differences were observed across LNP drug products in terms of key CQAs, indicating limited impact of Poly(A) molecular weight variability on overall LNP formulation performance. To further explore potential internal LNP structural features, advanced techniques such as electron microscopy, small-angle X-ray scattering, or calorimetry could offer deeper resolution into Poly(A) packing within LNPs. Importantly, correlated CQA outputs from Poly(A) drug substance analyses revealed consistent manufacturer-specific grouping across orthogonal methods, reinforcing the need for more analytics within drug substance development. In contrast, LNP drug product CQAs yielded a broader correlation network, highlighting the value of integrating both routine and high-resolution analytics to deepen understanding of how drug substance characteristics influence final drug product profile.

Chapter 5

Received: 13 June 2024 / Revised: 22 July 2024 / Accepted: 19 August 2024 / Published: 6 September 2024, *Nano Futures*, **8,** 035001, https://doi.org/10.1088/2399-1984/ad70e6

5. The Use of Orthogonal Analytical Approaches to Profile Lipid Nanoparticle Physicochemical Attributes

Callum G. Davidson[1], Rand Abdulrahman[1], Panida Punnabhum[1], Michael Cairns[1], Nicholas J W Rattray[1], Robin Capomaccio[2], Kevin Treacher[2], Yvonne Perrie[1], Zahra Rattray[1*]
[1]Strathclyde Institute of Pharmacy and Biomedical Sciences, University of Strathclyde, Glasgow, UK
[2]New Modalities and Parenterals Development, Pharmaceutical Technology & Development, Operations, AstraZeneca, Macclesfield, UK
*corresponding author: zahra.rattray@strath.ac.uk

This chapter includes the full text of the published article in Nano Futures including the introduction, methods, results and conclusions. For this work I primarily designed and carried out all experiments. Analyses, data visualisation and manuscript drafting was performed by the author of this thesis.

5.1. Introduction

Lipid nanoparticles (LNPs) as nanocarriers for the delivery of oligonucleotide-based therapeutics have sparked a profound change in the industry sector, owing to their success in delivering vaccines during the COVID-19 pandemic. The successful global implementation of lipid nanoparticles has seen a rapid growth in their implementation as platform nanocarriers for the delivery of cargo in a range of therapy areas of unmet clinical need. Alterations in lipid nanoparticle constituent lipid ratios and their implementation as platform formulations has led to the discovery of a broad spectrum of prospective nanomedicine candidates in pharmaceutical industry pipelines, increasing the popularity of lipid nanoparticles, and their versatility and applicability to a diverse oligonucleotide molecular portfolio(103,146,301–303).

The successful clinical and commercial translation of lipid nanoparticles for oligonucleotide delivery hinges upon acceptable formulation physicochemical stability of the nanocarrier during its shelf life, and the ability to protect oligonucleotide cargo from premature degradation. Highlighted by recent reviews (304,305), there is a critical need for developing orthogonal analytical pipelines to profile prototype LNP physicochemical attributes during early formulation development stages. Once manufactured, the LNP formulation critical quality attributes (CQAs) are quantified through more-established analytical techniques, such as dynamic light scattering (DLS: size and polydispersity), electrophoretic light scattering (ELS: zeta potential) and RiboGreen™ Assay (drug encapsulation efficiency and recovery) (81,306,307).

Due to significant research interest and field novelty, testing of prototype LNP candidates remains on a case-by-case basis. Continuing the process to harmonise the measurement of LNP physicochemical attributes, the Nanotechnology Characterisation Laboratory (NCL) and European NCL have issued guidelines for the analysis of prototype nanoparticulate formulations(290,308,309), recommending the use of at least one low-resolution technique and an orthogonal high-resolution technique for the measurement of nanoparticle size, ensuring that robust and representative results are obtained while standardised reference materials are under development. LNPs are composed of five main excipients, i) the oligonucleotide active pharmaceutical ingredient (API)(47,48), ii) ionisable/cationic main lipid(82,85,88), iii) sterol(82,85,88), iv) helper phospholipid (22,83), and v) polyethylene glycol functionalised lipid(90–92).

Orthogonal analytical techniques measure equivalent CQAs via differing physical principles. Since LNP research has seen an exponential growth in size, the routine implementation of novel analytical pipelines has not kept pace with advancements in LNP formulation.

To deepen our understanding of manufacture process and input material impacts on LNP CQAs and stability profile, techniques currently used within the field were selected, in combination with orthogonal higher resolution techniques that are currently not adopted into routine analytical testing of LNP CQAs, and correlate and cross-validate results between orthogonal techniques. In this study, the use of an analytical pipeline for measuring LNP stability is reported using a range of physical techniques spanning the low- to high-resolution analytical space(290) (**Figure 5.1**).

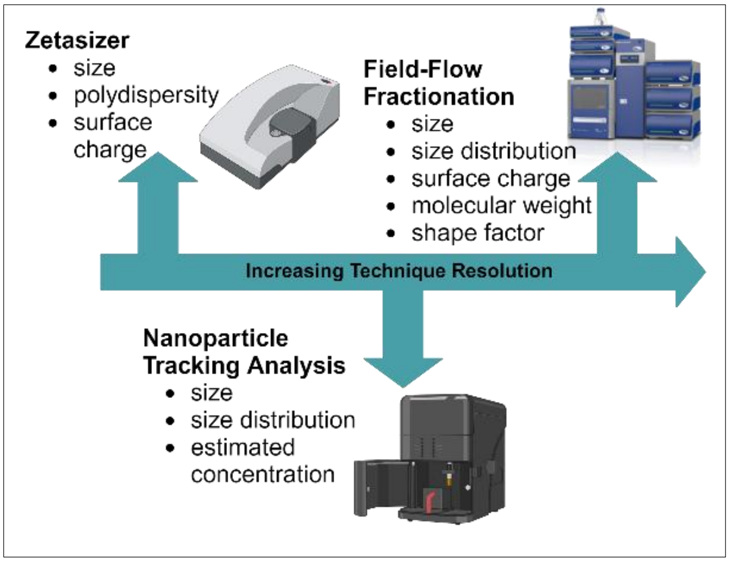

Figure 5.1 *– Analytical techniques used in this study for the characterisation of lipid nanoparticles in order of increasing resolution, annotated with respective critical quality attributes.*

Trends in current LNP literature demonstrate a decreased adoption of high-resolution analytical techniques in the routine testing of novel LNPs. DLS remains the most used technique **(Figure 5.1)** for measuring size and polydispersity, with DLS being cited as a gold-standard technique in particle size, size distribution and surface charge determination. However, Nanoparticle Tracking Analysis (NTA) has emerged as a higher-resolution particle sizing technique in recent years, where particle size and size distributions are determined on a particle-particle basis in contrast to the bulk light scattering properties of DLS. NTA tracks the movement of particles over a set frame distance to correlate movement velocity with size, and thus size distribution. NTA can also determine the estimated concentration of particles in an LNP formulation. Previous work within the field using a complex nanocarrier system has correlated LNP CQAs with DLS and NTA techniques main ionisable/cationic lipid(147).

Increasing in measurement resolution beyond DLS and NTA, is asymmetric Flow Field-Flow Fractionation (AF4), which gently separates complex and labile nanoparticles and downstream detection of the resolved fractions is achieved using a hyphenated inline multidetector (MD) system. These detectors include and are not limited to, UV/Vis spectroscopy, Multi-Angle Light Scattering (MALS), DLS, fluorescence, and refractive index. Combining different detectors and field flow fractionation (FFF) modalities (e.g., AF4, electrical AF4, centrifugal FFF), the LNP particle size, size distribution, surface charge, molecular weight and shape factor can be determined simultaneously during a single measurement run. Fractions generated during LNP fractionation can also be collected according to eluted fractions for further offline analysis with additional analytical techniques (e.g., liquid chromatography mass spectrometry).

The techniques discussed here have been used in several studies to characterise complex nanocarriers (184,310–313) including specialist LNP systems(133,309,314,315), however to deepen our understanding of CQAs, simpler systems must be used and evaluated through the full manufacture pipeline from microfluidic, to purification and, filtration, refrigerated and frozen (-80 °C) storage conditions. -80 °C frozen storage temperature was selected as Pfizer/BioNTech COVID-19 vaccine was stored at -80 °C, and lowest commercial freezer temperature prior to liquid nitrogen storage. Final product storage conditions must be incorporated into early development LNP testing to ensure storage suitability. Frozen storage at ultra-low conditions poses supply chain problems with transport of LNPs noted during mass immunisation against COVID-19.

This work highlights the need for high resolution techniques to profile LNP candidate physicochemical properties during early nanomedicine development to facilitate translation using model oligonucleotide lipid nanoparticles. 1,2-dioleoyl-3-trimethylammonium-propane chloride salt (DOTAP), was used as the main ionisable lipid within the formulation due to its permeant cationic charge and Poly(A) as a model mRNA oligonucleotide as the complexed drug encapsulated within the LNP formulation. Both components have been widely used within the field, however a cross-comparison of techniques has not been attempted to the best of our knowledge using our microfluidics-based manufacture, downstream processes, and MD-AF4 setup.

5.2. Materials

1,2-dioleoyl-3-trimethylammonium-propane chloride salt (DOTAP), 1,2-distearoyl-sn-glycero-3-phosphocholine (DSPC) and 1,2-dimyristoyl-rac-glycero-3-methoxypolyethylene glycol-2000 (DMG-PEG2000) were purchased from Avanti Polar Lipids (Alabaster, USA). Cholesterol (CHOL),cellulose dialysis membrane (MWCO 14 kDa), and Poly(A) were purchased from Sigma Aldrich (Merck, Poole, UK). Polyethersulfone (PES) 0.2 µm Acrodisc® filters were purchased from Pall Corporation. DNA/RNA free water, ethanol, 10X phosphate-buffered saline (PBS) pH 7.4, polyvinylidene difluoride (PVDF) 0.22 µm filters, Quant-iT™ RiboGreen™ RNA Assay Quantitation Kit (R4110), sodium citrate dihydrate were acquired from ThermoFisher (Fisher Scientific, Leicestershire, UK). All solvents and other chemicals used were of analytical grade, and milliQ-water (18.2 Ω cm^{-1}) was provided by an in-house system.

5.3. Methods

5.3.1. Manufacture of Poly(A)-DOTAP-LNPs

LNPs were formulated on the NanoAssemblr® IgniteTM Platform (Precision Nanosystems Inc, Vancouver, BC, Canada.) in a torroidal micromixer single-use cartridges (Ref: NIN0002). The system channel was 300 µm wide with a height of 130 µm [33]. The lipid nanoparticle prototype was composed of DOTAP:CHOL:DSPC:DMG-PEG2000. All initial lipid stock solutions were prepared in ethanol at 5 mg/mL and combined at a 50:38.5:10:1.5 molar ratio for cationic lipid:cholesterol:helper:PEG-lipid, respectively based on Onpattro®, and Comirnaty® formulations (23). Poly(A) was prepared in DNAse/RNAse free water at 1.5 mg/mL and diluted in citrate buffer pH 6 (50 mM), which used as the aqueous phase. Lipid organic phase and Poly(A) aqueous phases were injected simultaneously into the micromixer at a 3:1 aqueous:organic flow rate ratio (FRR), 15 mL/min total flow rate (TFR) with an NP ratio of 6:1. The final lipid theoretical concentration after microfluidic preparation was 1.25 mg/mL, with a corresponding theoretical Poly(A) concentration of 0.055 mg/mL. Newly formulated Poly(A) DOTAP-LNPs were dialysed against filtered 1 × PBS (pH 7.4) (X200 dialysate ratio) to remove residual ethanol/citrate buffer. Dialysis was performed using cellulose dialysis membrane (MWCO 14 kDa) at ambient temperature for one hour under magnetic stirring using an established method(81).

Table 5.1 *- DOTAP-LNP Formualtion parameters.*

Process	**Description**
Manufacture	• Toroidal Microfluidics Chip • 5 mg/mL DOTAP:CHOL:DSPC:DMG-PEG$_{2K}$ • 50:38.5:10:1.5 mol% respectively in ethanol. • Poly(A) 1.5 mg/mL in water, diluted in 50 mM citrate (pH6) • FRR 3:1, TFR 15 mL/min
Purification	1 mL to 200 mL (1X) PBS pH 7.4 dialysis for 1 hr at ambient temperature. 5, 10, 20 % w/v sucrose was added to PBS as a cryoprotectant for F/T stability study using equivalent dialysate ratio, duration and temperature.
Storage	Refrigerated (4 °C) stability and - 80°C for frozen storage stability.

5.3.2. Stability Testing of Prototype LNPs

5.3.2.1. Process Parameter testing of LNPs

LNPs were tested at various stages throughout the manufacture process pipeline, including post-microfluidics manufacture, post-dialysis purification, and post-filtration (PES and PVDF filtration).

5.3.2.2. Stability Testing of Refrigerated LNP Formulations

LNP aliquots were stored at 4 °C from day of manufacture (day 0) to one month (day 28), with testing timepoints at day 0, 1, 2, 3, 4, 7, 10, 14, 21 and day 28.

5.3.2.3. Stability Testing of LNP Formulation at Ultra Low Temperature (-80 °C)

LNPs were manufactured and buffer-exchanged via dialysis into a frozen storage buffer containing various sucrose concentrations for use as a cryoprotectant. Sucrose was added at 0 % (PBS control), 5 %, 10 % and 20 % (w/v) concentrations to the dialysis buffer (phosphate-buffered saline). All LNP samples were analysed on the day of manufacture (day zero) and following 1 x freeze/thaw (F/T) cycle from -80 °C (18 hr frozen storage) to ambient temperature.

5.3.3. Characterisation of LNP Formulations

5.3.3.1. Dynamic Light Scattering (DLS)

Particle size (Z-average) and polydispersity index (PDI) were measured by dynamic light scattering (DLS) using a Zetasizer Nano ZS system (Malvern Panalytical, Worcestershire, UK) equipped with a 633 nm Helium-Neon laser and a detection angle of 173° (non-invasive back scattering). Unless otherwise stated, all measurements were performed at 25 °C and at a 1:10 dilution in PBS (pH 7.4) for all LNP samples, to achieve a final theoretical lipid concentration of 125 µg/mL (corresponding theoretical Poly(A) concentration- 5.50 µg/mL). All measurements were performed in three independent replicate measurements consisting of at least two technical replicates.

5.3.3.2. Electrophoretic Light Scattering (ELS)

LNP ζ-potential surface charge was measured using ELS post manufacture/process test. Unless otherwise stated, all measurements were performed at 25 °C and at a 1:10 dilution in DNA/RNA free water established in (81) for all LNP samples, to produce a final lipid theoretical concentration of 125 µg/mL (corresponding theoretical Poly(A) concentration- 5.50 µg/mL). All ζ-potential measurements were performed using three independent replicate measurements consisting of at least two technical replicates.

5.3.3.3. Nanoparticle Tracking Analysis

Particle size, particle size distribution and estimated concentration were measured by nanoparticle tracking analysis (NTA) using a NanoSight NS300 system (Malvern, Worcestershire, UK), equipped with a low volume flow cell, a 488 nm laser, an automated syringe driver, and a sCMOS camera. All samples were diluted in PBS (pH 7.4) prior to analysis with NTA, dilutions are noted in **Table S 11.1**, dilutions vary due to LNP recovery post-dialysis and experimental testing.

All measurements were performed at 25 °C and injected onto the flow cell using a syringe driver set at an infusion rate of 50. Corresponding NTA data acquisition parameters were five replicate videos of 60 seconds duration, and a camera level of 15. All data were analysed in the NTA 3.4 Build 3.4.003 program with a detection threshold set to five. Three independent replicate measurements consisted of five technical replicates each were performed for each sample.

5.3.3.4. Frit-Inlet Asymmetric Flow Field-Flow Fractionation

An AF2000 asymmetric-flow Field-flow fractionation (AF4) module (PostNova Analytics, Germany) hyphenated with multiple inline detectors (MD) multiangle light scattering (MALS-PN3621, PostNova Analytics), UV detector (PN3242, 280 nm- PostNova Analytics) and DLS Zetasizer Nano ZS system (Malvern Panalytical, Worcestershire, UK) was used to perform the separation and inline analysis of model LNPs. A frit-inlet (FI) channel, with a channel spacer thickness of 350 µm, and a 10 kDa molecular weight cut-off (MWCO) size amphiphilic regenerated cellulose membrane was used, with a 100 µL sample injection loop, and an injection volume of 20 µL. PBS (pH7.4) was used as the eluent buffer, and a corresponding injection flow rate of 0.2 mL/min, crossflow rate of 0.75 mL/min (exponential power decay 0.2), and a detector flow rate of 0.3 mL/min were used as the elution conditions. The channel membrane was conditioned with triplicate injections of BSA (5 mg/mL) and five injections of fresh LNPs (0.5 mg/mL). Each LNP sample was injected in technical replicates of four (0.5 mg/mL). LNP recovery (% Rec) was calculated by integrating UV area under curve (AUC) from direct injection (cross-flow = 0 mL/min) and cross-flow applied (0.75 mL/min) area under UV curve, using **Equation 5.1**.

$$\% \, Recovery = \frac{AUC_{cross-flow\ separation}}{AUC_{direct\ injection}} * 100$$

Equation 5.1 *– Calculation determining recovery of LNPs using UV integrated AUC from LNP direct injection and cross-flow applied separation profile.*

Data were analysed in the Nova FFF software version 2.2.0.1 (PostNova Analytics, Landsberg, Germany) using the MALS spherical model for fresh day 0 LNPs and random coil for stress-induced freeze/thaw LNPs.

5.3.3.5. Quantification of Encapsulation Efficiency (EE) and Mass Balance (MB)

The encapsulation efficiency (EE – **Equation 5.2**) and drug recovery (mass balance, MB – **Equation 5.3**) of the Poly(A) cargo during LNP formulation was measured using the Quant-iT™ RiboGreen™ RNA Quantitation assay Kit (Thermo Fisher #4110) and used as per manufacturer's instructions. The kit quantifies the total RNA and unentrapped RNA on the outside of the LNP to calculate the efficiency of drug encapsulation during formulation. The assay also determines recovery by comparing total RNA of the formulation to a theoretical RNA concentration.

$$\%\,EE = \frac{Total_{drug} - Free_{drug}}{Total_{drug}} * 100$$

***Equation 5.2** – Calculation determining encapsulation efficiency (drug loading) of encapsulated RNA drug.*

$$\%\,MB = \frac{Total_{drug}}{Theoretical\ Cocnentration\ of\ Drug} * 100$$

***Equation 5.3** – Calculation determining mass balance (drug recovery) of encapsulated RNA drug.*

Corresponding fluorescence intensity of the RiboGreen™ signal was measured on the GloMax® Explorer GM3500 microplate reader (Promega, UK) at an excitation wavelength of 475 nm, with the emitted fluorescence measured 500-550 nm. All fluorescence data were captured at ambient temperature (25 °C) using GloMax® firmware version 4.29.0 and processed using GloMax® Fluorescence software version 3.1.0.

5.3.4. Statistical Analysis

The corresponding mean ± standard deviation (SD) was calculated for all experiments with a minimum of two independent and two technical replicates, unless otherwise stated. A one-way Analysis of Variance (ANOVA) was performed to compare and highlight the impact of process parameters and stability on prototype LNP formulations. Statistical analyses were performed using Minitab® version 20.4 software. Data were graphed using OriginPro version 9.9.0.220. Unless otherwise specified, no significant difference was noted between evaluated conditions, where $^{*}p < 0.05$, $^{**}p < 0.005$, $^{***}p < 0.0005$.

5.4. Results

5.4.1. Process Parameter Impact on Formulation CQAs

Firstly, the influence of key LNP manufacture process parameters on measured attributes from samples collected during the initial microfluidics manufacture, formulation purification, and sterile filtration using two common filtration membranes, PES and PVDF was investigated. Samples collected from each process step were characterised using pipeline assays developed and standardised in our labs consisting of Zetasizer, NTA and RiboGreen$^{\text{TM}}$.

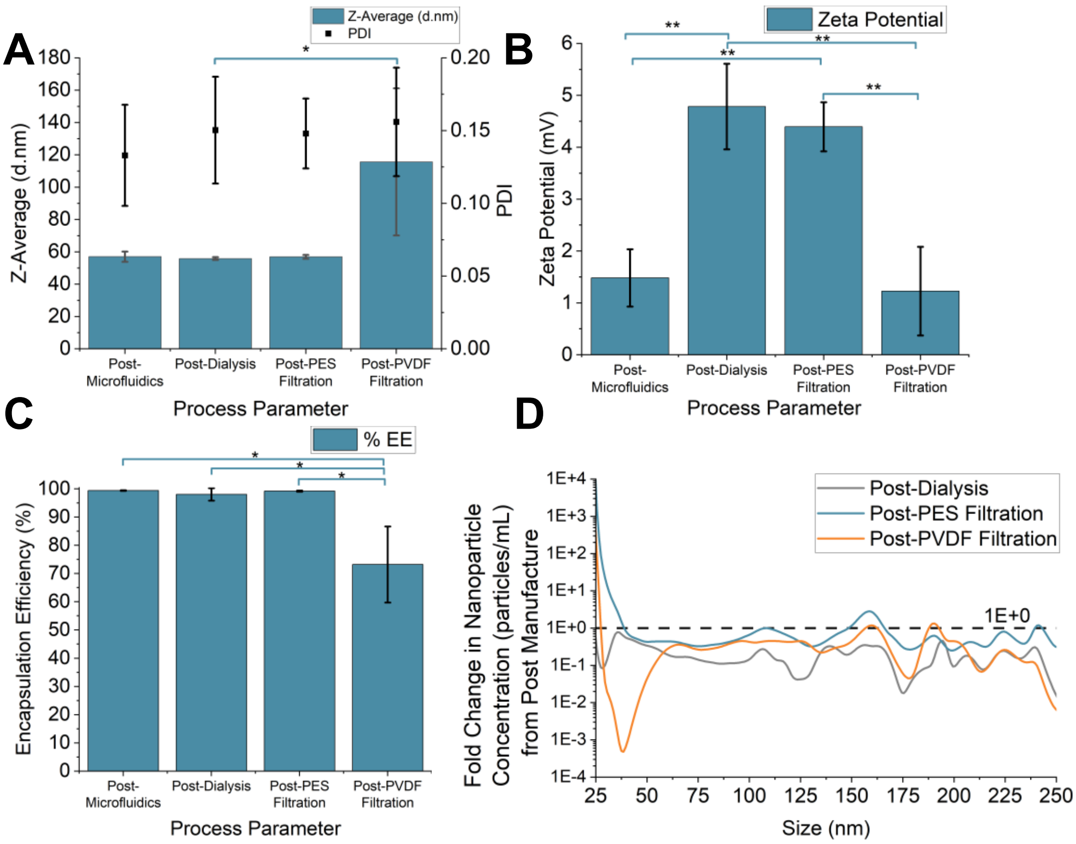

Figure 5.2 *- Physicochemical trend analysis of process parameter impact on Poly(A)-DOTAP-LNPs using A) (5.50 µg/mL Poly(A)) DLS to measure size and polydispersity index (PDI), B) (5.50 µg/mL Poly(A)) ELS for measurement of zeta potential, C) (0.75 µg/mL Poly(A)) encapsulation efficiency (%EE) assay, and D) NTA for mean and mode size (****Table S 11.1****for Poly(A) conc.) normalised against post-microfluidics,(mean ± standard deviation, n=3), one way ANOVA Tukey Test comparing each process parameter per CQA, *$p < 0.05$, **$p < 0.005$, ***$p < 0.0005$.*

Process parameter impact on Poly(A)-DOTAP-LNPs **(Figure 5.2, Figure S 11.1, Table S 11.2,Table S 11.3)** demonstrate similar trends in size and size distribution (~ 60 nm) with lower particle size measured via PDI/NTA span values for all measured in-process stages, excluding PVDF-filtration. Dialysis and PES filtration steps highlighted higher reproducibility with minimal aggregates and sub-populations in comparison to the PVDF filtration step. PVDF filtered LNPs exhibited the largest particle size, highest measured PDI, lowest surface charge, and lowest encapsulation efficiency and mass balance. Mass balance indicating minimal drug recovery post filtration process, of which 70 % of the Poly(A) was encapsulated and 30 % free (**Table S 11.2**).

Collectively, combining CQAs and cross-comparison of the post-dialysis and PES filtration stages, it hypothesised that PVDF filtration resulted in the loss of DOTAP lipid-Poly(A) drug electrostatic complexes due to membrane adsorption, resulting in aggregation and particle self-association leading to a 110 % increase in size (115.7 nm versus 56.9 nm post-PES filtration). Size distribution measurements, PDI and NTA span, increase in value with each succeeding process step. PDI increased by 23 % from post-microfluidic (0.13) manufacture to post-PVDF filtration (0.16), whereas NTA span increased by 66 % (0.27) from post-microfluidic manufacture to post-PVDF filtration. These increased shifts in size distribution indicate detectable sub-population formation with each process parameter compared with post-microfluidic manufacture as expected as manufacture buffer is removed and filtration stress/strain impact on LNP integrity. DLS highlights main changes in PDI via size distribution intensity **(Figure S 11.1A)** for PVDF filtration, whereas a larger difference in size distribution is visualised **(Figure 5.2D)** and noted **(Table S 11.3)** for NTA span. Post-dialysis and post-PES conditions produce size distributions which are not significantly different, showing PES membrane suitability for LNP filtration post-dialysis purification.

The post-manufacture buffer contains 25 % ethanol and 75 % citrate buffer (37.5 mM sodium citrate pH 6.0). At pH 6.0, citrate is deprotonated at two carboxyl groups (316) resulting in an electrostatic attraction with the cationic surface of LNPs, thus masking the surface potential charge lowering zeta potential measurements. Alternatively, unencapsulated Poly(A) could be bound loosely to LNP surface post-microfluidics, lowering surface charge. With the removal of manufacture buffer post-dialysis purification with PBS, an increase in surface charge was noted, potentially removing loose bound Poly(A). PDI also increased in post-dialysis samples, showing sub-population formation with the removal of manufacture buffer conditions. The PDI measured for post-microfluidic to post-dialysis samples increased, which was accompanied with a decrease in size due to citrate molecule removal from smaller particles, noting dialysis within detectable range, increasing PDI but reducing overall size.

NTA estimated particle concentration varied at each process stage, with the highest measured particle concentration post manufacture as expected due to the lack of further downstream processes, whereas dialysis and filtration both impacted the overall estimated particle concentration measured by NTA **(Figure S 11.1B).** With dilutions decreasing from 10,000-fold to 100-fold, producing a decreased in estimated concentration by 72 % from post-microfluidic manufacture to post-PVDF filtration.

5.4.2. Short Term Physicochemical Stability Evaluation

The physical stability of DOTAP-LNPs was evaluated over a 28-day period analysing formulation CQAs using DLS, NTA, and the RiboGreen™ assay. Day-0 refers to the day of manufacture. Formulations were analysed post-dialysis, without filtration and stored in glass vials under refrigerated conditions.

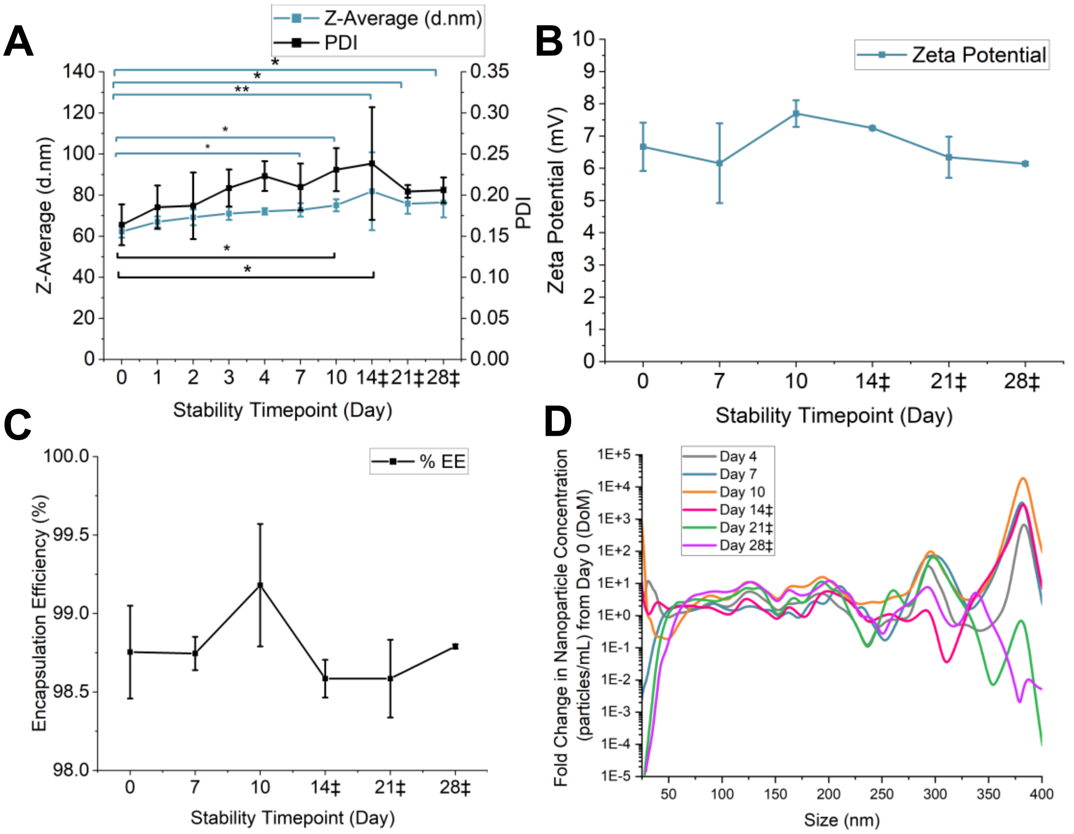

Figure 5.3 - Physicochemical trend analysis of refrigerated (4 °C) storage stability impact on Poly(A)-DOTAP-LNPs using A) (5.50 µg/mL Poly(A)) DLS to measure size and polydispersity index (PDI), B) (5.50 µg/mL Poly(A)) ELS for measurement of zeta potential, C) (0.75 µg/mL Poly(A)) encapsulation efficiency (%EE) assay, and D) NTA for mean and mode size normalised against Day 0(Table.S1 for Poly(A) conc.) (mean ± standard deviation, ‡n=2, n=3), one way ANOVA Dunnett Test comparing each timepoint with day 0 CQAs, *p < 0.05, **p < 0.005, ***p < 0.0005.

Across the 28-day stability study, all measured CQAs exhibited time dependant changes as measured **(Figure 5.3, Figure S 11.2, Table S 11.4,Table S 11.5).** DLS size and PDI **(Figure 5.3A**) show changes in size and size distribution across the study. DLS size increased by 14 nm from day-0 to day-28, with significantly different average size LNPs on day-7 compared to day-0. Changes in z-average could be attributed to DLS bias towards larger particles, consistently resulting in larger measured size. With the increased particle size, size distribution remained similar to previous and subsequent day analysis (~ 0.2) **(Table S 11.4)**. Comparing size distributions **(Figure S 11.2A)** showed an increase in aggregate detection intensity on day-10 and day-14 relative to day-0, thus increasing polydispersity measurements.

Measured zeta potential surface remained cationic within + 6-8 mV with no significant differences noted over measured timepoints **(Table S 11.4).** Changes in surface charge could be due to the conformation of the DOTAP lipid within the formulation migrating towards to a more thermodynamically favourable position on the outer surface of the LNP, thus producing varied cationic surface charges compared to day 0 LNPs. Poly(A) encapsulation remained high (> 98%) throughout the 28-day evaluation, highlighting that no Poly(A) leaked from the formulation over the stability period, and that Poly(A) remained within the LNP complex **(Table S 11.4**). Poly(A) recovery was also high on day 0 (> 60 %).

NTA data produced varying results over the analysed stability period (**Figure 5.3D**) for mean, mode, and span values, indicating **(Figure S 11.2A-B)** sub-population formation . Subsequent timepoint analysis (day-14, -21, and -28) showed increasing mean and mode sizes with variable associated span values. A decrease in size distributions > 325 nm were noted for day-21 and day-28 timepoints **(Figure 5.3D),** highlighting a narrower size distribution than previous timepoints. Narrowed size distributions are confirmed through decreased PDI and NTA span values **(Table S 11.5).** Alike DLS data denoting significant differences in size and PDI data, equivalent statistical differences on evaluated stability timepoints were not produced within NTA analysis. Contrasting results between low- and high- resolution techniques indicate the need for higher resolution analytical techniques for CQA evaluation.

5.4.3. Frozen Storage Physicochemical Stability Evaluation

With a vast array of cryoprotectants available for use in frozen storage of LNPs, sucrose inclusion as the cryoprotectant was focussed on as sucrose used in the Moderna and Pfizer/BioNTech COVID-19 vaccination storage buffers (317). LNPs were manufactured and dialysed into PBS (pH 7.4) containing sucrose at different concentrations (% w/v). LNPs were stored and frozen in DNAase/RNAase free low-protein binding microcentrifuge tubes at – 80 °C and subjected to a single freeze-thaw cycle at ambient temperature.

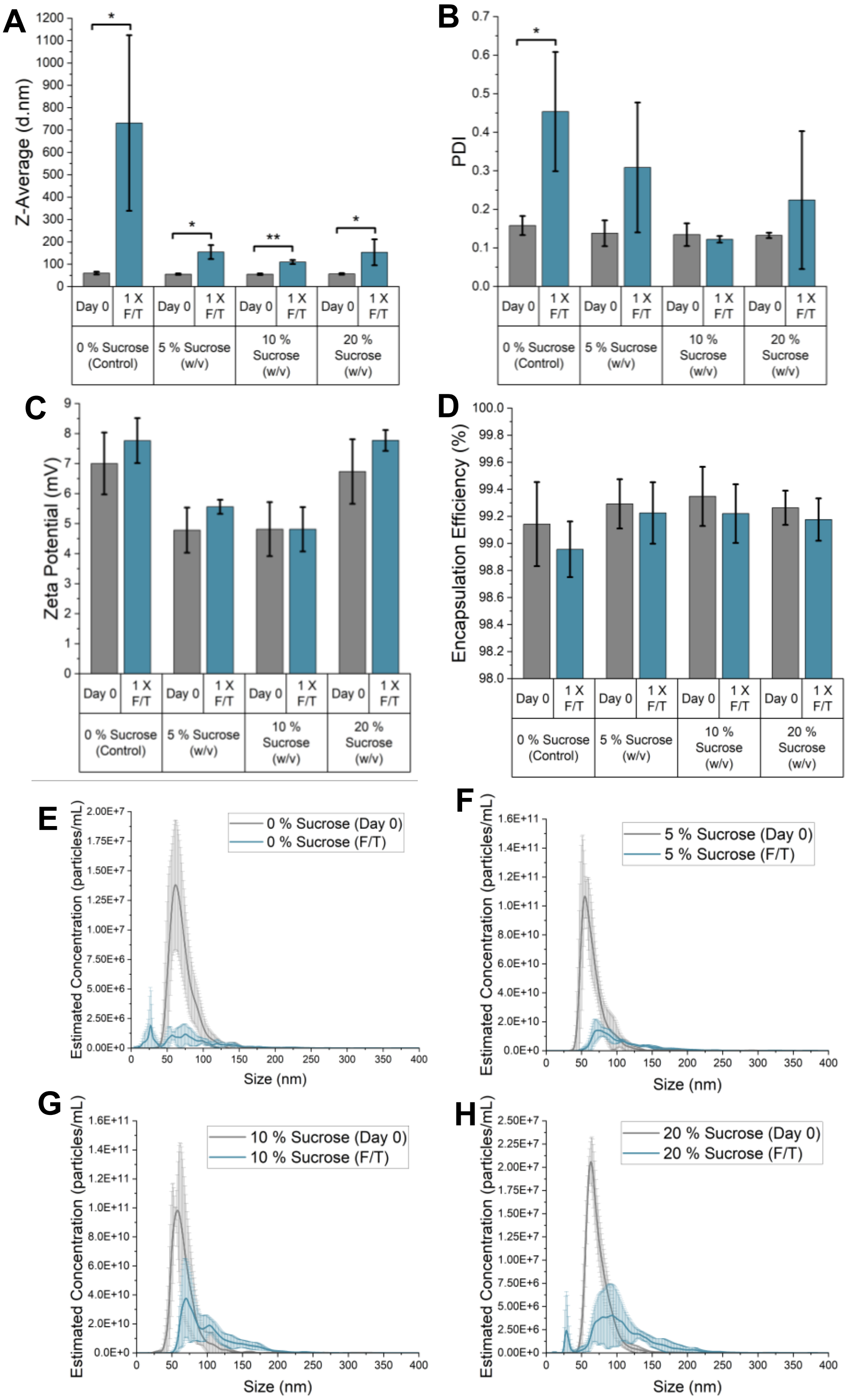

***Figure 5.4** - Physicochemical trend analysis of frozen storage stability of Poly(A)-DOTAP-LNPs formulated with 0 %, 5 %, 10 % and 20 % sucrose (w/v) cryoprotectant on Day 0 (day of manufacture) and after 1 X freeze/thaw cycle (1 X F/T) from -80 °C to ambient temperature. DLS was used to measure A) size and B) polydispersity index (PDI) (5.50 µg/mL Poly(A)), C) ELS was used to measure zeta potential (5.50 µg/mL Poly(A)), and D) RiboGreen™ for Poly(A) encapsulation efficiency measurement (0.75 µg/mL Poly(A)), and NTA for E) 0 % sucrose, F) 5 % sucrose, G) 10 % sucrose, and H) 20 % sucrose storage buffer on day 0 and post freeze/thaw (**Table S 11.1** for Poly(A) conc.) (mean ± standard deviation, n=3), one way ANOVA Dunnett Test comparing each timepoint with day 0 CQAs per individual sucrose concentration condition, *p < 0.05, **p < 0.005, ***p < 0.0005.*

Overall, the inclusion of sucrose in the formulation storage buffer impacted measured LNP CQAs (**Figure 5.4, Figure S 11.3, Table S 11.6, Table S 11.7).**

Post manufacture/purification day 0 measurements align with previous data for day 0 samples. Across all sucrose concentrations studied on day 0, particle size and Poly(A) encapsulation efficiency measurements were reproducible. Irrespective of the sucrose concentration used, a decrease in surface charge has been noted with an ~ 30 % reduction in the measured zeta potential, correlating with an increase in the formulation buffer sucrose concentration was Poly(A) recovery. An increase in Poly(A) recovery (16 %) was noted when the sucrose concentration was increased to 20 % (w/v), which was accompanied by a reduction in PDI and NTA span, highlighting a decrease in measured particle size.

Measured z-average, PDI, NTA mean, mode and span CQAs increased with induced stress from freeze/thaw cycling process, highlighted by **Figure 5.4** and **Figure S 11.3**. Sucrose disrupted the formation of ice crystals as size distribution and NTA span decreased with increasing sucrose content post F/T, PDI < 0.45 and NTA span < 1.3.

Comparing DLS and NTA data following LNP exposure to freeze/thaw stress highlights vast differences in technique results and CQAs, highlighting the need for in-depth high resolution analytical methodology and evaluation. To further probe colloidal stability in the absence of cryoprotectant, frit-inlet asymmetric flow field-flow fractionation (FI-AF4) and inline hyphenated UV-MALS-DLS multidetector (MD) methodology was developed and employed to evaluate the impact of F/T stress on LNP attributes.

5.4.4. FI-AF4 Evaluation of LNP Colloidal Stability

Here, an analytical pipeline was developed for the evaluation of Poly(A)-DOTAP-LNP colloidal stability after freeze/thraw stress in the absence of cryoprotectant. For corresponding information on method simulated elution profiles, **(Figure S 11.4),** ISO performance criteria are noted in supplementary information **(Table S 11.8).** LNPs were manufactured and dialysed into formulation buffer **(section 5.3.1)** and analysed using FI-AF4-UV-MALS-DLS. LNPs (0% sucrose) from frozen stability were thawed to ambient temperature from -80 °C prior to analysis.

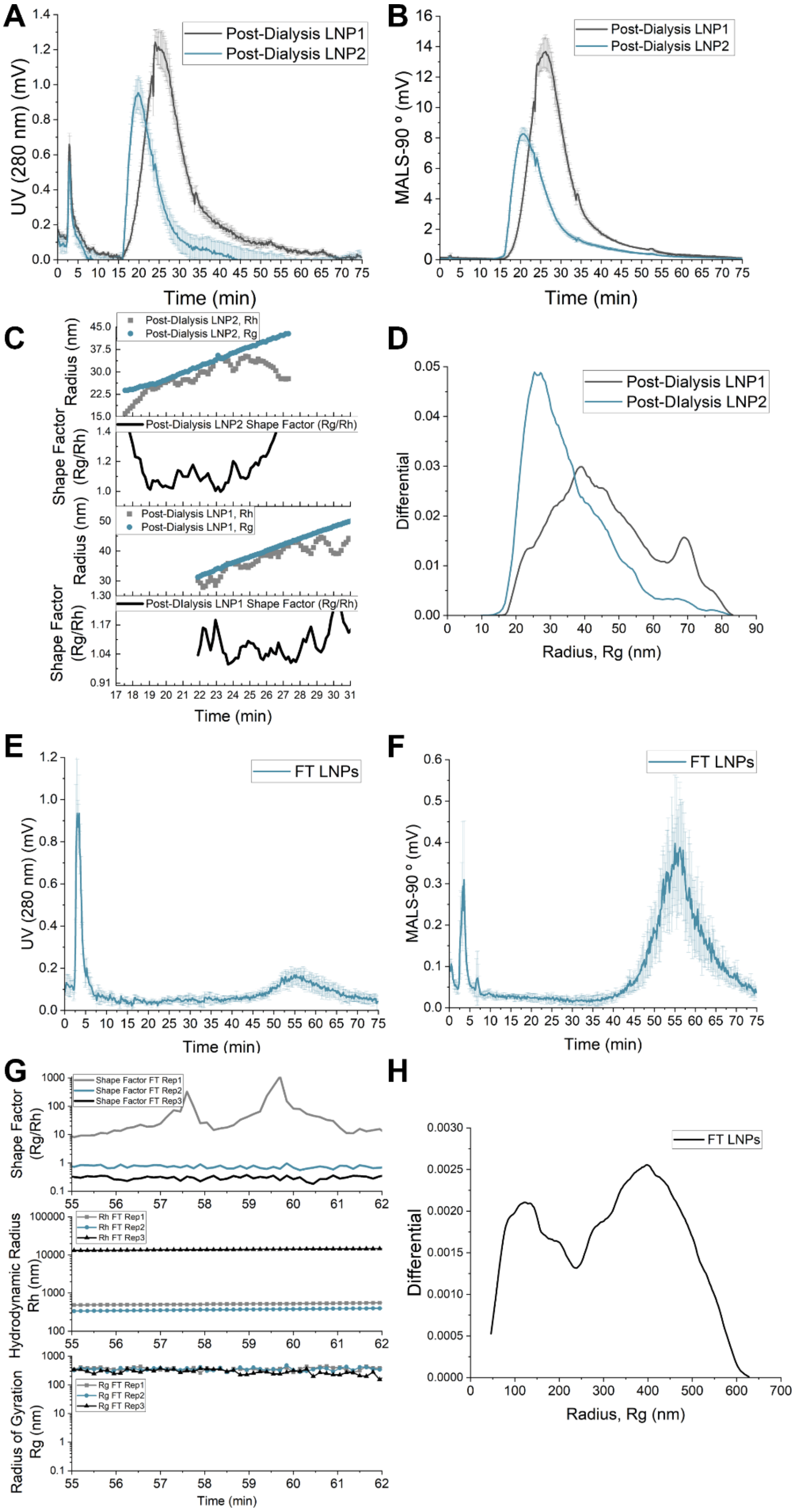

Figure 5.5 *- FI-AF4-MD evaluation of Poly(A)-DOTAP-LNPs post-dialysis A) UV elution profile, B) MALS elution profile, C) Shape Factor (R_G/R_H) and D) size distribution (n=1, mean of triplicate injections ± standard deviation). Evaluations of freeze/thaw cycled Poly(A)-DOTAP-LNPs E) UV elution profile, F) MALS elution profile, G) Shape Factor (R_G/R_H) and H) size distribution (A, B, E, F, n=3, mean of triplicate injections ± standard deviation, C, D, G H, n=1, mean of triplicate injections).*

***Table 5.2** - Cross-comparison of mode Poly(A) DOTAP-LNP formulation size between high resolution orthogonal NTA (n=3 ± STD) and FI-AF4-MD techniques, ET: elution time (n=3 injections ± STD).*

Sample Type	NTA	FI-AF4-MD		
	Mode Size (nm)	ET (min)	Mode Size (nm)	Recovery (%)
Day 0, LNP batch 1	61.4 ± 7.4	26	78.8 ± 1.0	97.1 ± 7.9
Day 0 LNP batch 2		21	58.1 ± 0.3	97.3 ± 5.7
1 x F/T cycled, Poly(A) DOTAP-LNP	62.7 ± 15.4	56	831.6 ± 92.0	13.8 ± 1.9

From high resolution AF4 data, two batches of LNPs were analysed on day-0 demonstrating interbatch variation in the manufacture process at small scale. Identical formulation process steps were followed for each batch manufacture, producing two distinct sized batches of LNPs, highlighting manufacture variability. Elution profile retention times observed at 26 and 21 minutes for LNP1 and LNP2 batches correspond to cross-flow decay flow rates of 0.216 mL/min and 0.277 mL/min, respectively. Changes in retention time were noted in **Figure 5.5A-B** with corresponding UV (280 nm) and MALS 90 ° detector signals. Both figures highlight a decrease in detector signal intensity with the LNP1 batch producing a higher UV signal (29%) and MALS signal (47%) than the LNP2 batch. Although both LNP batches produced varying retention times, detector signal intensities, radius of gyration, hydrodynamic radius, the shape factor remained consistent at 1, highlighting that both batches have similar morphology, changing throughout the elution profile from 15-40 minutes **(Figure 5.5C).** A high AF4 LNP recovery (>97%) shows minimal LNP-membrane interactions, meeting the ISO standard performance criteria for an AF4 technique **(Table 5.2,Table S 11.8**). Size distributions denote that the LNP1 batch led to a more polydisperse population distribution, highlighted by a broader peak profile and reduced signal intensity in comparison to the LNP2 batch, which produced a narrower and more intense peak (**Figure 5.5D**).

Freeze/thaw stressed LNPs aggregated extensively as expected from the DLS/NTA data with enhanced visual turbidity and precipitation. LNPs produced a retention time of 56 minutes, suggesting a change in structure/size with a corresponding cross-flow flow rate of 0.055 mL/min, suggesting poor size separation. UV detector produced a minimal signal (> 0.2 mV), less than void peak signal (1 mV) (**Figure 5.5E**), and MALS detector produced a signal around 0.37 mV demonstrating LNP aggregates scatter less light in comparison to fresh LNPs (**Figure 5.5F**). Further confirmation of poor separation and detection was confirmed with low UV-MALS detector signals, which aligned with low inline DLS signal with detector intensity < 40 kcps.

Radius of gyration and hydrodynamic radius data highlight a vast difference in detector sensitivity and poor recovery of LNPs following F/T (13%, **Table 5.2**) as fresh LNPs produced a shape factor of ~ 1. At sizes > 1 µm, non-Brownian movement forces dominate so larger particles are unsuitable for DLS detection, hence large hydrodynamic radii were noted for FT Rep1 (**Figure 5.5G**). F/T LNP replicates produced varying shape factors. Our data highlights, aggregation analysis variability within sample technical replicates and between independent sample replicates. A large size distribution was noted in **Figure 5.5G-H** with a broad and flat distribution, countless studies have aimed to prevent aggregation within LNP formulations in frozen storage conditions, however little is known about physical/mechanical aggregation formation of LNP formulations. Due to high intra-sample and inter-sample variability and overall low recovery, hydrodynamic radius, radius of gyration and shape factor ratio used to demonstrate LNP CQA changes and consequent AF4 analytical impact.

As NTA and AF4 are high-resolution techniques, **Table 5.2** cross-compares mode LNP sizes for each condition. Particle size measured for LNPs analysed on day-0 yielded the most comparable values across all techniques. In contrast, measured aggregate size distributions varied between techniques, due to the low recovery from AF4, whereas all LNPs are recovered from NTA analysis.

5.4.5. Correlation of LNP CQAs Between Analytical Assays

From the overall pipelines demonstrated within this study, the correlation between CQAs were analysed using Pearson’s correlation. Samples also included in the correlation matrix were from day of manufacture (day-0), post dialysis without filtration. To successfully correlate CQAs, data assumptions were followed. 1) Measured CQAs must be measured at the continuous level, 2) a linear relationship must exist between CQAs, 3) CQAs must contain no significant outliers, and 4) CQA measurements must be normally distributed using the Shapiro-Wilk normality test. All CQA data satisfied these assumptions, however a single replicate of encapsulation efficiency from manufacture process parameter study was removed as a statistical outlier.

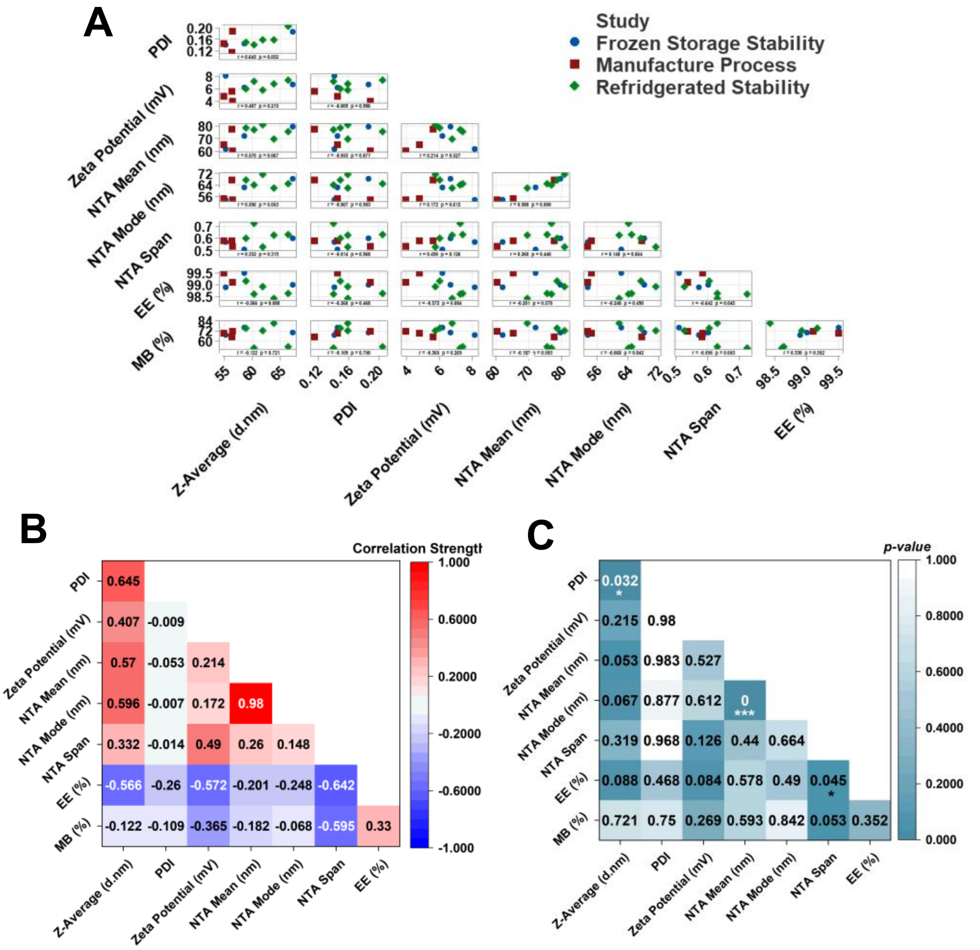

***Figure 5.6** - Pearson Correlation analysis of inter-batch CQA linear relationship analysis A) sample grouping distribution and B) correlation weighting of Poly(A) DOTAP-LNP CQAs, calculated through division of covariance by compared CQA standard deviation, and C) correlation significance, *p < 0.05, **p < 0.005, ***p < 0.0005. Zetasizer z-average size and PDI, ELS measure zeta potential, NTA measured mean size, mode size and span, and RiboGreen™ Assay for Poly(A) encapsulation efficiency (EE%), and mass balance recovery (MB%).*

From visualising each individual replicate from each study (**Figure 5.6A**), it was noted that evaluated pairwise-CQAs do not cluster per study highlighting variability within small-scale manufacturing and purification of LNP formulations. Variability in clustering also demonstrated batch-to-batch differences of LNPs. Also, though tight clustering between study replicates was not visualised, ranges of measured CQA values remained low with the CQA producing smallest variable range being 1 % difference between highest and lowest Poly(A) encapsulation efficiencies and the largest variation being surface zeta potential at 88 % between study replicate highest and lowest values. Grouping all study Day-0 measured LNP replicates has produced generic trends of visualised CQA values with average sized particles around 60 nm, low size distribution (PDI< 0.2), near neutral cationic surface charge (+6 mV) and high encapsulation efficiency (> 95%), and mass balance (> 60%).

Linear correlation weightings (**Figure 5.6B**) show how strongly two observed LNP CQAs are positively correlated, negatively correlated, or neutrally correlated. Anti-correlations (<0) indicated an increase in the CQA value for one characteristic with a reduction in the opposite CQA measurement, whereas positive correlations (>0) indicated an increase in one measured CQA value and an increase in the other measured CQA value. The matrix highlighted techniques measuring particle size and size distributions produced more positive linear correlation (Z-average, NTA mode/mean/span) with each other, higher positive correlations extended from analytical techniques used to evaluate both CQAs being compared (NTA mean/mode, DLS z-average/PDI). PDI produced neutral correlation values, compared with zeta potential and NTA CQAs. Poly(A) drug encapsulation/recovery CQAs produced negative correlations between zetasizer and NTA evaluated CQAs, with only a positive correlation noted between both EE/MB (Figure.6B). Both negative correlations highlight maximal Poly(A) drug loading and recovery with smaller particle sizes and near neutral surface charge.

Matching correlation strength, the statistical significance of pairwise correlations is shown (**Figure 5.6C**). Statistically significant linear correlations produced a weighting of > 0.6, equalling a p-value < 0.05, with a weight of 0.98 matching a calculated p-value < 0.0005. Both sets of p-values denote statistically significant linear relationships between Z-average/PDI and NTA mean/mode size, both measured CQAs originating from the same analytical instrument, whereas Poly(A) encapsulation efficiency/NTA produced a significantly linear relationship between both CQAs highlighting inter-technique anti-correlation and statistical significant linear relationship, as EE% increased, NTA span decreased, meaning LNP formulations with higher drug encapsulation, also contained smaller size distributions measured through NTA. Incorporating correlative strength of measured CQAs and statistical significance within particle evaluation is a necessary step to obtain a deeper understanding of LNP CQAs to understand physicochemical parameter behaviour and connections between measured characteristics.

5.5. Discussion

Interest in the use of lipid nanoparticles as a drug delivery platform for gene delivery has seen an exponential increase over the past decade, with the regulatory approval of three LNP-based nanomedicine products, one therapeutic and two vaccines for use with clinical settings. Since oligonucleotides encapsulated in LNPs can consist of a range of constituents, screening prototype formulations during early development is crucial. As the range of academic and industrial applications of LNPs have seen tremendous growth, established techniques within the nanomedicine field have translated into adopted routine techniques for characterising physicochemical attributes of LNP formulation candidates. Trend analysis of LNP research highlights that novel high-resolution analytical pipelines have not experienced an equivalent growth in their implementation in line with advancements in lipid research and remain underutilised for studying prototype formulations (**Figure 5.1**).

The goal of this study was to apply high resolution analytical techniques for profiling LNP nanomedicine physicochemical properties during early prototype development to facilitate clinical translation for therapeutic applications. In this work DOTAP LNPs were used as a model lipid nanoparticle system, using Poly(A) as a model payload. The evaluation of process parameter manufacture and purification steps on LNP physical parameters were reported, and an assessment of their physicochemical stability under refrigerated and ultra-low temperature storage (-80 °C) conditions using increasing resolution orthogonal techniques. These advanced techniques provide deeper insights into LNP CQAs, enabling better control over CQAs and thereby advancing their translation.

Analysis of process parameter samples demonstrated post-dialysis exchange of manufacture buffer to formulation storage buffer resulted in unmasking surface charge, increasing the LNP particle size distribution through sub-population formation and decreasing Poly(A) recovery (**Table S 11.2**). Our results highlight the importance of filter membrane selection. Both PES and PVDF membranes selected were hydrophilic and low-binding, ideally suited to biological, aqueous formulated samples. PVDF membrane contains electronegative fluoride groups, whereas PES contains sulfone moieties. Formulation post-filtration using a PVDF membrane, resulted in a 73 % encapsulation efficiency and loss of 98 % of Poly(A) drug, compared to PES membrane with 99 % encapsulation and 67 % drug recovery. Estimated changes in LNP particle concentration were noted during the manufacture stages, which would be expected when the LNP formulation is subjected to different process parameters (**Figure 5.2A**). PES membrane is more suitable for our LNPs than PVDF as the sulfone group is less electronegative than fluoride groups and does not disrupt cationic lipid-Poly(A) electrostatic interactions. Roces *et al.* (81) reported similar DLS z-average increases from post-manufacture to post-dialysis stages, while also reporting a PDI increase from < 0.2 to > 0.2. The study did not process Poly(A)-DOTAP-LNPs further by filtration, however the study used a lower molar percentage of DOTAP than our formulation, and different manufacture operating conditions (TFR 5, 10 and 20 mL/min, FRR 1:1, 3:1 and 5:1) which could account for differences noted, where our manufacturing conditions remained constant throughout all batch manufacturing. Ma *et al.* (318) screened two- and three-component LNP formulations using DOTAP as the main lipid and a selection of mRNA drugs, which resulted in reported DLS z-averages > 200 nm, and zeta potentials of ~ – 25 mV.

Our 28-day stability evaluation study under refrigerated conditions highlighted the variable nature of LNP formulations and challenges in defining specifications based on CQA analysis.

Zetasizer z-averages showed gradual increase across 28-days with significant differences in sizes noted at day-7 with a 11 nm increase (**Table S 11.4**), however DLS inherent bias towards larger particles skewed results to overall higher value, contrastingly no significant size differences were observed with NTA. Zetasizer PDI increased significantly at day-10 and day-14 (**Table S 11.4**), where NTA span results (**Table S 11.5**), did not significantly change across all evaluated timepoints. NTA mean/mode day-10 size values produced were significantly different from other measured timepoints, as mean/mode sizes increased without span, these differences indicate equivalent LNP size distributions, with all particle sizes shifting larger in size. Subsequent timepoints did not exhibit a significant change in size. Demonstrating that methods with higher resolution aren't flawless. Stability studies have provided information on formulation changes over a 28-day timeframe (**Table S 11.4**). Literature within the field is extensive on LNP stability, however with the vastly different prototype formulations used, studies often report conflicting results, with formulations increasing in size over time (319), and other formulation sizes exhibiting stable particle size throughout the measurement duration (119,320).

Current commercial LNP formulations are stored under a variety of conditions, ranging from storage at ambient to refrigerated and frozen conditions. As such, each condition will require buffer excipients to aid with LNP formulation stabilisation throughout the target product shelf life. Here sucrose was used as a model cryoprotectant and measured the impact of sucrose addition on LNP CCQAs using standardised and high-resolution techniques. The addition of sucrose at 5-20 % (w/v) concentrations in PBS on day-0 did not result in significant alterations in LNP particle size or size distributions when analysing zetasizer and NTA data. Significant differences were noted with zeta potential (**Figure 5.4C**), Poly(A) mass balance percentage (**Table S 11.6**) and the initial estimated particle concentration as measured by NTA (**Figure 5.4E-H**). Following freeze/thaw stress induction (storage at – 80 °C and subsequent thawing to ambient temperature) produced varied results from day-0.

DLS-measured parameters highlighted the presence of larger particles accompanied by PDI increases following freeze/thaw stress, with ≥10-fold increase in size and 3-fold increase in PDI relative to day-0 (**Table S 11.6**). LNP formulation containing 10 % sucrose produced the lowest size (50 nm), PDI (0.01) and zeta potential (0) differences in comparison to other test conditions. NTA data agreed with DLS trends, with 10 % sucrose producing the highest estimated particle concentration (3×10^{10} particles/mL) post freeze/thaw (**Figure 5.4G**) of all tested conditions. Across all measured frozen storage conditions, NTA mean, mode and span produced less variation in measured parameters in comparison to DLS. Our results demonstrate sucrose concentrations >20 % are required to prevent F/T induced agglomeration and ensure formulation stability with suitable cryoprotectant. Comparison of the size distribution profiles between DLS (**Figure S 11.3A-B**) and NTA (**Figure 5.4E-H**), demonstrates the need for orthogonal analysis of LNP candidates during the early development, evidenced by NTA detecting stress induced sub-population formation. Prior work also demonstrates that NTA offers higher resolution particle size analysis over DLS size measurements in a variety of nanomaterials (186,321,322).

Beyond the resolution scope of zetasizer DLS and NTA techniques is Field-Flow Fractionation, a gentle separation technique used to separate and evaluate colloidal size and morphological distributions through hyphenation with in-line multidetectors. Method development for FI-AF4-UV-MALS-DLS was demonstrated and the use of simulations to model formulation distribution outcomes (**Figure S 11.4**) was highlighted. Our AF4 method was developed in accordance with ISO guidelines, ensuring a robust method and reliable results with criteria noted in **Table S 11.8**, noting high LNP recovery post AF4 separation and detection, acceptable selectivity, and resolution factor. LNPs analysed on day-0 show two differing sized batches of 79 nm (LNP1) and 58 nm (LNP2), each respective batch produced differing UV and MALS detector signals with LNP1 producing higher detector signal intensities than LNP2. As both batches produced high recovery, differences in signal were accounted to post-dialysis concentration and thus a knock-on effect of equivalent AF4 sample prep dilution would further decrease sample concentration and detector signal intensity. As both batches of LNPs followed equal formulation process', not all environmental could be controlled for due to different laboratory ambient temperatures and lighting. These differences could impact formulation component solubility, stability, and miscibility between organic:aqueuous phases, thus producing variable outcomes.

Within each batch of LNPs analysed on Day-0 multiple peaks are visible in both UV/MALS profiles (**Figure 5.5A-B**), highlighting sub-populations present within the overall sample population distribution (**Figure 5.5D**). Freeze/thaw stress induction produced multiple sub-populations within stressed samples, producing low, fragmented, noisy detector signals for both UV and MALS data. Signals produced were also indicative of 13 % sample recovery from separation, denoting 87 % of stressed samples are lost within the AF4 separation and detection process. Prior to AF4 analysis, freeze/thaw stressed LNPs appeared turbid indicating sample loss from the freeze/thaw process contributing to poor overall AF4 freeze/thaw sample recovery. Increasing resolution of techniques from DLS to NTA, and AF4 demonstrated that stress induced LNP sub populations were detected using NTA and AF4 compared to DLS. Main peaks noted in **Figure 5.5E-F**, occurred at 0.055 mL/min cross-flow rate, highlighting minimal membrane-aggregate interactions, negligible separation and elution when minimal cross-flow is applied. As LNPs are recovered after NTA, no sample loss is observed using the technique, producing a representative size distribution. Whereas AF4 produced a size distribution reflecting 13 % if injected sample. AF4 indicated morphological impacts of stress on LNPs with visualising a broad range of spheres through to rods.

Graewart *et al.* (133) manufactured ionisable liposomes containing mRNA and conventional AF4 for separation, and multiplexed with inline small-angle x-ray scattering. While there are few studies reporting the use of AF4 for LNP analysis (308,309,314), all these studies have highlighted the need for higher resolution methodologies for analysing lipid nanoparticle systems using a broader range of components to facilitate routine use of high resolution and AF4 within routine analytical testing of LNPs. The implementation of AF4-MD enables high-resolution analysis of LNPs during early development to identify early developability challenges and facilitate clinical translation.

Our statistical correlations of day-0 LNP formulations post-dialysis without filtration (**Figure 5.6**) highlight inconsistencies of small-scale batch manufacture emphasising batch-to-batch variation within LNPs. This was further highlighted through the correlation of physicochemical CQAs measured by routine and high-resolution techniques. For a deeper insight into LNP , global interlaboratory harmonization efforts and sharing of larger datasets are needed Hassett *et al.* (147) demonstrate the use of statistical correlations between LNP CQAs; however, due to individual LNP formulation components, correlation strengths differ from our calculated correlation weightings (**Figure 5.6B**) and statistical significance strengths (**Figure 5.6C**). LNP CQA statistical correlation approach provides a deeper understanding of the relationship between LNP process design and associated physicochemical CQAs derived from orthogonal analysis, which can aid bench to bedside translation.

5.6. Conclusion

Within this work the impact of manufacture, purification, and filtration process parameters on formulation physiochemical characteristics has been shown. Refrigerated and ultra-low temperature stability results show the need for high-resolution analytical techniques within early-stage formulation development. AF4 analysis evaluated formulations beyond the scope of adopted routine analytical techniques, further emphasising the need for high resolution analytical techniques within routine characterisation of early LNP candidates. For a true representative reference material model, further cryoprotectant or refrigerated storage excipients are required to stabilise formulation CQAs to allow for extensive, comprehensive use. AF4 data highlight detectable sub-populations from fresh and freeze/thawed LNP samples, which were undetected using DLS and NTA techniques. Physiochemical correlation and statistical significance evaluations presented a deeper insight into LNP associated critical quality attributes, deepening the understanding of formulation behaviour.

Chapter 6

6. Increasing the Resolution of Asymmetric-Flow Field-Flow Fractionation Data Analysis of RNA-LNP Nanomedicines

All work was carried out by the author of this thesis.

Graphical Abstract

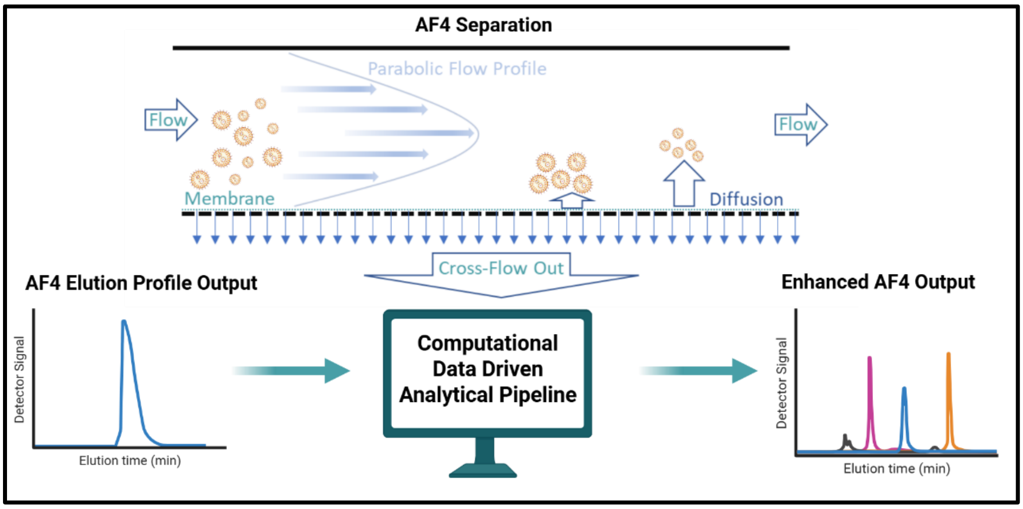

6.1. Introduction

The medicinal landscape has undergone a significant transformation over the past decade with the successful clinical translation of gene-editing therapies (323,324). These genetic engineering medicines have been implemented either as singular, chemically modified ribonucleic acid active pharmaceutical ingredients (APIs) (48,209), or in conjunction with drug delivery systems The utilisation of lipid nanoparticle (LNP) delivery systems has fundamentally advanced the field, as RNA is actively encapsulated during the formulation process (81). The application of LNP technology for RNA-based drug delivery proved highly effective during the Coronavirus pandemic (15,24,120) and more recently for respiratory syncytial virus, with the approval of mRESVIA in 2024. These advances in nanomedicine have renewed emphasis on high-resolution analytical techniques capable of resolving the structural and compositional complexity of these therapeutics.

LNP formulations typically consist of five key components, i) a main ionisable lipid (325,326), ii) sterol (88,327), iii) a helper phospholipid (83,89), iv) polyethylene glycol lipid (90,91) and v) the RNA drug substance (121). These components are rapidly mixed to produce heterogeneous RNA-LNP populations that are defined by critical quality attributes (CQAs) such as particle size, size distribution, surface charge, RNA encapsulation efficiency, and recovery. Historically, CQA analysis has relied on batch-mode light scattering techniques and fluorescence assays for RNA quantification. However, as formulation complexity has increased, more advanced high resolution analytical approaches such as nanoparticle tracking analysis (NTA)(186,187) and field-flow fractionation (25) have been increasingly adopted to achieve higher resolution characterisation. These techniques are needed to characterise polydisperse LNPs, PEG shedding (91), bleb formation (328,329) and intermediates within LNP formation (330,331).

Asymmetric flow field-flow fractionation (AF4), a subtype of FFF, has emerged as a powerful technique for LNP characterisation. AF4 separates particles based on hydrodynamic size using a crossflow field applied across a semi-permeable membrane, where smaller particles elute earlier than larger ones, opposite to the separation principle of size-exclusion chromatography. AF4 as a separation-based method is gentle, non-destructive, and highly adaptable, making it particularly suitable for fragile nanomedicines such as RNA-LNPs. Separation occurs within a membrane-covered channel, where the laminar flow profile combines with a perpendicular crossflow. Smaller sized particles, with higher diffusion coefficients, migrate further from the accumulation wall into faster flow streams and elute earlier, while larger particles remain closer to the wall and elute later. The diffusion behaviour of particles can therefore be related to hydrodynamic size through the Giddings and Stokes–Einstein equations.

AF4 operation consists of three main stages: i) sample injection, ii) focusing, and iii) elution. During focusing, the injected sample is concentrated into a narrow band near the accumulation wall; however, RNA-LNPs are inherently soft materials, and direct particle–membrane interactions during this process can induce stress and aggregation (134). To mitigate this, frit-inlet channel designs have been introduced (314). In this configuration, carrier liquid is introduced through a porous frit, distributing the sample more evenly across the membrane surface and reducing particle–membrane contact while maintaining effective separation (315,332).

AF4 can be coupled with a range of online detection systems to provide comprehensive insight into formulation CQAs, surpassing the resolution limits of batch-mode techniques such as dynamic light scattering (DLS). Typical hyphenated detectors include multi-angle light scattering (MALS), ultraviolet/visible (UV/Vis) absorption spectroscopy, differential refractive index (dRI), fluorescence, DLS viscometry, Raman scattering, small-angle X-ray scattering (SAXS) and mass spectrometry. Recent studies have demonstrated the applicability of AF4 for routine analysis of LNP formulations containing ionisable lipids such as MC3 and SM102 (110,156,309,314,333), as well as cationic DOTAP-based systems (254). However, the rapid expansion of RNA-LNP research has outpaced the development of appropriate analytical reference materials. As a result, regulatory agencies now recommend that critical quality attributes be verified using two orthogonal analytical techniques (290,308), each assessing the same property through different physicochemical principles.

While advanced AF4 separation combined with online detection provides valuable information on population distributions based on elution profiles and detector outputs, there are inherent limitations to the level of detail attainable solely from experimental data. Complex AF4 datasets therefore require further computational processing to accurately interpret subpopulation distributions and assess formulation heterogeneity. By integrating AF4 experimental data with computational frameworks, it becomes possible to extract deeper insights into formulation quality, stability, and performance beyond the capabilities of traditional analytical approaches.

In this work, this analytical gap was addressed by developing a data-driven strategy for the interpretation of AF4 datasets across LNP formulations formulated with different lipid compositions, nucleic acid cargo, and as a function of manufacturing parameters used in their preparation. Using AF4 coupled with MALS, UV, dRI, and DLS detection, relationships between size, shape and RNA loading distributions in formulations with varying ionisable lipid compositions, N/P ratios, and payload types were investigated. Through the application of computational modelling to these experimental datasets, an approach for studying underlying formulation heterogeneity was established, which can support rational candidate selection during the early stages of RNA-LNP therapeutic development.

6.2. Materials

(6Z,9Z,28Z,31Z)-heptatriaconta6,9,28,31-tetraen-19-yl-4-(dimethylamino)-butanoate (MC3) and 8-[(2-hydroxyethyl)[6-oxo-6-(undecyloxy)hexyl]amino]-octanoic acid, 1-octylnonyl ester (SM102) were sourced from BroadPharm. 1,2-distearoyl-sn-glycero-3-phosphocholine (DSPC) and 1,2-dimyristoyl-rac-glycero-3-methoxypolyethylene glycol-2000 (DMG-PEG$_{2000}$) were purchased from Avanti Polar Lipids (Alabaster, USA). Cholesterol (CHOL), dialysis membrane (MWCO 14 kDa), and, Merck Poly(A), Roche Poly(A) and Cytiva Poly(A) were purchased from Sigma Aldrich (Merck, Poole, UK). DNA/RNA Quantitation Kit (R4110), sodium citrate dihydrate were acquired from ThermoFisher (Fisher Scientific, Leicestershire, UK). All solvents and other chemicals used were of analytical grade, and milliQ-water (18.2 Ω cm $^{-1}$) was provided by an in-house system.

***Table 6.1** – Formulations tested under data-driven analytical framework and associated parameters.*

LNP #	Ionisable Lipid	N/P Ratio	RNA Drug	Storage Buffer	Microfluidic Mixer
LNP-1	DOTAP	6	Poly(A)	1 × PBS pH 7.4	Toroidal
LNP-2	SM102	6	Poly(A)	1 × PBS pH 7.4	Toroidal
LNP-3	SM102	6	ASO 18-mer	1 × PBS pH 7.4	Toroidal
LNP-4	SM102	12	ASO 18-mer	1 × PBS pH 7.4	Toroidal
LNP-5	MC3	6	ASO 18-mer	1 × PBS pH 7.4	Toroidal Flow Rate Ratio 3:1
LNP-6	MC3	6	ASO 18-mer	1 × PBS pH 7.4	Toroidal Flow Rate Ratio 6:1
LNP-7	MC3	6	ASO 18-mer	1 × PBS pH 7.4	Toroidal Total Flow Rate 5 mL/min
LNP-8	SM102	6	Fluc mRNA	10 mM Tris pH 7.5	T-junction
LNP-9	C12	8	Fluc mRNA	10 mM Tris pH 7.5	T-junction
LNP-10	ALC-0315	8	Fluc mRNA	10 mM Tris pH 7.5	T-junction
LNP-11	SM102	8	Fluc mRNA	10 mM Tris pH 7.5	T-junction
LNP-12	SM102	8	Fluc mRNA	10 mM Tris pH 7.5	T-junction

*Table 6.2 – Corresponding CQAs from LNP1-12 formulations (*n=3 ± STD, **n=3-4 ± STD, ***n=2 ± STD, ****n=1).*

LNP #	DLS Z-avg (nm)	PDI	ZP (mV)	% EE	% MB
LNP-1*	62.3 ± 3.0	0.16 ± 0.02	6.7 ± 0.7	98.8 ± 0.3	66.9 ± 13.7
LNP-2*	65.7 ± 7.1	0.12 ± 0.05	-3.1 ± 1.9	99.4 ± 0.8	82.3 ± 6.8
LNP-3*	76.7 ± 6.7	0.14 ± 0.07	-1.2 ± 0.3	98.0 ± 0.4	54.4 ± 10.6
LNP-4*	77.4 ± 1.1	0.08 ± 0.01	-1.3 ± 0.3	97.2 ± 0.3	50.3 ± 3.7
LNP-5*	87.5 ± 1.2	0.04 ± 0.00	-3.2 ± 0.4	98.2 ± 0.2	39.8 ± 3.9
LNP-6*	93.3 ± 1.1	0.06 ± 0.01	-2.9 ± 0.2	97.4 ± 0.6	35.2 ± 9.8
LNP-7*	96.9 ± 1.9	0.05 ± 0.01	-3.3 ± 0.4	97.0 ± 0.4	43.8 ± 2.9
LNP-8**	150.8 ± 27.5	0.15 ± 0.07	0.0 ± 2.2	83.1 ± 7.0	-
LNP-9***	138.1 ± 9.6	0.22 ± 0.03	-5.0 ± 5.0	83.0 ± 14.3	68.0 ± 2.7
LNP-10***	120.8 ± 5.7	0.06 ± 0.01	1.4 ± 1.6	78.9 ± 9.4	94.4 ± 14.9
LNP-11****	153.9	0.12	5.0	81.7	98.8
LNP-12****	150.1	0.07	17.1	92.3	91.8

6.3. Methods

6.3.1. Manufacture of RNA-LNPs

LNPs 1-3 were formulated on the NanoAssemblr® Ignite™ Platform (Precision Nanosystems Inc, Vancouver, BC, Canada.) in a toroidal micromixer single-use cartridge (Ref: NIN0002). The lipid nanoparticle prototype was composed of cationic/ionisable lipid:CHOL:DSPC:DMG-PEG$_{2000}$. All initial lipid stock solutions were prepared in ethanol at 5 mg/mL and combined at a 50:38.5:10:1.5 molar ratio for ionisable lipid:cholesterol:helper:PEG-lipid, respectively. Each RNA stock was prepared in DNAse/RNAse free water at either 1.5 or 2 mg/mL and diluted in 50 mM citrate buffer pH 6 (LNP1,2) and pH 4 (LNP-3-7) which used as the aqueous phase. Unless otherwise stated in **Table 6.1**, Lipid organic phase and RNA aqueous phases were injected simultaneously into the micromixer at a 3:1 aqueous:organic flow rate ratio (FRR), 15 mL/min total flow rate (TFR), with a N/P ratio of 6. Formulated LNP-1 (254), (2 mL LNPs) were dialysed against 1 × PBS (pH 7.4, 600 mL) for one hour under magnetic stirring. LNP 2-7 formulations (253) were purified using spin column centrifugation (100 kDa MWCO). Briefly LNPs were diluted (1:40) in 1 × PBS pH 7.4 and centrifuged at 2,000 x g at 4 °C. LNP formulations 8-12 were used from previous published (110) and unpublished studies.

6.3.2. Frit-Inlet Asymmetric-Flow Field-Flow Fractionation

An AF2000 asymmetric-flow Field-flow fractionation (AF4) module (PostNova Analytics, Germany) hyphenated with multiple inline detectors (MD) multiangle light scattering (MALS-PostNova Analytics), UV detector (260 nm, +0.5, PostNova Analytics) and DLS Zetasizer Nano ZS system (Malvern Panalytical, Worcestershire, UK) was used to perform the separation and inline analysis of model LNPs. A frit-inlet (FI) channel, with a channel spacer thickness of 350 µm, and a 10 kDa molecular weight cut-off (MWCO) size amphiphilic regenerated cellulose membrane was used, with a 100 µL sample injection loop. Eluent used aligned buffer associated buffer in **Table 6.1**, and a corresponding injection flow rate of 0.2 mL/min**,** crossflow rate of 0.75 mL/min **(Figure S 12.1)**. Samples were diluted from 2.5-fold from formulation concentration, 20 µL was injected. Data was analysed in the Nova FFF software version 2.2.0.1 (Postnova Analytics, Landsberg, Germany) using a spherical model to fit data using angles 28-148°.

Data treatment and analysis scripts per each study are associated within supplementary information. MALS/UV data were obtained from three cross-flow induced separation injections. MALS/UV data were normalised prior to usage within manuscript. UV data was further processed by baseline subtraction through non-linear 2nd derivation to set x axis equal to zero.

6.3.3. AF4 Simulation versus AF4 Experimental Elution Profile

LNP separation profiles were modelled using NovaAnalysis software (version 2509) with a developed cross-flow decay profile. Each formulation was parameterized using the hydrodynamic radius derived from batch-mode DLS measurements (diameter/2). These values were entered into the simulation software, which employs proprietary algorithms to model LNP formulations based on size alone, assuming hard spheres of uniform density in accordance with classical FFF theory.

$$t_R = \frac{w^2}{6D} \ln\left(1 + \frac{V_C}{V}\right)$$

Equation 6.1 *- Giddings Equation modified for AF4 separation. Where* t_R *is retention time w is channel thickness, D is diffusion coefficient,* V_C/V *is volumetric cross flow divided by volumetric flow rate through the channel (outlet flow). 6 corresponds to a spherical particle shape (288).*

Particle diffusion coefficient can be substituted with Stokes-Einstein equation, relating retention time to particle hydrodynamic radius.

$$D = \frac{kT}{3\pi\eta d_H}$$

Equation 6.2 *– Stokes-Einstein modified for diffusion coefficient determination based on hydrodynamic diameter* (d_H)*. D is diffusion coefficient, k is Boltzmann constant, T is absolute temperature, and* η *is viscosity (288).*

Simulated methods assume spherical particle morphology and associated dense core structure of latex particle, which FFF theory is based on, consisting of a monomodal particle size distribution (288). Since spherical particles exhibit a characteristic radius of gyration to hydrodynamic radius ratio (~0.775), the expected MALS profiles are approximately 22.5% smaller in apparent size, accounting for PEG and water shells undetected by MALS. The simulations did not incorporate UV detection profiles or RNA loading distributions. Simulated profiles were compared with experimental AF4 elution profiles obtained via inline MALS detection. The comparison was performed through interpolation between simulated and experimental datasets to identify key similarities and deviations in separation behaviour.

6.3.4. AF4 Multidetector Interpolation

MALS and UV elution profiles were interpolated to assess their degree of similarity and to visualize size and RNA distributions across elution peaks. Overlapping MALS and UV signals indicate regions of RNA-loaded LNPs, enabling identification of the most and least RNA-enriched fractions within the elution profile.

6.3.5. AF4 Elution Profile Fittings

Since AF4 elution profiles represent a convolution of multiple LNP sub-populations, Gaussian fitting algorithms were applied to deconvolute the composite peak shape. Both MALS and UV data were fitted to reveal sub-populations differentiated by particle size and RNA loading. These fitted sub-populations were then correlated with the experimental elution profiles to link computational outputs to experimentally resolved AF4 fractions.

Gaussian-fitted sub-populations were subsequently related back to experimental data to establish proof-of-concept correlations between RNA loading, particle size, and calculated morphology. Sub-population sizes were compared against a calibration curve of simulated particle sizes and expected elution times. The resulting linear regression enabled assessment of the predictive accuracy of the simulation model for each sub-population.

6.3.6. RNA Loading per LNP

A dual-detector (dRI/UV) approach was employed to estimate RNA molecule counts per LNP population. Each formulation was considered as comprising two major components: lipids and RNA using the parameters shown in **Table 6.3**. UV profiles were corrected for particle scattering by subtracting UV_{280nm} signal. Particle scattering should be corrected using UV wavelength where RNA does not absorb (320-350 nm), however only 260/280 nm channel wavelengths were collected. As a result, RNA numbers may be underrepresented in addition with generic dn/dc values from literature, rather than specific lipids/buffer and sequence/buffer values.

Table 6.3 - RNA per LNP dual detector approximation detector values(134,334).

Component	dRI dn/dc (mL/g)	Extinction Coefficient (mL/(mg*cm))
Lipids	0.16	0
ASO	0.17	28.6
Poly(A)	0.17	40.0
Fluc mRNA	0.17	40.0

Nova Analysis v2509 was utilised where BSA (2 mg/mL) was used to calibrate direct injection program at 40 ug and 60 ug injection concentrations at using RI and equivalent UV detector wavelength and sensitivity to LNP sample separation method. UV/RI signals were then aligned. BSA separations were used to calibrate MALS angles between 12-184° by selecting the monomer peak using MW 66.5 kDa and R_H of 3.46 nm. The calibration file was then used as a template and applied to each LNP sample for enhanced analysis. LNP samples were integrated using spherical fit with the RI as the concentration detector using angles between 28-148° and UV detector at 260 nm (+0.5).

6.3.7. Statistical Analysis

Data corresponds to a mean of at least single independent replicate comprising triplicate injections for AF4 elution profile data which have been averaged. Interpolation and gaussian scripts are attached within supplemental information **(section 12)**. Statistical outlier tests were carried out using Minitab v 20.9 software. Figures were graphed using OriginPro v 9.9.0.220.

6.4. Results

6.4.1. Simulation versus Experimental Profile

Both the simulated and experimental data were generated using the same cross-flow decay profiles, enabling direct comparison between their separation profiles. The simulated profiles report hydrodynamic radius (R_H), whereas the experimental AF4-MALS-90° profiles report the radius of gyration (R_G) obtained from the MALS detector. Assuming spherical particle geometry, R_H is expected to be approximately 22.5% larger than R_G, allowing the two measurements to be related and their profiles compared quantitatively. This relationship provides the basis for interpreting the extent to which the simulated profile accurately reflects the experimental elution behaviour of the ASO LNP formulations.

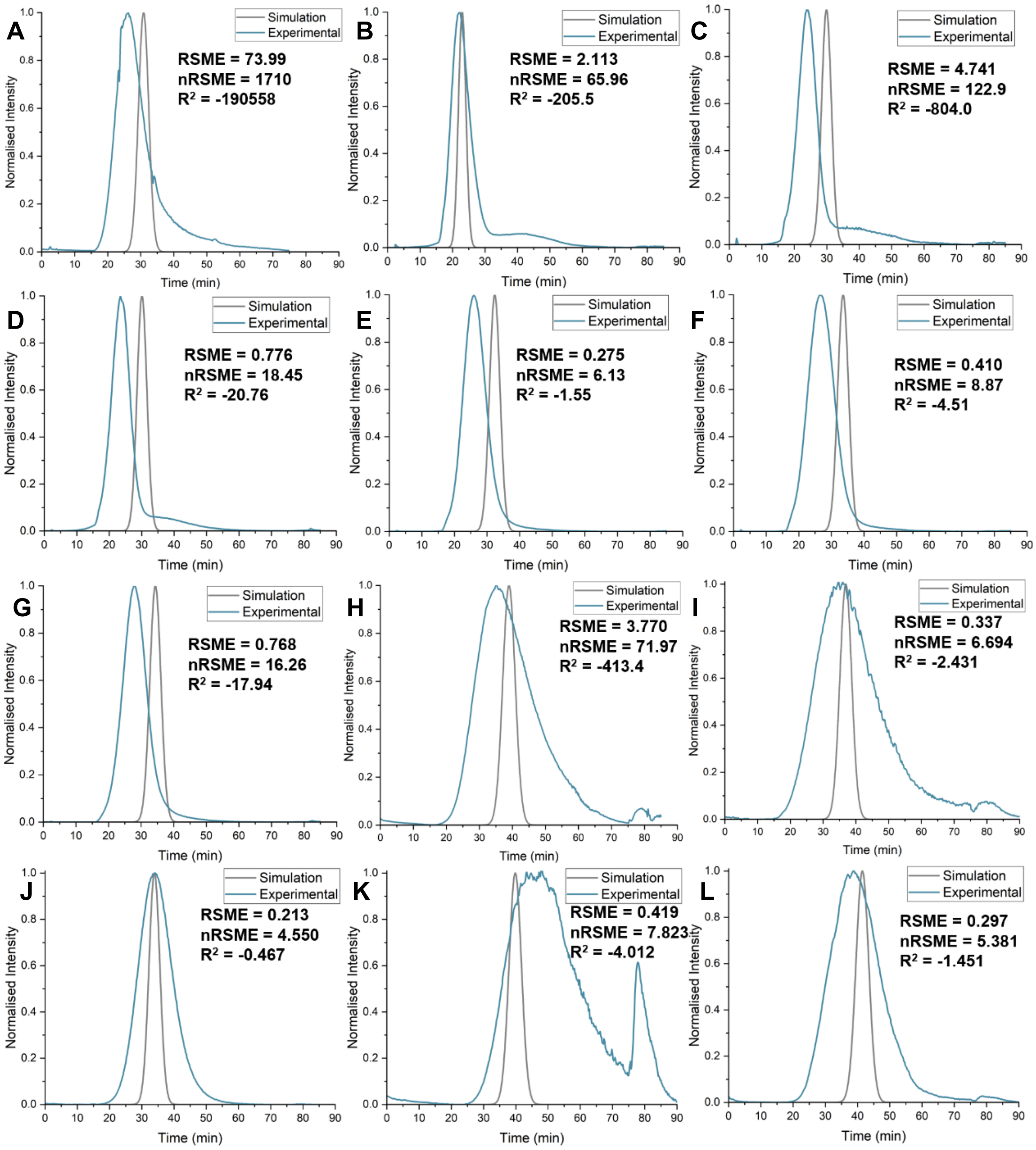

***Figure 6.1** - Simulated method comparison against experimentally obtained MALS R_G size elution profile data. Comprising of interpolated results scoring data fits with root mean square error (RMSE), normalised root mean square error (nRMSE) and R^2 comparability values. A-L represents LNP1-12 respectively according to **Table 6.1**.*

Separation profiles revealed clear distinctions between simulated elution profiles and experimentally obtained elution profiles.R^2 values were expected to be between 0-1, representing 1 as a perfect fit between experimental and simulated elution profiles, matching FFF theory which use latex beads. As negative R^2 values were obtained across all interpolated simulation and experimental elution profiles, this highlights the significant differences in simulated versus experimental data fitting for LNP usage. These negative R^2 values also demonstrate unsuitable model usage, however more comparative models are yet to be established, which would require large datasets to use and average to out for complex and heterogenic LNP samples. Simulated methodologies assume monodisperse spherical particles and rely on R_H from batch mode DLS, further emphasising the real-world underlying heterogeneity between simulated and experimental LNP formulations. This highlights the underlying heterogeneity of the LNP formulations, as real RNA-LNPs deviate from the idealised conditions assumed in field-flow fractionation theory, which was originally developed for rigid, monodisperse latex bead standards. In contrast, soft, deformable RNA-LNPs exhibit diverse morphological states that influence their retention and separation behaviour within the AF4 channel. The interpolation of simulated and experimental elution profiles provides a valuable framework for data-driven decision making when appropriate simulation model is utilised for the specific LNP system under investigation. Our interpolations showed that LNP-1 **(Figure 6.1A)** produced the greatest divergence between simulated and experimental chromatogram profiles, reflecting the structural complexity of Poly(A)-DOTAP formulations. Notably, the simulation did not incorporate interactions with the regenerated cellulose membrane, nor reflect the membrane pre-conditioning needed for cationic LNP formulations. In contrast, LNP-10 **(Figure 6.1J)** formulated using a Fluc-ALC formulation, suggesting a dense core structure, with higher levels of heterogeneity compared to the simulated profile.

6.4.2. Determining RNA Loading from AF4-MALS-UV

To further assess RNA loading across LNP size distribution, MALS and UV elution profiles were interpolated to quantify the degree of RNA incorporation based-on their comparative elution profiles. The MALS-90° detector was used for LNP detection, with the UV detector set at 260 nm for RNA detection (LNP-1 used UV detection at 280 nm).

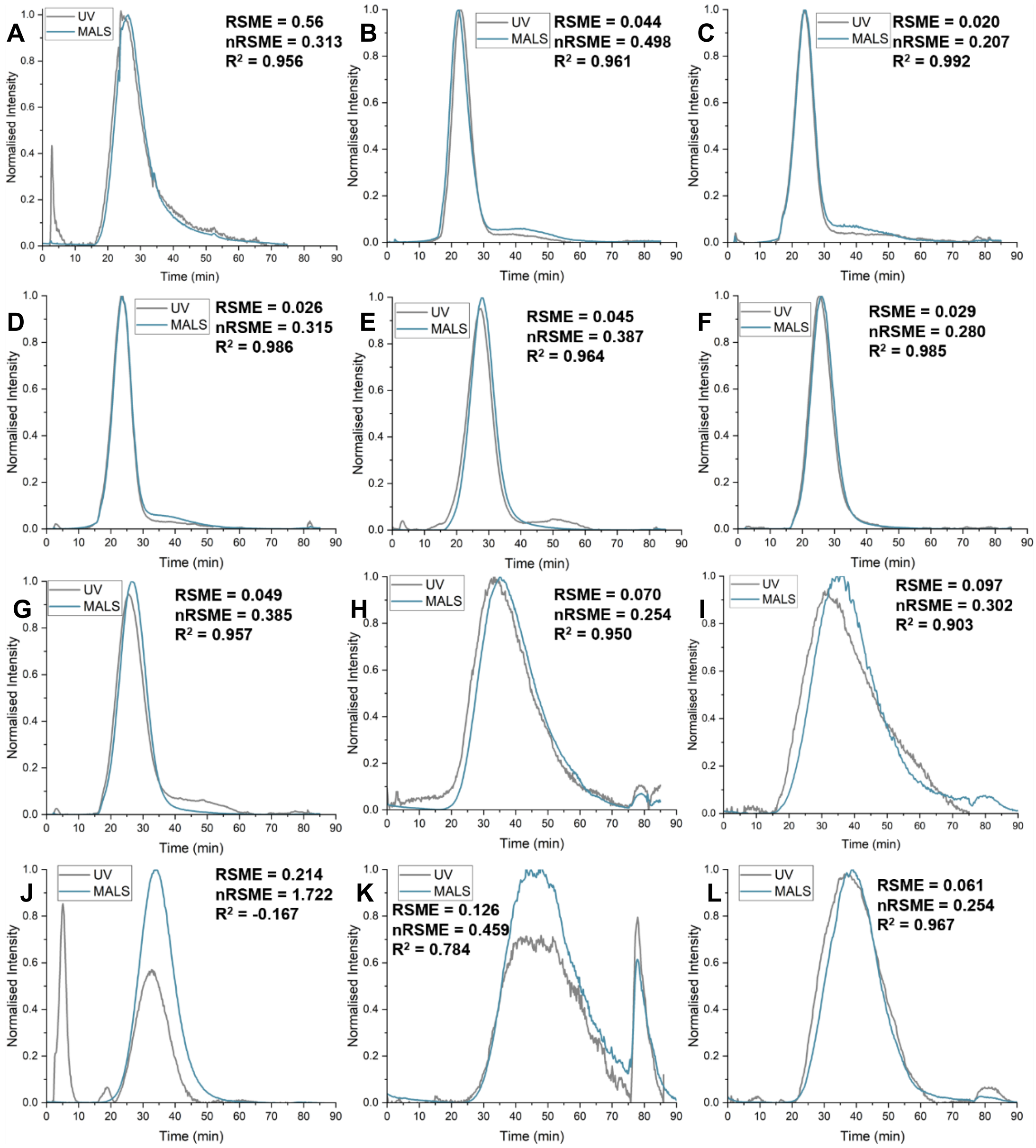

***Figure 6.2** – Interpolation of experimentally obtained UV absorbance and MALS R_G size elution profile data. Comprising of interpolated results scoring data fits with root mean square error (RMSE), normalised root mean square error (nRMSE) and R^2 comparability values. A-H represent LNP1-8 according to **Table 6.1**.*

Both elution traces revealed similarities between the MALS and UV detectors, enabling qualitative assessment of RNA loading across formulations. This correspondence was reflected in the calculated RMSE, nRMSE and R^2 values. Each formulation highlights RNA loading within the main LNP elution peak. However, both LNP-1 and LNP-10 displayed evidence of RNA leakage, as shown by pre-elution UV peaks at the start of the fractogram **(Figure 6.2)** within the UV traces. LNP-10 also showed a small shoulder preceding the main peak, which could be attributed to RNA adsorbing to the surface of smaller LNPs or the agglomeration of smaller sized LNPs to form a pre-main elution peak complex. The separation profiles also revealed the presence of aggregates in several LNP formulations, denoted by late-eluting peaks at > 75 minutes, coinciding with the membrane washing step **(Figure 6.2**). Aggregates were detected in LNP-8, LNP-9, LNP-11, and LNP-12 formulations, with LNP-11 showing the most aggregation, highlighted by normalised intensities > 0.2 a.u. Interpolation of MALS/UV traces highlighted differences in loading heterogeneity across formulations. LNP-3 exhibited the narrowest elution profile, consistent with a more uniform size distribution; this aligns with its use of SM102 as the ionisable lipid and an ASO payload. In contrast, broader peaks indicative of larger size heterogeneity were observed in LNP-8, LNP-9, LNP-10, LNP-11, LNP-12. Although all of these contained Fluc mRNA, they differed in ionisable lipid identity and N/P ratio: LNP-8 (SM102, N/P 6), LNP-9 (C12, N/P 8), LNP-10 (ALC, N/P 8), and LNP-11/12 (SM102, N/P 8). These variations were reflected not only in peak width but also in differing levels of reproducibility across replicates **(Figure 6.2).**

To further dissect RNA loading and particle size heterogeneity of sub-populations within these distributions, Gaussian deconvolution was applied for both MALS and UV elution profiles. This enabled enhanced resolution of sub-populations and provided deeper insights into the distribution of RNA across distinct LNP size classes.

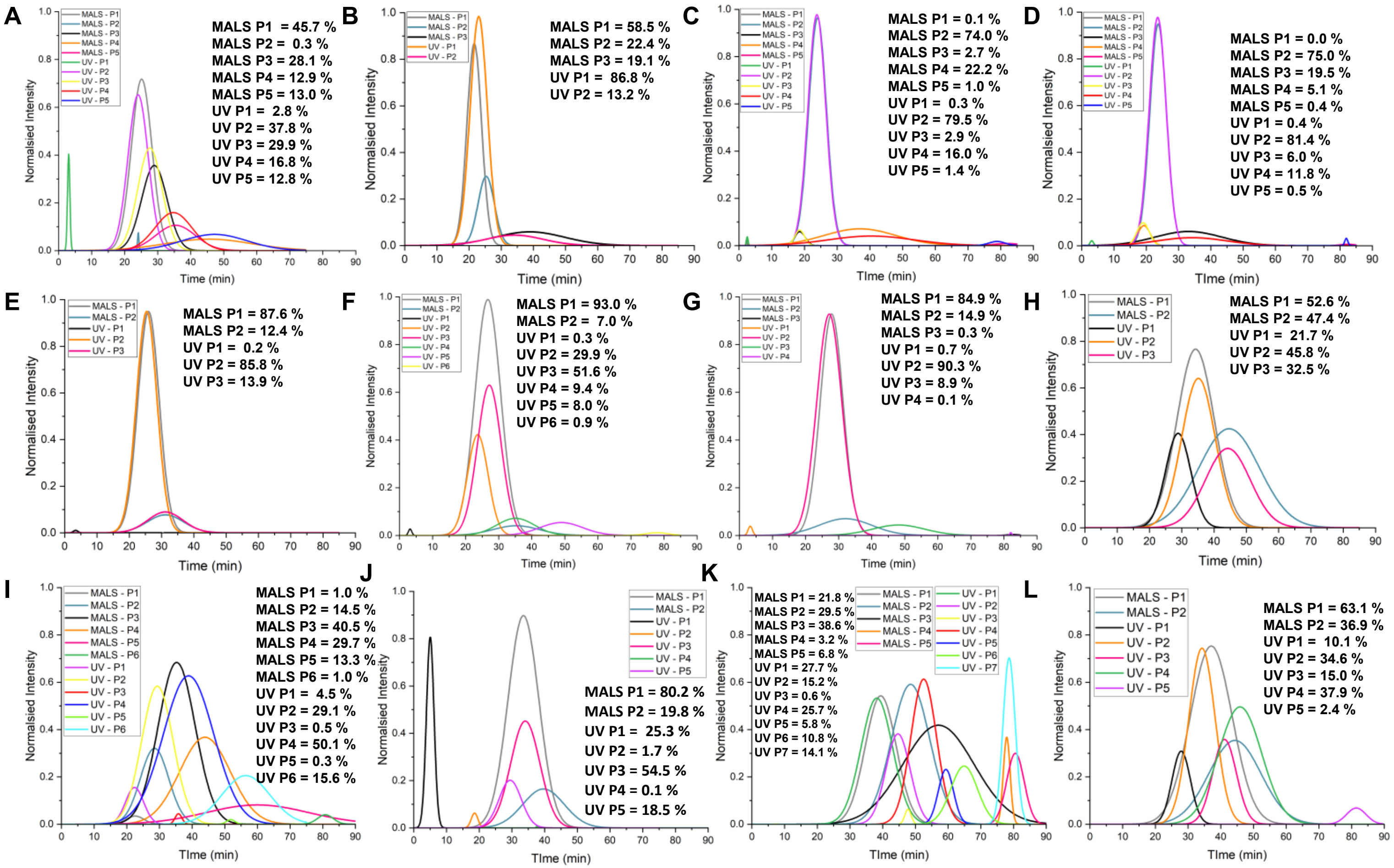

Figure 6.3 *– Gaussian fits of experimentally obtained UV absorbance and MALS R_G size elution profile data. Gaussian fitting script and sub-population elucidation script parameters can be found* ***in supplementary information within chapter 12*** *respectively. Peak area was calculated from overall gaussian fitted elution profile as percentage of sub-population present within sample. Overlaps in MALS/UV peaks show loading distributions within overall particle population distribution. A-L represents LNP1-12 respectively according to* ***Table 6.1****. Gaussian fitting R^2 scores are noted in* ***Table S 12.1****.*

Since elution profiles are composed of particle sub-populations, gaussian fittings were applied to provide further insights into sub-population elucidation, which collectively contribute to overall elution profiles. The fitted models demonstrated a high degree of accuracy ($R^2 > 0.977$) across MALS (particle mass) /UV (RNA concentration) elution profile traces **(Table S 12.1).** Deconvolution of these profiles and associated overlapping of sub-populations further showed particle loading and structural heterogeneity distributions across size-defined fractions, revealing overlapping MALS/UV sub-populations that link RNA loading to specific particle size and morphology.

Sub-population peaks were quantified as a percentage of the total elution profile area to identify dominant sub-populations within each formulation. UV-derived peak areas were further used to infer RNA leakage from LNP formulations, with **Figure 6.3A, F** indicating 2.8% and 25.3 % RNA leakage, respectively. LNP-9 **(Figure 6.3E)** exhibited the highest degree of structural complexity with the highest number of distinct MALS sub-populations (six identified). LNP-11 **(Figure 6.3G)** displayed the broadest RNA loading distribution, comprising seven elucidated sub-populations, indicating substantial heterogeneity in RNA association across particle classes. In contrast, LNP-3 **(Figure 6.3C)** showed a prominent overlap of MALS/UV peak 2 with a high percentage area (>74%), indicative of concentrated RNA loading within a single sub-population. LNP-8 displayed a single MALS peak (peak 1) composed of two UV-resolved RNA-loading sub-populations underlying the same size-based distribution, indicating that structurally similar particles may very compositionally or in RNA content (**Table 6.4**).

6.4.3. LNP Simulation Enhancements

To support experimental observations, simulated elution profiles were generated across a range of R_H values (15–100 nm) and fitted using a second-order polynomial **(Figure S 12.3).** Sub-population elution times were then inputted into this model to calculate corresponding simulated values. As the simulation employed R_H parameters, resulting R_H values were adjusted by experimentally determined 50% distributional shape factors to align with R_G dimensions. The percentage differences between experimental and simulated R_G values were subsequently calculated to assess comparability and model accuracy.

Table 6.4 *- Experimentally obtained size per sub-population peak maxima elution size versus simulated size per expected elution time. Both values compared through calculating percentage difference. Simulated size utilised particle hydrodynamic radius (R_H), which has been multiplied by SF50 (R_H*SF50=R_G) accounting for calculated shape factor morphologies. *Low MALS detector signal. **Statistical outlier at 95 % CI. P denotes peak.*

LNP Formulation	Sub-population Peak	Elution Time (min)	Expected R_G Size (nm)	Simulated R_G Size (nm)	% Difference
LNP-1	**P1**	25.1	38.2	29.3	26.2
	P2	24.1	36.4	27.1	29.4
	P3	29.0	46.3	41.0	12.0
	P4*	45.5	68.6	491.9	151.0**
	P5	35.4	57.0	83.2	37.4
LNP-2	**P1**	21.6	24.5	15.7	43.8
	P2	25.3	29.3	22.6	25.9
	P3	38.9	61.6	58.0	6.0
LNP-3	**P2**	24.0	20.1	14.3	33.9
	P3*	18.6	*	*	*
	P4	37.0	41.6	24.0	53.8
LNP-4	**P2**	23.7	26.8	18.0	33.9
	P3	33.1	51.5	40.8	23.1
	P4	19.3	23.5	13.0	57.3
LNP-5	**P1**	26.0	31.1	21.8	35.4
	P2	31.2	38.9	31.9	19.7
LNP-6	**P1**	26.7	32.9	26.1	23.2
	P2	35.3	49.0	43.0	13.0

LNP-7	**P1**	27.9	33.2	23.3	34.9
	P2	32.0	39.3	30.8	24.3
LNP-8	**P1**	34.3	53.6	37.6	35.0
	P2	44.7	73.1	67.1	8.6
LNP-9	**P1**	22.7	28.8	20.3	34.6
	P2	28.7	40.3	29.3	31.6
	P3	35.5	55.9	43.4	25.2
	P4	44.1	76.5	66.3	14.4
	P5	60.2	102.5	125.9	20.5
	P6	81.0	103.3	192.5	60.3
LNP-10	**P1**	33.5	45.1	36.4	21.5
	P2	39.7	56.7	49.3	13.9
LNP-11	**P1**	39.4	50.9	43.7	15.1
	P2	48.5	74.5	76.0	2.0
	P3	57.0	95.0	137.4	36.5
	P4	77.9	113.5	253.6	76.3
	P5	80.6	108.3	246.8	78.0
LNP-12	**P1**	37.1	60.0	47.1	24.0
	P2	44.3	78.0	68.0	13.7

Testing the percentage differences between experimental and simulated size values identified a deviation of 151.0%, which was determined as a statistical outlier relative to the remaining data. Upon removal of this outlier, the simulated approach yielded an average difference of approximately 30% compared with experimental size measurements. This level of deviation is consistent with expectations from classical FFF theory, where simulations are typically based on rigid, monodisperse spheres. Therefore, material-dependent density variations between soft lipid-based particles and rigid spheres are not accounted for in these simulations.

Sub-population analysis with individual formulations offered further resolution. For example, LNP-11 peak 2 differed by only 2.0% between experimental and simulated sizes, suggesting a well-defined core–shell structure that aligns more closely with idealised FFF behaviour. In contrast, the largest discrepancies were observed for sub-populations eluting after 77 minutes, corresponding to cross-flow rates below 0.1 mL/min **(Figure S 12.1**). Particles detected in this region are likely released from the membrane surface during the wash step rather than diffusing into the channel, resulting in reduced retention and artificial apparent size inflation. FWHM-derived parameters for each MALS peak were further integrated into the experimental profiles to assess how individual sub-populations contribute to overall particle size and morphological distributions. This allowed a more granular understanding of structural heterogeneity within each formulation and provided further context for interpreting the divergence between simulated and experimental AF4 profiles.

6.4.4. Sub-population Fitting to Experimental Data

The elucidated FWHM sub-populations were classified by cumulative distribution to obtain 10, 50 and 90 % distributional values from each R_G, R_H and shape factor for enhanced insights into distributions within a sub-population.

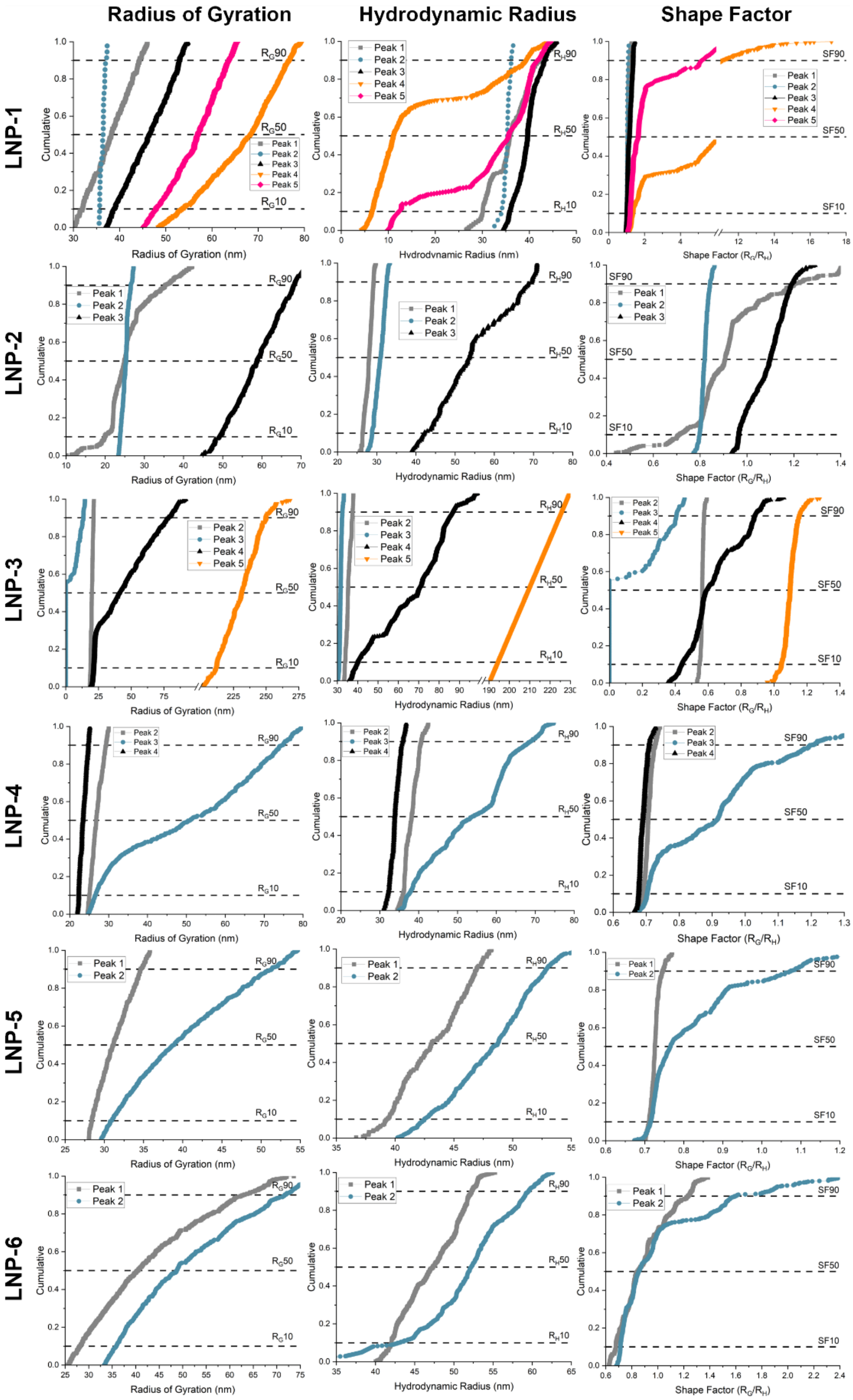

***Figure 6.4** – Using cumulative analysis each sub-population FWHM was integrated to obtain distributional values (D10, 50, 90). LNP formulation 1-6 are showcased with their respective MALS radius of gyration (R$_G$), hydrodynamic radius (R$_H$) and shape factor (SF, R$_G$/R$_H$) for each gaussian fitted subpopulation which were derived from experimental elution profiles.*

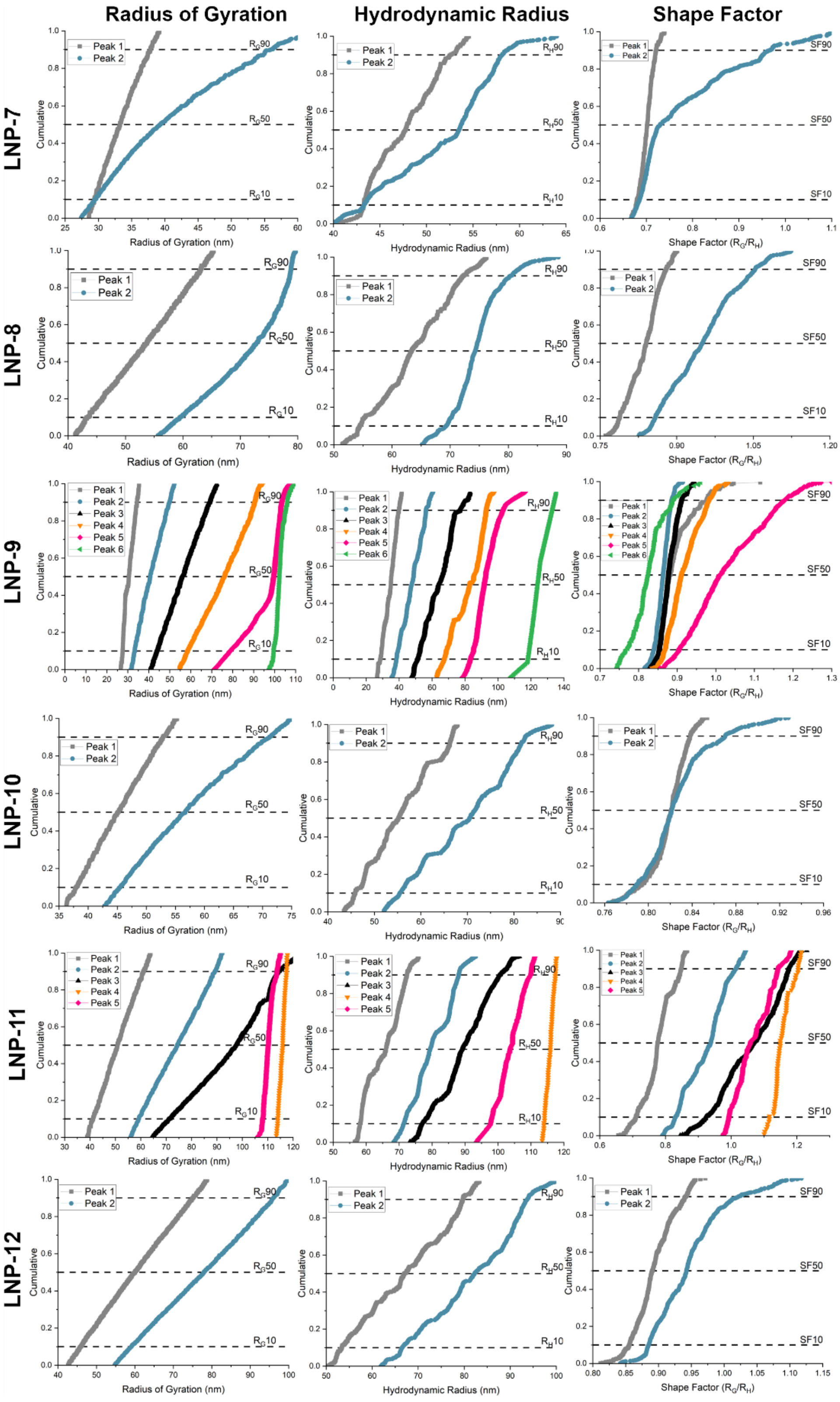

Figure 6.5 *– Using cumulative analysis each sub-population FWHM was integrated to obtain distributional values (D10, 50, 90). LNP formulation 7-12 are showcased with their respective MALS radius of gyration (R$_G$), hydrodynamic radius (R$_H$) and shape factor (SF, R$_G$/R$_H$) for each gaussian fitted subpopulation which were derived from experimental elution profiles..*

All LNP formulations produced distinct distributions in R_G, R_H, and shape factor (SF) values. SF values outside the 0.4–2.0 range are indicative of poor detector response from either the online MALS or DLS systems, resulting in unreliable SF estimations. A typical SF value of ~ 0.775 corresponds to a near-spherical morphology, such as that observed for latex standards. In contrast, LNPs, which possess a PEG2K surface layer with varying chain lengths, exhibit higher SF values as the apparent centre of mass extends outward, leading to larger R_G and overall SF values. Both early-eluting sub-populations and larger aggregates are susceptible to weaker detector signals due to low particle concentration at the elution edges. Consequently, AF4 elution profiles are evaluated around the FWHM region to ensure robust analytical assessment of CQAs.

Following sub-population predictive modelling, sub-populations showing < 10% difference between experimental and simulated values can be further examined under the dense-core FFF latex-bead hypothesis. This enables identification of LNP sub-populations containing more solid, compact cores versus those exhibiting more diffuse, deformable structures, as reflected in their size and shape distributions, suggesting tighter packing of RNA payload within the LNP.

Consistent with classical FFF theory, later-eluting sub-populations generally exhibit increased overall size and shape factors, unless Gaussian fitting has re-ordered overlapping peaks. These observed trends in sub-population size and morphology distributions provide additional insight into RNA payload distribution and loading variability, highlighting structural and conformational distinctions among formulations 1–12.

6.4.5. LNP Formulation RNA Loading

Here a dual-detector assumption (dRI and UV) was utilised to calculate the percentage weight and number of RNA molecules per LNP formulation, highlighting differences between formulation compositions and therapeutic payloads. A buffer blank was subtracted from UV and dRI data and light scattering contributions were subtracted from UV 260 nm wavelength using 280 nm wavelength. A scattering correction UV wavelength should be selected where RNA molecules do not absorb light (320-350 nm). LNP-2-8 formulation were analysed due to the presence of a strong RI signal, which was absent with other formulations.

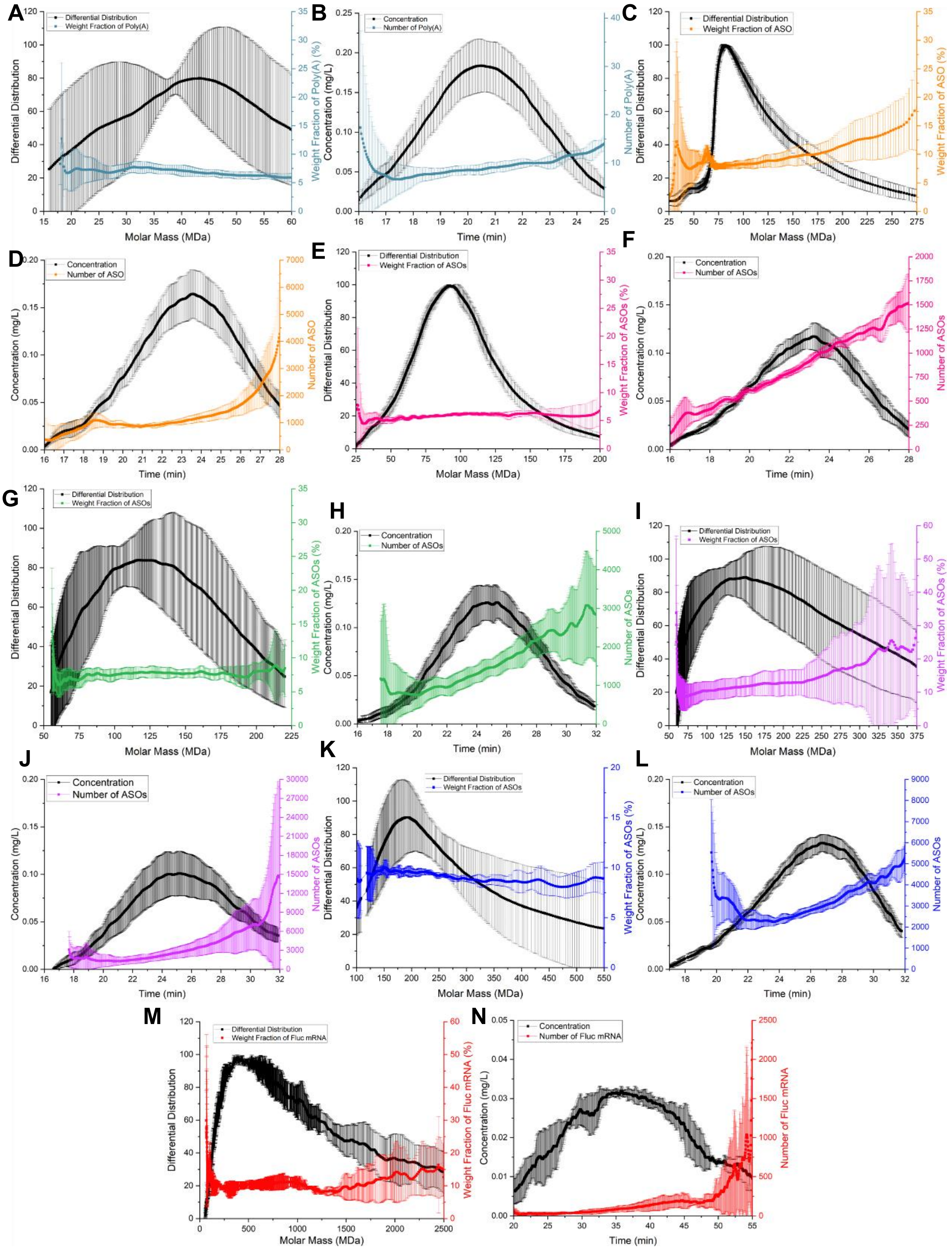

***Figure 6.6** - RNA per LNP using dual-detector assumptions for RNA payload and lipid components of LNPs. Including weight fractions of RNA and numbers of RNA over concentration detector elution profile. LNP-2 A) % weight and B) Poly(A) number, LNP-3 C) % weight and D) ASO number, LNP-4 E) % weight and F) ASO number, LNP-5 G) % weight and H) ASO number, LNP-6 I) % weight and J) ASO number, LNP-7 K) % weight and L) ASO number, and LNP-8 M) % weight and N) Fluc mRNA number, (n=3 ± STD).*

The RI trace was utilised as the concentration detector in tandem with the UV 260 nm elution profile. Comparing, classes of therapeutic allows for the elucidation of similarities and differences between therapeutic payload type and formulation-related conditions. LNP2-8, averaged at ~15-45 % weight fraction of RNA within the LNP formulation, with the remaining 85-55% being comprised of lipid components at the differential peak maxima **(Figure 6.6).** These weight fractions, in combination with known RNA molecular weights, allowed for the number of RNA molecules within the peak maxima of the concentration dRI elution profile to be estimated. LNP-2 formulations averaged at 20 Poly(A) molecules at LNP elution profile peak maxima, LNP-3-4 formulations averaged at ~3,400 ASO molecules, and LNP5-7 ASO numbers varied from ~ 8,000-13,000 whilst changing manufacture conditions (**Figure 6.6).** Following this trend, LNP-8 contained around 200 Fluc molecules **(Figure 6.6).**

All LNP formulations showed increasing RNA number in tandem with increasing LNP size and which eluted later from the AF4 channel. By linking back to size/shape sub-population in **Figure 6.4,** sub-populations were attributed accordingly.

***Table 6.5** - Quantifying RNA loading per LNP sub-population through size and shape composition for LNP-2-8. **low detector signal.*

LNP Formulation	Peak Number	Et (min)	R_G50 (nm)	R_H50 (nm)	SF50	Number of RNA molecule
LNP-2	**P1**	21.6	24.9	28.1	0.91	9.6
	P2	25.3	25.3	31.0	0.82	15.4
	P3	38.9	58.7	53.7	1.10	**
LNP-3	**P2**	24.0	20.0	35.4	0.56	1192
	P3	18.6	0.0**	31.7	0.00**	1090
	P4	37.0	40.8	70.2	0.59	**
LNP-4	**P2**	23.7	26.8	38.2	0.71	1009
	P3	33.1	50.9	53.7	0.91	**
	P4	19.3	23.4	33.8	0.69	521
LNP-5	**P1**	26.0	31.1	43.1	0.73	1672
	P2	31.2	38.9	48.7	0.77	2958
LNP-6	**P1**	26.7	40.4	47.3	0.84	3536
	P2	35.3	48.7	52.2	0.86	**
LNP-7	**P1**	27.9	33.2	47.7	0.70	3373
	P2	32.0	39.4	53.5	0.73	5337
LNP-8**	**P1**	34.3	53.7	63.4	0.84	75
	P2	44.7	72.8	74.3	0.95	198

Our results highlight loading differences across sub-populations of LNP formulations, which can be attributed to size and shape differences as a functions of RNA numbers per LNP **(Table 6.5).** These enhanced insights further elucidate differences in early formulation development to give further information into AF4 therapeutic RNA-LNP formulations.

6.5. Discussion

In this chapter, a frit-inlet AF4 (FI-AF4) channel configured with a multidetector setup (MALS-UV-RI) was applied to a series of RNA-LNP formulations. Three major CQAs: particle size, size distribution, and drug (RNA) loading were investigated across multiple RNA-LNP formulation conditions. Despite employing state-of-the-art FI-AF4 separation, resolution limitations constrained deeper exploration of LNP heterogeneity. The field is moving beyond traditional, low-resolution, batch-mode ensemble techniques toward higher-resolution analytical platforms. Among these, asymmetric flow field-flow fractionation (AF4) has become a valuable tool for analysing soft-matter therapeutics, making it well suited to RNA-LNP characterisation. However, even with state-of-the-art AF4 approaches, resolution remains a key limiting factor. Detector sensitivity, separation efficiency, membrane chemistry, cross-flow programming, spacer thickness, and eluent composition collectively determine the extent of achievable separation, and thus the level of structural insight obtainable.

In this study, a semi-empirical approach was applied to further evaluate RNA-LNP nanomedicines beyond the resolutive scope of AF4. As elution profiles represent LNP distributions (size, RNA loading),a key gap of technique resolution was missing in terms of approaches to evaluate contributing sub-populations towards overall population level distributions, This work highlights sub-population identification from overall AF4 population separation profiles, with corresponding sub-population $R_{G'}$, R_H sizes and shape factor morphologies attributed by increasing RNA numbers.

Previous research on RNA-LNPs has primarily focused on AF4 method development (134,308,314), formulation stability (156,254) and general therapeutic characterisation (110,309). Typically, LNP elution profiles obtained from AF4 serve as the main analytical output, with detector signals used to derive particle characteristics. However, most studies have relied on integrated elution profiles and metrics such as peak full width at half maximum (FWHM), with limited studies looking at distributional sub-population contributions (156,253).

Firstly, experimental elution profiles of RNA-LNPs were compared and interpolated against simulated profiles based on FFF theory which uses spherical solid latex particle diffusion and separation as a model (288,314). Simulated profiles highlighted major differences from experimentally obtained elution profiles which, showcase deviation from dense-core spherical latex beads which FFF separation theory is based on. The key use of interpolation of both profiles showcase data driven quantitative values assigned to elution profile, which could be used as a measure of comparability and could be used to enhanced AF4 separation method optimisation. Additionally, as FFF theory is based on a monodisperse population of particles, where clearly LNPs formulation are inherently heterogeneous in comparison with latex beads due to differences in manufacture controllability.

Following simulation/exponential elution profile interpolation, MALS 90° and UV detector signals were interpolated to highlight similarities within elution profiles to determine RNA loading within the size distribution of LNP populations. Each of the value outputs highlight differences in loading across differing formulations. RNA leakage was noted in LNP-1,10 **(Figure 6.2)**, displayed by pre-main peak elution profiles within 5-10 minutes of the cross-flow elution profile **(Figure S 12.1).** LNP-11 showcased a R^2 of 0.784 which showed higher levels of RNA with aggregates than within the main particle population. All other formulation produced high R^2 values (> 0.9), showing loading of RNA across LNP separation profiles. These data-driven interpolations emphasise RNA loading within formulation, showing a high-throughput two-detector size/loading screening method.

To further enhance AF4 outputs, AF4 UV/MALS traces were deconvoluted to elucidate sub-populations comprising the overall elution profile using a computational framework**.** Our fittings show high degree of fit ($R^2 > 0.97$), with gaussian applied fittings matching overall elution profiles from experimental data. Further, each sub-population area per inline detector was calculated, highlighting arial contributions to overall elution profile **(Figure 6.3).** Each detector elucidated sub-populations were overlaid to showcase size/RNA loading contributions across the elution profiles **(Figure 6.3).** Each figures highlights the levels of heterogenous RNA loadings across sub-population distribution, corresponding with varying R_G sizes from the MALS detector. Formulations range from high levels of subpopulations (LNP-9,11) using C12 and SM102 LNP formulations loaded with Fluc mRNA. Contrastingly, more monodisperse sub-populations (LNP-2-7) utilise SM102 formulations with Poly(A) and ASO RNA respectively **(Figure 6.3).** A key limitation of using the gaussian fitting approach was that the implementation of the code was not reversible, the overall elution profile could not be reconstructed by combining the individually fitted sub-population peaks. Even when simulating single-sized sub-populations, or enforcing experimentally derived FWHM values, the resulting subpopulations remained too monodisperse to reproduce the breadth and asymmetry of the experimental elution profile. This arises from Gaussian functions having infinite tails; and do not inherently capture the peak broadening and skew characteristic of AF4-based separations. Consequently, the deconvoluted peak set was most valuable for elucidating relative subpopulation contributions rather than serving as a fully reconstructive model of the separation.

With the sub-population contributions to each elution profile established, simulation profiles of each formulation were examined to develop a more mechanistic model for sized-based separation behaviour. Using Nova Analysis software, series of particle sizes were simulated, and an equation of best fit was generated to describe the relationship between simulated elution time and hydrodynamic radius (R_H) size **(Figure S 12.3).** The-population elution times were entered into experimental elution profiles for a representative result. The sub-population elution time was further entered into simulated equation to obtain a subsequent R_H size profile, size data was multiplied by experimentally obtained shape factor D50 value for R_G size determination. Each R_G size percentage difference was then calculated. Basing the results on FFF theory suggests that low differences between experimental and simulated sizes shows dense-core structure alike latex beads, founding particle used in FFF theory **(Table 6.4).** Averaged differences equate to 30% from experimental to simulated expected sizes, with seven sub-populations having differences <15%, with the lowest difference being 2%, equalling 1.5 nm for LNP7, peak 2 eluting at 48.5 minutes **(Table 6.4).** These simulations suggest further structural differences within sub-populations of LNPs formulations.

These elucidated sub-populations further emphasise key differences between formulations when developing therapeutic candidates within early development settings. Each MALS deconvoluted sub-population was further applied to a gaussian distribution profile to determine sub-population peak FWHM. Each sub-population FWHM values were entered into experimental elution profiles, cumulative distribution functions were then applied to R_G, R_H, and SF data **(Figure 6.4).** Each sub-population produced distinctive size and morphology values, with some being skewed from low detector signals due to low concentration within pre-elution times or towards the end of the elution profile. Sub-population radius sizes range from 0-230 nm, with shape factor values ranging from 0-18 **(Figure 6.4).** These insights can be used to further inform therapeutic development and optimisation.

With enhancing our understanding of AF4 usability with LNP therapeutics, a dual-detector approximation was applied to seven LNP formulations (LNP-2-8), which produced dRI signals that could be used in tandem with UV signals to calculate percentage weight of RNA and number of RNA copies within the formulation elution profile **(Figure 6.6).** Each of these formulations used SM102 formulations, however differed by RNA payload, storage buffer and formulation conditions. On applying a two-component compositional analysis, separating RNA and lipid components), fraction weight and RNA copy could be determined **(Figure 6.6).** As expected, larger numbers of smaller ASO molecules were present within the LNP-3, than Fluc mRNA in LNP4, these insights further inform sub-population size and morphology values denoted in **Table 6.5,** thus revealing enhanced insights into RNA loading, size and morphology characteristics.

Overall, this study demonstrates that combining AF4 with computational data analysis provides a more nuanced understanding of RNA-LNP formulation heterogeneity than is achievable with conventional AF4 peak-level metrics alone. By resolving the structural and compositional sub-populations across these formulations, this framework offers a more informed approach to LNP formulation optimisation, CQA definition, and ultimately, more predictive development pathways. As RNA-based nanomedicines continue to expand in complexity and clinical relevance, such hybrid analytical-computational strategies will play an essential role in bridging the gap between analytical and predictive formulation design.

6.6. Conclusion

High-resolution AF4 provides valuable insight into the critical quality attributes (CQAs) of RNA-LNP therapeutics, though its analytical capability remains constrained by resolution limits. In this work, a data-driven computational framework was applied to extend the interpretative power of AF4, enabling the identification and quantification of previously unresolved sub-populations within RNA-LNP formulations. By correlating RNA loading with sub-population size and morphology, the inherent heterogeneity present across all evaluated formulations was demonstrated. This workflow establishes a foundation for broader analytical applications, where future adaptation to electrical AF4 systems could enable separation based on differential surface charge, and centrifugal FFF could be employed for density-driven comparison of RNA-LNP populations. To validate our findings, fractions could be collected and test eluted components using analytical ultra-centrifugation. Overall, the data-driven computational pipeline developed here enhances the analytical resolution and interpretative depth achievable for RNA-LNP characterisation. By bridging the gap between experimental data and theoretical modelling, it provides a scalable platform for advancing formulation understanding and CQA assessment beyond the intrinsic limits of current analytical instrumentation.

Chapter 7

7. Overall Discussion, Future Directions and Conclusions

This chapter provides an overarching summary of the research findings from this thesis wherein ASO model drug substance purity was evaluated utilised several low resolution and comparable high-resolution analytical techniques to enhance the accessibility and uptake of lower-resolution mass spectrometry-based instrumentation in formulation laboratories (chapter 2). ASO drug substances were encapsulated into drug products using LNP delivery systems, where a panel of candidate LNP formulations were analysed using an orthogonal pipeline approach to provide deeper insights into analytical technique CQA outputs (chapter 3). Emphasising drug substance to drug product translation, three commercial brands of mRNA surrogate, Poly(A), were analysed to evaluate the impact of branded manufacturer on Poly(A) and resultant Poly(A)-LNP formulations CQAs using novel AF4 methodology. Understanding stability of candidate formulations remains critical within early-development, therefore an orthogonal analytical pipeline was applied to a cationic Poly(A)-DOTAP-LNP model formulation and evaluated resultant CQAs from process parameter impact, short term stability and frozen storage stability. Finally, combining all collected AF4 LNP generated data during the PhD, a computational-based data-processing pipeline for AF4 data was generated to enhance analysis of output size, size distribution, shape and RNA loading CQA outputs beyond the technique resolution limitations.

7.1. Thesis Summary

Nucleic acid therapeutic translation through the clinic remains slow, with a variety of late-stage failures within the trial process (196,258,261,335). Since RNA-LNP advanced therapeutics are complex within their design, excipient use and drug cargo, their remains a lack of reference materials within the field to evaluate candidate formulations against a known control. The gap created here is further expanded by evaluation of candidate formulations on a case-by-case basis through differentiated formulation design, manufacture conditions, downstream process parameters and formulation stability shelf-life. Coupled with the need for enhanced analytical techniques to deepen our understanding of CQAs, a bottleneck remains within clinical translation.

As discussed previously, the goal of this thesis is to improve the clinical translation of RNA-LNP formulations and novel therapeutics through developing more advanced, high resolution analytical methods and orthogonal analytical pipelines. Current analytical techniques used within the field are limited to those used within the quality control (QC) settings (batch-mode DLS). These methods while suitable for a QC setting, lack resolution for detailed insights into resultant formulation CQAs, which remain separated in terms of interfacing with drug substance critical quality attributes until regulatory filing submission. With a broad range of RNA therapeutics two types, gene silencing and vaccines were focused on. Gene silencing technology utilised small antisense oligonucleotide drugs (10-30 nts), compared to vaccines, which use large mRNA sequences (>1000 nts). Both drug classifications hold extensive potential for broad applicability to numerous conditions and diseases that will ultimately improve patient care if successfully clinically translated.

Chapter 2 used small ASO drugs to showcase impurity evaluation method development using HILIC separation and differential mass spectrometry systems, results derived from HILIC separation were orthogonally characterised using gel electrophoresis and IPRPLC-UV to cross-validate and verify results. Currently, there exists an accessibility gap with high-resolution MS systems with increased cost and the requirement for specialist technical expertise present significant barriers to their broader adoption across the field. To fill this gap, a lower-resolution SQ MS system was evaluated and compared to orbitrap MS to enhance ON characterisation and broader uptake within resource-limited settings. Results demonstrate similarities and differences (ON *n-1* determination) impurity analysis between MS systems, thus enabling viable low resolution system usage.

ON sequence from chapter 2, (ON2) was encapsulated in MC3 and SM102 LNP delivery systems within **chapter 3**. As ASO-LNPs remain under characterised compared to other RNA-LNP types (siRNA-LNPs, mRNA-LNPs), this work sought to address this gap. A pipeline orthogonal analytical technique approach was utilised with a panel of ASO-LNPs with varying manufacture parameters to obtain further information on output LNP CQAs, but also ASO drug substance to drug product translation. This work showcased ASO-LNP changes in size and ASO recovery CQAs were most varied when optimising formulation main ionisable lipid and microfluidic total flow rate, thus enabling deeper insights into ASO-LNP CQAs using an orthogonal pipeline approach. These insights can be used to further inform ASO-LNP formulation for novel candidate therapeutics.

As ASOs are primarily used within gene editing therapeutics, another class of RNA-LNP nanomedicines was studied. Poly(A) (mRNA surrogates), their manufacturer impact and LNP formulation CQAs using enhanced, novel analytical techniques in chapter 3. Classically, Poly(A) has served as a model RNA payload for LNP formulations and is available from three primary vendors. However, the critical quality attributes (CQAs) of these Poly(A) materials have not previously been compared with respect to molecular weight (MW), chain length, and purity profiles. In **Chapter 4**, vendor-derived Poly(A) samples were investigated, and how vendor differences influence formulation performance. This chapter also broadened the scope from RNA drug substance to drug product, an area typically examined separately in the field until late-stage regulatory development. To address this gap, three vendor-specific Poly(A) materials were sourced, characterised, and subsequently encapsulated within SM102-LNPs for further evaluation. This work presents the first application of EAF4 to characterise RNA drug substance, enabling detailed profiling of MW distribution and population-separated zeta potential, thereby providing greater resolution than conventional ensemble ELS batch-mode zeta potential measurements. Orthogonal analytical approaches revealed substantial variation in chain length and corresponding molecular weight across vendor-specific Poly(A) samples. However, these differences did not translate into the final drug product. Following encapsulation into SM102-LNPs using controlled microfluidic manufacturing and purification processes, no significant differences were observed between Poly(A)-LNP formulations. Overall, this work advances the field by supporting the integration of high-resolution analytical methods into early-stage evaluation of both drug substance and drug product, and by demonstrating that Poly(A) charge and molecular weight uniformity do not significantly influence LNP formulation properties.

Following from chapter 4, in **chapter 5,** the developed enhanced analytical orthogonal pipeline was used to characterise resultant CQAs of a candidate cationic DOTAP-LNP formulation using Poly(A) as a model drug substance within early formulation development phase. This study evaluated process parameter impact as a function of formulation CQAs, from microfluidic formulation, dialysis purification and filtration steps. Short-term stability and freeze/thaw stability using a model cryoprotectant was investigated. This study was the first to examine routine process/stability parameter impact on CQA outputs using this high-resolution pipeline. Results demonstrated enhanced insights using our orthogonal pipeline to evaluate early development formulations and obtain a higher level of detail of output CQAs, showcasing that even permanent cationic main lipid (DOTAP) LNP formulations are compatible with AF4-MD separation and multidetector platforms.

The concluding chapter (**chapter 6**) of this thesis uses obtained AF4-separated RNA-LNP formulations using pooled data from published (110,253,254) and unpublished in-house LNP formulations. Although FFF was first reported in the 1960s (194), with advancements and further modalities becoming possible with inline detection systems (197,310,336,337). Routine adoption within soft-material separation and particularly pharmaceutical research uptake remains low and enhanced insights beyond resolution limitations remains unexplored. AF4-MD data collected was applied to a computational-based data processing pipeline which was developed to analyse AF4 outputs beyond the scope of the resolving power of the technique. These CQA insights showcased distinct size and shape sub-populations which were attributed to heterogeneous loading levels of RNA across the formulations. These insights detail advanced CQA insights beyond previous studies within the field and literature. The panel of analysed LNP formulations showcased differing RNA loading and size distributions, comparing to simulated profiles showcases different microarchitectures within LNPs. RNA drug loading was also evaluated to showcase a dual-detector approximation to estimate number of RNA molecules per LNP which were matched with size and morphology outputs for enhanced insights,

7.2. Future Work

Whilst the development of novel analytical pipelines for the evaluation of RNA-based LNP formulations was achieved through analysing RNA drug substance and RNA-LNP drug products, enhanced insights into CQA outputs were obtained. Through obtaining these enhanced CQA insights, further questions were raised which could be addressed within the continuation of this work in future studies.

7.2.1. Internal LNP Architecture

After extensively analysing RNA-LNP size and size distribution using the developed pipeline across chapters 3-6, findings showed defined size and shape features of RNA-LNP formulations. Further work would enhance insights into internalised RNA-particle architecture using a panel of increasing RNA sizes in tandem with increasing ionisable lipid LNP components using x-ray scattering experiments (133,164). A mechanistic approach would simulate differing LNP environments from atomistic scale, and coarse grain molecular dynamics modelling (338,339). However, a main barrier with computational modelling and simulations is LNP complexity, with biological-based processes (endosomal maturation, RNA release) being at the longer-end of the time-scale barrier than classical micro-to-millisecond simulation experiments. This work would detail if different RNA distributions and ionisable lipids pack homogeneously within LNPs, ultimately affecting release kinetics within targeted cellular cytoplasm. With knowledge of the internal and external microarchitectural features of RNA-LNP formulations, further parameters such as particle rigidity, fluidity and porosity could be obtained to further enhance release kinetic evaluations and serve as inputs into *in-silico* models.

7.2.2. Enhanced Drug Loading Investigation

Drug loading remains a key critical quality attribute of LNP formulations regarding associated encapsulation and recovery quantification. A key limitation of the current routine fluorescence-based Ribo Green assay workflows is that they neither quantify nor resolve how the RNA drug payload is distributed across the lipid nanoparticle population and therefore do not account for population-specific loading heterogeneity. In chapter 6, preliminary data showing the relationship of ASO number loading with size and shape distributions of LNPs was shown. However enhanced insights would quantify sub-population encapsulation efficiency and recovery based on fraction collections, analysed in tandem with nanoparticle tracking analysis offering a higher degree of resolution in quantifying encapsulation efficiency. The study would utilise EAF4 developed methodology to analyse a panel of increasing nucleotide chain lengths RNA therapeutics to understand impact of chain length on higher order structures of RNA molecules to obtain deeper insights into the evaluation of higher order structure on overall RNA loading within LNPs. Further insights on LNP density and thus RNA loading could be gained by developing a centrifugal-FFF (CF3) pipeline using a singular RNA or dual fluorescently labelled RNAs for enhanced insights into dual RNA payload encapsulation and heterogeneous distribution.

7.2.3. Enhanced Endosomal Uptake and Escape

A key focus of future work will be to investigate PEG moiety shedding from LNPs as a means of tracking changes in critical quality attributes (CQAs). Quantifying PEG shedding rates can directly inform formulation design, as progressive loss of PEG alters LNP surface chemistry and, in turn, biological performance (143,340). PEG shedding could be systematically evaluated using PEG–lipids with differential chain lengths that are intentionally hydrolysed under defined environments, with resulting CQA changes assessed through mass spectrometry and AF4-based analytical pipelines. Current workflows use cryogenic electron microscopy, where less invasive methods could be used to probe these effects. These data would provide a quantitative framework to guide LNP surface decoration, including the timing and density of enhanced targeting moieties.

Building on this understanding, insights into PEG shedding would naturally extend to optimizing cellular uptake and endosomal escape. As PEG loss modulates circulation half-life and clearance, it is expected to directly influence uptake profiles and intracellular delivery efficiency. LNP designs could therefore be iteratively enhanced with uptake-promoting ligands and endosomal escape moieties to improve intracellular release of candidates. Endosomal escape efficiency could be monitored using fluorescent probes in combination with LNP-complexed cell-penetrating peptides and endosomal escape peptides (341–344). Together, this integrated and iterative experimental strategy would enable stepwise refinements in formulation design, linking PEG shedding dynamics to improved cellular uptake and endosomal escape performance.

7.2.4. Formulation Biological Interactions

With successful analysis of post-formulation RNA-LNP CQAs, the subsequent stage would be to evaluate LNP interactions with biological matrices, representing the complexity and biological composition of administration sites (e.g., intramuscular versus intravenous) (149,345). Insights gained from mimicking the site of administration could unlock LNP interaction and complexation with endogenous material to form the biomolecular corona surrounding the LNP. By mimicking administration sites like intravenous, intramuscular, intrathecal and intranasal, deeper insights into LNP CQA changes can be derived and utilised to further enhance the design of RNA-LNP formulations. These insights could also inform candidate design to translate from, *in-vitro*, to 3D-organoid and *in-vivo* work use to correlate physiochemical CQAs with each biological evaluation platform for overall LNP biological fate evaluation.

Overall deeper CQA insights from thesis future work could be combined from RNA design and impurity analysis, through formulation evaluation, biological impact and resultant overall fate within a single matrix using ML or AI networks, although limited by the need for large data sets with clear CQA trends. This overall combination would drive RNA-LNP therapeutics even further to build a library of CQAs to start to move to predictive modelling and analytics.

7.3. Conclusion

This thesis is one of the first to examine drug substance to drug product translation, with an emphasis on state-of-the-art novel analytical techniques. The outcomes of each chapter highlight the need for individualistic case-by-case evaluation of advanced nucleic acid therapeutics from drug substance through drug product within early discovery and development process. These evaluations will further increase clinical translation of novel nanomedicines to ultimately improve patient care.

References

1. Radoux CJ, Vianello F, McGreig J, Desai N, Bradley AR. The druggable genome: Twenty years later. Front Bioinform. 2022 Sep 30;2. doi:10.3389/fbinf.2022.958378

2. Smith MD, Darryl Quarles L, Demerdash O, Smith JC. Drugging the entire human proteome: Are we there yet? Drug Discovery Today. 2024 Mar 1;29(3):103891. doi:10.1016/j.drudis.2024.103891

3. Adepu S, Ramakrishna S. Controlled Drug Delivery Systems: Current Status and Future Directions. Molecules. 2021 Sep 29;26(19). doi:10.3390/molecules26195905 PubMed Central PMCID: PMC8512302.

4. Islam Ahmed Hamed Khalil IAA and MA. Overview on Nanomedicine Market. 2020.

5. Jan Moschwitzer. Special Aspects of Nanomedicines: Viewpoint from the Industry. In. Abbott; 2010.

6. Thapa RK, Kim JO. Nanomedicine-based commercial formulations: current developments and future prospects. Journal of Pharmaceutical Investigation. 2023 Jan 1;53(1):19–33. doi:10.1007/s40005-022-00607-6

7. Shan X, Gong X, Li J, Wen J, Li Y, Zhang Z. Current approaches of nanomedicines in the market and various stage of clinical translation. Acta Pharm Sin B. 2022 Jul;12(7):3028–48. doi:10.1016/j.apsb.2022.02.025 PubMed Central PMCID: PMC9293719.

8. Kulkarni JA, Witzigmann D, Thomson SB, Chen S, Leavitt BR, Cullis PR, et al. The current landscape of nucleic acid therapeutics. Nature Nanotechnology. 2021 Jun 1;16(6):630–43. doi:10.1038/s41565-021-00898-0

9. Anchordoquy T, Artzi N, Balyasnikova IV, Barenholz Y, La-Beck NM, Brenner JS, et al. Mechanisms and Barriers in Nanomedicine: Progress in the Field and Future Directions. ACS Nano. 2024 Jun 4;18(22):13983–99. doi:10.1021/acsnano.4c00182

10. Rehan F, Zhang M, Fang J, Greish K. Therapeutic Applications of Nanomedicine: Recent Developments and Future Perspectives. Molecules. 2024 Jan;29(9):9. doi:10.3390/molecules29092073

11. Jia Y, Jiang Y, He Y, Zhang W, Zou J, Magar KT, et al. Approved Nanomedicine against Diseases. Pharmaceutics. 2023 Feb 26;15(3). doi:10.3390/pharmaceutics15030774 PubMed Central PMCID: PMC10059816.

12. Abraham SA, Waterhouse DN, Mayer LD, Cullis PR, Madden TD, Bally MB. The Liposomal Formulation of Doxorubicin. In: Methods in Enzymology. Academic Press; 2005. p. 71–97.

13. Elsadek B, Kratz F. Impact of albumin on drug delivery — New applications on the horizon. Journal of Controlled Release. 2012 Jan 10;157(1):4–28. doi:10.1016/j.jconrel.2011.09.069

14. Li X, Le Y, Zhang Z, Nian X, Liu B, Yang X. Viral Vector-Based Gene Therapy. International Journal of Molecular Sciences. 2023 Jan;24(9):7736. doi:10.3390/ijms24097736

15. Ahmed A. H. Abdellatif, Abdullah Fahad Alsowinea. Approved and marketed nanoparticles for disease targeting and applications in COVID-19. Nanotechnology Reviews. 2021;10(1):1941–77. doi:doi:10.1515/ntrev-2021-0115

16. Keating GM. Ferric Carboxymaltose: A Review of Its Use in Iron Deficiency. Drugs. 2015 Jan 1;75(1):101–27. doi:10.1007/s40265-014-0332-3

17. Mishra HK, Kalyuzhny A. Revolutionizing Cancer Treatments through Stem Cell-Derived CAR T Cells for Immunotherapy: Opening New Horizons for the Future of Oncology. Cells. 2024 Jan;13(18):1516. doi:10.3390/cells13181516

18. Mah F, Milner M, Yiu S, Donnenfeld E, Conway TM, Hollander DA. PERSIST: Physician's Evaluation of Restasis® Satisfaction in Second Trial of topical cyclosporine ophthalmic emulsion 0.05% for dry eye: a retrospective review. Clinical Ophthalmology. 2012 Nov 28;6:1971–6. doi:10.2147/OPTH.S30261 PubMed PMID: 23226002.

19. Kalhapure RS, Palekar S, Patel K, Monpara J. Nanocrystals for controlled delivery: state of the art and approved drug products. Expert Opinion on Drug Delivery. 2022 Oct 3;19(10):1303–16. doi:10.1080/17425247.2022.2110579 PubMed PMID: 35930427.

20. Turecek PL, Romeder-Finger S, Apostol C, Bauer A, Crocker-Buqué A, Burger DA, et al. A world-wide survey and field study in clinical haemostasis laboratories to evaluate FVIII:C activity assay variability of ADYNOVATE and OBIZUR in comparison with ADVATE. Haemophilia. 2016;22(6):957–65. doi:10.1111/hae.13001

21. Bulbake U, Doppalapudi S, Kommineni N, Khan W. Liposomal Formulations in Clinical Use: An Updated Review. Pharmaceutics. 2017;9(2). doi:10.3390/pharmaceutics9020012

22. Hald Albertsen C, Kulkarni JA, Witzigmann D, Lind M, Petersson K, Simonsen JB. The role of lipid components in lipid nanoparticles for vaccines and gene therapy. Adv Drug Deliv Rev. 2022 Sep;188:114416. doi:10.1016/j.addr.2022.114416 PubMed Central PMCID: PMC9250827.

23. Suzuki Y, Ishihara H. Difference in the lipid nanoparticle technology employed in three approved siRNA (Patisiran) and mRNA (COVID-19 vaccine) drugs. DMPK. 2021 Dec;41:100424. doi:10.1016/j.dmpk.2021.100424 PubMed Central PMCID: PMC8502116.

24. Liu T, Tian Y, Zheng A, Cui C. Design Strategies for and Stability of mRNA-Lipid Nanoparticle COVID-19 Vaccines. Polymers (Basel). 2022 Oct 6;14(19). doi:10.3390/polym14194195 PubMed Central PMCID: PMC9572882.

25. Close AM, Handbook AG. Grading of Recommendations, Assessment, Development, and Evaluation (GRADE): Moderna mRNA RSV Vaccine (mResvia) in older adults About. 2024.

26. Zhu Y, Zhu L, Wang X, Jin H. RNA-based therapeutics: an overview and prospectus. Cell Death & Disease. 2022 Jul 23;13(7):644. doi:10.1038/s41419-022-05075-2

27. Sun X, Setrerrahmane S, Li C, Hu J, Xu H. Nucleic acid drugs: recent progress and future perspectives. Sig Transduct Target Ther. 2024 Nov 29;9(1):1–31. doi:10.1038/s41392-024-02035-4

28. Liu M, Wang Y, Zhang Y, Hu D, Tang L, Zhou B, et al. Landscape of small nucleic acid therapeutics: moving from the bench to the clinic as next-generation medicines. Sig Transduct Target Ther. 2025 Mar 10;10(1):1–57. doi:10.1038/s41392-024-02112-8

29. Saw PE, Song E. Advancements in clinical RNA therapeutics: Present developments and prospective outlooks. CR Med. 2024 May 21;5(5). doi:10.1016/j.xcrm.2024.101555 PubMed PMID: 38744276.

30. Thakur S, Sinhari A, Jain P, Jadhav HR. A perspective on oligonucleotide therapy: Approaches to patient customization. Frontiers in Pharmacology. 2022 Oct;13. doi:10.3389/fphar.2022.1006304

31. Junetsu Igarashi, Yasuharu Niwa, Daisuke Sugiyama. Research and development of oligonucleotide therapeutics in Japan for rare diseases. Future Rare Diseases. 2022;2(1):FRD19. doi:10.2217/frd-2021-0008

32. Xiao B, Wang S, Pan Y, Zhi W, Gu C, Guo T, et al. Development, opportunities, and challenges of siRNA nucleic acid drugs. Molecular Therapy Nucleic Acids. 2025 Mar 11;36(1). doi:10.1016/j.omtn.2024.102437

33. Alshaer W, Zureigat H, Al Karaki A, Al-Kadash A, Gharaibeh L, Hatmal MM, et al. siRNA: Mechanism of action, challenges, and therapeutic approaches. European Journal of Pharmacology. 2021 Aug 15;905:174178. doi:10.1016/j.ejphar.2021.174178

34. Deng Z, Tian Y, Song J, An G, Yang P. mRNA Vaccines: The Dawn of a New Era of Cancer Immunotherapy. Front Immunol. 2022 Jun 2;13. doi:10.3389/fimmu.2022.887125

35. Gote V, Bolla PK, Kommineni N, Butreddy A, Nukala PK, Palakurthi SS, et al. A Comprehensive Review of mRNA Vaccines. International Journal of Molecular Sciences. 2023 Jan 30;24(3). doi:10.3390/ijms24032700

36. Guilherme J Guimaraes, J. Michael Sutton, Martin Gilar, Michael Donegan, Michael G. Bartlett. Impact of Nonspecific Adsorption to Metal Surfaces in Ion Pair-RP LC-MS Impurity Analysis of Oligonucleotides. Journal of Pharmaceutical and Biomedical Analysis. 2022. doi:10.1016/j.jpba.2021.114439

37. Chan JH, Lim S, Wong WF. ANTISENSE OLIGONUCLEOTIDES: FROM DESIGN TO THERAPEUTIC APPLICATION. Clinical and Experimental Pharmacology and Physiology. 2006;33(5–6):533–40. doi:https://doi.org/10.1111/j.1440-1681.2006.04403.x

38. Roberts TC, Langer R, Wood MJA. Advances in oligonucleotide drug delivery. Nature Reviews Drug Discovery. 2020 Oct 1;19(10):673–94. doi:10.1038/s41573-020-0075-7

39. Moumné L, Marie AC, Crouvezier N. Oligonucleotide Therapeutics: From Discovery and Development to Patentability. Pharmaceutics. 2022 Jan 22;14(2). doi:10.3390/pharmaceutics14020260 PubMed Central PMCID: PMC8876811.

40. Muslehiddinoglu J, Simler R, Hill ML, Mueller C, Amery JHA, Dixon L, et al. Technical Considerations for Use of Oligonucleotide Solution API. Nucleic Acid Ther. 2020 Aug;30(4):189–97. doi:10.1089/nat.2020.0846 PubMed Central PMCID: PMC7415879.

41. Lönnberg H. Solid-Phase Synthesis of Oligonucleotide Conjugates Useful for Delivery and Targeting of Potential Nucleic Acid Therapeutics. Bioconjugate Chem. 2009 Jun 17;20(6):1065–94. doi:10.1021/bc800406a

42. Bizat PN, Sabat N, Hollenstein M. Recent Advances in Biocatalytic and Chemoenzymatic Synthesis of Oligonucleotides. ChemBioChem. 2025;26(9):e202400987. doi:10.1002/cbic.202400987

43. Nourafkan E, Kenyon C, Nair A, Loveday KA, Welbourne EN, Tao M, et al. An Experimental and Modeling Approach to Study Tangential Flow Filtration Performance for mRNA Drug Substance Purification. Biotechnology Journal. 2024;19(11):e202400473. doi:10.1002/biot.202400473

44. Welbourne EN, Loveday KA, Nair A, Nourafkan E, Qu J, Cook K, et al. Anion exchange HPLC monitoring of mRNA in vitro transcription reactions to support mRNA manufacturing process development. Front Mol Biosci. 2024 Mar 7;11. doi:10.3389/fmolb.2024.1250833

45. Camperi J, Lippold S, Ayalew L, Roper B, Shao S, Freund E, et al. Comprehensive Impurity Profiling of mRNA: Evaluating Current Technologies and Advanced Analytical Techniques. Anal Chem. 2024 Mar 5;96(9):3886–97. doi:10.1021/acs.analchem.3c05539

46. Rentel C, Gaus H, Bradley K, Luu N, Kolkey K, Mai B, et al. Assay, Purity, and Impurity Profile of Phosphorothioate Oligonucleotide Therapeutics by Ion Pair-HPLC-MS. Nucleic Acid Ther. 2022 Jun;32(3):206–20. doi:10.1089/nat.2021.0056

47. Hammond SM, Aartsma-Rus A, Alves S, Borgos SE, Buijsen RAM, Collin RWJ, et al. Delivery of oligonucleotide-based therapeutics: challenges and opportunities. EMBO Mol Med. 2021 Apr 9;13(4):e13243. doi:10.15252/emmm.202013243 PubMed Central PMCID: PMC8033518.

48. Bost JP, Barriga H, Holme MN, Gallud A, Maugeri M, Gupta D, et al. Delivery of Oligonucleotide Therapeutics: Chemical Modifications, Lipid Nanoparticles, and Extracellular Vesicles. ACS nano. 2021 Sep 28;15(9):13993–4021. doi:10.1021/acsnano.1c05099 PubMed Central PMCID: PMC8482762.

49. Ebrahimi SB, Bhattacharjee H, Sonti S, Fuerst D, Doyle PS, Lu Y, et al. Engineering considerations for next-generation oligonucleotide therapeutics. Nat Chem Eng. 2024 Dec;1(12):741–50. doi:10.1038/s44286-024-00152-z

50. Pan Y, Guan J, Gao Y, Zhu Y, Li H, Guo H, et al. Modified ASO conjugates encapsulated with cytidinyl/cationic lipids exhibit more potent and longer-lasting anti-HCC effects. Molecular Therapy Nucleic Acids. 2023 Jun 13;32:807–21. doi:10.1016/j.omtn.2023.04.028 PubMed PMID: 37251692.

51. Osawa T, Kita R, Kasahara Y, Yamaguma H, Nakayama T, Kamada H, et al. *In vitro* screening of chemically synthesized dipeptide-antisense oligonucleotide conjugates to identify ligand molecules enhancing their activity. Bioorganic & Medicinal Chemistry. 2024 Aug 1;110:117814. doi:10.1016/j.bmc.2024.117814

52. Kay E, Stulz R, Becquart C, Lovric J, Tängemo C, Thomen A, et al. NanoSIMS Imaging Reveals the Impact of Ligand-ASO Conjugate Stability on ASO Subcellular Distribution. Pharmaceutics. 2022 Feb;14(2):2. doi:10.3390/pharmaceutics14020463

53. Cochran M, Arias D, Burke R, Chu D, Erdogan G, Hood M, et al. Structure–Activity Relationship of Antibody–Oligonucleotide Conjugates: Evaluating Bioconjugation Strategies for Antibody–siRNA Conjugates for Drug Development. J Med Chem. 2024 Sep 12;67(17):14852–67. doi:10.1021/acs.jmedchem.4c00802

54. Jiao J, Qian Y, Lv Y, Wei W, Long Y, Guo X, et al. Overcoming limitations and advancing the therapeutic potential of antibody-oligonucleotide conjugates (AOCs): Current status and future perspectives. Pharmacological Research. 2024 Nov 1;209:107469. doi:10.1016/j.phrs.2024.107469

55. Meng Q, Yang M, Xing F, Xie Z, Hao Y, Jiang P, et al. Antibody-oligonucleotide conjugates in cancer therapy: Potential and Promise. Critical Reviews in Oncology/Hematology. 2025 Nov 1;215:104858. doi:10.1016/j.critrevonc.2025.104858

56. Zhao C, Li X, He Z, Ye C, Chen F, Cheng J. PEG-ASO conjugates for efficient targeted delivery and migration inhibition in Cancer cell. Bioorganic & Medicinal Chemistry Letters. 2025 Jul 1;122:130208. doi:10.1016/j.bmcl.2025.130208

57. Marchesi E, Cortesi R, Preti L, Rimessi P, Sguizzato M, Bovolenta M, et al. Antisense Oligonucleotides Conjugated with Lipophilic Compounds: Synthesis and In Vitro Evaluation of Exon Skipping in Duchenne Muscular Dystrophy. International Journal of Molecular Sciences. 2022 Jan;23(8):8. doi:10.3390/ijms23084270

58. Debacker AJ, Voutila J, Catley M, Blakey D, Habib N. Delivery of Oligonucleotides to the Liver with GalNAc: From Research to Registered Therapeutic Drug. Molecular Therapy. 2020 Aug 5;28(8):1759–71. doi:10.1016/j.ymthe.2020.06.015 PubMed PMID: 32592692.

59. Prakash TP, Yu J, Migawa MT, Kinberger GA, Wan WB, Østergaard ME, et al. Comprehensive Structure–Activity Relationship of Triantennary N-Acetylgalactosamine Conjugated Antisense Oligonucleotides for Targeted Delivery to Hepatocytes. J Med Chem. 2016 Mar 24;59(6):2718–33. doi:10.1021/acs.jmedchem.5b01948

60. Sharma K, Sharma KK, Sharma A, Jain R. Peptide-based drug discovery: Current status and recent advances. Drug Discovery Today. 2023 Feb 1;28(2):103464. doi:10.1016/j.drudis.2022.103464

61. Wang L, Wang N, Zhang W, Cheng X, Yan Z, Shao G, et al. Therapeutic peptides: current applications and future directions. Sig Transduct Target Ther. 2022 Feb 14;7(1):48. doi:10.1038/s41392-022-00904-4

62. Zhao B, Tian Q, Bagheri Y, You M. Lipid–oligonucleotide conjugates for simple and efficient cell membrane engineering and bioanalysis. Current Opinion in Biomedical Engineering. 2020 Mar 1;Futures of Biomedical Engineering: Bioengineering of Organoids and Tissue Development ● Biomaterials: Biosensors13:76–83. doi:10.1016/j.cobme.2019.12.006

63. Witten J, Hu Y, Langer R, Anderson DG. Recent advances in nanoparticulate RNA delivery systems. Proceedings of the National Academy of Sciences. 2024 Mar 12;121(11):e2307798120. doi:10.1073/pnas.2307798120

64. Cox A, Lim SA, Chung EJ. Strategies to deliver RNA by nanoparticles for therapeutic potential. Molecular Aspects of Medicine. 2022 Feb 1;Delivery to tissues83:100991. doi:10.1016/j.mam.2021.100991

65. Kaczmarek JC, Kowalski PS, Anderson DG. Advances in the delivery of RNA therapeutics: from concept to clinical reality. Genome Medicine. 2017 Jun 27;9(1):60. doi:10.1186/s13073-017-0450-0

66. Vosoughi P, Naghib SM, Kangarshahi BM, Mozafari MR. A review of RNA nanoparticles for drug/gene/protein delivery in advanced therapies: Current state and future prospects. International Journal of Biological Macromolecules. 2025 Mar 1;295:139532. doi:10.1016/j.ijbiomac.2025.139532

67. Revia RA, Stephen ZR, Zhang M. Theranostic Nanoparticles for RNA-Based Cancer Treatment. Acc Chem Res. 2019 Jun 18;52(6):1496–506. doi:10.1021/acs.accounts.9b00101

68. Emiliano Ferdows B, Neal Patel D, Chen W, Huang X, Kong N, Tao W. RNA cancer nanomedicine: nanotechnology-mediated RNA therapy. Nanoscale. 2022;14(12):4448–55. doi:10.1039/D1NR06991H

69. van der Meel R, Wender PA, Merkel OM, Lostalé-Seijo I, Montenegro J, Miserez A, et al. Next-generation materials for nucleic acid delivery. Nat Rev Mater. 2025 Jun 16;1–10. doi:10.1038/s41578-025-00814-1

70. Martins C, Mitchell MJ, Peer D, Perrie Y, Siegwart DJ, Alonso MJ, et al. The RNA delivery dilemma—lipid versus polymer nanoparticle platforms. Drug Deliv and Transl Res. 2026 Jan 30. doi:10.1007/s13346-026-02044-6

71. Gu Y, Chen J, Wang Z, Liu C, Wang T, Kim CJ, et al. mRNA delivery enabled by metal–organic nanoparticles. Nat Commun. 2024 Nov 8;15(1):9664. doi:10.1038/s41467-024-53969-w

72. Zhang N, Xiong G, Liu Z. Toxicity of metal-based nanoparticles: Challenges in the nano era. Front Bioeng Biotechnol. 2022 Nov 10;10:1001572. doi:10.3389/fbioe.2022.1001572 PubMed PMID: 36619393; PubMed Central PMCID: PMC9822575.

73. Egli M, Manoharan M. Chemistry, structure and function of approved oligonucleotide therapeutics. Nucleic acids research. 2023 07;51. doi:10.1093/nar/gkad067

74. Deamer DW. From “Banghasomes” to liposomes: A memoir of Alec Bangham, 1921–2010. The FASEB Journal. 2010 May 1;24(5):1308–10. doi:https://doi.org/10.1096/fj.10-0503

75. Sessa G, Weissmann G. Phospholipid spherules (liposomes) as a model for biological membranes. J Lipid Res. 1968 May;9(3):310–8.

76. Exelead. Liposomes and Lipid Nanoparticles as Delivery Vehicles for Personalized Medicine. 2018.

77. Anselmo AC, Mitragotri S. Nanoparticles in the clinic: An update. Bioeng Transl Med. 2019 Sep;4(3):e10143. doi:10.1002/btm2.10143 PubMed Central PMCID: PMC6764803.

78. Thi TTH, Suys EJA, Lee JS, Nguyen DH, Park KD, Truong NP. Lipid-Based Nanoparticles in the Clinic and Clinical Trials: From Cancer Nanomedicine to COVID-19 Vaccines. Vaccines (Basel). 2021 Apr 8;9(4). doi:10.3390/vaccines9040359 PubMed Central PMCID: PMC8069344.

79. Eygeris Y, Gupta M, Kim J, Sahay G. Chemistry of Lipid Nanoparticles for RNA Delivery. Acc Chem Res. 2022 Jan 4;55(1):2–12. doi:10.1021/acs.accounts.1c00544

80. He Y, Bi D, Plantinga JA, Molema G, Bussmann J, Kamps J. Development of a Combined Lipid-Based Nanoparticle Formulation for Enhanced siRNA Delivery to Vascular Endothelial Cells. Pharmaceutics. 2022 Sep 29;14(10). doi:10.3390/pharmaceutics14102086 PubMed Central PMCID: PMC9609090.

81. Roces CB, Lou G, Jain N, Abraham S, Thomas A, Halbert GW, et al. Manufacturing Considerations for the Development of Lipid Nanoparticles Using Microfluidics. Pharmaceutics. 2020 Nov 15;12(11). doi:10.3390/pharmaceutics12111095 PubMed Central PMCID: PMC7697682.

82. Hou X, Zaks T, Langer R, Dong Y. Lipid nanoparticles for mRNA delivery. Nat Rev Mater. 2021;6(12):1078–94. doi:10.1038/s41578-021-00358-0

83. Kulkarni JA, Witzigmann D, Leung J, Tam YYC, Cullis PR. On the role of helper lipids in lipid nanoparticle formulations of siRNA. Nanoscale. 2019 Nov 21;11(45):21733–9. doi:10.1039/c9nr09347h

84. McMillan C, Druschitz A, Rumbelow S, Borah A, Macfarlane R, Rattray Z, et al. Influence of ionisable lipid and sterol variations on lipid nanoparticle properties and performance. Journal of Controlled Release. 2025 Oct 10;386:114056. doi:10.1016/j.jconrel.2025.114056

85. Semple SC, Chonn A, Cullis PR. Influence of cholesterol on the association of plasma proteins with liposomes. Biochem. 1996 Feb 27;35(8):2521–5. doi:10.1021/bi950414i

86. Kulkarni JA, Darjuan MM, Mercer JE, Chen S, van der Meel R, Thewalt JL, et al. On the Formation and Morphology of Lipid Nanoparticles Containing Ionizable Cationic Lipids and siRNA. ACS nano. 2018 May 22;12(5):4787–95. doi:10.1021/acsnano.8b01516

87. Yanez Arteta M, Kjellman T, Bartesaghi S, Wallin S, Wu X, Kvist AJ, et al. Successful reprogramming of cellular protein production through mRNA delivered by functionalized lipid

nanoparticles. Proceedings of the National Academy of Sciences. 2018 Apr 10;115(15):E3351–60. doi:10.1073/pnas.1720542115

88. Patel S, Ashwanikumar N, Robinson E, Xia Y, Mihai C, Griffith JP, et al. Naturally-occurring cholesterol analogues in lipid nanoparticles induce polymorphic shape and enhance intracellular delivery of mRNA. Nat Commun. 2020 Feb 20;11(1):983. doi:10.1038/s41467-020-14527-2

89. Zhang R, El-Mayta R, Murdoch TJ, Warzecha CC, Billingsley MM, Shepherd SJ, et al. Helper lipid structure influences protein adsorption and delivery of lipid nanoparticles to spleen and liver. Biomaterials Science. 2021;9(4):1449–63. doi:10.1039/D0BM01609H

90. Ge X, Chen L, Zhao B, Yuan W. Rationale and Application of PEGylated Lipid-Based System for Advanced Target Delivery of siRNA. Front pharmacol. 2020;11:598175. doi:10.3389/fphar.2020.598175 PubMed Central PMCID: PMC7944141.

91. Suzuki T, Suzuki Y, Hihara T, Kubara K, Kondo K, Hyodo K, et al. PEG shedding-rate-dependent blood clearance of PEGylated lipid nanoparticles in mice: Faster PEG shedding attenuates anti-PEG IgM production. Int J Pharm. 2020 Oct 15;588:119792. doi:https://doi.org/10.1016/j.ijpharm.2020.119792

92. Moss KH, Popova P, Hadrup SR, Astakhova K, Taskova M. Lipid Nanoparticles for Delivery of Therapeutic RNA Oligonucleotides. Mol Pharmaceutics. 2019 Jun 3;16(6):2265–77. doi:10.1021/acs.molpharmaceut.8b01290

93. Zhang H. Thin-Film Hydration Followed by Extrusion Method for Liposome Preparation. In: D'Souza GGM, editor. Liposomes: Methods and Protocols. New York, NY: Springer New York; 2017. p. 17–22.

94. Xiang B, Cao DY. Preparation of drug liposomes by thin-film hydration and homogenization. Liposome-based drug delivery systems. 2021;25–35.

95. Patel RP, Patel H, Baria AH. Formulation and evaluation of liposomes of ketoconazole. Int J Drug Deliv Technol. 2009;1(1):16–23.

96. Gouda A, Sakr OS, Nasr M, Sammour O. Ethanol injection technique for liposomes formulation: An insight into development, influencing factors, challenges and applications. Journal of Drug Delivery Science and Technology. 2021 Feb 1;61:102174. doi:https://doi.org/10.1016/j.jddst.2020.102174

97. Deamer DW. PREPARATION AND PROPERTIES OF ETHER-INJECTION LIPOSOMES *. Annals of the New York Academy of Sciences. 1978 Jun 1;308(1):250–8. doi:https://doi.org/10.1111/j.1749-6632.1978.tb22027.x

98. Guimarães D, Noro J, Loureiro A, Lager F, Renault G, Cavaco-Paulo A, et al. Increased Encapsulation Efficiency of Methotrexate in Liposomes for Rheumatoid Arthritis Therapy. Biomedicines. 2020;8(12). doi:10.3390/biomedicines8120630

99. Khadke S, Roces CB, Donaghey R, Giacobbo V, Su Y, Perrie Y. Scalable solvent-free production of liposomes. Journal of Pharmacy and Pharmacology. 2020;72(10):1328–40. doi:10.1111/jphp.13329

100. Perrie Y, Kastner E, Khadke S, Roces CB, Stone P. Manufacturing Methods for Liposome Adjuvants. In: Fox CB, editor. Vaccine Adjuvants: Methods and Protocols. New York, NY: Springer New York; 2017. p. 127–44.

101. Vemuri S, Yu CD, Degroot JS, Roosdorp N. In Vitro Interaction of Sized and Unsized Liposome Vesicles with High Density Lipo Proteins. Drug Development and Industrial Pharmacy. 1990 Jan 1;16(9):1579–84. doi:10.3109/03639049009074385

102. Stachowiak JC, Richmond DL, Li TH, Liu AP, Parekh SH, Fletcher DA. Unilamellar vesicle formation and encapsulation by microfluidic jetting. Proc Natl Acad Sci U S A. 2008 Mar 25;105(12):4697–702. doi:10.1073/pnas.0710875105 PubMed Central PMCID: PMC2290793.

103. Chen Y, Chen W, Ren Y, Li S, Liu M, Xing J, et al. Lipid nanoparticle-encapsulated VEGFa siRNA facilitates cartilage formation by suppressing angiogenesis. Int J Biol Macromol. 2022 Nov 30;221:1313–24. doi:10.1016/j.ijbiomac.2022.09.065

104. Carugo D, Bottaro E, Owen J, Stride E, Nastruzzi C. Liposome production by microfluidics: potential and limiting factors. Sci Rep. 2016 May 19;6:25876. doi:10.1038/srep25876 PubMed Central PMCID: PMC4872163.

105. Hourdel L, Lebaz N, Peral F, Ripoll M, Briançon S, Bensaid F, et al. Overview on LNP-mRNA encapsulation unit operation: Mixing technologies, scalability, and influence of formulation & process parameters on physico-chemical characteristics. International Journal of Pharmaceutics. 2025 Mar 15;672:125297. doi:10.1016/j.ijpharm.2025.125297

106. Hengelbrock A, Schmidt A, Strube J. Formulation of Nucleic Acids by Encapsulation in Lipid Nanoparticles for Continuous Production of mRNA. Processes. 2023;11(6):1718.

107. Tam YYC, Chen S, Cullis PR. Advances in Lipid Nanoparticles for siRNA Delivery. Pharmaceutics. 2013;5(3):498–507.

108. Kim J, Eygeris Y, Gupta M, Sahay G. Self-assembled mRNA vaccines. Advanced Drug Delivery Reviews. 2021 Mar 1;170:83–112. doi:https://doi.org/10.1016/j.addr.2020.12.014

109. Lou G, Anderluzzi G, Schmidt ST, Woods S, Gallorini S, Brazzoli M, et al. Delivery of self-amplifying mRNA vaccines by cationic lipid nanoparticles: The impact of cationic lipid selection. JCR. 2020 Sep 10;325:370–9. doi:10.1016/j.jconrel.2020.06.027

110. Forrester J, Davidson CG, Blair M, Donlon L, McLoughlin DM, Obiora CR, et al. Low-Cost Microfluidic Mixers: Are They up to the Task? Pharmaceutics. 2025 May;17(5):5. doi:10.3390/pharmaceutics17050566

111. Zhigaltsev IV, Belliveau N, Hafez I, Leung AKK, Huft J, Hansen C, et al. Bottom-Up Design and Synthesis of Limit Size Lipid Nanoparticle Systems with Aqueous and Triglyceride Cores Using Millisecond Microfluidic Mixing. Langmuir. 2012 Feb 21;28(7):3633–40. doi:10.1021/la204833h

112. Webb C, Forbes N, Roces CB, Anderluzzi G, Lou G, Abraham S, et al. Using microfluidics for scalable manufacturing of nanomedicines from bench to GMP: A case study using protein-loaded liposomes. International Journal of Pharmaceutics. 2020 May 30;582:119266. doi:https://doi.org/10.1016/j.ijpharm.2020.119266

113. Shepherd SJ, Issadore D, Mitchell MJ. Microfluidic formulation of nanoparticles for biomedical applications. Biomaterials. 2021 Jul 1;274:120826. doi:https://doi.org/10.1016/j.biomaterials.2021.120826

114. Shepherd SJ, Warzecha CC, Yadavali S, El-Mayta R, Alameh MG, Wang L, et al. Scalable mRNA and siRNA Lipid Nanoparticle Production Using a Parallelized Microfluidic Device. Nano Letters. 2021 Jul 14;21(13):5671–80. doi:10.1021/acs.nanolett.1c01353

115. Tomeh MA, Zhao X. Recent Advances in Microfluidics for the Preparation of Drug and Gene Delivery Systems. Molecular Pharmaceutics. 2020 Dec 7;17(12):4421–34. doi:10.1021/acs.molpharmaceut.0c00913

116. Jaradat E, Weaver E, Meziane A, Lamprou DA. Microfluidic paclitaxel-loaded lipid nanoparticle formulations for chemotherapy. International Journal of Pharmaceutics. 2022 Nov 25;628:122320. doi:https://doi.org/10.1016/j.ijpharm.2022.122320

117. Terada T, Kulkarni JA, Huynh A, Chen S, van der Meel R, Tam YYC, et al. Characterization of Lipid Nanoparticles Containing Ionizable Cationic Lipids Using Design-of-Experiments Approach. Langmuir. 2021 Jan 26;37(3):1120–8. doi:10.1021/acs.langmuir.0c03039

118. Mashima R, Takada S. Lipid Nanoparticles: A Novel Gene Delivery Technique for Clinical Application. Curr Issues Mol Biol. 2022 Oct 19;44(10):5013–27. doi:10.3390/cimb44100341 PubMed Central PMCID: PMC9600891.

119. Kamiya M, Matsumoto M, Yamashita K, Izumi T, Kawaguchi M, Mizukami S, et al. Stability Study of mRNA-Lipid Nanoparticles Exposed to Various Conditions Based on the Evaluation between Physicochemical Properties and Their Relation with Protein Expression Ability. Pharmaceutics. 2022;14(11).

120. Schoenmaker L, Witzigmann D, Kulkarni JA, Verbeke R, Kersten G, Jiskoot W, et al. mRNA-lipid nanoparticle COVID-19 vaccines: Structure and stability. International Journal of Pharmaceutics. 2021 May 15;601:120586. doi:https://doi.org/10.1016/j.ijpharm.2021.120586

121. Blakney AK, McKay PF, Yus BI, Aldon Y, Shattock RJ. Inside out: optimization of lipid nanoparticle formulations for exterior complexation and in vivo delivery of saRNA. Gene Ther. 2019 Sep;26(9):363–72. doi:10.1038/s41434-019-0095-2 PubMed Central PMCID: PMC6760535.

122. Aburai K, Hatanaka K, Takano S, Fujii S, Sakurai K. Characterizing an siRNA-Containing Lipid-Nanoparticle Prepared by a Microfluidic Reactor: Small-Angle X-ray Scattering and Cryotransmission Electron Microscopic Studies. Langmuir. 2020 Oct 27;36(42):12545–54. doi:10.1021/acs.langmuir.0c01079

123. Jeengar MK, Kurakula M, Patil P, More A, Sistla R, Parashar D. Effect of Cationic Lipid Nanoparticle Loaded siRNA with Stearylamine against Chikungunya Virus. Molecules. 2022 Feb 9;27(4). doi:10.3390/molecules27041170 PubMed Central PMCID: PMC8877324.

124. Swart LE, Koekman CA, Seinen CW, Issa. H, Rasouli. M, Schiffelers RM, et al. A robust post-insertion method for the preparation of targeted siRNA LNPs. International Journal of Pharmaceutics. 2022 May 25;620:121741. doi:10.1016/j.ijpharm.2022.121741

125. Zimmermann CM, Deßloch L, Jürgens DC, Luciani P, Merkel OM. Evaluation of the effects of storage conditions on spray-dried siRNA-LNPs before and after subsequent drying. European Journal of Pharmaceutics and Biopharmaceutics. 2023 Dec 1;193:218–26. doi:10.1016/j.ejpb.2023.11.007

126. Farokhzad RA, Luo J, Jia L, Zhang Y, Shi J. Lipid Nanoparticle Delivery of mRNA and siRNA for Concurrent Restoration of Tumor Suppressor and Inhibition of Tumorigenic Driver in Prostate Cancer. ACS Nanosci Au. 2025 Aug 20;5(4):284–92. doi:10.1021/acsnanoscienceau.4c00066

127. Alabi CA, Love KT, Sahay G, Yin H, Luly KM, Langer R, et al. Multiparametric approach for the evaluation of lipid nanoparticles for siRNA delivery. Proceedings of the National Academy of Sciences. 2013 Aug 6;110(32):12881–6. doi:10.1073/pnas.1306529110

128. Hussain M, Binici B, O’Connor L, Perrie Y. Production of mRNA lipid nanoparticles using advanced crossflow micromixing. Journal of Pharmacy and Pharmacology. 2024. doi:10.1093/jpp/rgae122

129. Leighton LJ, Chaudhary N, Tompkins HT, Kulkarni A, Carrodus NL, Budzinska MA, et al. The design, manufacture and LNP formulation of mRNA for research use. Nat Protoc. 2025 Jun 10;1–30. doi:10.1038/s41596-025-01174-4

130. Binici B, Rattray Z, Perrie Y. A comparative study of cationic lipid-enriched LNPs for mRNA vaccine delivery. International Journal of Pharmaceutics. 2025 Sep 15;682:125941. doi:10.1016/j.ijpharm.2025.125941

131. Bepperling A, Richter G. Determination of mRNA copy number in degradable lipid nanoparticles via density contrast analytical ultracentrifugation. Eur Biophys J. 2023 Jul 1;52(4):393–400. doi:10.1007/s00249-023-01663-y

132. Li S, Hu Y, Li A, Lin J, Hsieh K, Schneiderman Z, et al. Payload distribution and capacity of mRNA lipid nanoparticles. Nat Commun. 2022 Sep 23;13(1):5561. doi:10.1038/s41467-022-33157-4

133. Graewert MA, Wilhelmy C, Bacic T, Schumacher J, Blanchet C, Meier F, et al. Quantitative size-resolved characterization of mRNA nanoparticles by in-line coupling of asymmetrical-flow field-flow fractionation with small angle X-ray scattering. Sci Rep. 2023 Sep 22;13(1):15764. doi:10.1038/s41598-023-42274-z

134. Gao Z, Lin J, Su WC, Zhang K, Gruenhagen J, Zhong W, et al. Development of an advanced separation and characterization platform for mRNA and lipid nanoparticles using multi-detector asymmetrical flow field-flow fractionation. Anal Bioanal Chem. 2024 Oct 1;416(24):5281–93. doi:10.1007/s00216-024-05455-x

135. Ly HH, Daniel S, Soriano SKV, Kis Z, Blakney AK. Optimization of Lipid Nanoparticles for saRNA Expression and Cellular Activation Using a Design-of-Experiment Approach. Molecular Pharmaceutics. 2022 Jun 6;19(6):1892–905. doi:10.1021/acs.molpharmaceut.2c00032

136. Anderluzzi G, Lou G, Woods S, Schmidt ST, Gallorini S, Brazzoli M, et al. The role of nanoparticle format and route of administration on self-amplifying mRNA vaccine potency. Journal of Controlled Release. 2022 Feb 1;342:388–99. doi:10.1016/j.jconrel.2021.12.008

137. Geall AJ, Verma A, Otten GR, Shaw CA, Hekele A, Banerjee K, et al. Nonviral delivery of self-amplifying RNA vaccines. Proceedings of the National Academy of Sciences. 2012 Sep 4;109(36):14604–9. doi:10.1073/pnas.1209367109

138. Goswami R, Chatzikleanthous D, Lou G, Giusti F, Bonci A, Taccone M, et al. Mannosylation of LNP Results in Improved Potency for Self-Amplifying RNA (SAM) Vaccines. ACS Infect Dis. 2019 Sep 13;5(9):1546–58. doi:10.1021/acsinfecdis.9b00084

139. Anderluzzi G, Lou G, Gallorini S, Brazzoli M, Johnson R, O’Hagan DT, et al. Investigating the Impact of Delivery System Design on the Efficacy of Self-Amplifying RNA Vaccines. Vaccines. 2020 Jun;8(2):212. doi:10.3390/vaccines8020212

140. Reid GL. Chapter 17 - Residual solvents. In: Riley CM, Nguyen KL, editors. Specification of Drug Substances and Products (Third Edition) [Internet]. Elsevier; 2025 [cited 2025 Jun 18]. p. 421–38. Available from: https://www.sciencedirect.com/science/article/pii/B9780443134661000362 doi:10.1016/B978-0-443-13466-1.00036-2

141. Binici B, Borah A, Watts JA, McLoughlin D, Perrie Y. The influence of citrate buffer molarity on mRNA-LNPs: Exploring factors beyond general critical quality attributes. International Journal of Pharmaceutics. 2025 Jan 5;668:124942. doi:10.1016/j.ijpharm.2024.124942

142. McMillan C, Druschitz A, Rumbelow S, Borah A, Binici B, Rattray Z, et al. Tailoring lipid nanoparticle dimensions through manufacturing processes. RSC Pharm. 2024 Oct 15;1(4):841–53. doi:10.1039/D4PM00128A

143. Mui BL, Tam YK, Jayaraman M, Ansell SM, Du X, Tam YY, et al. Influence of Polyethylene Glycol Lipid Desorption Rates on Pharmacokinetics and Pharmacodynamics of siRNA Lipid Nanoparticles. Mol Ther Nucleic Acids. 2013 Dec 17;2(12):e139. doi:10.1038/mtna.2013.66 PubMed Central PMCID: PMC3894582.

144. Larson NR, Hu G, Wei Y, Tuesca AD, Forrest ML, Middaugh CR. pH-Dependent Phase Behavior and Stability of Cationic Lipid–mRNA Nanoparticles. Journal of Pharmaceutical Sciences. 2022 Mar 1;111(3):690–8. doi:https://doi.org/10.1016/j.xphs.2021.11.004

145. Love KT, Mahon KP, Levins CG, Whitehead KA, Querbes W, Dorkin JR, et al. Lipid-like materials for low-dose, in vivo gene silencing. Proceedings of the National Academy of Sciences. 2010 Feb 2;107(5):1864–9. doi:10.1073/pnas.0910603106

146. Zhou JE, Sun L, Liu L, Jia Y, Han Y, Shao J, et al. Hepatic macrophage targeted siRNA lipid nanoparticles treat non-alcoholic steatohepatitis. JCR. 2022 Mar 1;343:175–86. doi:https://doi.org/10.1016/j.jconrel.2022.01.038

147. Hassett KJ, Higgins J, Woods A, Levy B, Xia Y, Hsiao CJ, et al. Impact of lipid nanoparticle size on mRNA vaccine immunogenicity. JCR. 2021 Jul 10;335:237–46. doi:https://doi.org/10.1016/j.jconrel.2021.05.021

148. Nakamura K, Aihara K, Ishida T. Importance of Process Parameters Influencing the Mean Diameters of siRNA-Containing Lipid Nanoparticles (LNPs) on the *in Vitro* Activity of Prepared LNPs. Biological and Pharmaceutical Bulletin. 2022;45(4):497–507. doi:10.1248/bpb.b21-01016

149. Münter R, Christensen E, Andresen TL, Larsen JB. Studying how administration route and dose regulates antibody generation against LNPs for mRNA delivery with single-particle resolution. Molecular Therapy - Methods & Clinical Development. 2023 Jun 8;29:450–9. doi:10.1016/j.omtm.2023.05.008

150. Xu X, Xia T. Recent Advances in Site-Specific Lipid Nanoparticles for mRNA Delivery. ACS Nanosci Au. 2023 Jun 21;3(3):192–203. doi:10.1021/acsnanoscienceau.2c00062

151. Ongun M, Lokras AG, Baghel S, Shi Z, Schmidt ST, Franzyk H, et al. Lipid nanoparticles for local delivery of mRNA to the respiratory tract: Effect of PEG-lipid content and administration route. European Journal of Pharmaceutics and Biopharmaceutics. 2024 May 1;198:114266. doi:10.1016/j.ejpb.2024.114266

152. Müller JA, Schäffler N, Kellerer T, Schwake G, Ligon TS, Rädler JO. Kinetics of RNA-LNP delivery and protein expression. European Journal of Pharmaceutics and Biopharmaceutics. 2024 Apr 1;197:114222. doi:10.1016/j.ejpb.2024.114222

153. Francia V, Zhang Y, Cheng MHY, Schiffelers RM, Witzigmann D, Cullis PR. A magnetic separation method for isolating and characterizing the biomolecular corona of lipid nanoparticles. Proceedings of the National Academy of Sciences. 2024 Mar 12;121(11):e2307803120. doi:10.1073/pnas.2307803120

154. Li S, Cortez-Jugo C, Ju Y, Caruso F. Approaching Two Decades: Biomolecular Coronas and Bio–Nano Interactions. ACS Nano. 2024 Dec 10;18(49):33257–63. doi:10.1021/acsnano.4c13214

155. Francia V, Schiffelers RM, Cullis PR, Witzigmann D. The Biomolecular Corona of Lipid Nanoparticles for Gene Therapy. Bioconjugate Chem. 2020 Sep 16;31(9):2046–59. doi:10.1021/acs.bioconjchem.0c00366

156. Abdulrahman R, Punnabhum P, Capomaccio R, Treacher K, Perrie Y, Rattray Z. Frit-inlet asymmetric flow field-flow fractionation for the analysis of lipid nanoparticle-protein interactions. Journal of Chromatography A. 2025 Feb 22;1743:465663. doi:10.1016/j.chroma.2025.465663

157. Stern A, Petersen AP, Zierden HC, Duncan GA. The mucosal protein corona in local nanoparticle drug delivery. Cell Biomaterials. 2025 Mar 25;1(2). doi:10.1016/j.celbio.2025.100043

158. Kim W, Ly NK, He Y, Li Y, Yuan Z, Yeo Y. Protein corona: Friend or foe? Co-opting serum proteins for nanoparticle delivery. Advanced Drug Delivery Reviews. 2023 Jan 1;192:114635. doi:10.1016/j.addr.2022.114635

159. Lindsay S, Hussain M, Binici B, Perrie Y. Exploring the Challenges of Lipid Nanoparticle Development: The In Vitro–In Vivo Correlation Gap. Vaccines. 2025 Apr;13(4):4. doi:10.3390/vaccines13040339

160. Zheng L, Bandara SR, Tan Z, Leal C. Lipid nanoparticle topology regulates endosomal escape and delivery of RNA to the cytoplasm. Proceedings of the National Academy of Sciences. 2023 Jul 4;120(27):e2301067120. doi:10.1073/pnas.2301067120

161. Liu H, Chen MZ, Payne T, Porter CJH, Pouton CW, Johnston APR. Beyond the Endosomal Bottleneck: Understanding the Efficiency of mRNA/LNP Delivery. Advanced Functional Materials. 2024;34(39):2404510. doi:10.1002/adfm.202404510

162. Maugeri M, Nawaz M, Papadimitriou A, Angerfors A, Camponeschi A, Na M, et al. Linkage between endosomal escape of LNP-mRNA and loading into EVs for transport to other cells. Nat Commun. 2019 Sep 24;10(1):4333. doi:10.1038/s41467-019-12275-6

163. Jung HN, Lee SY, Lee S, Youn H, Im HJ. Lipid nanoparticles for delivery of RNA therapeutics: Current status and the role of in vivo imaging. Theranostics. 2022 Oct 24;12(17):7509–31. doi:10.7150/thno.77259 PubMed PMID: 36438494; PubMed Central PMCID: PMC9691360.

164. Kovačič T, Haas H, Stotsky-Oterin L, Štrancar A, Bren U, Peer D. The impact of chemical reactivity on the quality and stability of RNA–LNP pharmaceuticals. Nat Rev Chem. 2025 Nov;9(11):790–802. doi:10.1038/s41570-025-00763-x

165. Kloczewiak M, Banks JM, Jin L, Brader ML. A Biopharmaceutical Perspective on Higher-Order Structure and Thermal Stability of mRNA Vaccines. Mol Pharmaceutics. 2022 Jul 4;19(7):2022–31. doi:10.1021/acs.molpharmaceut.2c00092

166. Lardellier P, Malburet C, Morani M, Willemin T, Rol-Moreno J, Noir A, et al. Comparative study of analytical methods for assessing mRNA integrity and identification of functional mRNA oligomers. Sci Rep. 2025 Dec 10;15(1):43557. doi:10.1038/s41598-025-27563-z

167. Furst T, Bettonville V, Farcas E, Frere A, Lechanteur A, Evrard B, et al. Capillary electrophoresis method to determine siRNA complexation with cationic liposomes. ELECTROPHORESIS. 2016;37(20):2685–91. doi:10.1002/elps.201600249

168. Hong J, Huang Y, Li J, Yi F, Zheng J, Huang H, et al. Comprehensive analysis of sequence-specific stability of siRNA. The FASEB Journal. 2010;24(12):4844–55. doi:10.1096/fj.09.142398

169. Mantri P, Juneja B, Henderson S, Koufos E, Moon Y, Dayeh DM, et al. Comparison of capillary electrophoresis-based methods for the analytical characterization of purity and stability of *in vitro*

transcribed mRNA. Journal of Pharmaceutical and Biomedical Analysis. 2024 Oct 15;249:116352. doi:10.1016/j.jpba.2024.116352

170. Guimaraes GJ, Kim J, Bartlett MG. Characterization of mRNA therapeutics. Mass Spectrometry Reviews. 2024;43(5):1066–90. doi:10.1002/mas.21856

171. ICH Q2(R2) Validation of analytical procedures - Scientific guideline | European Medicines Agency (EMA) [Internet]. 1994 [cited 2026 Apr 15]. Available from: https://www.ema.europa.eu/en/ich-q2r2-validation-analytical-procedures-scientific-guideline

172. ICH Q14 Analytical procedure development - Scientific guideline | European Medicines Agency (EMA) [Internet]. 2022 [cited 2026 Apr 15]. Available from: https://www.ema.europa.eu/en/ich-q14-analytical-procedure-development-scientific-guideline

173. Studzińska S, Nuckowski Ł, Buszewski B. Oligonucleotides Isolation and Separation—A Review on Adsorbent Selection. International Journal of Molecular Sciences. 2022 Jan;23(17):9546. doi:10.3390/ijms23179546

174. Christina Vanhinsbergh, Elliot C. Hook, Nicola Oxby, Mark J. Dickman. Optimization of orthogonal separations for the analysis of oligonucleotides using 2D-LC. Journal of Chromatography B. 2023. doi:10.1016/j.jchromb.2023.123812

175. Currie J, Dahlberg JR, Lundberg E, Thunberg L, Eriksson J, Schweikart F, et al. Stability indicating ion-pair reversed-phase liquid chromatography method for modified mRNA. Journal of Pharmaceutical and Biomedical Analysis. 2024 Aug 1;245:116144. doi:https://doi.org/10.1016/j.jpba.2024.116144

176. Donegan M, Nguyen JM, Gilar M. Effect of ion-pairing reagent hydrophobicity on liquid chromatography and mass spectrometry analysis of oligonucleotides. J Chromatogr A. 2022 Mar 15;1666:462860. doi:10.1016/j.chroma.2022.462860

177. Kilanowska A, Buszewski B, Studzińska S. Application of hydrophilic interaction liquid chromatography coupled with tandem mass spectrometry for the retention and sensitivity studies of antisense oligonucleotides. Journal of Chromatography A. 2020 Jul 5;1622:461100. doi:10.1016/j.chroma.2020.461100

178. Vosáhlová Z, Kalíková K, Gilar M, Szymarek J, Mazurkiewicz-Bełdzińska M, Studzińska S. Hydrophilic interaction liquid chromatography with mass spectrometry for the separation and identification of antisense oligonucleotides impurities and nusinersen metabolites. Journal of Chromatography A. 2024 Jan 4;1713:464535. doi:10.1016/j.chroma.2023.464535

179. Lobue PA, Jora M, Addepalli B, Limbach PA. Oligonucleotide analysis by hydrophilic interaction liquid chromatography-mass spectrometry in the absence of ion-pair reagents. Journal of Chromatography A. 2019 Jun 21;1595:39–48. doi:10.1016/j.chroma.2019.02.016

180. Sorensen MJ, Paulines MJ, Maloney TD. Evaluating orthogonality between ion-pair reversed phase, anion exchange, and hydrophilic interaction liquid chromatography for the separation of synthetic oligonucleotides. J Chromatogr A. 2023 Aug 30;1705:464184. doi:10.1016/j.chroma.2023.464184

181. Hara S, Arase S, Sano S, Suzuki T, Mizogaki I, Sato S, et al. Anion exchange-HPLC method for evaluating the encapsulation efficiency of mRNA-loaded lipid nanoparticles using analytical quality by design. Journal of Chromatography B. 2024 Oct 15;1247:124317. doi:10.1016/j.jchromb.2024.124317

182. Particle Size Analysis by Dynamic Light Scattering [Internet]. [cited 2026 Apr 15]. Available from: https://www.usp.org/harmonization-standards/pdg/general-chapters/particle-size-analysis-by-dynamic-light-scattering

183. Coones RT, Kestens V, Minelli C. A comparison of hydrodynamic diameter results from MADLS and DLS measurements for nanoparticle reference materials. J Nanopart Res. 2025 Jun 16;27(7):170. doi:10.1007/s11051-025-06284-4

184. Klein M, Menta M, Dacoba TG, Crecente-Campo J, Alonso MJ, Dupin D, et al. Advanced nanomedicine characterization by DLS and AF4-UV-MALS: Application to a HIV nanovaccine. JPBA. 2020 Feb 5;179:113017. doi:10.1016/j.jpba.2019.113017

185. British Standards Institution issuing body. Nanotechnologies. Requirements and recommendations for the identification of measurands that characterise nano-objects and materials that contain them [internet resource]. London: London : BSI; 2021.

186. Hole P, Sillence K, Hannell C, Maguire CM, Roesslein M, Suarez G, et al. Interlaboratory comparison of size measurements on nanoparticles using nanoparticle tracking analysis (NTA). J Nanoparticle Res. 2013 Nov 19;15(12):2101. doi:10.1007/s11051-013-2101-8

187. Filipe V, Hawe A, Jiskoot W. Critical evaluation of Nanoparticle Tracking Analysis (NTA) by NanoSight for the measurement of nanoparticles and protein aggregates. Pharm Res. 2010 May;27(5):796–810. doi:10.1007/s11095-010-0073-2 PubMed Central PMCID: PMC2852530.

188. Missana T, Adell A. On the Applicability of DLVO Theory to the Prediction of Clay Colloids Stability. Journal of Colloid and Interface Science. 2000 Oct 1;230(1):150–6. doi:10.1006/jcis.2000.7003

189. Tran V, Nguyen N, Renkes S, Nguyen KT, Nguyen T, Alexandrakis G. Current and Near-Future Technologies to Quantify Nanoparticle Therapeutic Loading Efficiency and Surface Coating Efficiency with Targeted Moieties. Bioengineering. 2025 Apr;12(4):4. doi:10.3390/bioengineering12040362

190. 〈1153〉 Drug Products Containing Nanomaterials [Internet]. [cited 2026 Apr 15]. Available from: https://doi.usp.org/USPNF/USPNF_M13775_02_01.html doi:10.31003/USPNF_M13775_02_01

191. Drennan BW, Schug KA. Challenges and advances in analytical separation techniques for RNA-lipid nanoparticle therapeutics. Anal Bioanal Chem. 2025 Sep 13. doi:10.1007/s00216-025-06096-4

192. Eliuk S, Makarov A. Evolution of Orbitrap Mass Spectrometry Instrumentation. Annu Rev Anal Chem (Palo Alto Calif). 2015;8:61–80. doi:10.1146/annurev-anchem-071114-040325 PubMed PMID: 26161972.

193. Zubarev RA, Makarov A. Orbitrap Mass Spectrometry. Anal Chem. 2013 Jun 4;85(11):5288–96. doi:10.1021/ac4001223

194. Giddings JC. Field-Flow Fractionation. Separation Science and Technology. 1984 Sep 1;19(11–12):831–47. doi:10.1080/01496398408068596

195. Drexel R, Siupa A, Carnell-Morris P, Carboni M, Sullivan J, Meier F. Fast and Purification-Free Characterization of Bio-Nanoparticles in Biological Media by Electrical Asymmetrical Flow Field-Flow Fractionation Hyphenated with Multi-Angle Light Scattering and Nanoparticle Tracking Analysis Detection. Molecules. 2020 Oct 14;25(20). doi:10.3390/molecules25204703 PubMed Central PMCID: PMC7587377.

196. Udepurkar A, Devos C, Sagmeister P, Destro F, Inguva P, Ahmadi S, et al. Structure and Morphology of Lipid Nanoparticles for Nucleic Acid Drug Delivery: A Review. ACS Nano. 2025 Jun 3. doi:10.1021/acsnano.4c18274

197. Considine P, Punnabhum ,Panida, Davidson ,Callum G., Armstrong ,Georgina B., Kreiner ,Michaela, Bax ,Heather J., et al. Assessment of biophysical properties of the first-in-class anti-cancer IgE antibody drug MOv18 IgE demonstrates monomeric purity and stability. mAbs. 2025 Dec 31;17(1):2512211. doi:10.1080/19420862.2025.2512211 PubMed PMID: 40432600.

198. Han X, Zhang H, Butowska K, Swingle KL, Alameh MG, Weissman D, et al. An ionizable lipid toolbox for RNA delivery. Nat Commun. 2021 Dec 13;12(1):7233. doi:10.1038/s41467-021-27493-0

199. Tanaka H, Takata N, Sakurai Y, Yoshida T, Inoue T, Tamagawa S, et al. Delivery of Oligonucleotides Using a Self-Degradable Lipid-Like Material. Pharmaceutics. 2021 Apr 13;13(4). doi:10.3390/pharmaceutics13040544 PubMed Central PMCID: PMC8070490.

200. Chan C, Du S, Dong Y, Cheng X. Computational and Experimental Approaches to Investigate Lipid Nanoparticles as Drug and Gene Delivery Systems. Curr Top Med Chem. 2021;21(2):92–114. doi:10.2174/1568026620666201126162945 PubMed Central PMCID: PMC8191596.

201. Ramezanpour M, Leung SS, Delgado-Magnero KH, Bashe BY, Thewalt J, Tieleman DP. Computational and experimental approaches for investigating nanoparticle-based drug delivery systems. Biochim Biophys Acta. 2016 Jul;1858(7 Pt B):1688–709. doi:10.1016/j.bbamem.2016.02.028

202. Khalkhali M, Mohammadinejad S, Khoeini F, Rostamizadeh K. Vesicle-like structure of lipid-based nanoparticles as drug delivery system revealed by molecular dynamics simulations. Int J Pharm. 2019 Mar 25;559:173–81. doi:10.1016/j.ijpharm.2019.01.036

203. Park S, Choi YK, Kim S, Lee J, Im W. CHARMM-GUI Membrane Builder for Lipid Nanoparticles with Ionizable Cationic Lipids and PEGylated Lipids. J Chem Inf Model. 2021 Oct 25;61(10):5192–202. doi:10.1021/acs.jcim.1c00770 PubMed Central PMCID: PMC8545881.

204. Fernandez-Luengo XF, Camacho J, Faraudo J. Computer Simulations of Lipid Nanoparticles. Nanomaterials (Basel). 2017 Dec 20;7(12). doi:10.3390/nano7120461 PubMed Central PMCID: PMC5746950.

205. Parchekani J, Allahverdi A, Taghdir M, Naderi-Manesh H. Design and simulation of the liposomal model by using a coarse-grained molecular dynamics approach towards drug delivery goals. Scientific Reports. 2022;12(1). doi:10.1038/s41598-022-06380-8

206. Paloncýová M, Šrejber M, Čechová P, Kührová P, Zaoral F, Otyepka M. Atomistic Insights into Organization of RNA-Loaded Lipid Nanoparticles. The Journal of Physical Chemistry B. 2023 Jan 5. doi:10.1021/acs.jpcb.2c07671

207. Catani M, De Luca C, Medeiros Garcia Alcântara J, Manfredini N, Perrone D, Marchesi E, et al. Oligonucleotides: Current Trends and Innovative Applications in the Synthesis, Characterization, and Purification. Biotechnol J. 2020 Aug;15(8):e1900226. doi:10.1002/biot.201900226

208. Sanghvi YS, Ferrazzano L, Cabri W, Tolomelli A. Sustainable Approaches in Solid-phase Oligonucleotide Synthesis: Current Status and Future Directions [Internet]. 2024 Oct 18. doi:10.1039/9781837674541-00228

209. Vinjamuri BP, Pan J, Peng P. A Review on Commercial Oligonucleotide Drug Products. Journal of Pharmaceutical Sciences. 2024 Jul 1;113(7):1749–68. doi:https://doi.org/10.1016/j.xphs.2024.04.021

210. Obexer R, Nassir M, Moody ER, Baran PS, Lovelock SL. Modern approaches to therapeutic oligonucleotide manufacturing. Science. 2024;384(6692):eadl4015. doi:doi:10.1126/science.adl4015

211. El Zahar NM, Magdy N, El-Kosasy AM, Bartlett MG. Chromatographic approaches for the characterization and quality control of therapeutic oligonucleotide impurities. Biomed Chromatogr. 2018 Jan;32(1). doi:10.1002/bmc.4088

212. Chen T, Tang S, Fu Y, Napolitano JG, Zhang K. Analytical techniques for characterizing diastereomers of phosphorothioated oligonucleotides. J Chromatogr A. 2022 Aug 16;1678:463349. doi:10.1016/j.chroma.2022.463349

213. Zuzana Kadlecová, Květa Kalíková, Eva Tesařová, Martin Gilar. Phosphorothioate oligonucleotides separation in ion-pairing reversed-phase liquid chromatography: effect of ion-pairing system. Journal of Chromatography A. 2022. doi:10.1016/j.chroma.2022.463201

214. Guilherme J Guimaraes, Michael G. Bartlett. The critical role of mobile phase pH in the performance of oligonucleotide ion-pair liquid chromatography–mass spectrometry methods. Future Science OA. 2021. doi:10.2144/fsoa-2021-0084

215. Gong L. Comparing ion-pairing reagents and counter anions for ion-pair reversed-phase liquid chromatography/electrospray ionization mass spectrometry analysis of synthetic oligonucleotides. Rapid Commun Mass Spectrom. 2015 Dec 30;29(24):2402–10. doi:10.1002/rcm.7409

216. Chen X, Liu Z, Gong L. Evaluating the interplay among stationary phases/ion-pairing reagents/sequences for liquid chromatography mass spectrometry analysis of oligonucleotides. Anal Biochem. 2021 Jul 15;625:114194. doi:10.1016/j.ab.2021.114194

217. Alice Demelenne, Alice Demelenne, Gwenaël Nys, Gwenaël Nys, Cindy Nix, Cindy Nix, et al. Separation of phosphorothioated oligonucleotide diastereomers using multiplexed drift tube ion mobility mass spectrometry. Analytica Chimica Acta. 2021. doi:10.1016/j.aca.2021.339297

218. Demelenne A, Gou MJ, Nys G, Parulski C, Crommen J, Servais AC, et al. Evaluation of hydrophilic interaction liquid chromatography, capillary zone electrophoresis and drift tube ion-mobility quadrupole time of flight mass spectrometry for the characterization of phosphodiester and phosphorothioate oligonucleotides. Journal of Chromatography A. 2020 Mar 15;1614:460716. doi:10.1016/j.chroma.2019.460716

219. Li F, Lämmerhofer M. Impurity profiling of siRNA by two-dimensional liquid chromatography-mass spectrometry with quinine carbamate anion-exchanger and ion-pair reversed-phase chromatography. Journal of Chromatography A. 2021 Apr 26;1643:462065. doi:10.1016/j.chroma.2021.462065

220. McCarthy SM, Gilar M, Gebler J. Reversed-phase ion-pair liquid chromatography analysis and purification of small interfering RNA. Anal Biochem. 2009 Jul 15;390(2):181–8. doi:10.1016/j.ab.2009.03.042

221. Goyon A, Zhang K. Characterization of Antisense Oligonucleotide Impurities by Ion-Pairing Reversed-Phase and Anion Exchange Chromatography Coupled to Hydrophilic Interaction Liquid Chromatography/Mass Spectrometry Using a Versatile Two-Dimensional Liquid Chromatography Setup. Anal Chem. 2020 Apr 21;92(8):5944–51. doi:10.1021/acs.analchem.0c00114

222. Hsiao J, Bertram L, Apffel A, Tripodi A, Coffey A, Wei TC, et al. Systematic Evaluation of HILIC Stationary Phases for MS Characterization of Oligonucleotides. Vol. 1. 2024 Oct 15;October 20241:10–20.

223. Hao Z, Xiao B, Weng N. Impact of column temperature and mobile phase components on selectivity of hydrophilic interaction chromatography (HILIC). Journal of Separation Science. 2008 May 1;31(9):1449–64. doi:https://doi.org/10.1002/jssc.200700624

224. Ming Huang, Ming Huang, Ming Huang, Xiaobin Xu, Xiaobin Xu, Haibo Qiu, et al. Analytical characterization of DNA and RNA oligonucleotides by hydrophilic interaction liquid chromatography-tandem mass spectrometry. Journal of Chromatography A. 2021. doi:10.1016/j.chroma.2021.462184

225. Azari S, Manellari S, Anderluzzi G, Minghetti P, Musazzi UM. Relevant factors to guarantee quality of oligonucleotide-based products. International Journal of Pharmaceutics. 2026 Jan 5;687:126393. doi:10.1016/j.ijpharm.2025.126393

226. Jora M, Manz C, Thunberg L, Hölttä M, Leek T, Czechtizky W. The complexities of oligonucleotide therapeutics: analytical challenges and opportunities within early drug discovery. Bioanalysis. 2025 Nov 17;17(22):1415–9. doi:10.1080/17576180.2025.2600912 PubMed PMID: 41379075.

227. Andersson P. Preclinical Safety Assessment of Therapeutic Oligonucleotides. In: Arechavala-Gomeza V, Garanto A, editors. Antisense RNA Design, Delivery, and Analysis [Internet]. New York, NY: Springer US; 2022 [cited 2026 Jan 30]. p. 355–70. Available from: https://doi.org/10.1007/978-1-0716-2010-6_25 doi:10.1007/978-1-0716-2010-6_25

228. Ersöz E, Demir-Dora D. Unveiling the potential of antisense oligonucleotides: Mechanisms, therapies, and safety insights. Drug Development Research. 2024;85(4):e22187. doi:10.1002/ddr.22187

229. Brenton AG, Godfrey AR. Accurate mass measurement: Terminology and treatment of data. J Am Soc Mass Spectrom. 2010 Nov 1;21(11):1821–35. doi:10.1016/j.jasms.2010.06.006

230. Li Y, Zhang S, Wang X, Li X, Guo L. LC-MS/MS quantification of nusinersen in rat cerebrospinal fluid and preclinical pharmacokinetics study application. Bioanalysis. 2025 Jul 3;17(13):839–46. doi:10.1080/17576180.2025.2535949 PubMed PMID: 40689874.

231. Xu T, Zuo W, Sun Z, Zhang S, Qiu Z, Zhang B, et al. Development and Validation of an LC–MS/MS Assay for Quantitative Analysis of Nusinersen in Human CSF and Plasma. Biomedical Chromatography. 2025;39(7):e70138. doi:10.1002/bmc.70138

232. Zhan Y, Guo J, Hu P, Huang R, Ning J, Bao X, et al. A sensitive analytical strategy of oligonucleotide functionalized fluorescent probes for detection of nusinersen sodium in human serum. Talanta. 2024 Aug 1;275:126153. doi:10.1016/j.talanta.2024.126153

233. Larson NR, Tong F, Li Z, Zhang Y, Xiao L, Zhou X, et al. Assessment of Stereochemical Comparability in Phosphorothioated Oligonucleotides by CD, 31P NMR, and NP1 Digestion Coupled to LC-MS. Anal Chem. 2025 Mar 25;97(11):6059–66. doi:10.1021/acs.analchem.4c06140

234. Liigand J, Kruve A, Leito I, Girod M, Antoine R. Effect of Mobile Phase on Electrospray Ionization Efficiency. J Am Soc Mass Spectrom. 2014 Nov 1;25(11):1853–61. doi:10.1007/s13361-014-0969-x

235. Kafeenah HIS, Osman R, Bakar NKA. Effect of Mobile Phase pH on the Electrospray Ionization Efficiency and Qualitative Analysis of Pharmaceuticals in ESI + LC-MS/MS. J Chromatogr Sci. 2019 Oct 17;57(9):847–54. doi:10.1093/chromsci/bmz061

236. Lardeux H, Guillarme D, D'Atri V. Comprehensive evaluation of zwitterionic hydrophilic liquid chromatography stationary phases for oligonucleotide characterization. Journal of Chromatography A. 2023 Feb 8;1690:463785. doi:10.1016/j.chroma.2023.463785

237. Miyazaki T, Asano N, Yamaki S, Yamaguchi T, Obika S. Hydrophilic additives enhancing electrospray ionization of oligonucleotides in hexafluoro-2-propanol-free reversed-phase ion-pair liquid chromatography/mass spectrometry. Journal of Chromatography A. 2026 Jan 4;1765:466485. doi:10.1016/j.chroma.2025.466485

238. Walker TE, Laganowsky A, Russell DH. Surface Activity of Amines Provides Evidence for the Combined ESI Mechanism of Charge Reduction for Protein Complexes. Anal Chem. 2022 Aug 2;94(30):10824–31. doi:10.1021/acs.analchem.2c01814

239. Wei X, Wei Y. Opportunities and challenges in the nanoparticles for nucleic acid therapeutics: the first approval of an RNAi nanoparticle for treatment of a rare disease. National Science Review. 2019;6(6):1105–6. doi:10.1093/nsr/nwz009

240. Jadhav V, Vaishnaw A, Fitzgerald K, Maier MA. RNA interference in the era of nucleic acid therapeutics. Nat Biotechnol. 2024 Mar;42(3):394–405. doi:10.1038/s41587-023-02105-y

241. Tang Q, Khvorova A. RNAi-based drug design: considerations and future directions. Nat Rev Drug Discov. 2024 May;23(5):341–64. doi:10.1038/s41573-024-00912-9

242. Damase TR, Sukhovershin R, Boada C, Taraballi F, Pettigrew RI, Cooke JP. The Limitless Future of RNA Therapeutics. Frontiers in Bioengineering and Biotechnology. 2021;9.

243. Crooke ST, Wang S, Vickers TA, Shen W, Liang X hai. Cellular uptake and trafficking of antisense oligonucleotides. Nature Biotechnology. 2017 Mar 1;35(3):230–7. doi:10.1038/nbt.3779

244. Schlegel MK, Janas MM, Jiang Y, Barry JD, Davis W, Agarwal S, et al. From bench to bedside: Improving the clinical safety of GalNAc–siRNA conjugates using seed-pairing destabilization. Nucleic Acids Res. 2022 Jul 8;50(12):6656–70. doi:10.1093/nar/gkac539

245. Springer AD, Dowdy SF. GalNAc-siRNA Conjugates: Leading the Way for Delivery of RNAi Therapeutics. Nucleic Acid Ther. 2018 Jun 1;28(3):109–18. doi:10.1089/nat.2018.0736 PubMed PMID: 29792572; PubMed Central PMCID: PMC5994659.

246. Janas MM, Schlegel MK, Harbison CE, Yilmaz VO, Jiang Y, Parmar R, et al. Selection of GalNAc-conjugated siRNAs with limited off-target-driven rat hepatotoxicity. Nature Communications. 2018 Feb 19;9(1):723. doi:10.1038/s41467-018-02989-4

247. Fàbrega C, Aviñó A, Navarro N, Jorge AF, Grijalvo S, Eritja R. Lipid and Peptide-Oligonucleotide Conjugates for Therapeutic Purposes: From Simple Hybrids to Complex Multifunctional Assemblies. Pharmaceutics. 2023 Jan 17;15(2). doi:10.3390/pharmaceutics15020320

248. Yeoh YQ, Amin A, Cuic B, Tomas D, Turner BJ, Shabanpoor F. Efficient systemic CNS delivery of a therapeutic antisense oligonucleotide with a blood-brain barrier-penetrating ApoE-derived peptide. Biomedicine & Pharmacotherapy. 2024 Jun 1;175:116737. doi:10.1016/j.biopha.2024.116737

249. Cui L, Pereira S, Sonzini S, van Pelt S, Romanelli SM, Liang L, et al. Development of a high-throughput platform for screening lipid nanoparticles for mRNA delivery. Nanoscale. 2022;14(4):1480–91. doi:10.1039/D1NR06858J

250. Byrnes AE, Dominguez SL, Yen CW, Laufer BI, Foreman O, Reichelt M, et al. Lipid nanoparticle delivery limits antisense oligonucleotide activity and cellular distribution in the brain after

intracerebroventricular injection. Molecular Therapy Nucleic Acids. 2023 Jun 13;32:773–93. doi:10.1016/j.omtn.2023.05.005

251. Sarode A, Fan Y, Byrnes AE, Hammel M, Hura GL, Fu Y, et al. Predictive high-throughput screening of PEGylated lipids in oligonucleotide-loaded lipid nanoparticles for neuronal gene silencing. Nanoscale Adv. 2022 May 3;4(9):2107–23. doi:10.1039/D1NA00712B

252. Fan Y, Yen CW, Lin HC, Hou W, Estevez A, Sarode A, et al. Automated high-throughput preparation and characterization of oligonucleotide-loaded lipid nanoparticles. International Journal of Pharmaceutics. 2021 Apr 15;599:120392. doi:10.1016/j.ijpharm.2021.120392

253. Davidson CG, Kapsali E, Ioannou S, Kopilovic B, Hussain M, Perrie Y, et al. The Use of Enhanced Analytical Pipelines for the Characterization of Poly(A) and Poly(A)-LNP Formulation Critical Quality Attributes. Mol Pharmaceutics. 2025 Dec 1;22(12):7383–99. doi:10.1021/acs.molpharmaceut.5c00614

254. Davidson CG, Abdulrahman R, Punnabhum P, Cairns M, Rattray NJW, Capomaccio R, et al. The use of orthogonal analytical approaches to profile lipid nanoparticle physicochemical attributes. Nano Futures. 2024 Sep 6;8(3):035001. doi:10.1088/2399-1984/ad70e6

255. Sheveleva NN, Konarev PV, Boyko KM, Tarasenko II, Mikhailova ME, Bezrodnyi VV, et al. SAXS, DLS, and MD studies of the Rg/Rh ratio for swollen and collapsed dendrimers. J Chem Phys. 2024 Nov 15;161(19):194901. doi:10.1063/5.0234864

256. Verma M, Ozer I, Xie W, Gallagher R, Teixeira A, Choy M. The landscape for lipid-nanoparticle-based genomic medicines. Nature Reviews Drug Discovery. 2023 Jan 10;22(5):349–50. doi:10.1038/d41573-023-00002-2

257. Booth BJ, Nourreddine S, Katrekar D, Savva Y, Bose D, Long TJ, et al. RNA editing: Expanding the potential of RNA therapeutics. Molecular Therapy. 2023;31(6):1533–49. doi:10.1016/j.ymthe.2023.01.005

258. Zhang C, Zhang B. RNA therapeutics: updates and future potential. Science China Life Sciences. 2023 Jan 1;66(1):12–30. doi:10.1007/s11427-022-2171-2

259. Zhao M, Wang R, Yang K, Jiang Y, Peng Y, Li Y, et al. Nucleic acid nanoassembly-enhanced RNA therapeutics and diagnosis. Acta Pharmaceutica Sinica B. 2023 Mar 1;13(3):916–41. doi:https://doi.org/10.1016/j.apsb.2022.10.019

260. Paunovska K, Loughrey D, Dahlman JE. Drug delivery systems for RNA therapeutics. Nature Reviews Genetics. 2022 May 1;23(5):265–80. doi:10.1038/s41576-021-00439-4

261. Curreri A, Sankholkar D, Mitragotri S, Zhao Z. RNA therapeutics in the clinic. Bioengineering & Translational Medicine. 2023 Jan 1;8(1):e10374. doi:https://doi.org/10.1002/btm2.10374

262. AboulFotouh K, Southard B, Dao HM, Xu H, Moon C, Williams Iii RO, et al. Effect of lipid composition on RNA-Lipid nanoparticle properties and their sensitivity to thin-film freezing and drying. International Journal of Pharmaceutics. 2024 Jan 25;650:123688. doi:https://doi.org/10.1016/j.ijpharm.2023.123688

263. Carrasco MJ, Alishetty S, Alameh MG, Said H, Wright L, Paige M, et al. Ionization and structural properties of mRNA lipid nanoparticles influence expression in intramuscular and intravascular administration. Communications Biology. 2021 Aug 11;4(1):956. doi:10.1038/s42003-021-02441-2

264. Shepherd SJ, Han X, Mukalel AJ, El-Mayta R, Thatte AS, Wu J, et al. Throughput-scalable manufacturing of SARS-CoV-2 mRNA lipid nanoparticle vaccines. Proceedings of the National Academy of Sciences. 2023 Aug 15;120(33):e2303567120. doi:10.1073/pnas.2303567120

265. Xiong C, Yuan J, Wang Z, Wang S, Yuan C, Wang L. Preparation and evaluation of a hydrophilic interaction and cation-exchange chromatography stationary phase modified with 2-methacryloyloxyethyl phosphorylcholine. J Chromatogr A. 2018 Apr 20;1546:56–65. doi:10.1016/j.chroma.2018.02.059

266. Cook K, Thayer J. Advantages of ion-exchange chromatography for oligonucleotide analysis. Bioanalysis. 2011 May;3(10):1109–20. doi:10.4155/bio.11.66

267. Gilar M, Doneanu C, Gaye MM. Liquid Chromatography Methods for Analysis of mRNA Poly(A) Tail Length and Heterogeneity. Anal Chem. 2023 Sep 26;95(38):14308–16. doi:10.1021/acs.analchem.3c02552 PubMed Central PMCID: PMC10535021.

268. D'Atri V, Lardeux H, Goyon A, Imiołek M, Fekete S, Lauber M, et al. Optimizing Messenger RNA Analysis Using Ultra-Wide Pore Size Exclusion Chromatography Columns. International Journal of Molecular Sciences. 2024;25(11). doi:10.3390/ijms25116254

269. Levanova A, Poranen MM. Application of steric exclusion chromatography on monoliths for separation and purification of RNA molecules. Journal of Chromatography A. 2018 Nov 2;1574:50–9. doi:https://doi.org/10.1016/j.chroma.2018.08.063

270. Goyon A, Tang S, Fekete S, Nguyen D, Hofmann K, Wang S, et al. Separation of Plasmid DNA Topological Forms, Messenger RNA, and Lipid Nanoparticle Aggregates Using an Ultrawide Pore Size Exclusion Chromatography Column. Anal Chem. 2023 Oct 10;95(40):15017–24. doi:10.1021/acs.analchem.3c02944

271. Katri E, Mirka L, Christine C, Jafargholi I, Karl-Heinz K, M PM. Analysis and purification of ssRNA and dsRNA molecules using asymmetrical flow field flow fractionation. J Chromatogr A. 2022 Nov 8;1683:463525. doi:10.1016/j.chroma.2022.463525

272. Levanova AA, Lampi M, Kalke K, Hukkanen V, Poranen MM, Eskelin K. Native RNA Purification Method for Small RNA Molecules Based on Asymmetrical Flow Field-Flow Fractionation. Pharmaceuticals (Basel). 2022 Feb 21;15(2). doi:10.3390/ph15020261 PubMed Central PMCID: PMC8876226.

273. Sánchez-Cachero A, López-Gutiérrez A, Fariñas NR, Bernardo FJG, Ríos Á, Martín-Doimeadios RCR. Electrical asymmetrical flow field-flow fractionation: Fundamentals, evolution, applications, and prospects. Journal of Chromatography A. 2025 Jan 4;1739:465522. doi:10.1016/j.chroma.2024.465522

274. Lopez-Gomollon S, Nicolas FE. Purification of DNA Oligos by denaturing polyacrylamide gel electrophoresis (PAGE). Methods Enzymol. 2013;529:65–83. doi:10.1016/b978-0-12-418687-3.00006-9

275. Aranda PS, LaJoie DM, Jorcyk CL. Bleach gel: a simple agarose gel for analyzing RNA quality. Electrophoresis. 2012 Jan;33(2):366–9. doi:10.1002/elps.201100335 PubMed Central PMCID: PMC3699176.

276. Chen B, Bartlett MG. Determination of therapeutic oligonucleotides using capillary gel electrophoresis. Biomedical Chromatography. 2012 Apr 1;26(4):409–18. doi:https://doi.org/10.1002/bmc.1696

277. Katayama Y, Arisawa T, Ozaki Y, Maeda M. An affinity capillary electrophoresis for the separation of sequence isomers of oligonucleotide. CHEMISTRY LETTERS. 2000 Feb 5;(2):106–7. doi:10.1246/cl.2000.106

278. Lauman R, Garcia BA. Unraveling the RNA modification code with mass spectrometry. Molecular Omics. 2020;16(4):305–15. doi:10.1039/C8MO00247A

279. Huang G, Zhang F, Xie D, Ma Y, Wang P, Cao G, et al. High-throughput profiling of RNA modifications by ultra-performance liquid chromatography coupled to complementary mass spectrometry: Methods, quality control, and applications. Talanta. 2023 Oct 1;263:124697. doi:https://doi.org/10.1016/j.talanta.2023.124697

280. Amalric A, Bastide A, Attina A, Choquet A, Vialaret J, Lehmann S, et al. Quantifying RNA modifications by mass spectrometry: a novel source of biomarkers in oncology. Critical Reviews in Clinical Laboratory Sciences. 2022 Jan 2;59(1):1–18. doi:10.1080/10408363.2021.1958743

281. Sutton JM, Kim J, El Zahar NM, Bartlett MG. BIOANALYSIS AND BIOTRANSFORMATION OF OLIGONUCLEOTIDE THERAPEUTICS BY LIQUID CHROMATOGRAPHY-MASS SPECTROMETRY. Mass Spectrometry Reviews. 2021 Jul 1;40(4):334–58. doi:https://doi.org/10.1002/mas.21641

282. Eckmann CR, Rammelt C, Wahle E. Control of poly(A) tail length. WIREs RNA. 2011;2(3):348–61. doi:10.1002/wrna.56

283. Nicholson AL, Pasquinelli AE. Tales of Detailed Poly(A) Tails. Trends in Cell Biology. 2019 Mar 1;29(3):191–200. doi:10.1016/j.tcb.2018.11.002 PubMed PMID: 30503240.

284. Subtelny AO, Eichhorn SW, Chen GR, Sive H, Bartel DP. Poly(A)-tail profiling reveals an embryonic switch in translational control. Nature. 2014 Apr;508(7494):66–71. doi:10.1038/nature13007

285. Xiang K, Ly J, Bartel DP. Control of poly(A)-tail length and translation in vertebrate oocytes and early embryos. Developmental Cell. 2024 Apr 22;59(8):1058-1074.e11. doi:10.1016/j.devcel.2024.02.007

286. Biziaev N, Shuvalov A, Salman A, Egorova T, Shuvalova E, Alkalaeva E. The impact of mRNA poly(A) tail length on eukaryotic translation stages. Nucleic Acids Research. 2024 Jul 22;52(13):7792–808. doi:10.1093/nar/gkae510

287. Saluja A, Fesinmeyer RM, Hogan S, Brems DN, Gokarn YR. Diffusion and Sedimentation Interaction Parameters for Measuring the Second Virial Coefficient and Their Utility as Predictors of Protein Aggregation. Biophysical Journal. 2010 Oct 20;99(8):2657–65. doi:https://doi.org/10.1016/j.bpj.2010.08.020

288. PD CEN ISO/TS 21362:2021 | 30 Apr 2021 | BSI Knowledge [Internet]. [cited 2024 Dec 10]. Available from: https://knowledge.bsigroup.com/products/nanotechnologies-analysis-of-nano-objects-using-asymmetrical-flow-and-centrifugal-field-flow-fractionation-1?version=standard&tab=overview

289. Library QC in NGS workflow, 5200 Fragment Analyzer | Agilent [Internet]. [cited 2025 Sep 1]. Available from: https://www.agilent.com/en/product/automated-electrophoresis/fragment-analyzer-systems/fragment-analyzer-systems/5200-fragment-analyzer-system-365720#literature

290. Caputo F, Clogston J, Calzolai L, Roesslein M, Prina-Mello A. Measuring particle size distribution of nanoparticle enabled medicinal products, the joint view of EUNCL and NCI-NCL. A step by step approach combining orthogonal measurements with increasing complexity. JCR. 2019 01;299. doi:10.1016/j.jconrel.2019.02.030

291. Nonclinical Safety Assessment of Oligonucleotide-Based Therapeutics. 2024.

292. Delli Ponti R, Marti S, Armaos A, Tartaglia GG. A high-throughput approach to profile RNA structure. Nucleic acids research. 2017;45(5):e35–e35. doi:10.1093/nar/gkw1094

293. Wayment-Steele HK, Kladwang W, Strom AI, Lee J, Treuille A, Becka A, et al. RNA secondary structure packages evaluated and improved by high-throughput experiments. Nature Methods. 2022 Oct 1;19(10):1234–42. doi:10.1038/s41592-022-01605-0

294. Ding J, Lee YT, Bhandari Y, Schwieters CD, Fan L, Yu P, et al. Visualizing RNA conformational and architectural heterogeneity in solution. Nature Communications. 2023 Feb 9;14(1):714. doi:10.1038/s41467-023-36184-x

295. Ye R, Zhao H, Wang X, Xue Y. Technological advancements in deciphering RNA-RNA interactions. Molecular Cell. 2024 Jul 23. doi:https://doi.org/10.1016/j.molcel.2024.06.036

296. Leng M, Felsenfeld G. A study of polyadenylic acid at neutral pH. Journal of Molecular Biology. 1966 Feb 1;15(2):455–66. doi:https://doi.org/10.1016/S0022-2836(66)80121-3

297. Baba Y, Tanaka S, Kagemoto A. Influence of pH and Salt Concentration on the Helix—Coil Transition of Poly A Determined by a Modified DSC. Polymer Journal. 1975 Nov 1;7(6):641–5. doi:10.1295/polymj.7.641

298. Akeson M, Branton D, Kasianowicz JJ, Brandin E, Deamer DW. Microsecond Time-Scale Discrimination Among Polycytidylic Acid, Polyadenylic Acid, and Polyuridylic Acid as Homopolymers or as Segments Within Single RNA Molecules. Biophysical Journal. 1999;77(6):3227–33. doi:10.1016/S0006-3495(99)77153-5

299. Saenger W, Riecke J, Suck D. A structural model for the polyadenylic acid single helix. Journal of Molecular Biology. 1975 Apr 25;93(4):529–34. doi:https://doi.org/10.1016/0022-2836(75)90244-2

300. Rich A, Davies DR. A new two stranded helical structure: polyadenylic acid and polyuridylic acid. Journal of the American Chemical Society. 1956;78(14):3548–9.

301. Robinson E, MacDonald KD, Slaughter K, McKinney M, Patel S, Sun C, et al. Lipid Nanoparticle-Delivered Chemically Modified mRNA Restores Chloride Secretion in Cystic Fibrosis. Mol Ther. 2018 Aug 1;26(8):2034–46. doi:https://doi.org/10.1016/j.ymthe.2018.05.014

302. Fattore L, Cafaro G, Di Martile M, Campani V, Sacconi A, Liguoro D, et al. Oncosuppressive miRNAs loaded in lipid nanoparticles potentiate targeted therapies in BRAF-mutant melanoma by inhibiting core escape pathways of resistance. Oncogene. 2023 Jan 1;42(4):293–307. doi:10.1038/s41388-022-02547-9

303. Qiu M, Li Y, Bloomer H, Xu Q. Developing Biodegradable Lipid Nanoparticles for Intracellular mRNA Delivery and Genome Editing. Acc Chem Res. 2021 Nov 2;54(21):4001–11. doi:10.1021/acs.accounts.1c00500

304. Afonin KA, Dobrovolskaia MA, Church G, Bathe M. Opportunities, Barriers, and a Strategy for Overcoming Translational Challenges to Therapeutic Nucleic Acid Nanotechnology. ACS nano. 2020 Aug 25;14(8):9221–7. doi:10.1021/acsnano.0c04753

305. Gabizon AA, de Rosales RTM, La-Beck NM. Translational considerations in nanomedicine: The oncology perspective. Adv Drug Deliv Rev. 2020 Jan 1;158:140–57. doi:https://doi.org/10.1016/j.addr.2020.05.012

306. Simon CG, Borgos SE, Calzolai L, Nelson BC, Parot J, Petersen EJ, et al. Orthogonal and complementary measurements of properties of drug products containing nanomaterials. JCR. 2023 Feb 1;354:120–7. doi:https://doi.org/10.1016/j.jconrel.2022.12.049

307. Bastogne T, Caputo F, Prina-Mello A, Borgos S, Barberi-Heyob M. A state of the art in analytical quality-by-design and perspectives in characterization of nano-enabled medicinal products. JPBA. 2022 Sep 20;219:114911. doi:10.1016/j.jpba.2022.114911

308. Caputo F, Arnould A, Bacia M, Ling WL, Rustique E, Texier I, et al. Measuring Particle Size Distribution by Asymmetric Flow Field Flow Fractionation: A Powerful Method for the Preclinical Characterization of Lipid-Based Nanoparticles. Mol Pharmaceutics. 2019 Feb 4;16(2):756–67. doi:10.1021/acs.molpharmaceut.8b01033 PubMed Central PMCID: PMC6377179.

309. Parot J, Mehn D, Jankevics H, Markova N, Carboni M, Olaisen C, et al. Quality assessment of LNP-RNA therapeutics with orthogonal analytical techniques. JCR. 2024 Mar 1;367:385–401. doi:https://doi.org/10.1016/j.jconrel.2024.01.037

310. Choi J, Fuentes C, Fransson J, Wahlgren M, Nilsson L. Separation and zeta-potential determination of proteins and their oligomers using electrical asymmetrical flow field-flow fractionation (EAF4). J Chromatogr A. 2020 Dec 6;1633:461625. doi:10.1016/j.chroma.2020.461625

311. Fuentes C, Choi J, Wahlgren M, Nilsson L. Charge and zeta-potential distribution in starch modified with octenyl succinic anhydride (OSA) determined using electrical asymmetrical flow field-flow fractionation (EAF4). Colloid Surface A. 2023 Jan 20;657:130570. doi:https://doi.org/10.1016/j.colsurfa.2022.130570

312. Ramirez LMF, Rihouey C, Chaubet F, Le Cerf D, Picton L. Characterization of dextran particle size: How frit-inlet asymmetrical flow field-flow fractionation (FI-AF4) coupled online with dynamic light scattering (DLS) leads to enhanced size distribution. J Chromatogr A. 2021 Sep 13;1653:462404. doi:10.1016/j.chroma.2021.462404

313. Velimirovic M, Pancaro A, Mildner R, Georgiou PG, Tirez K, Nelissen I, et al. Joint Forces of HR-Spicp-MS and EAF4-MALS for Characterization of Gold Nanorods Conjugated with Synthetic Glycopolymers. The 2nd International Online-Conference on Nanomaterials. 2020.

314. Mildner R, Hak S, Parot J, Hyldbakk A, Borgos SE, Some D, et al. Improved multidetector asymmetrical-flow field-flow fractionation method for particle sizing and concentration measurements of lipid-based nanocarriers for RNA delivery. Eur J Pharm Biopharm. 2021 Jun;163:252–65. doi:10.1016/j.ejpb.2021.03.004

315. Bian J, Gobalasingham N, Purchel A, Lin J. The Power of Field-Flow Fractionation in Characterization of Nanoparticles in Drug Delivery. Mol. 2023;28(10).

316. Gervais C, Grissom C, Little N, Wachoviak M. Cleaning Marble with Ammonium Citrate. Stud Conserv. 2010 01;55:164–76. doi:10.1179/sic.2010.55.3.164

317. Uddin MN, Roni MA. Challenges of Storage and Stability of mRNA-Based COVID-19 Vaccines. Vaccines. 2021 Sep 17;9(9). doi:10.3390/vaccines9091033 PubMed Central PMCID: PMC8473088.

318. Ma X, Wu F, Peng C, Chen H, Zhang D, Han T. Exploration of mRNA nanoparticles based on DOTAP through optimization of the helper lipids. Biotechnol J. 2023 Nov 1;18(11):2300123. doi:https://doi.org/10.1002/biot.202300123

319. Ball RL, Bajaj P, Whitehead KA. Achieving long-term stability of lipid nanoparticles: examining the effect of pH, temperature, and lyophilization. Int J Nanomed. 2017;12:305–15. doi:10.2147/ijn.S123062 PubMed Central PMCID: PMC5221800.

320. Muramatsu H, Lam K, Bajusz C, Laczkó D, Karikó K, Schreiner P, et al. Lyophilization provides long-term stability for a lipid nanoparticle-formulated, nucleoside-modified mRNA vaccine. Mol Ther. 2022 May 4;30(5):1941–51. doi:https://doi.org/10.1016/j.ymthe.2022.02.001

321. Ray RM, Hansen AH, Taskova M, Jandl B, Hansen J, Soemardy C, et al. Enhanced target cell specificity and uptake of lipid nanoparticles using RNA aptamers and peptides. Beilstein J Org Chem. 2021;17:891–907. doi:10.3762/bjoc.17.75

322. Maguire CM, Rösslein M, Wick P, Prina-Mello A. Characterisation of particles in solution - a perspective on light scattering and comparative technologies. STAM. 2018;19(1):732–45. doi:10.1080/14686996.2018.1517587 PubMed Central PMCID: PMC6201793.

323. Baylot V, Le TK, Taïeb D, Rocchi P, Colleaux L. Between hope and reality: treatment of genetic diseases through nucleic acid-based drugs. Communications Biology. 2024 Apr 23;7(1):489. doi:10.1038/s42003-024-06121-9

324. Papaioannou I, Owen JS, Yáñez-Muñoz RJ. Clinical applications of gene therapy for rare diseases: A review. International Journal of Experimental Pathology. 2023 Aug 1;104(4):154–76. doi:https://doi.org/10.1111/iep.12478

325. Chen J, Xu Y, Zhou M, Xu S, Varley AJ, Golubovic A, et al. Combinatorial design of ionizable lipid nanoparticles for muscle-selective mRNA delivery with minimized off-target effects. Proceedings of the National Academy of Sciences. 2023 Dec 12;120(50):e2309472120. doi:10.1073/pnas.2309472120

326. Da Silva Sanchez AJ, Zhao K, Huayamares SG, Hatit MZC, Lokugamage MP, Loughrey D, et al. Substituting racemic ionizable lipids with stereopure ionizable lipids can increase mRNA delivery. J Control Release. 2022 Nov 30;353:270–7. doi:10.1016/j.jconrel.2022.11.037

327. Chakraborty S, Doktorova M, Molugu TR, Heberle FA, Scott HL, Dzikovski B, et al. How cholesterol stiffens unsaturated lipid membranes. Proc Natl Acad Sci U S A. 2020 Sep 8;117(36):21896–905. doi:10.1073/pnas.2004807117 PubMed Central PMCID: PMC7486787.

328. Cheng MHY, Leung J, Zhang Y, Strong C, Basha G, Momeni A, et al. Induction of Bleb Structures in Lipid Nanoparticle Formulations of mRNA Leads to Improved Transfection Potency. Advanced Materials. 2023;35(31):2303370. doi:10.1002/adma.202303370

329. Simonsen JB. A perspective on bleb and empty LNP structures. Journal of Controlled Release. 2024 Sep 1;373:952–61. doi:10.1016/j.jconrel.2024.07.046

330. Gindy ME, DiFelice K, Kumar V, Prud'homme RK, Celano R, Haas RM, et al. Mechanism of Macromolecular Structure Evolution in Self-Assembled Lipid Nanoparticles for siRNA Delivery. Langmuir. 2014 Apr 29;30(16):4613–22. doi:10.1021/la500630h

331. Maeki M, Fujishima Y, Sato Y, Yasui T, Kaji N, Ishida A, et al. Understanding the formation mechanism of lipid nanoparticles in microfluidic devices with chaotic micromixers. PLOS ONE. 2017 Nov 28;12(11):e0187962. doi:10.1371/journal.pone.0187962

332. Börjesdotter AM, Bolinsson H, Dagø T, Herranz-Trillo F, Palmiero UC, Schagerlöf H, et al. Lipid nanoparticle properties explored using online asymmetric flow field-flow fractionation coupled with small angle X-ray scattering: Beyond average characterisation. International Journal of Pharmaceutics. 2024 Nov 10;124940. doi:https://doi.org/10.1016/j.ijpharm.2024.124940

333. Padilla MS, Shepherd SJ, Hanna AR, Kurnik M, Zhang X, Chen M, et al. Elucidating lipid nanoparticle properties and structure through biophysical analyses. Nat Biotechnol. 2025 Oct 23;1–14. doi:10.1038/s41587-025-02855-x

334. Jia X, Liu Y, Wagner AM, Chen M, Zhao Y, Smith KJ, et al. Enabling online determination of the size-dependent RNA content of lipid nanoparticle-based RNA formulations. J Chromatogr B Analyt Technol Biomed Life Sci. 2021 Dec 1;1186:123015. doi:10.1016/j.jchromb.2021.123015

335. Androsavich JR. Frameworks for transformational breakthroughs in RNA-based medicines. Nature Reviews Drug Discovery. 2024 Jun 1;23(6):421–44. doi:10.1038/s41573-024-00943-2

336. Roamcharern N, Punnabhum P, Seib FP, Rattray Z. Evaluating the impact of bioinspired counterion inclusion on silk nanoparticle physicochemical attributes and physical stability. Nanoscale Adv. 2025;7(18):5519–35. doi:10.1039/D5NA00365B

337. Kato H, Nakamura A, Banno H. Determination of number-based size distribution of silica particles using centrifugal field-flow fractionation. J Chromatogr A. 2019 Sep 27;1602:409–18. doi:10.1016/j.chroma.2019.05.055

338. Schmidt A, Helgers H, Vetter FL, Juckers A, Strube J. Digital Twin of mRNA-Based SARS-COVID-19 Vaccine Manufacturing towards Autonomous Operation for Improvements in Speed, Scale, Robustness, Flexibility and Real-Time Release Testing. Processes. 2021 Apr 22;9(5). doi:10.3390/pr9050748

339. Bhujel R, Enkmann V, Burgstaller H, Maharjan R. Artificial Intelligence-Driven Strategies for Targeted Delivery and Enhanced Stability of RNA-Based Lipid Nanoparticle Cancer Vaccines. Pharmaceutics. 2025 Jul 29;17(8). doi:10.3390/pharmaceutics17080992

340. Niederkofler S, Parkkila P, Aliakbarinodehi N, Sasanian N, Emilsson G, Ulkoski D, et al. Effects of Serum Incubation on Lipid Nanoparticle PEG Shedding, mRNA Retention, and Membrane Interactions. ACS Appl Mater Interfaces. 2025 Nov 26;17(47):64219–31. doi:10.1021/acsami.5c17052

341. Zeng Y, Shen M, Pattipeiluhu R, Zhou X, Zhang Y, Bakkum T, et al. Efficient mRNA delivery using lipid nanoparticles modified with fusogenic coiled-coil peptides. Nanoscale. 2023;15(37):15206–18. doi:10.1039/D3NR02175K

342. Yokoo H, Oba M, Uchida S. Cell-Penetrating Peptides: Emerging Tools for mRNA Delivery. Pharmaceutics. 2021 Dec 28;14(1). doi:10.3390/pharmaceutics14010078

343. Dowdy SF, Setten RL, Cui XS, Jadhav SG. Delivery of RNA Therapeutics: The Great Endosomal Escape! Nucleic Acid Therapeutics. 2022 Oct 1;32(5):361–8. doi:10.1089/nat.2022.0004

344. Allen R, Yokota T. Endosomal Escape and Nuclear Localization: Critical Barriers for Therapeutic Nucleic Acids. Molecules. 2024 Dec 18;29(24). doi:10.3390/molecules29245997

345. Boye Jallow M, Huang K, Qiu M. Versatility of LNPs across different administration routes for targeted RNA delivery. Journal of Materials Chemistry B. 2025;13(26):7637–52. doi:10.1039/D5TB00575B

Supplemental Information

8. Chapter 2

HILIC-PDA Optimisation

Within HILIC separation optimisation, only flow rate and pre-treatment PDA chromatograms utilised blank buffer/gradient subtraction.

Column Oven

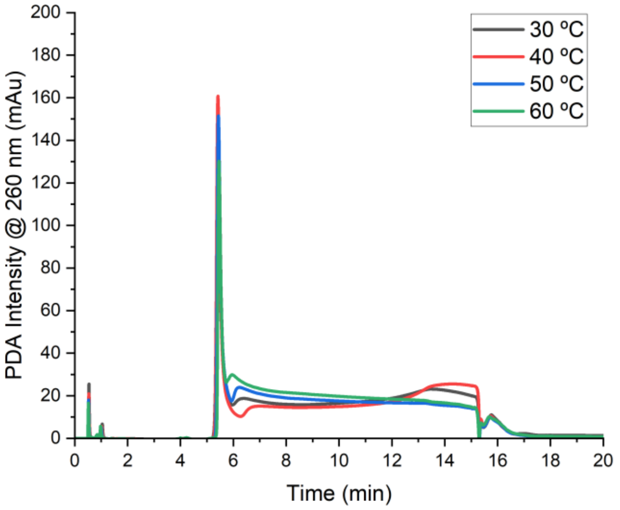

Figure S 8.1 *- Column oven temperature optimisation for the separation of ON1. LC separation profile uses Thermo Accucore HILIC column at 20 mM ammonium formate pH 3, at 0.4 mL/min, 1 µg injection concentration, n=1.*

Column Selection

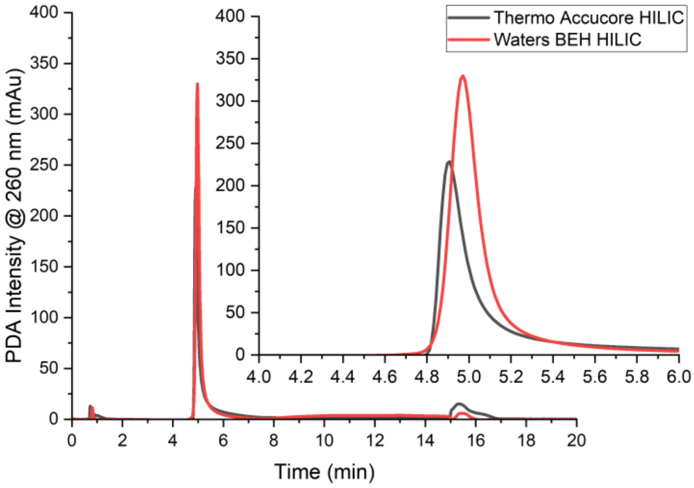

Figure S 8.2*- LC separation profile ON1 uses HILIC column at 20 mM ammonium formate pH 3, 40 °C column oven, at 0.4 mL/min , 1 µg injection concentration, n=1.*

Mobile Phase Ionic Strength

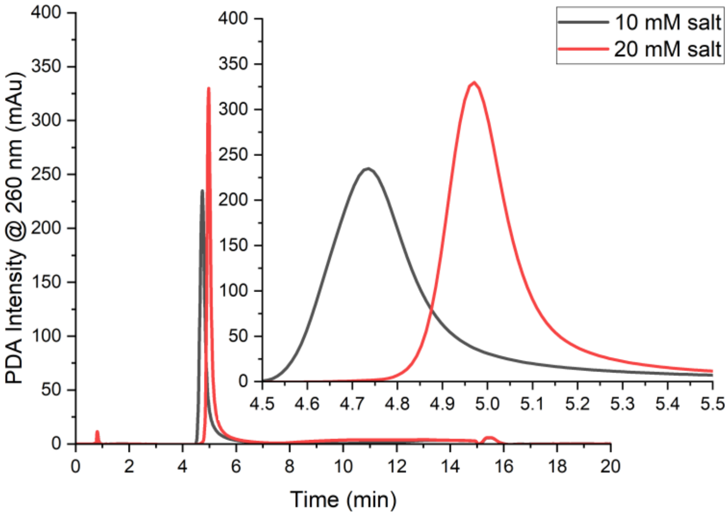

Figure S 8.3 - *Mobile phase A salt ionic strength optimisation on the separation and detection of ON1 sample. LC separation profile uses Waters BEH HILIC column at ammonium formate pH 3, 40 °C column oven, at 0.4 mL/min , 1 µg injection concentration, n=1.*

Orbitrap Optimisation

Polarity

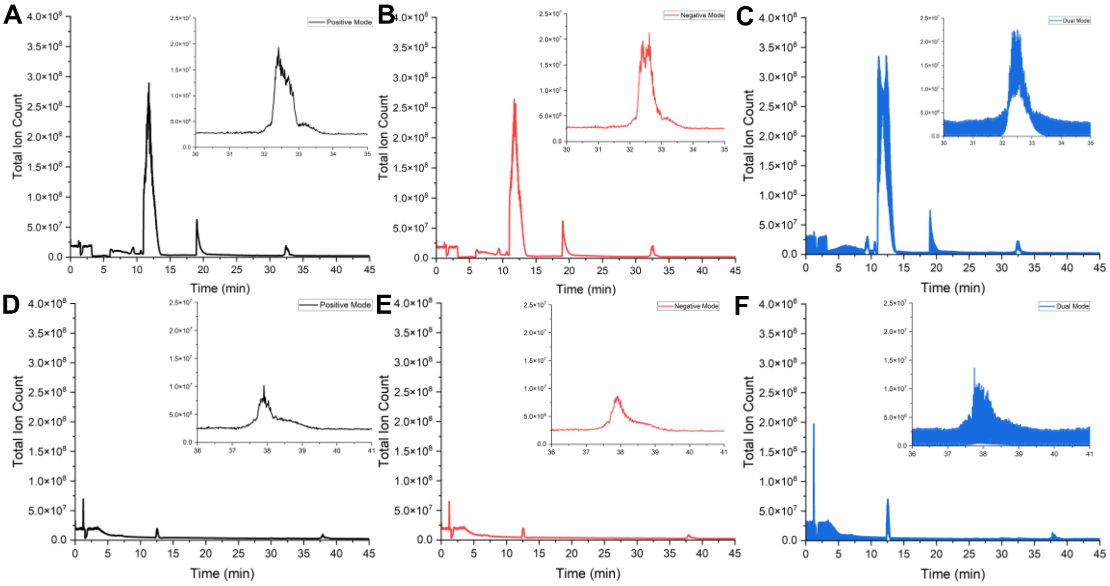

Figure S 8.4 – *LC-Orbi Optimisation of Polarity modes for ON1 A) positive mode, B) negative mode, C) dual mode, and ON2 in D) positive mode, E) negative mode, F) dual mode. LC separation profile uses Waters BEH Amide column at 20 mM ammonium acetate pH 7, 40 °C column oven, 1 µg injection concentration at 0.3 mL/min without pretreatment, n=1.*

Scan Range

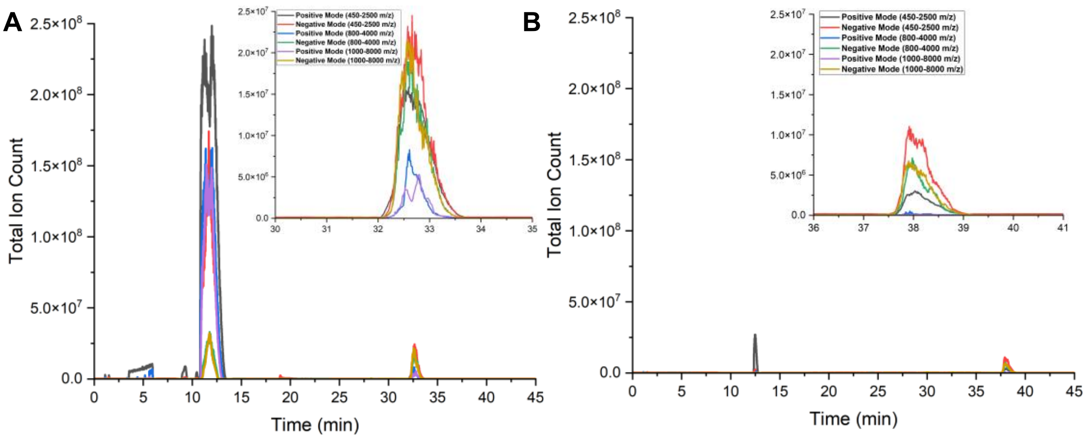

Figure S 8.5 *- Scan range windows for in detectable ranges 450-2500, 800-400 and 1000-8000 m/z for A) ON1, and B) ON2. LC separation profile uses Waters BEH Amide column at 20 mM ammonium acetate pH 7, 40 °C column oven, 1 µg injection concentration at 0.3 mL/min without pretreatment, n=1.*

Table S 8.1 *– Deconvolution parameters for positive mode scan range spectra. Other criteria not changed from* ***section 2.3.4****.*

Sample	**Scan Range (m/z)**	**Target Avg. Spectrum Width(min)**	**Target Avg. Spectrum Offset (%)**	**Max. RT Gap (min)**
ON1	450-2500	0.02	25	1
	800-4000	0.05	25	0.2
	1000-8000	0.05	25	1
ON2	450-2500	0.02	27	1
	800-4000	0.40	25	1
	1000-8000	1.44	25	1

Automatic Gain Control, Injection Time and Microscans (MS1)

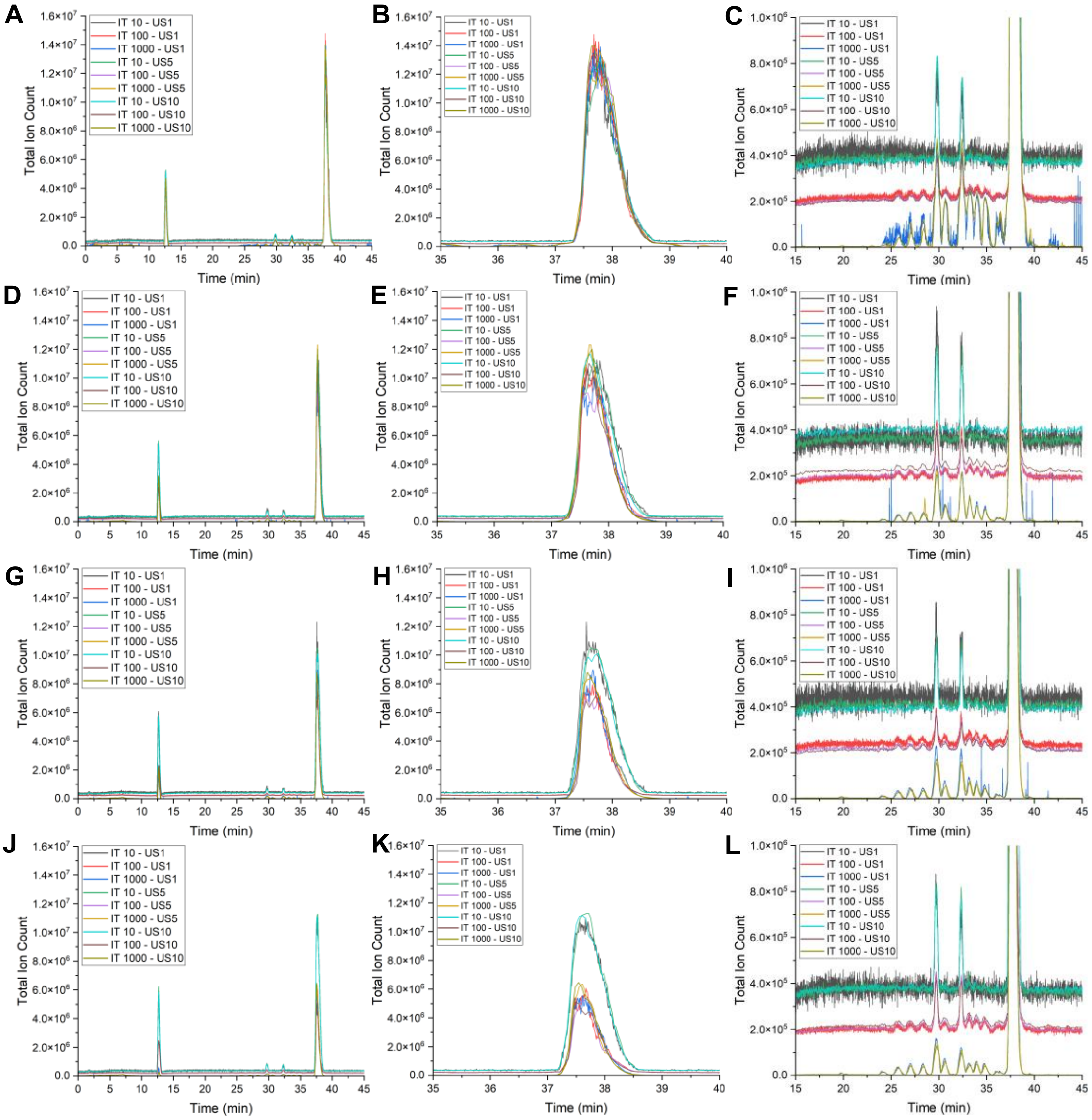

__Figure S 8.6__ - AGC, injection time and microscan optimisation using ON2. AGC 100% A) TIC profile, B) FLP TIC, C) impurity TIC, AGC 300% D) TIC profile, E) FLP TIC, F) Impurity TIC, AGC 500 %, G) TIC profile, H) FLP TIC, I) Impurity TIC, AGC 1000%, J) TIC profile, K) FLP TIC, L) Impurity TIC. LC separation profile uses Waters BEH Amide column at 20 mM ammonium acetate pH 7, 40 °C column oven, 1 µg injection concentration at 0.3 mL/min without pretreatment, n=1.

9. Chapter 3

Table S 9.1 *- Insights into FI-AF4-MD distributional values for R_G, R_H and shape factor elution profiles for ASO-LNP formulations. FRR: Flow Rate Ratio; TFR: Total Flow Rate Tukey Tests compared LNP1-2(*), LNP1-3(‡) and LNP3-4/5(#) where *$p < 0.05$, **$p < 0.005$ and ***$p < 0.0005$, (n=3), error bars represent mean ± standard deviation.*

Sample	FI-AF4-MD														
	Et (min)	**Rec (%)**	**R_G Mode (nm)**	**R_G 10 (nm)**	**R_G 50 (nm)**	**R_G 90 (nm)**	**R_G Span**	**R_H 10 (nm)**	**R_H 50 (nm)**	**R_H 90 (nm)**	**R_H Span**	**SF 10**	**SF 50**	**SF 90**	**SF Span**
SM102 LNP-1 (N/P: 6, FRR 3, TFR 15**)**	24.2 ± 0.2	86.5 ± 8.5	24.7 ± 0.7	19.6 ± 1.5	22.1 ± 0.9	24.9 ± 1.6	0.24 ± 0.01	33.7 ± 0.3	36.5 ± 0.5	40.3 ± 1.0	0.18 ± 0.03	0.58 ± 0.04	0.60 ± 0.03	0.63 ± 0.04	0.08 ± 0.01
SM102 LNP-2 (N/P: 12, FRR 3, TFR 15**)**	23.7 ± 0.4	84.3 ± 1.2	26.7 ± 0.7	24.4 ± 0.8^{*}	26.5 ± 0.6^{**}	29.2 ± 1.1^{*}	0.18 ± 0.02^{*}	35.6 ± 0.4^{**}	38.2 ± 0.4^{*}	41.6 ± 0.5	0.16 ± 0.00	0.68 ± 0.01^{*}	0.70 ± 0.01^{*}	0.71 ± 0.01^{*}	0.04 ± 0.01^{*}
MC3 LNP-3 (N/P: 6, FRR 3, TFR 15)	25.9 ± $0.5^{\ddagger}$	88.9 ± 3.4	31.0 ± $0.8^{\ddagger}$	27.3 ± $0.4^{\ddagger\ddagger}$	30.7 ± $0.6^{\ddagger\ddagger\ddagger}$	35.0 ± $0.6^{\ddagger\ddagger\ddagger}$	0.25 ± 0.02	38.3 ± $0.6^{\ddagger\ddagger\ddagger}$	42.8 ± $0.5^{\ddagger\ddagger\ddagger}$	47.6 ± $0.5^{\ddagger\ddagger\ddagger}$	0.22 ± 0.01	0.71 ± $0.00^{\ddagger}$	0.72 ± $0.00^{\ddagger\ddagger}$	0.74± $0.00^{\ddagger}$	0.04 ± $0.01^{\ddagger}$
MC3 LNP-4 (N/P: 6, **FRR 6**, TFR 15)	26.7 ± 0.6	87.2 ± 2.4	33.4 ± $0.3^{\#\#}$	26.1 ± 0.2	31.6 ± 0.6	37.4 ± $0.7^{\#}$	0.36 ± $0.02^{\#\#}$	40.1 ± 0.1	46.1 ± $1.0^{\#}$	52.0 ± $1.1^{\#\#}$	0.26 ± 0.02	0.65 ± $0.01^{\#\#\#}$	0.69 ± $0.00^{\#\#\#}$	0.72 ± $0.00^{\#}$	0.10 ± $0.01^{\#\#}$
MC3 LNP 5 (N/P: 6, FRR 3, **TFR 5**)	27.9± $0.2^{\#}$	85.8 ± 4.8	34.7 ± $0.8^{\#\#\#}$	29.2 ± $0.2^{\#\#}$	32.9 ± $0.9^{\#}$	37.5 ± $0.9^{\#}$	0.25 ± 0.01	42.8 ± $1.1^{\#\#}$	47.1 ± $1.0^{\#\#}$	52.3 ± $0.8^{\#\#}$	0.23 ± 0.04	0.68 ± $0.00^{\#\#}$	0.70 ± $0.01^{\#\#}$	0.72 ± $0.01^{\#}$	0.05 ± 0.01

10. Chapter 4

Verification of Concentration

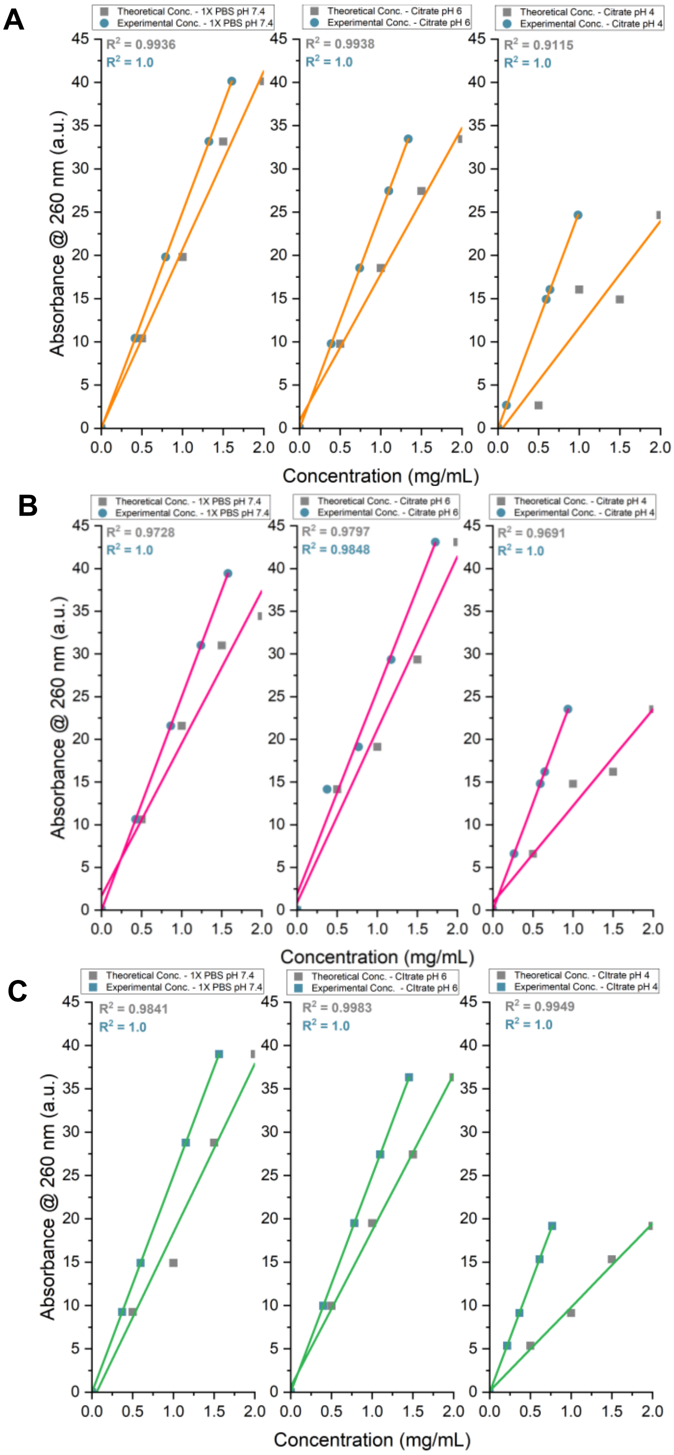

***Figure S 10.1** - Absorbance calibration curves of theoretical concentration versus experimentally calculated concentration of Poly(A) in formulation buffers from A) Brand A, B) Brand B and C) Brand C, as a function of absorbance @ 260 nm. Data represents n=2.*

***Table S 10.1** - Average percentage difference between theoretical and experimental Poly(A) concentrations (0.5-2.0 mg/mL)(n=2), linearity (R2) Limit of Detection (LOD) and Limit of Quantification (LOQ) for Poly(A) in manufacture buffer conditions from NanoDrop linear regression of calibration curves (0.5 mg/mL – 2.0 mg/mL) (n=1). LOD = 3.3*(Standard Error/Slope) and LOQ = 10*(Standard Error/Slope).*

Brand	**Brand A**			**Brand B**			**Brand C**		
Buffer	**PBS**	**Cit pH 6**	**Cit pH 4**	**PBS**	**Cit pH 6**	**Cit pH 4**	**PBS**	**Cit pH 6**	**Cit pH 4**
Avg. % Diff.	18.9	31.2	81.9	18.4	23.6	66.2	32.8	27.5	86.4
RSD (%)	25.7	20.2	44.5	21.5	25.8	18.5	36.6	16.6	6.6
R^2	0.9988	0.9987	0.8436	0.9993	0.9997	0.9985	0.9996	0.9986	0.9976
LOD (ng/mL)	70.1	86.3	72.6	1068.1	855.8.	3983.4	107.4	111.2	1177.3
LOQ (ng/mL)	212.4	261.4	220.0	3236.7	2593.4	12071.0	325.5	336.9	3567.5

Nanodrop analysis of branded Poly(A) samples (0.5–2.0 mg/mL) across different formulation buffers revealed significant discrepancies between theoretical and experimental concentrations, primarily due to salt content in lyophilised forms. Experimental concentrations differed by 18.3–32.8% in PBS and citrate pH 6 buffers, and up to 86.4% in citrate pH 4 **(Figure S 10.1, Table S 10.1)**, emphasising the impact of residual salts upon reconstitution. Despite strong linearity in calibration curves ($R^2 > 0.997$), Brand A in pH 4 citrate showed reduced linearity ($R^2 = 0.8436$), further indicating buffer-dependent variability. Lower absorbance at 260 nm in acidic buffers suggested conformational changes affecting adenine exposure and quantification accuracy. LODs and LOQs varied widely between brands and buffers, with up to an 11-fold difference **(Table S 10.1)**, reinforcing the importance of pre-checking Poly(A) concentrations via Nanodrop before downstream applications like nanoparticle encapsulation.

Dynamic Light Scattering

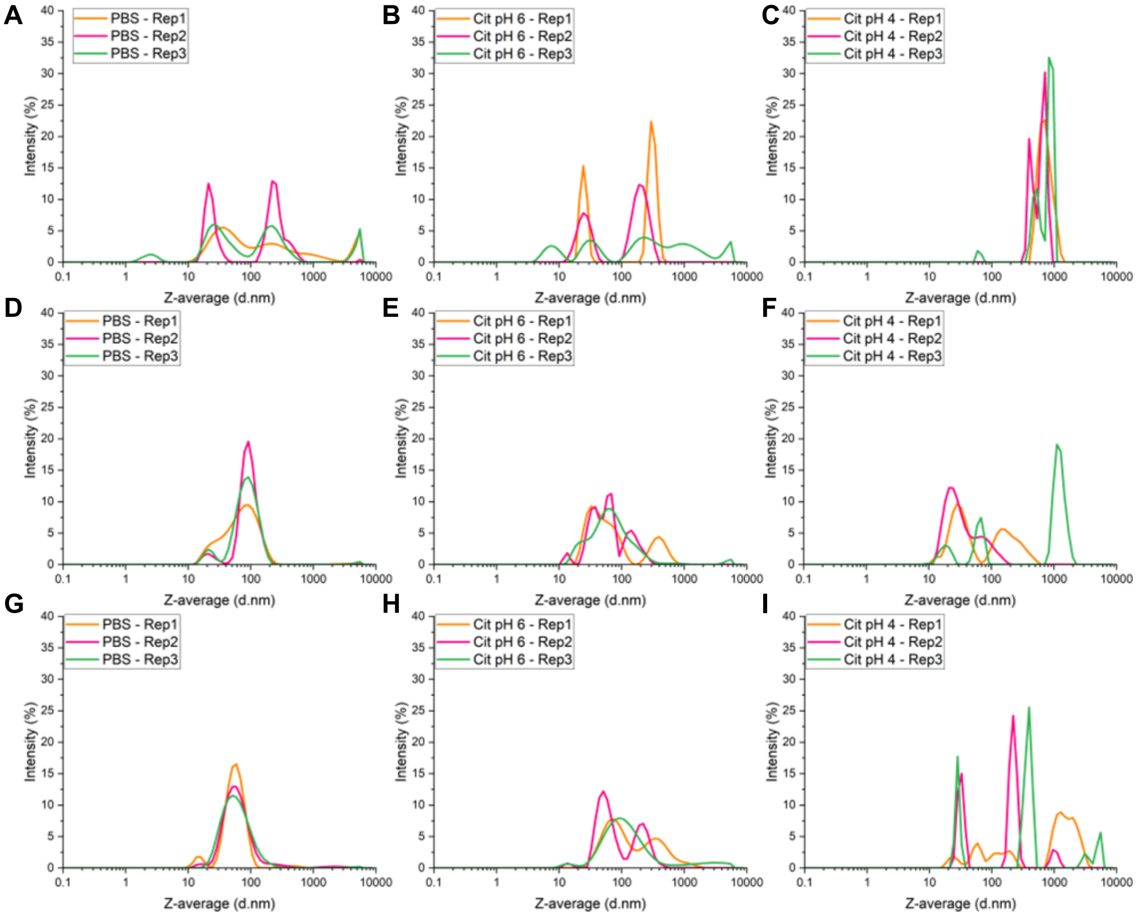

Figure S 10.2 *- Intensity-based light scattering profiles of Poly(A) brand manufacturer drug substances in different formulation buffers with A) Brand A, B) Brand B and C) Brand C (n=3).*

Table S 10.2 *- DLS Z-average, polydispersity index, and corresponding three highest intensity peak sizes (n=3 ± STD).*

Brand	**Buffer**	**Z-Average (d.nm)**	**PDI**	**Peak 1 (nm)**	**Peak 2 (nm)**	**Peak 3 (nm)**
Brand A	**1 × PBS pH 7.4**	193.1 ± 44.2	0.337 ± 0.064	270	21	5560
	Citrate pH 6	186.8 ± 49.1	0.311 ± 0.039	295	24.4	5560
	Citrate pH 4	845.4 ± 13.0	0.248 ± 0.076	955	68.1	-
Brand B	**1 × PBS pH 7.4**	66.4 ± 9.8	0.288 ± 0.076	91.1	21	-
	Citrate pH 6	54.5 ± 2.2	0.442 ± 0.085	58.8	37.8	396
	Citrate pH 4	128.0 ± 158.2	0.557 ± 0.264	24.4	1110	68.1
Brand C	**1 × PBS pH 7.4**	49.5 ± 1.0	0.250 ± 0.010	58.8	15.7	-
	Citrate pH 6	82.9 ± 12.1	0.456 ± 0.039	58.8	190	13.5
	Citrate pH 4	291.5 ± 89.9	0.716 ± 0.219	28.2	220	396

DLS analysis of branded Poly(A) samples across formulation buffers revealed highly variable size and size distribution profiles, with broad polydispersity and inconsistent z-averages **(Figure S 10.2, Table S 10.2).** These differences reflect the limited light-scattering capability of RNA, particularly for smaller or highly polydisperse species. Brand-specific differences were observed, with Brand A showing the highest PDI in PBS and large aggregates in citrate pH 4 (z-average 955 nm). Brand B and C showed smaller average sizes and lower PDIs in PBS and citrate pH 6. Citrate pH 4 consistently led to multimodal distributions and irreversible sample gelation at analysed concentrations, regardless of manufacturer. Overall, DLS results were influenced by buffer conditions, RNA conformation, and gelation potential at low pH, highlighting the method’s limitations for RNA characterisation due to weak scattering and high sample heterogeneity. Gelation potential was probed by measuring Poly(A) diffusion coefficients and calculating interaction parameter (K_D).

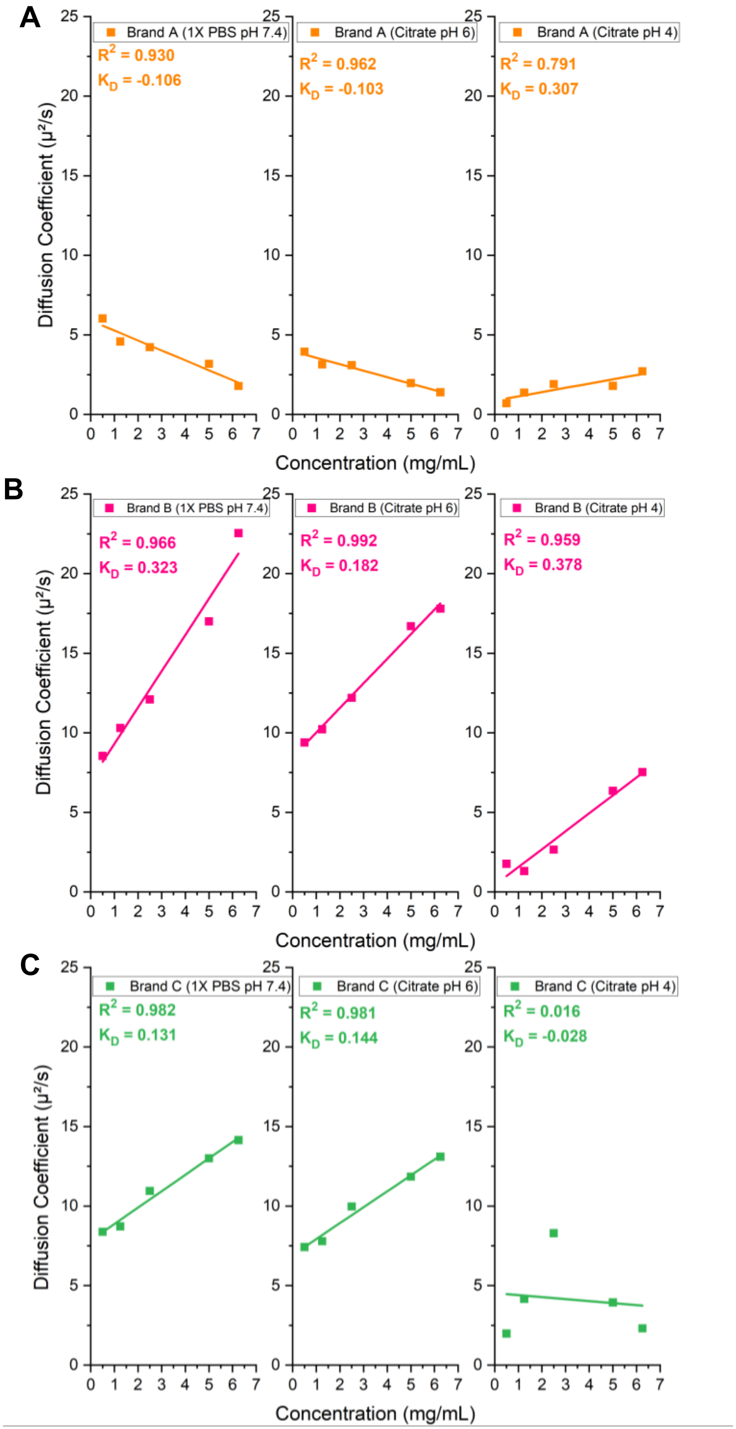

Figure S 10.3 *- Concentration dependent diffusion coefficients over a series of Poly(A) concentrations in different formulation buffers (0.50-6.25 mg/mL) , A) Brand A, B) Brand B, and C) Brand C. K_D calculated from linear regression slope/intercept, n=2.*

Calculated interaction parameter values (K_D) produced neither high repulsive values (positive K_D) nor high attractive values (negative K_D) **(Figure S 10.3),** indicating gelation noted was not detectable through diffusion coefficient measurements, however differences between sample buffers were noticed.

Capillary Gel Electrophoresis

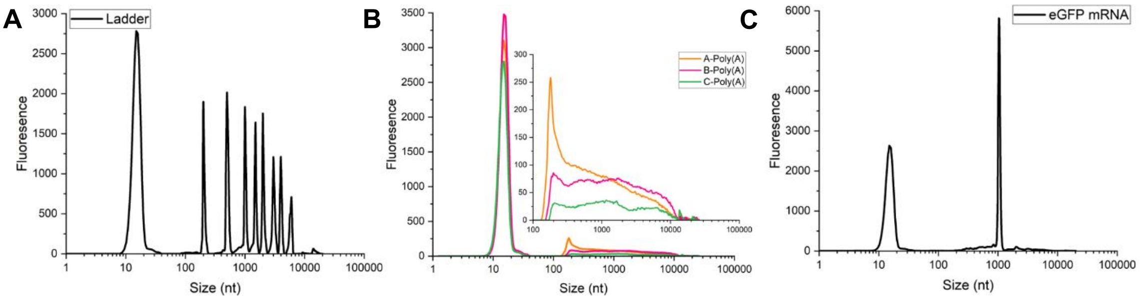

Figure S 10.4 *- CGE evaluation of Poly(A) vendor specific chain length distribution profiles of A) RNA Ladder, B) A, B, C--Poly(A)s and C) eGFP mRNA control (n=3).*

RiboGreen^{TM} Assay Evaluation

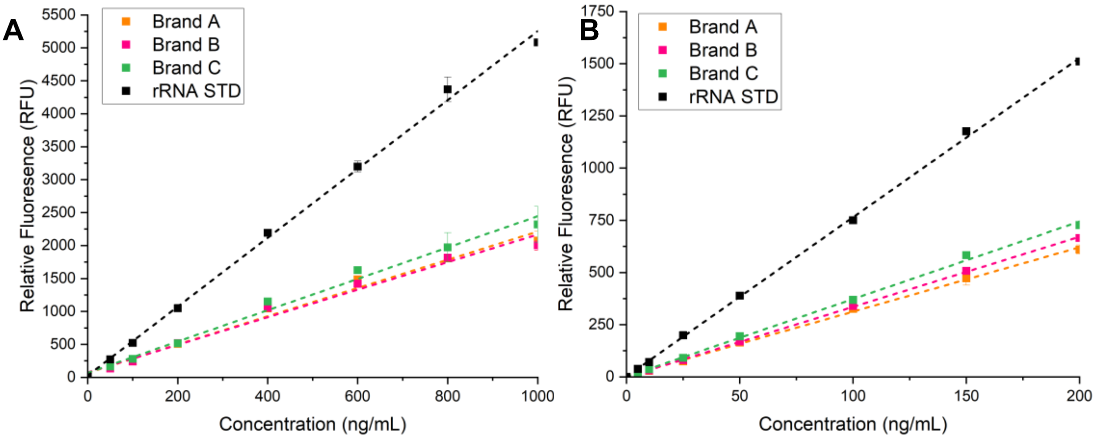

Figure S 10.5 *- Calibration curves of Branded Poly(A) drug substances and rRNA Standard using RIboGreen^{TM} Assay in A) Triton X-100 buffer and B) Tris-EDTA (TE) buffer, n=2 ± STD.*

Table S 10.3 *- Limit of Detection (LOD) and Limit of Quantification (LOQ) for Poly(A) in RIboGreen^{TM} buffer conditions. Linear regression of calibration curves. LOD = 3.3*(Standard Error/Slope) and LOQ = 10*(Standard Error/Slope), n=2.*

Brand	**rRNA STD**		**Brand A**		**Brand B**		**Brand C**	
Condition	**Tri X**	**TE**	**Tri X**	**TE**	**Tri X**	**TE**	**Tri X**	**TE**
R^2	0.998	0.999	0.987	0.999	0.984	0.999	0.990	0.998
LOD (ng/mL)	65.5	7.0	152.6	9.5	170.6	3.9	135.2	11.4
LOQ (ng/mL)	198.4	21.1	462.4	29.0	516.9	12.0	409.6	34.6

Table S 10.4 *- RIboGreen^{TM} concentration comparative differences between Poly(A) manufacturer drug substances, n=2, using one-way ANOVA Tukey test with samples analysed in Triton X-100 buffer. Ns = no statistical significance between means of relative fluorescence intensities per concentration level per Poly(A) manufacturer.*

Conc. (ng/mL)	Brand A-B	Brand A-C	Brand B-C
1000	ns	ns	ns
800	ns	ns	ns
600	ns	$p < 0.05$	$p < 0.005$
400	ns	$p < 0.05$	ns
200	ns	ns	ns
100	ns	ns	ns
50	ns	ns	ns

Table S 10.5 *- RiboGreen^{TM} concentration comparative differences between Poly(A) manufacturer drug substances, n=2, using one-way ANOVA Tukey test with samples analysed in TE buffer. Ns = no statistical significance between means of relative fluorescence intensities per concentration level per Poly(A) manufacturer.*

Conc. (ng/mL)	Brand A-B	Brand A-C	Brand B-C
200	ns	$p < 0.05$	ns
150	ns	$p < 0.05$	ns
100	ns	$p < 0.05$	$p < 0.05$
50	ns	$p < 0.05$	$p < 0.05$
25	ns	ns	ns
12.5	ns	ns	ns
5	ns	ns	ns

Further Quantification of Poly(A)-LNP Drug Product CQAs

Table S 10.6 *- NTA evaluation of Branded Poly(A) LNP formulations, (n=3 ± STD).*

LNP	**NTA**						
	Mean (nm)	**Mode (nm)**	**D10 (nm)**	**D50 (nm)**	**D90 (nm)**	**Span**	**Est. Conc (x10^{11} particles/mL)**
Brand A	68.3 ± 1.0	62.0 ± 0.9	46.8 ± 0.4	64.4 ± 1.3	90.4 ± 3.0	0.68 ± 0.03	2.35 ± 0.60
Brand B	66.8 ± 1.6	60.7 ± 1.6	45.5 ± 1.3	63.3 ± 1.7	90.2 ± 3.1	0.71 ± 0.04	3.04 ± 0.84
Brand C	68.8 ± 3.2	61.3 ± 3.4	46.2 ± 1.9	64.4 ± 3.1	92.9 ± 4.5	0.73 ± 0.01	2.54 ± 0.10

Table S 10.7 *- FI-AF4-MD evaluation of Branded Poly(A) LNP formulations and associated cumulative distribution values for radius of gyration, hydrodynamic radius and shape factor. Span values and shape factor distributional standard deviations not shown as rounding would produce standard deviation of ± 0.0 due to reproducible replicates. (n=3 ± STD).*

LNP	**FI-AF4-MD**													
	Et (min)	**Rec (%)**	**R_G Mode**	**R_G 10 (nm)**	**R_G 50 (nm)**	**R_G 90 (nm)**	**R_G Span**	**R_H 10 (nm)**	**R_H 50 (nm)**	**R_H 90 (nm)**	**R_H Span**	**SF 10**	**SF 50**	**SF 90**	**SF Span**
Brand A	22.3	88.8 ± 1.3	24.7 ± 0.1	23.1 ± 0.4	24.8 ± 0.2	27.1 ± 0.4	0.159	27.3 ± 0.8	29.9 ± 0.8	32.3 ± 0.9	0.167	0.824	0.838	0.856	0.038
Brand B	21.9	91.9 ± 7.1	24.2 ± 0.2	22.4 ± 0.5	24.1 ± 0.3	26.1 ± 0.2	0.152	26.9 ± 1.1	29.5 ± 0.8	32.0 ± 0.5	0.174	0.807	0.822	0.839	0.040
Brand C	22.3	92.6 ± 8.5	24.6 ± 0.3	22.8 ± 0.2	24.7 ± 0.2	27.4 ± 0.4	0.189	27.3 ± 1.0	30.1 ± 0.9	33.3 ± 0.6	0.200	0.809	0.826	0.847	0.046

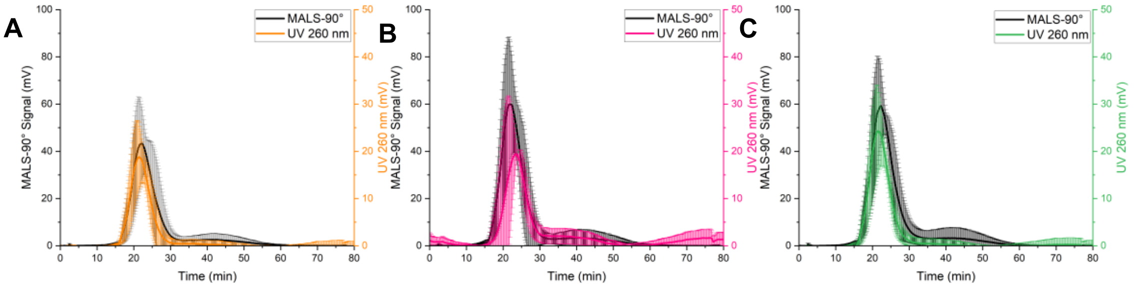

Figure S 10.6 *-- FI-AF4-MD of Poly(A) LNP formulations. MALS-90° and UV (260 nm) elution profiles or A) A-LNPs, B) B-LNPs, and C) C-LNPs. (n=3 ± STD).*

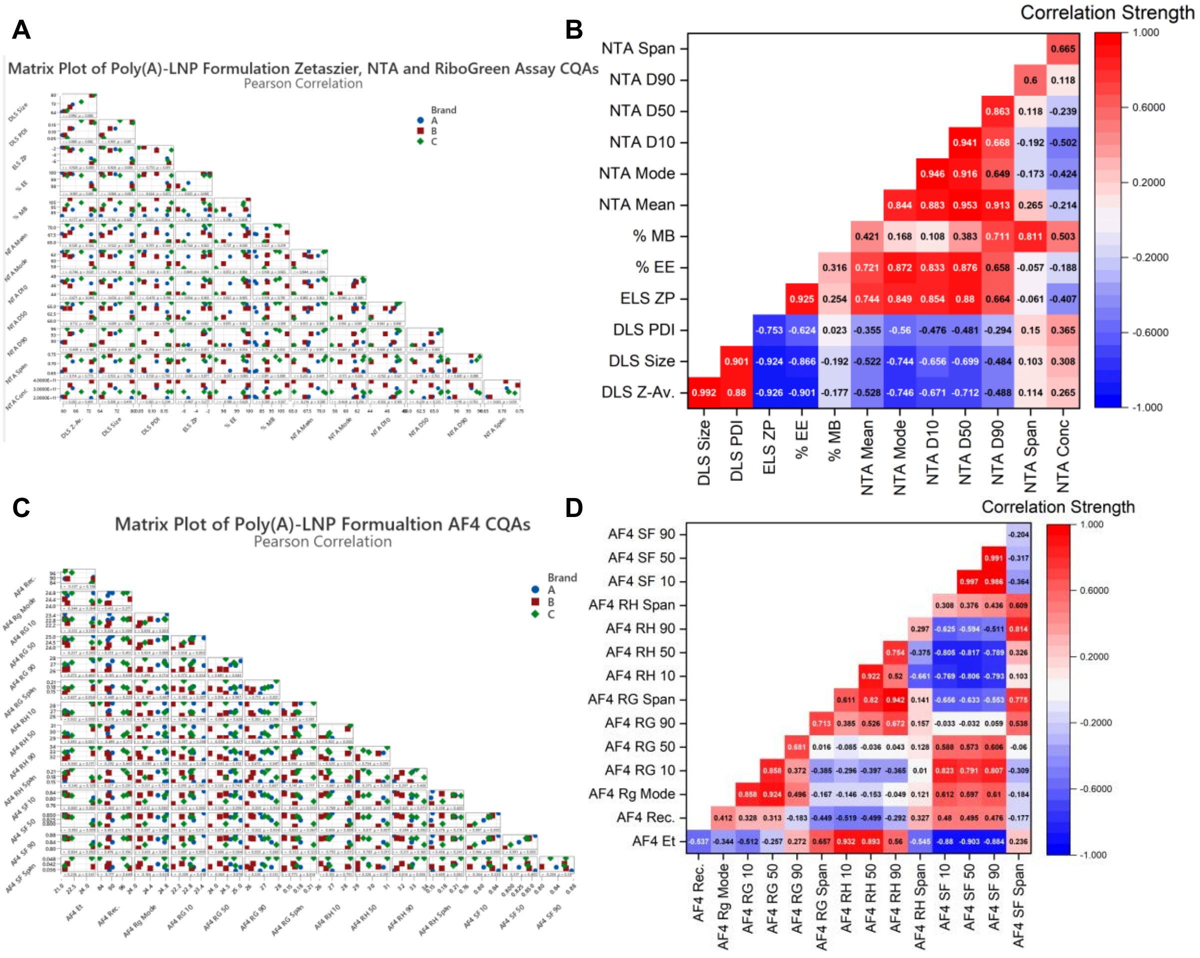

Figure S 10.7 *– Correlation matrix and heatmap correlation strength plots of evaluated Branded Poly(A)-LNP drug product CQAs split by technique pipelines. A) Matrix plot of Zetasizer, RiboGreen^{TM}, and NTA CQAs, B) correlation strengths of Zetasizer, RiboGreen^{TM}, and NTA CQAs. C) Matrix plot of FI-AF4-MD CQA outputs and D) correlation strengths of FI-AF4-MD CQA outputs.*

11. Chapter 5

***Table S 11.1** – Nanoparticle Tracking Analysis Poly(A) DOTAP-LNP dilution factor per experimental test.*

Parameter	NTA Dilution Factor	Poly(A) Concentration (μg/mL)
Post-Microfluidics	X10000	0.0055
Post Dialysis	X4000-8000	0.0137-0.00687
Post PVDF-Filtration	X100	0.55
Post PES-Filtration	X4000-8000	0.0137-0.00687
Post Day 0 and 1 x F/T Stress		

Process Parameter Testing of Prototype LNPs

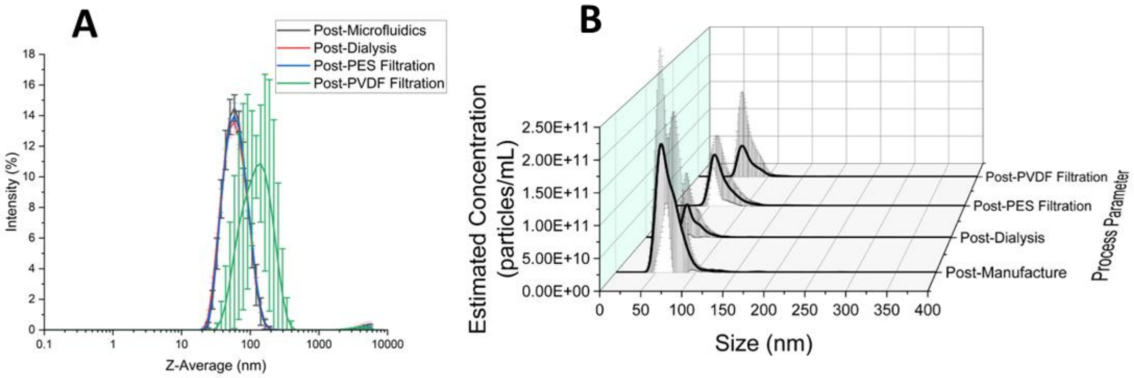

***Figure S 11.1** – Physicochemical trend analysis of process parameter impact on Poly(A)-DOTAP-LNP CQAs. A) DLS and B) NTA measured particle size distribution, (mean ± standard deviation, n=3).*

***Table S 11.2** – Physicochemical characterisation of Poly(A)-DOTAP-LNPs at various in-process steps using DLS, ELS, particle tracking analysis and Poly(A) encapsulation efficiency assay, (mean ± standard deviation, n=3), one way ANOVA Dunnett Test comparing each process parameter with post-dialysis parameter per CQA, *p < 0.05, **p < 0.005, ***p < 0.0005 .*

Process Parameter	Zetasizer			NTA		RiboGreen™	
	Z-average (d.nm)	PDI	Zeta Potential (mV)	Mean Size (nm)	Mode Size (nm)	EE (%)	MB (%)
Post-Microfluidics	57 (± 3)	0.13 ± 0.03	1.5 ± 0.6**	66 (± 10)	61 (± 10)	99 (± 0)	102 (± 10)***
Post-Dialysis (Final Product)	56 (± 1)	0.15 ± 0.04	4.8 ± 0.8	68 (± 9)	59 (± 8)	98.0 ± 2.2	69 (± 3)
Post-PES Filtration	56.9 ± 1.2	0.15 ± 0.02	4.4 ± 0.5	66.1 ± 6.0	56.7 ± 4.3	99.2 ± 0.2	67.0 ± 0.8
Post-PVDF Filtration	115.7 ± 45.5*	0.16 ± 0.04	1.2 ± 0.9**	87.4 ± 20.5	74.3 ± 14.0	73.2 ± 13.5*	2.9 ± 1.1***

***Table S 11.3** - Physicochemical trend analysis of process parameter impact on Poly(A)-DOTAP-LNP CQAs, using NTA size distributions and span data (mean ± standard deviation, n=3).*

Process Parameter	**NTA Size Distribution**			
	D10 (nm)	D50 (nm)	D90 (nm)	Span
Post-Microfluidics	53.8 ± 8.5	63.4 ± 10.1	79.7 ± 12.6	0.41 ± 0.11
Post-Dialysis	52.2 ± 6.0	63.7 ± 8.7	87.5 ± 12.4	0.55 ± 0.03
Post PES Filtration	50.3 ± 3.4	61.6 ± 5.0	86.2 ± 7.9	0.58 ± 0.04
Post PVDF Filtration	63.2 ± 12.0	80.9 ± 16.9	120.0 ± 34.8	0.68 ± 0.17

Stability Testing of Refrigerated LNP Formulations

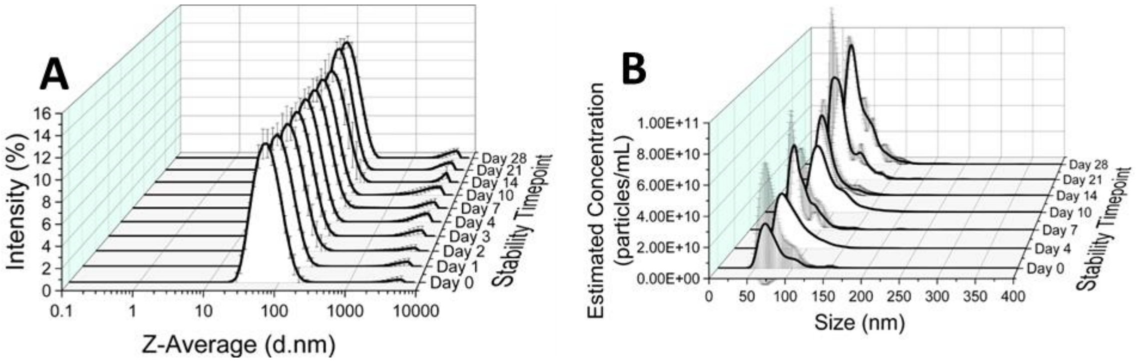

***Figure S 11.2** - Physicochemical trend analysis of Poly(A)-DOTAP-LNPs over a 28-day period. Using A) DLS and B) NTA measured particle size distribution, (mean ± standard deviation, n=2‡, n=3).*

Table S 11.4 *– Physicochemical characterisation of refrigerated (4 °C) storage stability impact on Poly(A)-DOTAP-LNPs using DLS, ELS, particle tracking analysis and Poly(A) encapsulation efficiency assay, (mean ± standard deviation, n=2‡, n=3), one way ANOVA Dunnett Test comparing each timepoint with day 0 CQAs, *p < 0.05, **p < 0.005,***p < 0.0005.*

Stability Timepoint	**Zetasizer**			**NTA**		**RiboGreen™**	
	Z-average (d.nm)	PDI	Zeta Potential (mV)	Mean Size (nm)	Mode Size (nm)	EE (%)	MB (%)
Day 0	62 (± 3)	0.16 ± 0.02	6.7 ± 0.7	77 (± 5)	66 (± 4)	99 (± 0)	66.9 ± 13.7
Day 1	67 (± 3)	0.19 ± 0.03	-	-	-	-	-
Day 2	69 (± 4)	0.19 ± 0.04	-	-	-	-	-
Day 3	71 (± 3)	0.21 ± 0.02	-	-	-	-	-
Day 4	72 (± 2)	0.22 ± 0.02	-	85 (± 12)	68 (± 5)	-	-
Day 7	73 (± 3)*	0.21 ± 0.03	6.2 ± 1.2	69 (± 13)	56 (± 9)	99 (± 0)	-
Day 10	75 (± 3)*	0.23 ± 0.03*	7.7 ± 0.4	97 (± 7)*	79 (± 3)*	99 (± 0)	-
Day 14‡	82 (± 19)**	0.24 ± 0.07*	7.3 ± 0.0	75 (± 5)	64 (± 6)	99 (± 0)	-
Day 21‡	76 (± 5)*	0.20 ± 0.01	6.3 ± 0.6	81 (± 7)	68 (± 6)	99 (± 0)	-
Day 28‡	76 (± 7.3)*	0.21 ± 0.02	6.1 ± 0.0	86 (± 4)	73 (± 1)	99 (± 0)	-

Table S 11.5 *- Physicochemical trend analysis of Poly(A)-DOTAP-LNPs over a 28-day period, using NTA size distributions and span data (mean ± standard deviation, n=2‡, n=3).*

Stability Timepoint	**NTA Size Distribution**			
	D10 (nm)	**D50 (nm)**	**D90 (nm)**	**Span**
Day 0	56.6 ± 4.4	71.6 ± 4.7	101.1 ± 5.2	0.62 ± 0.07
Day 4	58.0 ± 4.1	79.6 ± 13.0	117.4 ± 19.7	0.74 ± 0.09
Day 7	50.2 ± 6.8	62.7 ± 11.3	92.8 ± 14.6	0.68 ± 0.00
Day 10	66.6 ± 1.8	89.1 ± 7.9	133.5 ± 14.1	0.75 ± 0.08
Day 14‡	55.4 ± 2.4	69.2 ± 3.4	99.9 ± 10.5	0.64 ± 0.09
Day 21‡	59.0 ± 3.7	73.5 ± 5.2	110.3 ± 0.3	0.70 ± 0.01
Day 28‡	64.1 ± 2.5	80.4 ± 3.9	115.7 ± 8.1	0.64 ± 0.04

Stability Testing of LNP Formulations at Ultra Low Temperature (-80 °C)

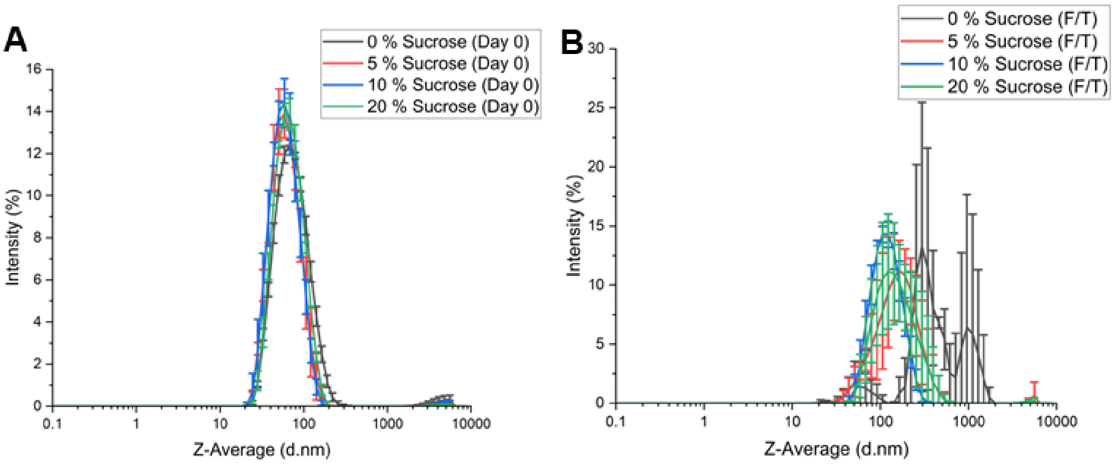

Figure S 11.3 *- Physicochemical trend analysis of frozen storage stability of Poly(A)-DOTAP-LNPs formulated with varying concentration of cryoprotectant on the day of manufacture and after 1 X freeze/thaw cycle (1 X F/T) from -80 °C to room temperature. DLS measured particle size distribution on A) Day 0 and B) post freeze/thaw stress. (mean ± standard deviation, n=3).*

Table S 11.6 *– Physicochemical trend analysis of frozen storage stability of Poly(A)-DOTAP-LNPs formulated with varying concentrations of sucrose (0-20%) on the day of manufacture and after 1 X freeze/thaw cycle (1 X F/T) from -80 °C to ambient temperature using DLS (5.50 µg/mL Poly(A)), ELS (5.50 µg/mL Poly(A)), nanoparticle tracking analysis (Table.S1 for Poly(A) conc.) and the RiboGreen^{TM} assay for measuring encapsulation efficiency (0.75 µg/mL Poly(A)), (mean ± standard deviation, n=3), one way ANOVA Dunnett Test comparing each timepoint with day 0 CQAs per individual sucrose concentration condition, *p < 0.05, **p < 0.005, ***p < 0.0005.*

		Zetasizer			**NTA**		**RiboGreen™**	
Sample	**Timepoint**	**Z-Average (d.nm)**	**PDI**	**Zeta Potential (mV)**	**Mean Size (nm)**	**Mode Size (nm)**	**EE (%)**	**MB (%)**
0 % (Control)	**Day 0**	60 (± 5)	0.16 (± 0.02)	7.2 (± 0.8)	71 (± 9)	61 (± 7)	99.1 (±0.3)	71 (± 5)
	1 X F/T	732 (± 366)*	0.45 (±0.18)*	7.8 (± 0.7)	91 (± 17)	63 (± 15)	99.0 (± 0.2)	-
5 % Sucrose (w/v)	**Day 0**	56 (± 3)	0.14 (± 0.03)	4.8 (± 0.7)	67 (± 8.0)	57 (± 5)	99.3 (± 0.2)	72 (± 4)
	1 X F/T	155 (± 31)**	0.31 (± 0.17)	5.6 (± 0.2)	108 (± 8)**	75 (± 4) *	99.2 (± 0.2)	-
10 % Sucrose (w/v)	**Day 0**	56 (± 3)	0.13 (± 0.03)	4.8 (± 0.9)	66 (± 7)	57 (± 5)	99.3 (± 0.2)	81 (± 6)
	1 X F/T	110 (± 9)**	0.12 (± 0.01)	4.8 (± 0.7)	104 (± 11)*	79 (± 15)	99.2 (± 0.2)	-
20 % Sucrose (w/v)	**Day 0**	55 (± 3)	0.13 (± 0.01)	6.7 (± 1.1)	74 (± 4)	64 (± 3)	99.3 (± 0.1)	87 (± 8)
	1 X F/T	149 (± 57)*	0.22 (± 0.18)	7.8 (± 0.3)*	109 (± 4)*	81 (± 14)	99.2 (± 0.2)	-

Table S 11.7 - *Physicochemical trend analysis of frozen storage stability of Poly(A)-DOTAP-LNPs formulated with varying concentration of cryoprotectant on the day of manufacture and after 1 X freeze/thaw cycle (1 X F/T) from -80 °C to room temperature, using NTA size distributions and span data (mean ± standard deviation, n=3), one-way ANOVA comparison from day 0 per condition,*p < 0.05, **p < 0.005 .*

Frozen Storage Condition	**Timepoint**	**NTA Size Distribution**			
		D10 (nm)	**D50 (nm)**	**D90 (nm)**	**Span**
0 % Sucrose (Control)	Day 0	54.4 ± 5.7	66.4 ± 8.1	91.7 ± 11.3	0.56 ± 0.05
	1 X F/T	44.0 ± 18.5	81.4 ± 22.5	150.8 ± 16.1	1.28 ± 0.48*
5 % Sucrose (w/v)	Day 0	50.4 ± 3.5	61.1 ± 5.4	86.6 ± 12.5	0.59 ± 0.12
	1 X F/T	69.0 ± 4.2	95.5 ± 8.1	167.7 ± 20.7	1.03 ± 0.16*
10 % Sucrose (w/v)	Day 0	50.2 ± 4.5	61.4 ± 6.1	86.3 ± 10.3	0.59 ± 0.07
	1 X F/T	67.5 ± 4.6	94.9 ± 13.1	156.8 ± 15.2	0.94 ± 0.07**
20 % Sucrose (w/v)	Day 0	57.0 ± 2.6	69.1 ± 3.7	93.7 ± 6.0	0.53 ± 0.03
	1 X F/T	60.2 ± 2.6	104.8 ± 3.7	167.0 ± 27.7	1.01 ± 0.36

Frit-Inlet Asymmetric-flow Field-Flow Fractionation Method Development

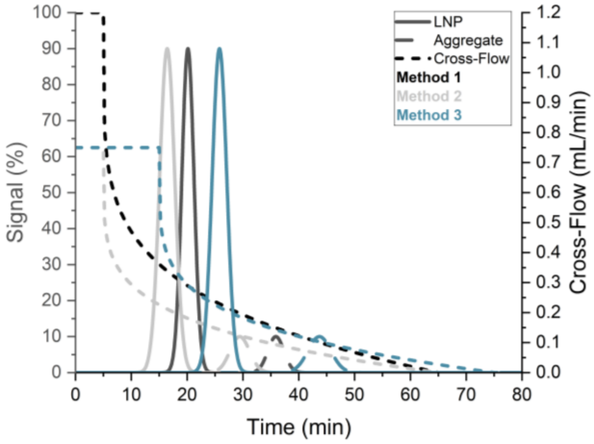

Figure S 11.4 – *Frit-inlet Asymmetric-Flow Field-Flow Fractionation hyphenated multidetector method development. Method simulations of monodisperse 60 nm LNPs and 150 nm aggregates.*

Table S 11.8 – *Performance criteria Guidelines for Developed FI-AF4-MD Methodology.*

Performance Criterion	**ISO Standard**	**Experimental Value**
Recovery	≥ 70 %	97 %
Selectivity	> 1	1.54
Retention Factor	$0.03 \leq R \leq 0.2$	0.1
Resolution Factor	> 1.5	LNPs are poly disperse.

12. Chapter 6

AF4 Separation Profile

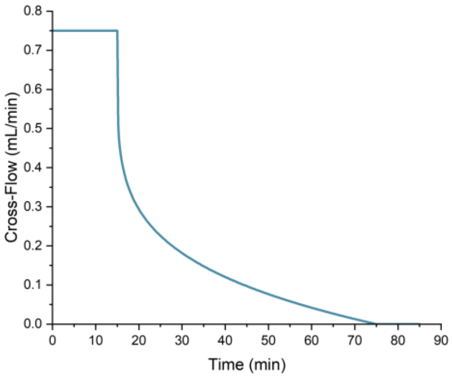

Figure S 12.1 *- AF4 cross-flow decay profile. Profile used for all LNP formulations, with extended wash step (10 minutes instead of 5 minutes) for LNP-7/8.*

Interpolation Script using MALS and UV Data as Exemplar Inputs

- import numpy as np
- import pandas as pd
- from scipy.optimize import curve_fit
- import matplotlib.pyplot as plt
- from scipy.interpolate import interp1d

- MALS = pd.read_csv("file.csv")
- print(MALS.columns)
- #relative_abundance or time(min)
- Time = MALS['Time'].to_numpy()
- #np.set_printoptions(threshold=np.inf)
- #print(time)
- print(', '.join(map(str, Time)))

- import numpy as np
- from sklearn.metrics import mean_squared_error, r2_score
- #MALS data
- time_MALS = np.array([example data])
- MALS_data = np.array([example data])
- # UV data
- time_UV = np.array([example data])
- UV_data = np.array([example data])

- # Step 1: Create interpolation function for M1 (model) data
- interp_func = interp1d(time_MALS, MALS_data, kind='cubic', fill_value='extrapolate')
- # Step 2: Interpolate model data at MALS timestamps
- MALS_interpolated = interp_func(time_UV)
- r2 = r2_score(UV_data, MALS_interpolated)
- rmse = np.sqrt(mean_squared_error(UV_data, MALS_interpolated))
- nrmse = rmse / np.mean(UV_data)
- print("RMSE:", rmse)

- print(f"Normalized RMSE = {nrmse:.4f}")
- print("R²:", r2)

- # Generate a smooth x-range for plotting the interpolation
- x_dense = np.linspace(min(time_UV), max(time_UV), 500)
- y_interp_dense = interp_func(x_dense) # using the same function as used before
- # Plot everything
- plt.figure(figsize=(10, 6))
- plt.plot(time_UV, UV_data, label="UV Data (Model)", color="blue")
- plt.plot(time_MALS, MALS_data, label="MALS Data (Experimental)", color="red")
- plt.xlabel("Time (min)")
- plt.ylabel("Normalised Detector Signal")
- plt.legend()
- plt.show()

Gaussian Fitting Script

- import numpy as np
- import pandas as pd
- import matplotlib.pyplot as plt
- from scipy.optimize import curve_fit
- from scipy.signal import find_peaks

- # Gaussian
- def gaussian(x, amp, mu, sigma):
- return amp * np.exp(-(x - mu)**2 / (2 * sigma**2))
- def total_gaussian(x, *params):
- y = np.zeros_like(x)
- n = int(len(params) / 3)
- for i in range(n):
- amp, mu, sigma = params[3*i:3*i+3]
- y += gaussian(x, amp, mu, sigma)
- return y

- # Load CSV data
- df = pd.read_csv("example data")
- x = df['Time'].values
- y = df['nMALS'].values

- # Auto-detect peaks
- peaks, _ = find_peaks(y, height=np.max(y)*0.02, distance=40)
- print(f"Detected {len(peaks)} peaks at volumes:", x[peaks])

- # Build initial guess from peaks
- init_guess = []
- for p in peaks:
- amp = y[p]
- mu = x[p]
- sigma = 0.2 # start with narrow width
- init_guess += [amp, mu, sigma]

```
•   # Fit model
•   popt, _ = curve_fit(total_gaussian, x, y, p0=init_guess)

•   # Compute areas
•   n_peaks = len(peaks)
•   areas = []
•   for i in range(n_peaks):
•   amp, mu, sigma = popt[3*i:3*i+3]
•   area = amp * sigma * np.sqrt(2 * np.pi)
•   areas.append(area)
•   areas = np.array(areas)
•   percentages = 100 * areas / areas.sum()

•   # Plot
•   colors = ['g', 'b', 'orange', 'purple', 'cyan']
•   plt.plot(x, y, label='Raw Data')
•   plt.plot(x, total_gaussian(x, *popt), 'r--', label='Fitted Total')
•   for i in range(n_peaks):
•   amp, mu, sigma = popt[3*i:3*i+3]
•   peak = gaussian(x, amp, mu, sigma)
•   plt.fill_between(x, peak, alpha=0.3, color=colors[i % len(colors)],
•   label=f"Peak {i+1}: {percentages[i]:.1f}%")
•   plt.xlabel("Elution Time (min)")
•   plt.ylabel("Normalised MALS Signal")
•   plt.title("Auto-Detected AF4-MALS (Gaussian)")
•   plt.legend()
•   plt.show()

•   n_peaks = int(len(popt) / 3)
•   for i in range(n_peaks):
•   amp, mu, sigma = popt[3*i:3*i+3]
•   print(f"Peak {i+1}: Amplitude={amp:.2f}, Mean (mu)={mu:.2f}, Width (σ)={sigma:.2f}")

•   # Print exact values
•   for i in range(n_peaks):
•   print(f"Peak {i+1}: Area = {areas[i]:.4f}, % Total = {percentages[i]:.2f}%")

•   # Calculate R² (coefficient of determination)
•   y_fit = total_gaussian(x, *popt) # or total_skewed(x, *popt) for skewed fits
•   ss_res = np.sum((y - y_fit) ** 2)
•   ss_tot = np.sum((y - np.mean(y)) ** 2)
•   r_squared = 1 - (ss_res / ss_tot)
•   print(f"R² of fit: {r_squared:.4f}")
```

AF4 System Pressure Traces per LNP Sample

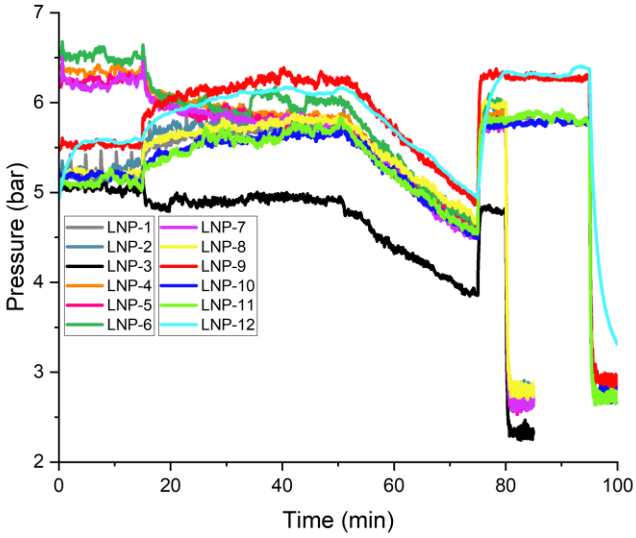

***Figure S 12.2** - AF4 averaged system pressure traces per each LNP in **Table 6.1**, with extended wash step (10 minutes instead of 5 minutes) for LNPs 9-12, (n=4).*

Gaussian Fitting Parameters

Table S 12.1 *- Gaussian Fitting Parameters used within code for fitting MALS and UV detector elution profiles.*

LNP Sample #	Detector	Height	Distance	R^2 Fitting Score
LNP-1	**MALS**	0.200	5	0.9993
	UV	0.200	20	0.9953
LNP-2	**MALS**	0.050	30	0.9998
	UV	0.040	10	0.9979
LNP-3	**MALS**	0.010	90	0.9997
	UV	0.010	90	0.9994
LNP-4	**MALS**	0.002	90	0.9999
	UV	0.010	70	0.9997
LNP-5	**MALS**	0.010	50	0.9997
	UV	0.010	50	0.9996
LNP-6	**MALS**	0.008	100	0.9998
	UV	0.010	50	0.9997
LNP-7	**MALS**	0.005	90	0.9998
	UV	0.005	90	0.9978
LNP-8	**MALS**	0.100	40	0.9949
	UV	0.100	50	0.9968
LNP-9	**MALS**	0.200	20	0.9995
	UV	0.200	40	0.9962
LNP-10	**MALS**	0.030	2	0.9990
	UV	0.020	20	0.9955
LNP-11	**MALS**	0.050	40	0.9978
	UV	0.200	30	0.9778
LNP-12	**MALS**	0.050	20	0.9982
	UV	0.050	30	0.9991

Calibration Curve of Simulated Hydrodynamic Diameter Particle Size against Expected Elution Time

Separation and detection defined methodology was utilised from **section 6.3.2**, with simulation profiles particle hydrodynamic radii sizes, 15 nm, to 100 nm. The calibration plot was fitted to 2nd order polynomial regression to obtain an equation of best fit to apply experimental elution times to further compare between simulated *versus* experimental sub-population elution profiles.

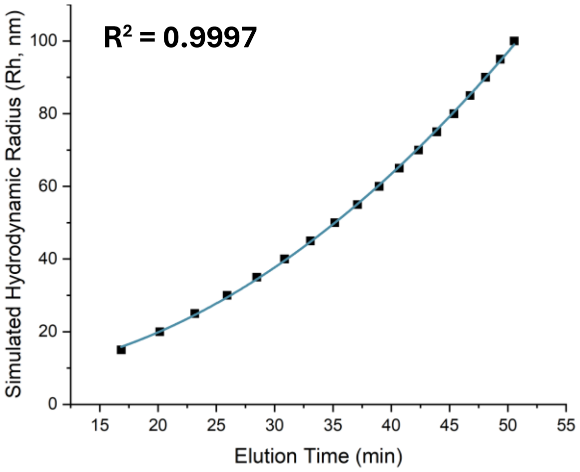

Figure S 12.3 *– Polynomial (2nd order) regression of increasing particle sizes versus expected elution time according to simulated AF4 separation profile.*